



PATHWAYS AND PROCESSES UNDERPINNING AXONAL BIOLOGY AND PATHOBIOLOGY

EDITED BY: Pabitra Sahoo, Dianna E. Willis and James N. Sleigh
PUBLISHED IN: Frontiers in Molecular Neuroscience



frontiers

Frontiers eBook Copyright Statement

The copyright in the text of individual articles in this eBook is the property of their respective authors or their respective institutions or funders. The copyright in graphics and images within each article may be subject to copyright of other parties. In both cases this is subject to a license granted to Frontiers.

The compilation of articles constituting this eBook is the property of Frontiers.

Each article within this eBook, and the eBook itself, are published under the most recent version of the Creative Commons CC-BY licence.

The version current at the date of publication of this eBook is CC-BY 4.0. If the CC-BY licence is updated, the licence granted by Frontiers is automatically updated to the new version.

When exercising any right under the CC-BY licence, Frontiers must be attributed as the original publisher of the article or eBook, as applicable.

Authors have the responsibility of ensuring that any graphics or other materials which are the property of others may be included in the CC-BY licence, but this should be checked before relying on the CC-BY licence to reproduce those materials. Any copyright notices relating to those materials must be complied with.

Copyright and source acknowledgement notices may not be removed and must be displayed in any copy, derivative work or partial copy which includes the elements in question.

All copyright, and all rights therein, are protected by national and international copyright laws. The above represents a summary only. For further information please read Frontiers' Conditions for Website Use and Copyright Statement, and the applicable CC-BY licence.

ISSN 1664-8714

ISBN 978-2-88974-917-1

DOI 10.3389/978-2-88974-917-1

About Frontiers

Frontiers is more than just an open-access publisher of scholarly articles: it is a pioneering approach to the world of academia, radically improving the way scholarly research is managed. The grand vision of Frontiers is a world where all people have an equal opportunity to seek, share and generate knowledge. Frontiers provides immediate and permanent online open access to all its publications, but this alone is not enough to realize our grand goals.

Frontiers Journal Series

The Frontiers Journal Series is a multi-tier and interdisciplinary set of open-access, online journals, promising a paradigm shift from the current review, selection and dissemination processes in academic publishing. All Frontiers journals are driven by researchers for researchers; therefore, they constitute a service to the scholarly community. At the same time, the Frontiers Journal Series operates on a revolutionary invention, the tiered publishing system, initially addressing specific communities of scholars, and gradually climbing up to broader public understanding, thus serving the interests of the lay society, too.

Dedication to Quality

Each Frontiers article is a landmark of the highest quality, thanks to genuinely collaborative interactions between authors and review editors, who include some of the world's best academicians. Research must be certified by peers before entering a stream of knowledge that may eventually reach the public - and shape society; therefore, Frontiers only applies the most rigorous and unbiased reviews. Frontiers revolutionizes research publishing by freely delivering the most outstanding research, evaluated with no bias from both the academic and social point of view. By applying the most advanced information technologies, Frontiers is catapulting scholarly publishing into a new generation.

What are Frontiers Research Topics?

Frontiers Research Topics are very popular trademarks of the Frontiers Journals Series: they are collections of at least ten articles, all centered on a particular subject. With their unique mix of varied contributions from Original Research to Review Articles, Frontiers Research Topics unify the most influential researchers, the latest key findings and historical advances in a hot research area! Find out more on how to host your own Frontiers Research Topic or contribute to one as an author by contacting the Frontiers Editorial Office: frontiersin.org/about/contact

PATHWAYS AND PROCESSES UNDERPINNING AXONAL BIOLOGY AND PATHOBIOLOGY

Topic Editors:

Pabitra Sahoo, University of South Carolina, United States

Dianna E. Willis, Burke-Cornell Medical Research Institute, United States

James N. Sleigh, University College London, United Kingdom

Citation: Sahoo, P., Willis, D. E., Sleigh, J. N., eds. (2022). Pathways and Processes Underpinning Axonal Biology and Pathobiology. Lausanne: Frontiers Media SA.
doi: 10.3389/978-2-88974-917-1

Table of Contents

- 04 Editorial: Pathways and Processes Underpinning Axonal Biology and Pathobiology**
Pabitra K. Sahoo, Dianna E. Willis and James N. Sleight
- 07 Axotomy Induces Drp1-Dependent Fragmentation of Axonal Mitochondria**
Joseph Kedra, Shen Lin, Almudena Pacheco, Gianluca Gallo and George M. Smith
- 24 Axonal Transport and Local Translation of mRNA in Neurodegenerative Diseases**
Seiichi Nagano and Toshiyuki Araki
- 32 The Curious Anti-Pathology of the Wld^s Mutation: Paradoxical Postsynaptic Spine Growth Accompanies Delayed Presynaptic Wallerian Degeneration**
Oswald Steward, Jennifer M. Yonan and Paula M. Falk
- 45 MFN2 Deficiency Impairs Mitochondrial Transport and Downregulates Motor Protein Expression in Human Spinal Motor Neurons**
Yongchao Mou, Joshua Dein, Zhenyu Chen, Mrunali Jagdale and Xue-Jun Li
- 59 Bioenergetic Requirements and Spatiotemporal Profile of Nerve Growth Factor Induced PI3K-Akt Signaling Along Sensory Axons**
Rajiv Sainath and Gianluca Gallo
- 73 Neuronal Activity in the Sciatic Nerve Is Accompanied by Immediate Cytoskeletal Changes**
Bossmat Yehuda, Tal Gradus Pery, Efrat Ophir, Tamar Blumenfeld-Katzir, Anton Sheinin, Yael Alon, Noy Danino, Eran Perlson and Uri Nevo
- 82 Failure to Upregulate the RNA Binding Protein ZBP After Injury Leads to Impaired Regeneration in a Rodent Model of Diabetic Peripheral Neuropathy**
James I. Jones, Christopher J. Costa, Caitlin Cooney, David C. Goldberg, Matthew Ponticello, Melanie W. Cohen, Wilfredo Mellado, Thong C. Ma and Dianna E. Willis
- 95 SARM1 Suppresses Axon Branching Through Attenuation of Axonal Cytoskeletal Dynamics**
Andrea Ketschek, Sabrina M. Holland and Gianluca Gallo
- 112 LIS1 and NDEL1 Regulate Axonal Trafficking of Mitochondria in Mature Neurons**
Jai P. Pandey, Liang Shi, Remi A. Brebion and Deanna S. Smith
- 125 SARM1 Depletion Slows Axon Degeneration in a CNS Model of Neurotropic Viral Infection**
Colin L. Crawford, Christina Antoniou, Lina Komarek, Verena Schultz, Claire L. Donald, Paul Montague, Susan C. Barnett, Christopher Linington, Hugh J. Willison, Alain Kohl, Michael P. Coleman and Julia M. Edgar



Editorial: Pathways and Processes Underpinning Axonal Biology and Pathobiology

Pabitra K. Sahoo^{1*}, Dianna E. Willis^{2,3*} and James N. Sleigh^{4,5*}

¹ Department of Biological Sciences, University of South Carolina, Columbia, SC, United States, ² Burke Neurological Institute, White Plains, NY, United States, ³ Feil Family Brain & Mind Research Institute, Weill Cornell Medicine, New York, NY, United States, ⁴ Department of Neuromuscular Diseases and UCL Queen Square Motor Neuron Disease Centre, UCL Queen Square Institute of Neurology, University College London, London, United Kingdom, ⁵ UK Dementia Research Institute, University College London, London, United Kingdom

Keywords: axonal translation, axonal transport, nerve injury, nerve regeneration, neurotrophins, Wallerian degeneration

Editorial on the Research Topic

Pathways and Processes Underpinning Axonal Biology and Pathobiology

Neurons are highly polarized cells with axons that can extend beyond a meter. Axons provide long-range connections between somas and target cells, permitting rapid electrical communication. Given these distances, axons require a continuous supply of organelles, mRNAs, and proteins. This is achieved through bi-directional cargo trafficking along microtubules by motor proteins in the process of axonal transport; however, *in vivo* axonal transport rates are well below 10 $\mu\text{m/s}$ (Tosolini et al., 2021), thus additional mechanisms are required for distal axons to efficiently respond to environmental stimuli. Consequently, local translation of readily-available transcripts provides an important mechanism to overcome distance constraints and allow proteome modification (Dalla Costa et al., 2021). Nevertheless, these vital processes are not independent since mRNA must travel from the nucleus to translation sites. In fact, transport and translation are intricately linked through a process called “hitchhiking,” whereby mRNAs are co-transported with organelles through tethering of RNA-binding proteins (RBPs) for on-demand axonal translation (Vargas et al., 2022). Accordingly, disruption of transport or translation in axons can impair neurodevelopment and drive neurodegeneration (Costa and Willis, 2018; Sleigh et al., 2019). Nonetheless, despite recent developments in axon-specific methods (Farias et al., 2019; Surana et al., 2020), it is often unclear whether perturbations are a cause or consequence of neurodegeneration.

With this special issue, we aim to showcase recent advances in axon biology to stimulate a field poised to generate a comprehensive understanding of pathways and processes critical to axonal integrity. We present ten articles covering themes of transport/translation, degeneration, and nerve injury/regeneration (Figure 1).

Nagano and Araki present a review discussing the significance of axonal transport and translation to pathogenesis of neurodegenerative diseases. After introducing the physiological importance of these processes, evidence linking their impairment to neurodegeneration is reviewed. It is highlighted that many dysregulated axonal transcripts encode cytoskeleton components of growth cones/synapses, indicating that these mRNAs are required for formation and function of axon terminals.

OPEN ACCESS

Edited and reviewed by:

Jean-Marc Taymans,
Institut National de la Santé et de la
Recherche Médicale
(INSERM), France

*Correspondence:

Pabitra K. Sahoo
sahoop@mailbox.sc.edu
orcid.org/0000-0002-1076-9409
Dianna E. Willis
diw2004@med.cornell.edu
orcid.org/0000-0003-1442-3533
James N. Sleigh
j.sleigh@ucl.ac.uk
orcid.org/0000-0002-3782-9045

Specialty section:

This article was submitted to
Molecular Signalling and Pathways,
a section of the journal
Frontiers in Molecular Neuroscience

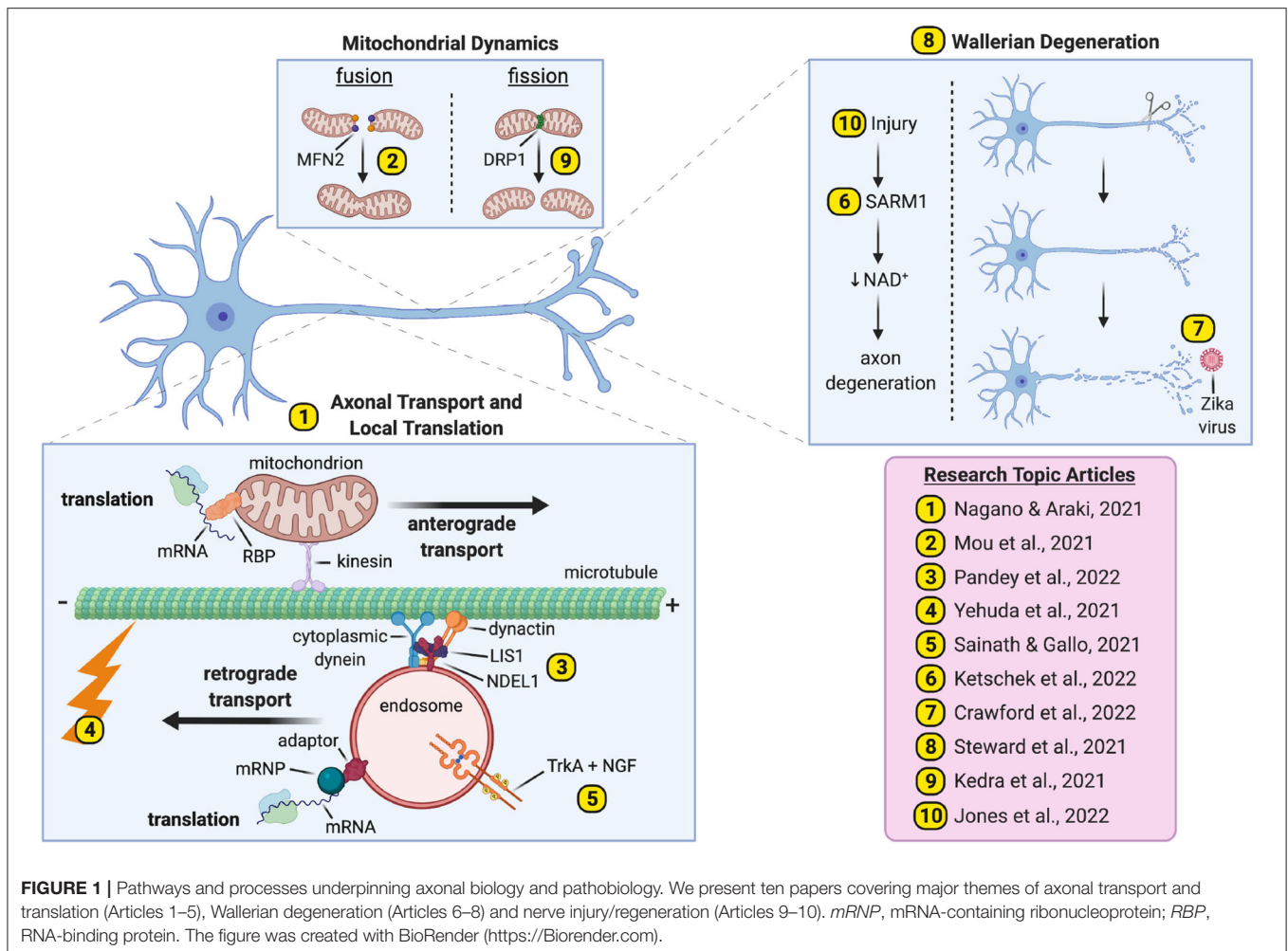
Received: 24 February 2022

Accepted: 02 March 2022

Published: 23 March 2022

Citation:

Sahoo PK, Willis DE and Sleigh JN
(2022) Editorial: Pathways and
Processes Underpinning Axonal
Biology and Pathobiology.
Front. Mol. Neurosci. 15:883244.
doi: 10.3389/fnmol.2022.883244



Mou et al. present a human motor neuron model for mitofusin-2 (*MFN2*) deficiency. *MFN2* mediates mitochondrial fusion and dominantly inherited *MFN2* mutations cause Charcot-Marie-Tooth; however, the mechanisms driving peripheral neuropathy remain unresolved. To address this, *MFN2* was knocked-down and shown to impair morphology, function, and trafficking of axonal mitochondria. Additionally, *MFN2*-deficient motor neurons displayed increased phosphorylated neurofilament inclusions, as well as diminished motor protein availability.

LIS1 and *NDEL1* stimulate dynein activity; however, their role in mitochondrial transport remains unclear. Pandey et al. thus evaluated mitochondria in sciatic axons of *LIS1*^{+/-} mice and showed them to be more prevalent than in controls, replicating a disruption in rats caused by dynein inhibition. *LIS1* and *NDEL1* knockdown in rat sensory neurons perturbed physiological morphology, percentage motility and transport speeds of axonal mitochondria. Conversely, *LIS1* overexpression enhanced mitochondrial trafficking.

The axonal cytoskeleton provides the extensive microtubule network along which motor proteins transport cargoes; however, the effects of neuronal activity on this structure remain

understudied. Yehuda et al. thus electrically stimulated mouse sciatic nerves prior to nerve excision and electron microscopy. This short, physiological excitation caused clear reductions in microtubule and neurofilament density, indicating that neuronal activity can rapidly depolarize cytoskeletal structures, likely to facilitate morphological changes like axon extension/growth.

Neurotrophins bind Trk receptors on neurons (e.g., NGF preferentially signals through TrkA) to activate homeostatic pathways, including PI3K-Akt. To better understand spatiotemporal aspects of this process, Sainath and Gallo studied the NGF-TrkA axis and PI3K-Akt signaling in mouse sensory neurons. NGF stimulated PI3K-Akt activity preferentially at sites populated with axonal mitochondria. Moreover, this initial activation was oxidative phosphorylation-dependent, but not glycolysis-dependent, differing from longer-term observations, suggesting temporal distinctions in bioenergetic requirements of neurotrophin signaling.

Caused by injury, Wallerian degeneration (WD) is a pathway of programmed axon death driven by SARM1-mediated depletion of axonal NAD⁺. Ketschek et al. studied *Sarm1* knockout mice to assess its role in axon branching. *Sarm1* disruption increased axonal branching in skin and cultured

sensory neurons. Moreover, through live imaging, *Sarm1*^{-/-} axons were shown to display altered cytoskeletal dynamics, decreased axonal mitochondrial motility, and increased actin-patch formation leading to enhanced filopodia establishment.

Crawford et al. generated mouse myelinating-spinal cord cultures to study SARM1 function in Zika virus (ZV) infection. ZV causes axon degeneration *in vitro* and is associated with congenital neurological complications, although the etiology is unclear. To evaluate WD involvement, neurons were cultured from *Sarm1* knockout mice before ZV infection. ZV caused a rapid, but *Sarm1*-independent, reduction of NAD⁺; however, *Sarm1* loss prolonged survival of neuronal processes, suggesting a role in ZV-driven pathogenesis.

WD is dramatically delayed in *Wld^Δ* mice by up to 2 weeks but is less well studied in the CNS than PNS. To combat this, Steward et al. combined WD-eliciting lesions of the entorhinal cortex with electron microscopy to assess synaptic degeneration in the dentate gyrus. Expectedly, synapse loss in *Wld^Δ* mutants was substantially delayed. Less predictably, however, *Wld^Δ* mice displayed dendritic spine hypertrophy and enlarged post-synaptic membrane specializations, similar in effect to long-term potentiation.

Mitochondria aid WD execution, while their dysfunction can also trigger WD. Their putative role(s) in nerve injury response is less well understood. Using a mouse spinal cord injury model, Kedra et al. thus analyzed mitochondrial response in corticospinal tract axons. Injury caused increased mitophagy and persistent mitochondrial fragmentation, which was dependent on both calcium uptake and Drp1, a GTPase required for mitochondrial fission. Nerve injury therefore caused increased mitochondrial fission in CNS neurons.

REFERENCES

- Costa, C. J., and Willis, D. E. (2018). To the end of the line: Axonal mRNA transport and local translation in health and neurodegenerative disease. *Dev. Neurobiol.* 78, 209–220. doi: 10.1002/dneu.22555
- Dalla Costa, I., Buchanan, C. N., Zdradzinski, M. D., Sahoo, P. K., Smith, T. P., Thames, E., et al. (2021). The functional organization of axonal mRNA transport and translation. *Nat. Rev. Neurosci.* 22, 77–91. doi: 10.1038/s41583-020-00407-7
- Farias, J., Sotelo, J. R., and Sotelo-Silveira, J. (2019). Toward axonal system biology: genome wide views of local mRNA translation. *Proteomics* 19, e1900054. doi: 10.1002/pmic.201900054
- Sleigh, J. N., Rossor, A. M., Fellows, A. D., Tosolini, A. P., and Schiavo, G. (2019). Axonal transport and neurological disease. *Nat. Rev. Neurol.* 15, 691–703. doi: 10.1038/s41582-019-0257-2
- Surana, S., Villarreal-Campos, D., Lazo, O. M., Moretto, E., Tosolini, A. P., Rhymes, E. R., et al. (2020). The evolution of the axonal transport toolkit. *Traffic* 21, 13–33. doi: 10.1111/tra.12710
- Tosolini, A. P., Sleigh, J. N., Surana, S., Rhymes, E. R., Cahalan, S. D., and Schiavo, G. (2021). BDNF-dependent modulation of axonal transport is selectively impaired in ALS. *bioRxiv*. doi: 10.1101/2021.12.06.471484

Diabetes can cause peripheral neuropathy through undefined mechanisms, although impaired nerve regeneration may contribute. Jones et al. used rats to assess the ability of diabetic peripheral nerves to regenerate post-injury. Impaired nerve regeneration in diabetic rats was linked to reduced axonal mRNA transport caused by reduced availability of the RBP ZBP1. ZBP1 overexpression rescued regrowth in diabetic neurons post-injury, indicating that perturbed ZBP1-mediated transcript mobilization into regenerating axons contributes to diabetes-induced neuropathy.

In summary, the ten articles presented in this collection cover a breadth of topics converging on mechanisms governing axonal homeostasis. We believe this Research Topic will be of interest to researchers working on areas including developmental neurobiology, neuronal signaling and neurological diseases.

AUTHOR CONTRIBUTIONS

JS drafted the manuscript and figure. All authors contributed to the completion of the work and approved its submission.

FUNDING

This work was supported by South Carolina Spinal Cord Injury Research Fund (PS), the Burke Foundation (DW), and the Medical Research Council Career Development Award (MR/S006990/1) (JS).

ACKNOWLEDGMENTS

We thank the authors for their contributions, and we hope that you enjoy reading their articles.

Vargas, J. N. S., Sleigh, J. N., and Schiavo, G. (2022). Coupling axonal mRNA transport and local translation to organelle maintenance and function. *Curr. Opin. Cell Biol.* 74, 97–103. doi: 10.1016/j.ccb.2022.01.008

Conflict of Interest: The authors declare that the research was conducted in the absence of any commercial or financial relationships that could be construed as a potential conflict of interest.

Publisher's Note: All claims expressed in this article are solely those of the authors and do not necessarily represent those of their affiliated organizations, or those of the publisher, the editors and the reviewers. Any product that may be evaluated in this article, or claim that may be made by its manufacturer, is not guaranteed or endorsed by the publisher.

Copyright © 2022 Sahoo, Willis and Sleigh. This is an open-access article distributed under the terms of the Creative Commons Attribution License (CC BY). The use, distribution or reproduction in other forums is permitted, provided the original author(s) and the copyright owner(s) are credited and that the original publication in this journal is cited, in accordance with accepted academic practice. No use, distribution or reproduction is permitted which does not comply with these terms.



Axotomy Induces Drp1-Dependent Fragmentation of Axonal Mitochondria

Joseph Kedra¹, Shen Lin¹, Almudena Pacheco¹, Gianluca Gallo^{1,2†}
and George M. Smith^{1,3*†}

¹Shriners Hospitals Pediatric Research Center, Lewis Katz School of Medicine, Temple University, Philadelphia, PA, United States, ²Department of Anatomy and Cell Biology, Lewis Katz School of Medicine, Temple University, Philadelphia, PA, United States, ³Department of Neuroscience, Lewis Katz School of Medicine, Temple University, Philadelphia, PA, United States

OPEN ACCESS

Edited by:

Dianna E. Willis,
Burke-Cornell Medical Research
Institute, United States

Reviewed by:

Yongcheol Cho,
Korea University, South Korea
Woong Sun,
Korea University, South Korea

*Correspondence:

George M. Smith
george.smith@temple.edu

[†]These authors have contributed
equally to this work and share senior
authorship

Specialty section:

This article was submitted to
Molecular Signalling and Pathways,
a section of the journal
Frontiers in Molecular Neuroscience

Received: 16 February 2021

Accepted: 07 May 2021

Published: 03 June 2021

Citation:

Kedra J, Lin S, Pacheco A, Gallo G
and Smith GM (2021) Axotomy
Induces Drp1-Dependent
Fragmentation of Axonal
Mitochondria.
Front. Mol. Neurosci. 14:668670.
doi: 10.3389/fnmol.2021.668670

It is well established that CNS axons fail to regenerate, undergo retrograde dieback, and form dystrophic growth cones due to both intrinsic and extrinsic factors. We sought to investigate the role of axonal mitochondria in the axonal response to injury. A viral vector (AAV) containing a mitochondrially targeted fluorescent protein (mitoDsRed) as well as fluorescently tagged LC3 (GFP-LC3), an autophagosomal marker, was injected into the primary motor cortex, to label the corticospinal tract (CST), of adult rats. The axons of the CST were then injured by dorsal column lesion at C4-C5. We found that mitochondria in injured CST axons near the injury site are fragmented and fragmentation of mitochondria persists for 2 weeks before returning to pre-injury lengths. Fragmented mitochondria have consistently been shown to be dysfunctional and detrimental to cellular health. Inhibition of Drp1, the GTPase responsible for mitochondrial fission, using a specific pharmacological inhibitor (mDivi-1) blocked fragmentation. Additionally, it was determined that there is increased mitophagy in CST axons following Spinal cord injury (SCI) based on increased colocalization of mitochondria and LC3. *In vitro* models revealed that mitochondrial divalent ion uptake is necessary for injury-induced mitochondrial fission, as inhibiting the mitochondrial calcium uniporter (MCU) using RU360 prevented injury-induced fission. This phenomenon was also observed *in vivo*. These studies indicate that following the injury, both *in vivo* and *in vitro*, axonal mitochondria undergo increased fission, which may contribute to the lack of regeneration seen in CNS neurons.

Keywords: regeneration, mitochondria, mitophagy, corticospinal tract (CST), spinal cord injury

INTRODUCTION

Spinal cord injury (SCI) is a severe medical problem with high mortality and long-term morbidity (Eckert and Martin, 2017) for which there is no effective treatment. Following injury, severed axons often undergo dieback/retraction from the site of injury and fail to exhibit subsequent regeneration up to and beyond the injury site. Additionally, many severed axons

within the CNS form retraction bulbs at the cut axon tip as opposed to new growth cones (Hill et al., 2001; Hill, 2017). Regenerative failure is due to cell intrinsic (Fawcett and Verhaagen, 2018) and extrinsic factors (Fitch and Silver, 2008). For functional regeneration and repair of injured circuitry to occur, it will be necessary to manipulate both intrinsic and extrinsic factors. Herein, we focus on elucidating the intrinsic factors that impair axon regeneration, specifically focusing on the mitochondrial response to axonal injury in the severed axon.

The mitochondrion has multiple functions in the regulation of cellular physiology by generating ATP, buffering cytosolic calcium, and when dysfunctional, generating excessive reactive oxygen species (ROS; Kasahara and Scorrano, 2014; Brennan-Minnella et al., 2016; Fonteriz et al., 2016; Islam, 2017). In neurons, mitochondria are highly dynamic (Saxton and Hollenbeck, 2012; Schwarz, 2013; Sheng, 2014; Barnhart, 2016). They undergo regulated fission and fusion to adjust their distribution and physiological functions, and if dysfunctional are fragmented by excessive fission before removal by mitophagy. Mitochondria also determine sites of axonal branching and provide important functions in axonal regeneration (Courchet et al., 2013; Spillane et al., 2013; Tao et al., 2014; Cartoni et al., 2016; Han et al., 2016; Winkle et al., 2016; Zhou et al., 2016; Sainath et al., 2017). It is well established that neuronal mitochondria are adversely affected in a variety of neurodegenerative disorders (Abeti and Abramov, 2015; Lane et al., 2015; Zhang et al., 2015; Arun et al., 2016; Bertholet et al., 2016; Krols et al., 2016; Golpich et al., 2017) and following spinal cord injury at the level of whole tissue (Jin et al., 2004; McEwen et al., 2007; Sullivan et al., 2007; Patel et al., 2009, 2010). However, the response of axonal mitochondria to spinal cord injury is yet to be fully understood. The primary features of mitochondrial dysfunction are the fragmentation of mitochondria through repeated bouts of fission into small submicron particles and the concurrent loss of the mitochondrial membrane potential resulting in ATP depletion and generation of ROS. The GTPase Dynamin-related protein 1 (Drp1) is the primary mediator of normal physiological mitochondrial fission, as well as excessive fission leading to fragmentation (Kageyama et al., 2011; Cho et al., 2013; Otera et al., 2013; Sesaki et al., 2014). Mitophagy, a mitochondria selective form of autophagy, serves as a protective mechanism to remove fragmented dysfunctional mitochondria in cells (Karbowski, 2010; Ashrafi and Schwarz, 2013; Balog et al., 2016).

We report that following spinal cord injury, there is a rapid fragmentation of mitochondria in corticospinal tract (CST) axons that persists for up to 3 days following injury before recovery of normal mitochondrial size begins, ultimately attaining sizes similar to uninjured axonal mitochondria 2 weeks after injury. The injury-induced mitochondrial fragmentation requires Drp1 and coincides with an increase in mitophagy that follows a temporal pattern similar to fragmentation. We developed *in vitro* model systems of axonal injury that mimic the *in vivo* response in order to address the injury-induced fission of mitochondria with high spatiotemporal resolution. Using these *in vitro* systems, we find that mitochondrial

calcium uptake is required for injury-induced mitochondrial fission, a finding supported by *in vivo* analysis of the role of mitochondria calcium uptake. These insights may pave the way for the development of new therapeutic approaches aimed at the manipulation of axonal mitochondria following injury.

MATERIALS AND METHODS

Animals

All surgical and animal care protocols were approved by the Temple University School of Medicine's Institutional Animal Care and Use Committee and performed per the National Institutes of Health *Guide for the Care and Use of Laboratory Animals*. Sprague-Dawley rats (65–75 days, 200–224 g; Harlan Laboratories) were housed two per cage, on a 12 h light-dark cycle with food and water provided *ad libitum*. Animals were allowed 7 days of acclimatization prior to any experimental procedure. At the time of surgery, animals ranged in weight from 225 to 250 g. To prevent infection after surgery, animals received an IP injection of 0.5 ml Cefazolin (10 mg/ml). All animals received a subcutaneous injection of 2–3 ml of 0.9% NaCl solution to prevent dehydration following surgery. Analgesia was provided by twice daily oral administration of Rimadyl tablets (1 mg) for 3 days beginning immediately postoperatively.

Viral Vectors

AAV2-GFP-P2A-mitoDsRed was generated by subcloning the mitoDsRed from the original adenovirus vector (Nasr et al., 2008) into MluI and XhoI sites downstream of the P2A of pAM-CBA-eGFP-P2A. To generate AAV2-eGFPLC3-P2A-mitoDsRed the GFP coding region was removed from AAV2-GFP-P2A-mitoDsRed plasmid and replaced with eGFPLC3 (Addgene: #22405). Purified AAV plasmid was packaged using the helper-free method as reported previously (Ayuso et al., 2010; Liu et al., 2014). In brief, HEK293T cells at 70–80% confluency were transfected with two packaging plasmids, one carrying AAV *rep* and *cap*, the other with AAV helper functions, and the transgene using a polyethylenimine method (PEI; polyethylenimine, linear, MW 25k, Warrington, PA). Three days post transfection, cell supernatant, and lysates were harvested. 40% PEG 8000 was added to precipitate crude virus for 2 h. AAV samples were double-ultracentrifuged in a cesium chloride gradient with isolated viral fractions dialyzed in 0.1 M PBS/0.5% Sorbital overnight (Ayuso et al., 2010; Liu et al., 2014). Purified fractions were added to HEK293T cells to verify function. Quantitative real-time PCR of purified viral fractions was done to determine viral titer. The viral titer of AAV2 was 1.2×10^{13} GC/ml.

Surgical Procedures

Cortical Injections

Animals were anesthetized with a ketamine (67 mg/kg)/xylazine (6.7 mg/kg, i.p.) mixture. Their scalps were shaved, and the animals were placed in a stereotaxic head holder. Under

aseptic conditions, a small bone flap was cut in the skull to expose the dorsal surface of the primary somatomotor cortex bilaterally. Bone flaps extended from 1 mm anterior to bregma to 1 mm posterior to bregma and from 1 mm from midline laterally to approximately 4.5 mm. Injections into the somatomotor cortex were performed using a beveled glass micropipette pulled to a diameter of 30–40 μm connected to a nanoliter injector (Nanoject, Drummond Scientific). All injections were made using a stereotaxic device or micromanipulator (Narishige International) for precise measurements. All coordinates were determined in relationship to bregma. Bilateral injections of either AAV2-GFP-P2A-mitoDsRed or AAV2-GFPLC3-P2A-mitoDsRed (1.5 μl /injection) were made using the following coordinates: AP axis: +0.5 mm ML axis: \pm 2.5 mm, AP axis: +0.5 mm ML axis: \pm 3.5 mm, AP axis: $-$ 0.5 mm ML axis: \pm 3.0 mm, AP axis: $-$ 0.5 mm ML axis: \pm 4.0 mm. Coordinates were carefully identified based on the rat brain atlas (Paxinos and Charles, 2007). Following virus injection, all animals were maintained for 4 weeks before cervical spinal cord injury was performed.

Corticospinal Tract Severing

Animals were anesthetized with a ketamine (67 mg/kg)/xylazine (6.7 mg/kg, i.p.) mixture. Under aseptic conditions, a 1 cm incision is made through the dorsal skin above vertebra C3–C6. The skin is retracted to expose the underlying muscle. The exposed spinotrapezius muscle is cut along the midline with scissors, then spread with a small Alm retractor. The muscles are freed from the cervical vertebrae with scissors. The first thoracic vertebrae has a very prominent dorsal spinal process for easy identification. A full laminectomy of vertebra C4 and C5 was performed, so as not to damage the spinal cord. Using micro scissors (Vannas Spring Scissors, Fine Science Tools, Inc.) the dorsal column was precisely transected bilaterally (1.5 mm width, 1.1 mm depth). The muscles overlying the spinal cord were loosely sutured together with a 5–0 suture and the wound closed. Animals were allowed to recover at 37°C. Animals were maintained for either 2 h, 8 h, 1 day, 3 days, 1 week, 2 weeks, or 6 weeks following surgery.

For experiments involving mDivi-1 (Cat# 338967-87-6, Sigma-Aldrich) rats had IP injections of either mDivi-1 (50 mg/kg for 250 g rats) or vehicle (10%DMSO/40% PEG300 in saline) 12 h prior to CST severing and immediately after for rats being maintained for 1 day. Rats being maintained for 6 weeks received IP injections 12 h prior to CST severing, immediately after surgery, and once per day for 7 days following the injury.

Tissue Processing and Histology

At the completion of each experiment, all animals were euthanized by injection of Fatal-Plus (Dearborn, MI, United States) and perfused with saline (0.9% NaCl) followed by 4% paraformaldehyde (PFA) in 0.1 M phosphate buffer (pH 7.5). The brain and spinal cord were promptly dissected. Spinal cord samples were dissected with dorsal roots intact for identification of each spinal level. Samples were post-fixed in 4% PFA overnight at 4°C. Tissue samples were then transferred to a series of

graded sucrose (10%, 20%, and 30%) where they remained for the following 24 h or until the brain section sunk to the bottom of the container. A 3 cm section of the spinal cord with the lesion at the center was removed from the whole spinal cord. The spinal cord samples were serially sectioned, sagittally at 30 μm intervals using a Leica CM3050S cryostat. Sections were collected and placed into cryoprotectant solution, then stored at -20°C until processed for histology.

Immunofluorescence

To amplify the GFP and DsRed signals, sections were permeabilized in 0.3% Triton X-100 with 5% normal goat serum to block non-specific binding sites. Samples were then incubated with chicken-anti-GFP primary antibody (1:1,000; #GFP-1020; Aves Labs Inc., Tigard, OR, United States) and rabbit-anti-DsRed primary antibody (1:500; #632496; Takara Bio USA, Inc., Mountain View, CA, United States) overnight at 4°C. The next day, samples were incubated with donkey-anti-chicken-AlexaFluor 488 sary antibody (1:400, Jackson ImmunoResearch Laboratories, Inc., West Grove, PA, United States) and goat-anti-rabbit-AlexaFluor 594 sary antibody (1:400, Jackson ImmunoResearch Laboratories, Inc., West Grove, PA, United States) then mounted on glass slides.

Tissue Section Imaging

Imaging was performed using AxioVision software (Carl Zeiss Microscopy, Thornwood, NY, United States). A 100 \times /1.3 N/A objective with a \sim 300 nm focal plane was used to generate Z-stacks using 250 nm Z-intervals through 30 μm of tissue sections. In order to maximize the power of the morphological analysis, 1 \times 1 camera binning was used to generate the highest spatial resolution in the images. Max-intensity 2D projections were then generated using sets of sections from the Z-stack that contained mitochondria.

Culturing of Primary Neurons

Chicken dorsal root ganglia (DRG) were dissected at embryonic day 7 (E7) or day 14 (E14; SPF eggs obtained from Charles River Laboratories). At this developmental stage, it is not possible to determine the sex, and both sexes were used at presumably a 50/50 ratio. Whole explants were cultured (3–4 explants/dish), or the DRG neurons were dissociated and transfected (as explained below; 1.5 explants/dish). The culturing substrata were previously coated with polylysine [Sigma; Catalog number (Cat#) P9011; 100 $\mu\text{g}/\text{ml}$ in borate buffer], for 4 h and following 3 \times washing with phosphate-buffered saline (PBS) with 25 $\mu\text{g}/\text{ml}$ laminin (Life Technologies Cat# 23017-015) in PBS overnight, all incubations were performed at 39°C. Explants and dissociated neurons were cultured in a defined F12H medium (Gibco; Cat#21700075) supplemented with NGF (20 ng/ml). For live imaging experiments, explants or dissociated neurons were plated in glass-bottom dishes.

For the preparation of dissociated neurons, sensory ganglia were incubated in Ca^{2+} - Mg^{2+} -free PBS (CMF-PBS), for 10 min at 37°C. Ganglia were then spun down for 1 min, and the supernatant was removed. Ganglia were then treated with 0.25% trypsin (Fisher Scientific Cat# MT25005CI), for 10 min at 37°C and spun down for 1 min. Ganglia were then pipette triturated

30 times in F12HS10 media (F12H medium supplemented with 10% fetal bovine serum; Fisher; Cat#MT350111CV) and then spun down for 4 min. The supernatant was removed and cells were transfected as described below.

Rat hippocampal neurons were dissociated from dissected E18 rat hippocampi as previously described (Thomas et al., 2012). Neurons were cultured in Neurobasal media supplemented with B27 (Thermo Fischer Scientific) in glass-bottomed dishes coated with polylysine [Sigma; Catalog number (Cat#) P9011; 100 µg/ml in borate buffer] and laminin (Life Technologies Cat# 23017-015; 25 µg/ml) as described above.

Adult rat DRG dissociated cultures were prepared as described previously (Pacheco et al., 2020).

Transfection

For transfection of plasmids into neurons, 40 chicken DRGs were dissociated as described above, and after F12HS10 was removed neurons were suspended in 100 µl nucleofector solution (Lonza Cat# VPG-1002) and gently resuspended through trituration. The DRG cell suspension was transferred to a nucleofector cuvette containing 10 µg of Plasmid DNA and electroporated using an Amaxa Nucleopator (program G-13). The electroporated solution was then immediately transferred to a tube containing F12H media as described above prior to plating.

Labeling of Mitochondria *In vitro*

For labeling mitochondria to determine mitochondrial fission rates, neurons were transfected with pDsRed2-Mito (Clontech Cat# 632421) as explained above. To measure mitochondrial length, mitochondria were labeled with mitochondria targeted dyes, which were prepared according to the manufacturer's directions. Labeling was performed through incubation for 30 min with MitoTracker green (50 nM, Molecular Probes, Cat# M7514) or Mitoview 633 (20 nM, Biotium®, Hayward, USA; Cat# 70055-T). Following labeling, the dye-containing medium was removed and cultures were washed three times with culturing medium not containing any dye. Imaging was performed at least 30 min after the dye was removed to allow cultures to acclimate.

In vitro Axonal Severing

For experiments in which DRG explants were used, explants were plated in glass-bottom dishes as described above and cultured for 48 h. Dishes were placed on the microscope stage for 10 min prior to severing. Axons were severed by dragging a No. 11 scalpel blade across the axon perpendicular to its direction of growth.

For experiments in which dissociated, transfected neurons were used, neurons were cultured in glass-bottom dishes as described above for 24 h, with the exception of neurons transfected with GCaMP6, which were cultured for 72 h (the time at which expression of GCaMP6 was optimal). Dishes were placed on the stage 10 min prior to severing. Severing was performed as previously described (Gallo, 2004). Briefly, only axons that exhibited a "healthy" uniform caliber axon were used in single-axon-severing experiments. The severing of axons was performed approximately 200 µm from the axon tip. For severing, borosilicate glass capillaries (AM Systems,

Carlsborg WA; catalog # 625500) were pulled to fine tips using a Pul-1 micropipette puller (World Precision Instruments, Sarasota FL). Capillary needles were mounted on a mechanical micromanipulator (Leica Inc., Bannockburn, IL). The tip was then brought into contact with the substratum and axons severed by maintaining the position of the tip steady while moving the stage relative to the tip. The stage was moved manually in a continuous swift motion resulting in the uniform severing of axons.

Live Imaging

Neurons were imaged using a Zeiss 200 M microscope equipped with an Orca-ER camera (Hamamatsu) in series with a PC workstation running Zeiss Axiovision software for image acquisition and analysis. Cultures were placed on a heated microscope stage (Zeiss temperable insert P with objective heater) for 10 min at a constant 39°C before and during imaging. Imaging was performed using a Zeiss Pan-Neofluar 100_objective (1.3 N.A.), 2 × 2 camera binning, and minimal light exposure. For the quantification of mitochondria length, mitochondria labeled with MitoTracker green (Chicken sensory neurons) or Mitoview 633 (rat hippocampal neurons), were imaged at 30 min intervals over a 180 min timeframe. For mitochondrial fission and attempted fission rate quantification, neurons were co-transfected with pDsRed2-Mito and either pEYFP-C1-Drp1 or pEYFP-C1-Drp1K38A [previously generated in our lab (Armijo-Weingart et al., 2019)]. Neurons were then imaged for 250 frames with a 3 s interframe interval. For analysis of changes in cytosolic and mitochondrial calcium, neurons were transfected with either GCaMP6 or mitoGCaMP2. Neurons were then imaged for 16 frames with a 1 min interframe interval.

Determination of Mitochondria Length

Imaging was performed as described in the tissue imaging and live imaging sections above. The length of mitochondria in the axon was measured using ImageJ software. Mitochondria length was determined by a line, segmented if the mitochondrion was not strictly linear, running from one end to the other of the mitochondrion. Occasionally, mitochondria in axons overlapped as clearly evidenced by the additive signal of their fluorescence in the region of overlap. Overlapping mitochondria were excluded from the analysis to ensure only mitochondria with clearly defined ends were used for quantification.

Determination of Rates of Fission and Fusion From Live Imaging Time-Lapse Videos

Instances of fission were determined manually by the user through frame-by-frame analysis. Using the settings described in the live imaging section each pixel in the resulting images has a radius of 0.12 µm. A completed fission event was defined as when the fluorescence intensity of the mitochondrion at the site of apparent fission had decreased to the background level of the axonal segment not containing mitochondria and the two resultant mitochondria were separated by over 5 pixels representing 0.6 µm. Attempted

fission events were defined as mitochondria undergoing constrictions but not continuing into a full fission event, as the constriction sites returned to exhibit the prior width and intensity.

GCaMP6 and mitoGCaMP2 Analysis

All analyses were performed using Zeiss Axiovision software. For GCaMP6, regions of interest (ROIs) were drawn around the cut axon tip and 50 μm proximal to the cut. For mitoGCaMP2, ROIs were drawn around axonal mitochondria proximal to the cut site. Image acquisition was performed using excitation filters of 405 nm and 488 nm (Need specifications on Filters). Fluorescence time courses were computed as the mean pixel intensity of all the pixels within the ROI. At each timepoint, fluorescence intensity for both excitation filters (F_{405} and F_{488}) was calculated as mean fluorescence within the ROI, F , relative to the background F_0 ($F - F_0$). Data is reported as a ratio of F_{488}/F_{405} .

Statistical Analysis

All data were analyzed using InStat software (GraphPad Software Inc.). The software determines the normalcy of data sets using the Kolmogorov-Smirnov test. All data sets were determined to be non-normally distributed, therefore non-parametric analysis was used (Mann-Whitney test). For multiple comparison tests within experimental designs, non-parametric Dunn's *post hoc* tests were used. For data sets representing categorical data falling into bins the Fischer's exact test was used on the raw data, although the data are expressed as percentages for ease of appreciation. One or two tailed p values are reported based on whether the hypothesis did or did not dictate the directionality of the expected change in mean or median, respectively. All graphs were generated using Prism (GraphPad Software Inc.). Sample sizes and qualitative statistical presentation are denoted in figure legends or figures.

RESULTS

Spinal Cord Injury Decreases the Length of Axonal Mitochondria

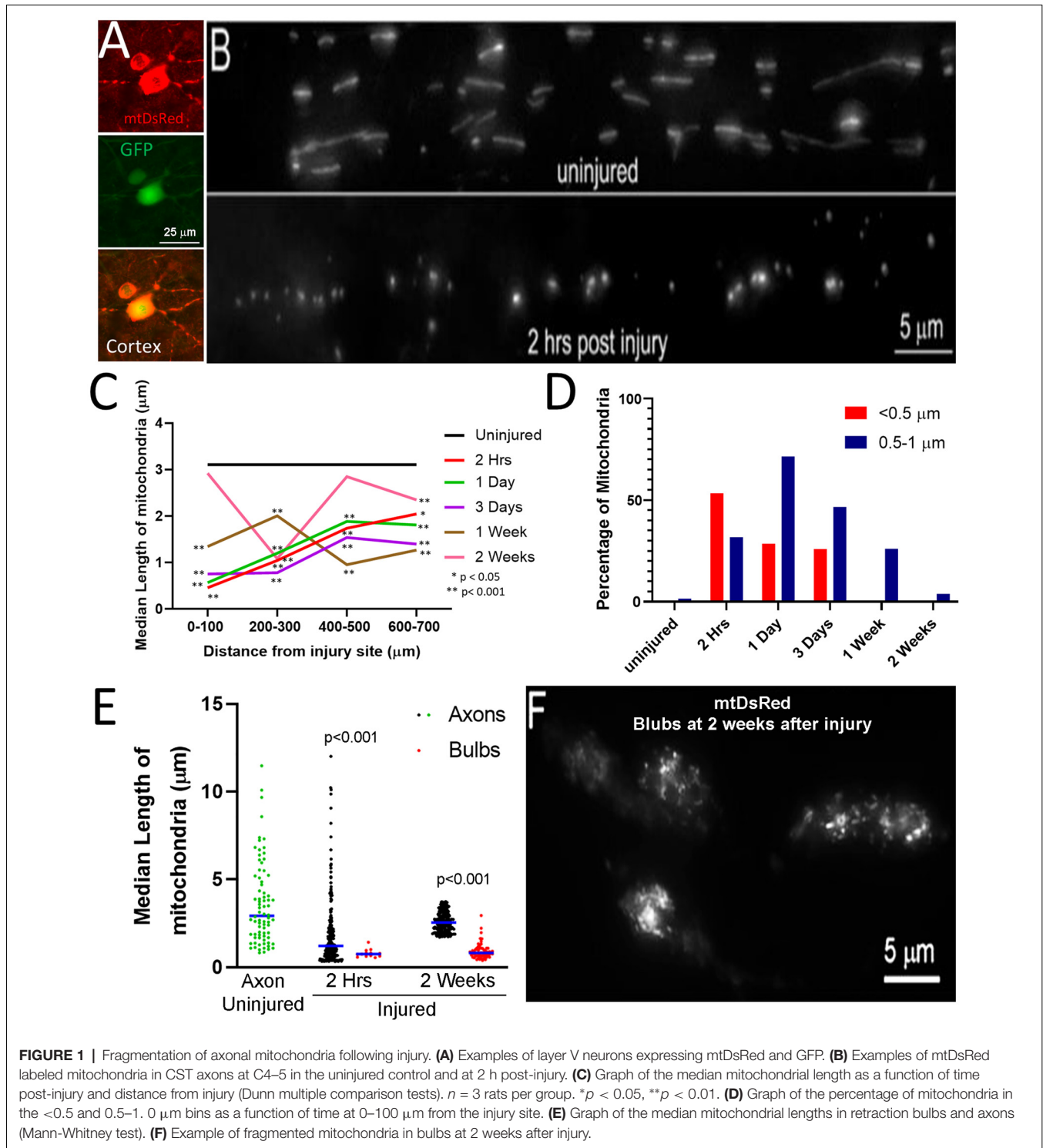
To assess axonal mitochondrial morphology following spinal cord injury, the mitochondria of CST neurons of adult Sprague-Dawley rats were labeled with mitochondrially targeted DsRed (mtDsRed) 4 weeks before performing dorsal column lesions at the C4-C5 level. Labeling was achieved by injecting adeno-associated virus co-expressing GFP and mitoDsRed (mitoDsRed/GFP/AAV) in the forelimb and hindlimb somatomotor cortex (Figures 1A,B). The mitochondria in non-injured axons at the C4-C5 level had a median length of 3.15 μm (Figure 1C). Mitochondria in C4-C5 CST axons severed following dorsal column lesion were analyzed in 100 μm bins from the site of injury as a function of time following injury. At 2 h following injury, mitochondria closest to the site of injury exhibited decreased length, while mitochondria more proximal along the injured axon maintained longer lengths although still decreased relative to controls (Figure 1C). Very small mitochondria in the vicinity of the injury site persisted for up to 3 days following injury (Figure 1C). Recovery of

median mitochondrial length began by 1 week after injury with normal lengths almost fully restored by 2 weeks (Figure 1C; see Supplementary Figure 1 for data point distributions of the medians presented in Figure 1C).

Mitochondria in the $<0.5 \mu\text{m}$ range are considered dysfunctional (Reddy, 2014; Galluzzi et al., 2016; Hu et al., 2017). In uninjured axons, less than 0.5% of mitochondria were shorter than 0.5 μm and only 4.4% of mitochondria fell within the 0.5–1.0 μm range. Herein, mitochondria with length $<0.5 \mu\text{m}$ are defined as fragments, while mitochondria 0.5–1.0 μm are considered to be in the low normal range for length. By 2 h following injury, the percentage of mitochondria in the submicron range dramatically increased resulting in 53% of mitochondria displaying lengths $<0.5 \mu\text{m}$ and 32% with length between 0.5 and 1.0 μm (Figure 1D). The presence of increased mitochondrial fragments persisted until 3 days following injury before returning to non-injury control levels by 1-week post-injury (Figure 1D). Fragmented mitochondria were identified throughout the distal region of severed axons and the axon tips. However, the length of mitochondria within retraction bulbs, defined as the distal end of the axon exhibiting a bulbous rounded morphology, relative to those in non-retraction bulb segments of axons, continued to exhibit sub- μm fragmentation up to at least 2 weeks (Figures 1E,F).

Fragmentation of Axonal Mitochondria Is Associated With Increased Colocalization of Mitochondria With Mitophagy Markers Following Spinal Cord Injury

Fragmented dysfunctional mitochondria are removed through mitophagy1 (Ashrafi and Schwarz, 2013). To determine if the mitochondrial fragmentation along CST axons observed after spinal cord injury correlates with increased mitophagy, we examined the association of mitochondria with the autophagocytic marker LC3 (Maday, 2016; Maday and Holzbaur, 2016). Adult Sprague-Dawley rats were injected with AAV co-expressing GFP-LC3 and mitoDsRed into the somatomotor cortex as described above. Four weeks after injections, the rats received a dorsal column lesion at the C4-C5 level to sever labeled CST axons. Line scans of fluorescent intensities from randomly selected axons were analyzed to measure the degree of LC3 association with mitochondria. Within the C4-C5 level of non-injured rats, GFP-LC3 fluorescence (Figures 2A,B, green line) was mostly uniformly distributed with few regions showing increased pixel intensity associated with DsRed labeled mitochondria (Figure 2A, red line). Prior to the injury, we observed that only 7.1% of axonal mitochondria were associated with localized increases in LC3. At 2 h after injury, 18.5% of mitochondria were associated with localized increases in the levels of LC3 (Figures 2C,F; hereafter referred to as LC3+ mitochondria). The increase in LC3+ mitochondria reached its peak 1 day after injury (31.8% LC3+ mitochondria) but continued until 3 days after injury (22.5% LC3+ mitochondria) before returning to non-injury control levels 7 days after injury (10.1% LC3+ mitochondria; Figure 2D). The percentage of LC3+ mitochondria was not dependent on the distance from



the injury site, as the percentage of LC3+ mitochondria was the same at all distances from the injury site at each time point (**Figure 2E**). These observations indicate that there is an increase in mitophagy that correlates with mitochondrial fragmentation up to 3 days following spinal cord injury. To determine if the association of GFP-LC3 accumulation along axon with

mitochondria might be due to volumetric or non-specific changes, we considered the association of GFP accumulation with mitochondria. For this analysis we focused on 1 day after the injury as at this time point reflects the peak value of the percentage of LC3+ mitochondria (**Figure 2D**). Using the same criteria and analysis as for GFP-LC3, at 1 day after injury 8.1%

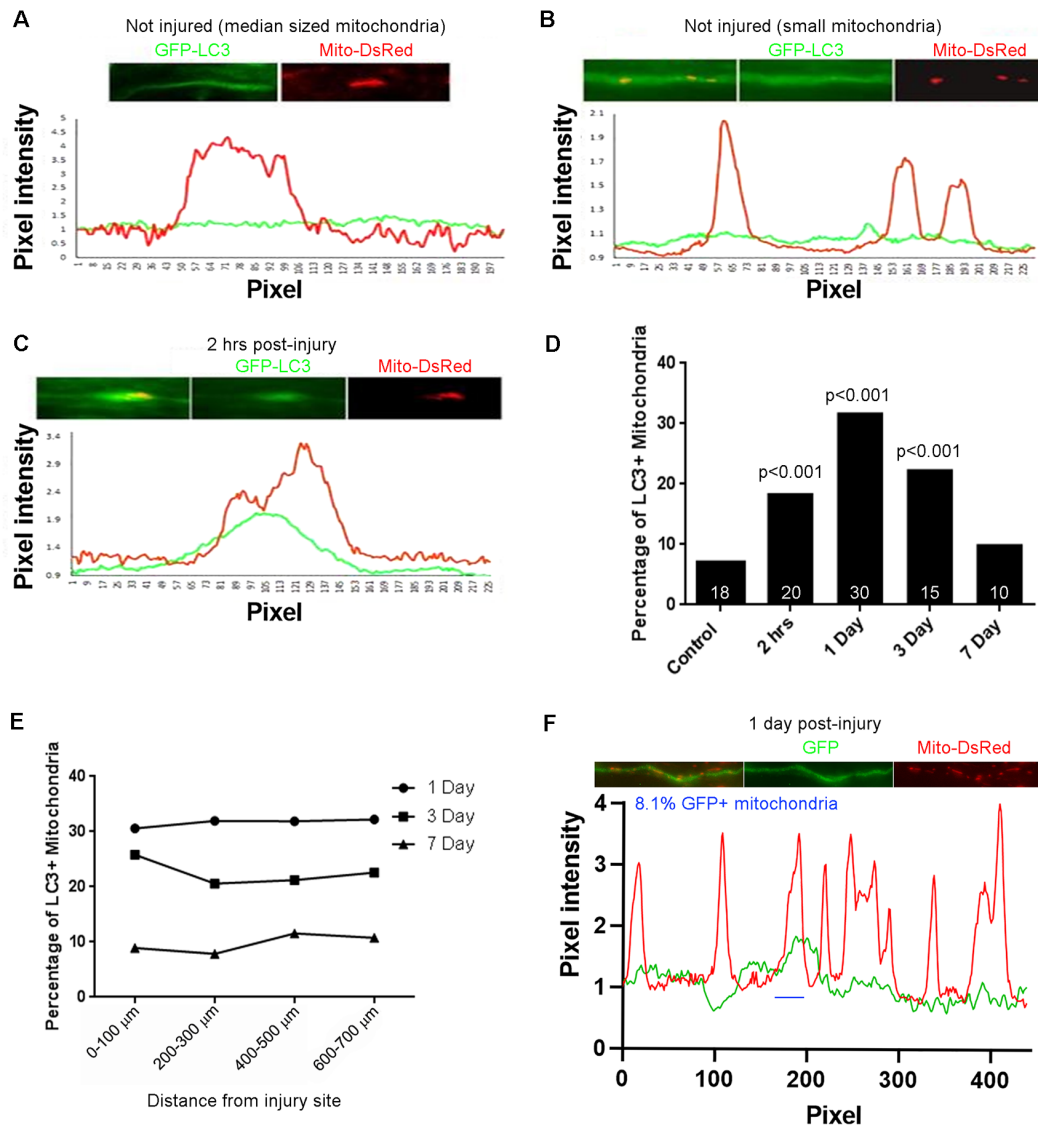


FIGURE 2 | Injury-induced accumulation of LC3 at sites populated by mitochondria. **(A)** Example of LC3 distribution in uninjured axons relative to mitochondria. Line scan shows no increase in LC3 at the mitochondrion. For both traces, values are normalized to the mean intensity in regions not containing mitochondria. **(B)** As in **(A)** but showing three uninjured small mitochondria not showing LC3 accumulation. **(C)** Two hours after injury, LC3 is observed associated with mitochondria. Positive LC3 accumulation was defined as a maximal increase greater than 15% from the mean baseline in the axon segment defined by the mitochondrion. **(D)** Percentage of LC3+ mitochondria as a function of time post-injury. n = axons shown in bars. **(E)** Graph of percentage of LC3+ mitochondria as a function of distance from the site of injury. **(F)** Analysis of colocalization of GFP intensity with mitochondria positioning along axons. Using the same criteria as for GFP-LC3, at 1 day after injury reflective of when the percentage of GFP-LC3+ mitochondria peaks, only 8.1% of mitochondria are GFP+ (one case denoted by blue line). n = 3 rats per group.

of mitochondria ($n = 20$ axons, 148 mitochondria) were found associated with accumulation of GFP. These data indicate that the accumulation of GFP-LC3 noted in the injury conditions is not non-specific.

Inhibition of Drp1-Mediated Fission Prevents Injury-Induced Fragmentation of Axonal Mitochondria

We next sought to assess the role of Drp1 mediated fission in the injury-induced mitochondrial shortening observed *in vivo*. mDivi-1 is a cell and blood-brain barrier permeable

pharmacological inhibitor of Drp1 that blocks mitochondrial fission both *in vitro* and *in vivo* (Lackner and Nunnari, 2010; Li et al., 2016; Smith and Gallo, 2017). Adult Sprague-Dawley rats were injected with mitoDsRed/AAV in the somatomotor cortex 4 weeks prior to CST severing at the C4-C5 level. mDivi-1 or vehicle was delivered *via* IP injections at 12 h before injury, and again immediately post-injury for the 1 day survival group, similar to published *in vivo* protocols (He et al., 2016). Mitochondria were then analyzed at 2 h and 1-day post-injury in the distal 0–300 μ m of axons. mDivi-1 treatment decreased injury-induced mitochondrial fragmentation at 2 h

and 1 day after injury. At 2 h, mDivi-1 treatment resulted in mitochondria with intermediate lengths, ranging between the non-injury and injury conditions (Figure 3A). However, the 1-day treatment group exhibited mitochondrial lengths not significantly different than non-injured controls (Figure 3A). Analysis of the percentage of mitochondria in the fragmented range ($<0.5 \mu\text{m}$) and lower end of the normal range ($0.5\text{--}1 \mu\text{m}$) revealed that mDivi-1 treatment prevented fragmentation at both 2 h and 1 day (Figure 3B).

The Drp-1 Fission Inhibitor mDivi-1 Reduces the Number of Retraction Bulbs on CST Axons

The fragmentation of axonal mitochondria was rapid and persistent in retraction bulbs even at longer times after injury. In order to determine whether mitochondria fragmentation could be a component of the mechanism that generates or supports retraction bulbs, the effects of mDivi-1 treatment on bulbs at the end of injured axons was examined. Adult Sprague-Dawley rats were injected with mtDsRed/GFP/AAV into the somatomotor cortex 4 weeks prior to the severing of CST axons at the C4-C5 level. The rats received IP injections of either mDivi-1 or vehicle the day before injury and once per day for 7 days after injury. Six weeks following injury, the animals were euthanized, and the spinal cord segments were analyzed. Vehicle injected controls showed cavitation at the injury site, axonal retraction, and numerous retraction bulbs at the distal tips of injured CST axons (Figure 3C). Consistent with a prior report (Li et al., 2016), animals treated with mDivi-1 showed a decreased lesion volume with lesioned axons adjacent the lesion site. In addition, there was a 73% decrease in the number of retraction bulbs observed at axon tips (Figure 3D).

Development of *In vitro* Model Systems to Study the Fission Response of Mitochondria to Axonal Injury

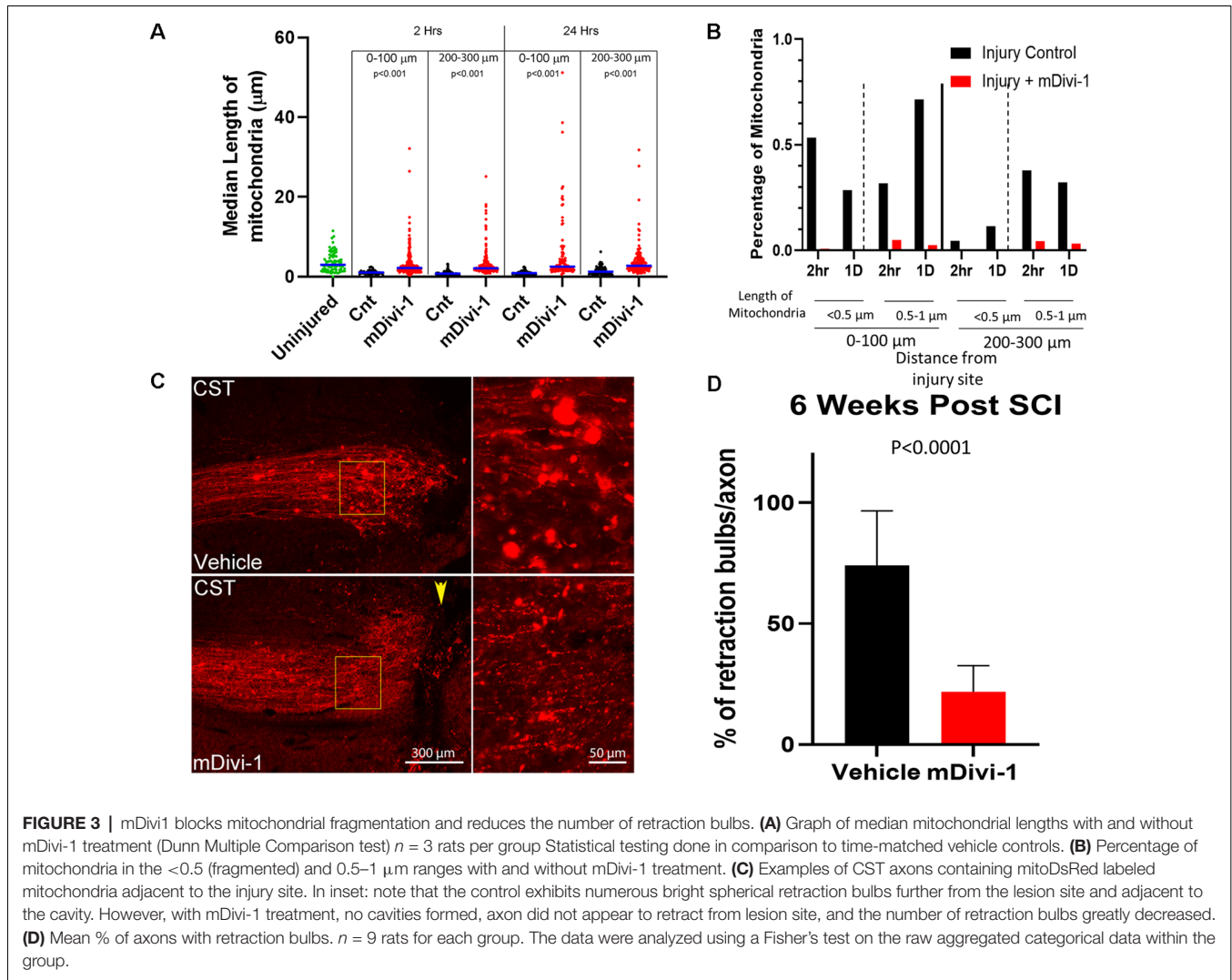
In order to perform mechanistic studies not amenable to *in vivo* examination and to determine whether the response of axonal mitochondria to axon severing may be cell-intrinsic within the cut end of axons, we sought to set up *in vitro* model systems for examining mitochondrial response to axonal injury. We investigated mitochondrial morphology after *in vitro* axonal injury using neurons from two species and representing early embryonic, late embryonic, and adult stages: (1) Embryonic day (E)7 and E14 chicken DRG explants, reflective of developmental stages when sensory axons are undergoing extension and have reached their proximal targets respectively (Figures 4A–D). (2) E18 rat dissociated hippocampal neurons (Figure 4E) and (3) adult rat DRG dissociated neurons (Figure 4F).

Mitochondria within embryonic chicken sensory axons were labeled with MitoTracker Green dye and axons were severed using a scalpel blade after 48 h in culture when axons attained lengths between 1–1.5 mm. The mitochondrial length was monitored using live imaging. Prior to scalpel axotomy, axonal mitochondria showed median lengths of $1.63 \mu\text{m}$ and

$2.41 \mu\text{m}$ in E7 and E14 neurons, respectively (Figures 4A–D), consistent with the prior demonstration of increased length in E14 neurons relative to E7 neurons (Armijo-Weingart et al., 2019). Following axotomy, both E7 and E14 axons showed a significant reduction in mitochondrial length 30 min after injury. Mitochondrial length began to recover between 120 min and 150 min post-injury before returning to pre-injury levels 180 min following injury (Figures 4C,D). The recovery from injury was faster in E7 (120 min) than E14 axons (180 min). E18 hippocampal neurons were cultured for 3 days, the time point at which axons attained lengths between 300 and $400 \mu\text{m}$ (stage III of *in vitro* development). Axonal mitochondria were labeled with Mitoview 633. Mitochondrial length decreased 30 min after injury and did not recover fully until at least 180 min (Figure 4E). Similar analysis using adult rat DRG neurons with mitochondria labeled using MitoTracker Green showed that lengths were decreased one hour after injury and the decrease in length persisted until sometime after 180 min (Figure 4F).

We next tested whether injury-induced mitochondrial shortening in sensory axons is Drp1 dependent *in vitro*. E14 chicken DRG explants were incubated with either DMSO (control) or $20 \mu\text{M}$ mDivi-1 for 30 min prior to scalpel blade axotomy. Mitochondria within sensory axons were labeled with MitoTracker green. Following axotomy mitochondrial size was monitored for 180 min. As with untreated neurons (Figure 4D), DMSO treated neurons demonstrated prominent mitochondrial shortening 30 min after injury before gradually returning to pre-injury lengths by 180 min. Neurons treated with mDivi-1 did not show mitochondrial shortening at any time point following axotomy (Figures 5A,B). Additionally, we tested whether injury-induced mitochondrial shortening in hippocampal neurons is Drp1 dependent *in vitro*. Axonal mitochondria length was measured in E18 hippocampal neurons (as in Figure 4E) treated with either DMSO or $20 \mu\text{M}$ mDivi-1 30 min before severing using a micro-needle as previously described (Gallo, 2004). The mitochondrial length was monitored using live imaging. Prior to axotomy, DMSO treated neurons displayed axonal mitochondria with a median length of $1.86 \mu\text{m}$. The median mitochondrial length was significantly reduced at 30 min after axotomy. By 180 min following injury, median mitochondrial length was still significantly smaller than before axotomy but was trending toward recovery of pre-axotomy length (Figures 5C,D). Neurons treated with $20 \mu\text{M}$ mDivi-1 showed no change in median mitochondrial length over the 180-min monitoring period (Figure 5C). These observations indicate that injury-induced mitochondrial shortening *in vitro* is a Drp1 dependent process.

To further test the hypothesis that mitochondria shortening is due to Drp1 mediated fission, we expressed a dominant-negative Drp1 mutant (Drp1K38A) that lacks GTPase activity and is, therefore, unable to carry out mitochondrial fission (Pitts et al., 1999; Barsoum et al., 2006). E14 chicken DRGs were transfected with either YFP-Drp1 (control) and mitoDsRed or YFP-Drp1K38A and mitoDsRed. Single axon axotomy was performed using a micro-needle as done previously (Gallo, 2004). Because transfection with Drp1K38A allows for unopposed mitochondrial fusion, mitochondria become

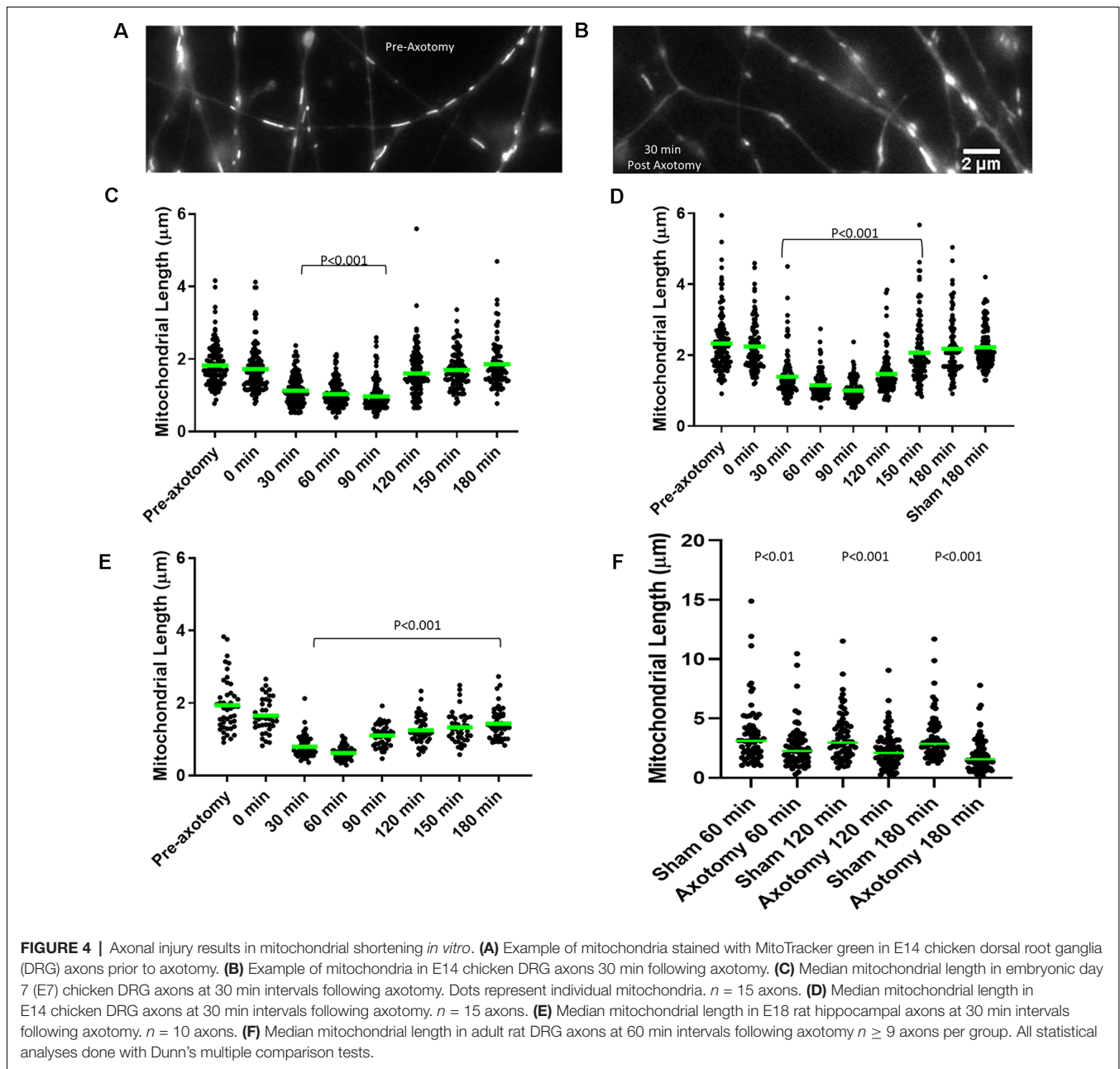


elongated ($20-30 \mu\text{m}$ or larger) in sensory neurons by 24 h of expression (Armijo-Weingart et al., 2019). Thus, comparison of mitochondrial length after axotomy between control and Drp1K38A expressing neurons is not a reasonable analysis. We, therefore, measured the number of fission events and attempted fission events per 10 microns of mitochondria per min for each group monitored over a 15-min period. As previously described (Armijo-Weingart et al., 2019), a fission event was defined as when the fluorescence intensity of the mitochondrion at the site of apparent fission had decreased to the background level of the axonal segment not containing mitochondria and the two resultant mitochondria were separated by over 5 pixels representing $0.6 \mu\text{m}$ (Figure 5E). Attempted fission events were defined as mitochondria that underwent apparent constrictions but did not continue into a full fission event, as the constriction sites returned to exhibit the prior width and intensity (Figure 5E). It should also be noted that overexpression of WT Drp1 does not increase mitochondrial fission events at baseline (Armijo-Weingart et al., 2019). Axotomy resulted in increased fission and attempted fission

events in control YFP-Drp1 expressing neurons (Figures 5F,G). The increases in fission and attempted fission events in response to axotomy were abolished by expression of YFP-Drp1K38A (Figures 5F,G).

Injury-Induced Mitochondrial Fission Requires the Mitochondrial Calcium Uniporter

Following axotomy, there is an influx of calcium into the axon, which is important in the formation of either a retraction bulb or a new growth cone (Bradke et al., 2012). We first transfected E7 chicken DRG neurons with GCaMP6, a cytosolic, ratiometric calcium-sensing protein (Chen et al., 2013). Individual axons were severed using a micro-needle, as above, and calcium changes were monitored over a 15-min period with live imaging. As expected axotomy caused a sustained influx of calcium resulting in a two-fold increase in GCaMP6 fluorescence (Figures 6A,B). To determine whether intra-mitochondrial calcium levels are increased following axotomy, E7 chicken DRG



neurons were transfected with a mitochondrially tagged calcium-sensing protein, mitoGCaMP2. We monitored mitochondrial calcium levels for 15 min following axotomy, observing a steady increase in mitochondrial calcium culminating in a three-fold increase in mitoGCaMP2 fluorescence at 15 min post axotomy (**Figures 6C,D**). To determine if this increase in mitochondrial calcium was dependent on injury-induced fission, we pretreated neurons with either DMSO or 20 μM mDivi-1 as above. Blocking fission following axotomy had no effect on mitochondrial calcium demonstrating that this was not a fission-dependent process (**Figure 6C**). Given the increase in cytosolic calcium after axotomy, we next addressed if injury-induced mitochondrial fission may be dependent on an increase

in mitochondrial calcium. Calcium is taken up into mitochondria through the mitochondrial calcium uniporter (MCU) present on the mitochondrial inner membrane (Gunter and Gunter, 1994). RU360 is an established inhibitor of calcium fluxes through MCU (Matlib et al., 1998; Zhou et al., 1998; Vanderluit et al., 2003). E7 chicken DRG explants were treated with either 10 μM RU360 or vehicle and mitochondria were labeled with MitoTracker Green 30 min prior to scalpel axotomy. Following axotomy, mitochondrial size was monitored for 30 min using live imaging. Application of RU360 had no effect on mitochondrial size in the absence of axotomy during the 30-min imaging period (**Figure 6E**). At 30 min after axotomy, vehicle treated neurons displayed a significantly reduced median mitochondrial length

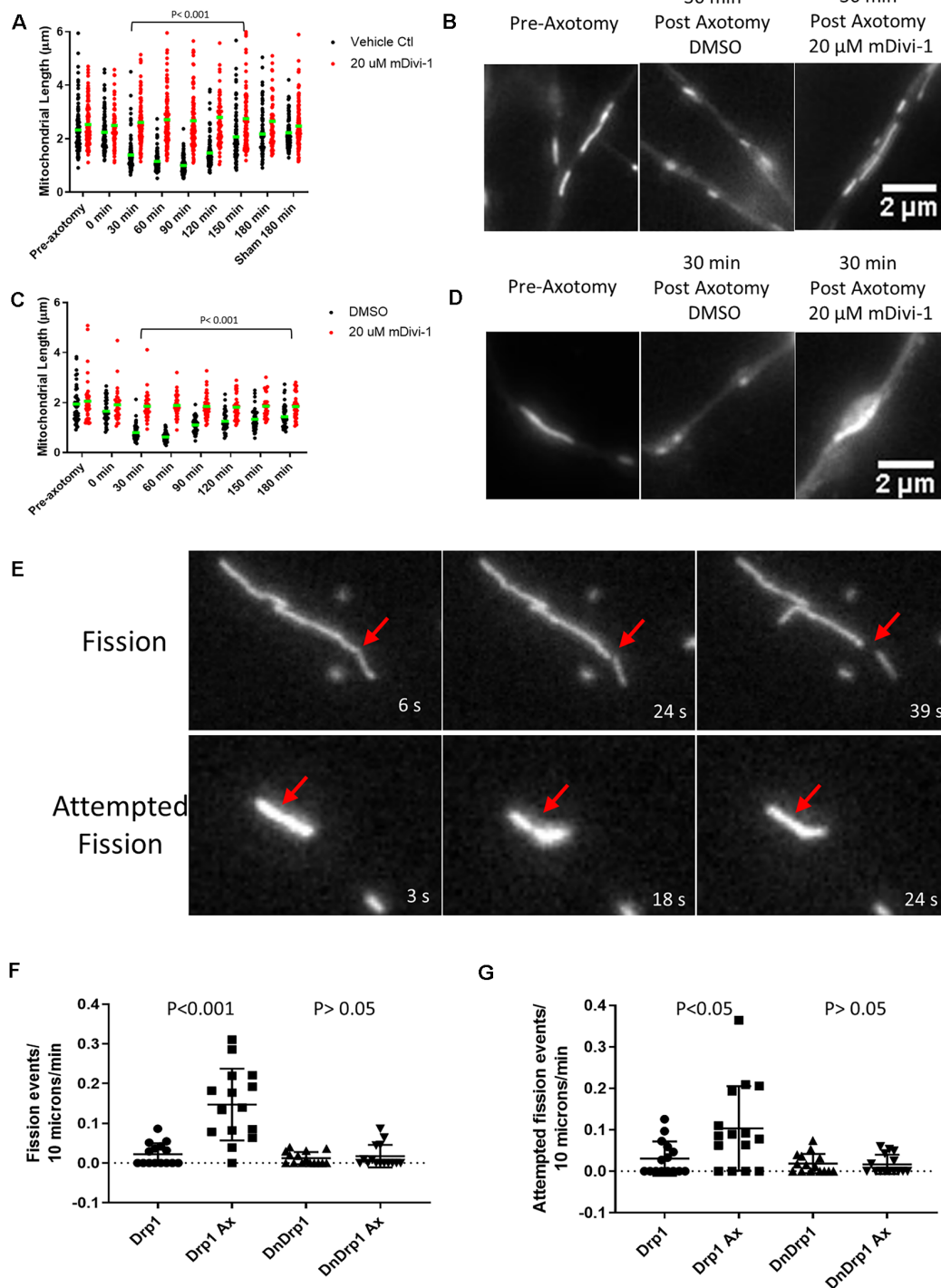


FIGURE 5 | Injury-induced mitochondrial fission is Drp1 dependent *in vitro*. **(A)** Median mitochondrial length in E14 chicken DRG axons with or without mDivi-1. Dots represent individual mitochondria (Dunn's multiple comparison tests). $n = 15$ axons for each group. **(B)** Examples of MitoTracker green stained mitochondria in E14 chicken DRG axons. **(C)** Median mitochondrial length in E18 rat hippocampal axons with or without mDivi-1. Dots represent individual mitochondria (Dunn's multiple comparison tests). $n = 10$ axons for each group. **(D)** Examples of Mitoview633 stained mitochondria in E18 rat hippocampal axons. **(E)** Example of mitochondria labeled with mitoDsRed undergoing fission or attempted fission following axonal injury. At 18 s a constriction is apparent at the site denoted by the arrow but by 24 s the constriction is no longer detectable, and the mitochondrion has returned to its prior morphology. **(F)** Graph of fission events per 10 μm of mitochondrial length per minute in E14 chicken DRG axons transfected with either YFP-Drp1 or YFP-Drp1K38A (DNDrp1) following injury (Dunn's multiple comparison tests). $n = 15$ axons. **(G)** Graph of attempted fission events per 10 μm of mitochondrial length per minute in E14 chicken DRG axons transfected with either YFP-Drp1 or YFP-Drp1K38A (DNDrp1) following injury (Dunn's multiple comparison tests). $n = 15$ axons.

when compared to mitochondrial length prior to axotomy, while neurons treated with 10 μM RU360 displayed no change in median mitochondrial length (**Figure 6E**). These observations indicate that ion fluxes through MCU are a required component of the mechanism that drives injury-induced mitochondrial fission *in vitro*. In order to determine whether mitochondrial ion fluxes through MCU could also have a role in the *in vivo* response of axonal mitochondria to spinal cord injury, adult Sprague-Dawley rats were injected with mtDsRed/GFP/AAV into the somatomotor cortex 4 weeks prior to the severing of CST axons at the C4-C5 level. Immediately following injury, gel foam soaked in either vehicle or 10 mM RU360 was placed at the site of injury. The animals were euthanized either 2 h or 24 h following injury and mitochondrial size as a function of time after injury and distance from the site of injury was analyzed as previously described. Treatment with RU360 resulted in longer mitochondria after injury compared to time-matched controls (**Figure 6F**). However, in all cases, the length of mitochondria was also shorter from that of uninjured controls (**Figure 6F**). Animals treated with RU360 showed greatly attenuated fragmentation in the vicinity of the injury site (0–100 micron) at either 2 h or 24 h post-injury (red percentages and *p* values in **Figure 6F**), indicating that mitochondrial ion fluxes through MCU are also a required component of the mechanism driving injury-induced mitochondrial fission *in vivo*.

DISCUSSION

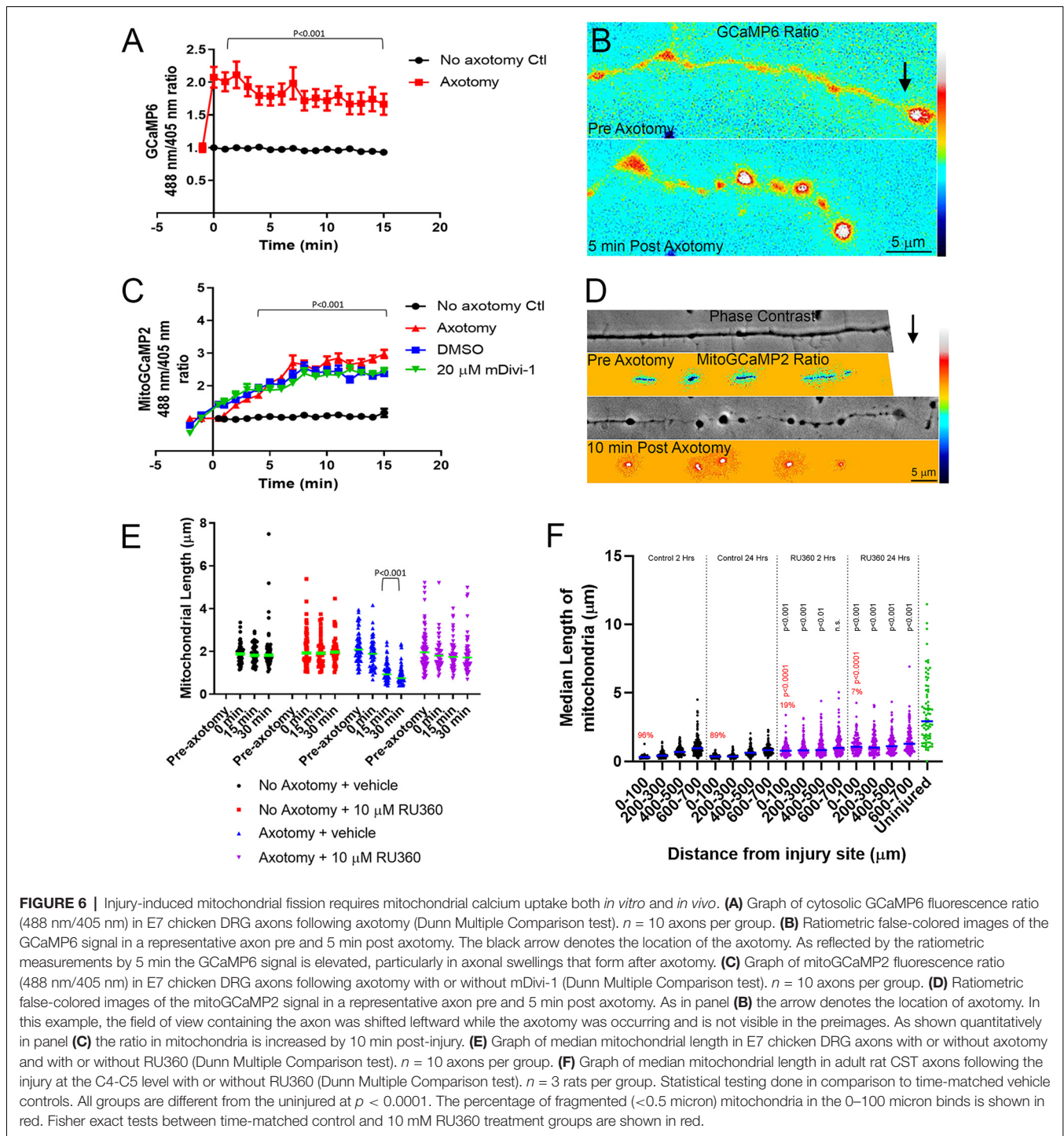
Dysfunctional mitochondria have consistently been associated with neuronal disease and injury (Reddy et al., 2011; Galloway et al., 2012; Reddy, 2014; Luo et al., 2015; Wu et al., 2016, 2017; Cherubini and Gines, 2017). In this study, we used both *in vitro* and *in vivo* models to investigate the response of axonal mitochondria to axonal injury. Mitochondria within CST axons undergo rapid fragmentation following severing. Mitochondrial fragmentation was persistent within retraction bulbs even after mitochondria in more proximal regions of the axon had recovered to normal length. Injury-induced mitochondrial shortening was also found in three different *in vitro* models of axonal injury. Drp1-mediated fission of mitochondria into fragments smaller than 0.5 μm is associated with neuronal malfunction and cell death in a variety of neurotoxic and disease states (Karbowski, 2010; Otera et al., 2013; Kasahara and Scorrano, 2014; Pradeep et al., 2014; Reddy, 2014; Balog et al., 2016; Bertholet et al., 2016; Galluzzi et al., 2016; Hu et al., 2017). The observed fragmentation of axonal mitochondria following injury could severely reduce mitochondrial bioenergetics and impair growth from the cut axon tip. This is in agreement with studies showing that, at the tissue level, mitochondrial respiration following spinal cord injury is impaired (Jin et al., 2004; McEwen et al., 2007; Sullivan et al., 2007; Patel et al., 2009, 2010), and there is a rise in mitochondrial oxidative stress (Jin et al., 2004; McEwen et al., 2007; Sullivan et al., 2007; Patel et al., 2009).

These findings raise the question of the physiological purpose for injury-induced mitochondrial fission. The speed and distance of mitochondrial movement are inversely related to

mitochondrial length (Steketee et al., 2012; Narayanareddy et al., 2014). Additionally, mitochondrial fission is necessary for axonal branching (Spillane et al., 2013; Armijo-Weingart et al., 2019). This raises the possibility that the fission of mitochondria into smaller, but not dysfunctional, fragments could increase their transport rate within axons to aid the redistribution of healthy mitochondria within axons, increasing the growth potential. However, it is unclear why many axonal mitochondria within the CNS become fragmented following injury, rendering them incapable of aiding in neuronal growth and recovery.

Retraction bulbs are formed as a consequence of new growth cone formation failure and the continued flow of axoplasm to the injured tip resulting in a swollen, bulbous axonal end. Retraction bulbs are marked by the presence of accumulated organelles, such as smooth endoplasmic reticulum and mitochondria, as well as disorganized microtubules (Hill, 2017). The fragmentation of mitochondria following injury may contribute to the formation of retraction bulbs, a main contributor to the lack of regenerative potential in the CNS. We observed that fragmented mitochondria persist within retraction bulbs up to 2 weeks after injury (**Figure 1E**), a time at which axonal mitochondria have re-attained lengths comparable to axonal mitochondria in non-injured controls. For axonal regrowth to occur after injury, the injured axon must first form a growth cone, an energy demanding multistep process that relies on ATP produced by healthy mitochondria (Campbell and Holt, 2001; Verma et al., 2005; Hill, 2017). Multiple recent studies show that increasing delivery of healthy mitochondria into injured axon tips positively contributes to axonal regeneration (Cartoni et al., 2016; Han et al., 2016; Zhou et al., 2016). Therefore, we posit that the injury-induced mitochondrial fragmentation in the CNS results in energy deficiency at the cut axon tip, leading to the formation of a retraction bulb and the failure of growth cone formation. Our observation that inhibiting injury-induced mitochondrial fragmentation using mDivi-1 reduced the number of retraction bulbs reinforces this hypothesis. Additionally, inhibiting injury-induced mitochondrial fragmentation reduced the lesion volume. It should be noted that the reduction in lesion volume and the reduction in the number of retraction bulbs may be caused by independent effects of mDivi-1 in different cell types. A previous study demonstrated that mDivi-1 treatment following spinal cord injury prevented astrocyte activation and astroglial scar formation, thereby reducing lesion volume (Li et al., 2016). Nonetheless, our findings demonstrate that inhibition of injury-induced mitochondrial fragmentation prevents retraction bulb formation and may ultimately contribute to axonal regeneration following injury.

Dysfunctional mitochondria are detrimental due to their incapability to produce enough ATP to meet cellular demand and increased generation of reactive oxygen species (ROS). Dysfunctional mitochondria are removed through mitophagy. Following spinal cord injury, a sharp increase in mitophagy occurs, as measured by LC3-mitochondria colocalization, beginning at 2 h after injury and peaking at 1 day following injury, before returning to non-injury control levels 7 days after injury. This timeline coincides with the observation that mitochondria in the vicinity of the injury site are fragmented



up to 3 days following injury before showing partial recovery of normal mitochondrial length. These observations are consistent with the notion that the injury-induced mitochondrial fragments are dysfunctional and must therefore be removed from the axon in the interest of maintaining neuronal health (Ribas and Lingor, 2015; Ribas et al., 2015). Activation of autophagy using a cell permeable Tat-Beclin1 peptide, a key component of autophagosome formation (Molino et al., 2017), reduces

retraction bulb formation acutely, as well as axonal dieback 6 weeks after SCI (He et al., 2016). In contrast, inhibiting VPS34, a phosphoinositide-3-kinase (PI3K) involved in autophagosome initiation, using 3MA prevents acute axonal degeneration and neuronal degeneration after either optic nerve injury or SCI (Knoflerle et al., 2010; Bisicchia et al., 2017). Although the underlying models are different and could differentially modulate the rate at which autophagosomes are cleared, another

explanation is that 3MA is a general PI3K inhibitor, and not specific to VPS34 (Knight and Shokat, 2007; Kong and Yamori, 2008). Our observations suggest that the specific promotion of mitophagy following spinal cord injury possibly proves beneficial in axonal regeneration and recovery.

Calcium dynamics following injury are important in determining whether a new growth cone or a retraction bulb will form (Bradke et al., 2012), thus we investigated whether calcium may contribute to Drp1-dependent injury-induced mitochondrial fragmentation. Following injury, there was an increase in both cytosolic and mitochondrial calcium content. Increases in mitochondrial calcium are due to increased permeability of the MCU to divalent ions, largely calcium and zinc. The increase in mitochondrial calcium content was not blocked by the application of mDivi-1, indicating that the observed mitochondrial uptake is independent of injury-induced mitochondrial fission. Inhibiting ionic fluxes through the MCU using RU360, both *in vitro* and *in vivo*, blocked injury-induced mitochondrial fission, showing that mitochondrial ionic uptake is a component of the mechanism underlying injury-induced mitochondrial fragmentation. Mitochondria are composed of an outer mitochondrial membrane (OMM) and an inner mitochondrial membrane (IMM), both of which must be fully constricted for fission to occur (Kuroiwa et al., 2008). Constriction of the IMM was shown to be dependent on mitochondrial calcium uptake, and could be blocked by administration of RU360 (Cho et al., 2017). Thus, the influx of mitochondrial calcium following injury may be required for fission to come to completion due to its role in IMM constriction. Additionally, Drp1 alone is unable to initiate mitochondrial constriction because Drp1 oligomers can only form contractile rings with a diameter of up to 100 nm, while mitochondria have diameters between 0.5 and 1.0 μm (Ingerman et al., 2005; Mears et al., 2011). Therefore, mitochondrial fission requires a pre-constriction step, in which actin filaments promote direct contact of mitochondria with the endoplasmic reticulum (ER; Friedman et al., 2011; Korobova et al., 2013). A rise in cytosolic calcium promotes actin-dependent pre-constriction, bringing mitochondria into closer contact with ER, allowing for efficient uptake of calcium into mitochondria through the MCU (Chakrabarti et al., 2018). These results suggest that following injury, a large influx of calcium into the cytosol results in actin polymerization, which drives mitochondrial pre-constriction and mitochondrial-ER contact. This in turn leads to an uptake of calcium into the mitochondria through the MCU and promotes constriction of the IMM priming mitochondria for Drp1-dependent fission. We cannot rule out a possible role for ionic fluxes through the MCU in regulating aspects of the Drp1-dependent mechanism of fission following injury, but given that the latter is occurring on the outer mitochondrial membrane while the fluxes are inside the mitochondrion this seems unlikely. While a case can be made for the role of mitochondrial calcium uptake, zinc uptake may also contribute. During fission, Drp1 promotes the flux of zinc through the MCU that in turn serves to suppress mitochondrial membrane potential and target mitochondria for mitophagy (Cho et al., 2019). Thus, both calcium and zinc fluxes through the MCU

could contribute to injury-induced mitochondria fragmentation and mitophagy. Regardless of the specific ion responsible, the mechanistic insight that fluxes through MCU is required may provide yet another target for inhibiting injury-induced mitochondrial fragmentation and perhaps promoting axonal regeneration in the future.

This report details the novel findings that following injury, axonal mitochondria of CST neurons undergo rapid fragmentation in a Drp1-dependent process. Mitochondrial fragments persist in retraction bulbs and may play a role in their initial formation or maintenance. An axonal injury also results in an increase in mitophagy, indicating that the injury-induced mitochondrial fragments are dysfunctional. Finally, we show that mitochondrial calcium uptake is a mechanistic contributor to injury-induced mitochondrial fragmentation. These observations pave the way for new strategies aimed at axonal mitochondrial dynamics in the effort to prevent axonal dieback, and to promote axonal regeneration following injury.

DATA AVAILABILITY STATEMENT

The raw data supporting the conclusions of this article will be made available by the authors, without undue reservation.

ETHICS STATEMENT

The animal studies were reviewed and approved by Institutional Animal Care and Use Committee.

AUTHOR CONTRIBUTIONS

JK, SL, and AP performed the majority of experimental studies. JK, GG, and GS designed the majority of experiments, performed data analyses, wrote and edited the manuscript. All authors contributed to the article and approved the submitted version.

FUNDING

This work was supported by NINDS NS095471 to GG, Shriners Hospitals for Pediatric Research 85120-PHI-19 to GS and GG, and 84051-PHI-16 to GS.

ACKNOWLEDGMENTS

We would also like to thank Dr. Yingpeng Liu and Fengsong Qin for viral production.

SUPPLEMENTARY MATERIAL

The Supplementary Material for this article can be found online at: <https://www.frontiersin.org/articles/10.3389/fnmol.2021.668670/full#supplementary-material>.

SUPPLEMENTARY FIGURE 1 | Distribution of mitochondrial length measurements for the post-injury time course and distance from injury suite analysis. Each dot represents a mitochondrion.

REFERENCES

- Abeti, R., and Abramov, A. Y. (2015). Mitochondrial Ca(2+) in neurodegenerative disorders. *Pharmacol. Res.* 99, 377–381. doi: 10.1016/j.phrs.2015.05.007
- Armijo-Weingart, L., Ketschek, A., Sainath, R., Pacheco, A., Smith, G. M., and Gallo, G. (2019). Neurotrophins induce fission of mitochondria along embryonic sensory axons. *eLife* 8:e49494. doi: 10.7554/eLife.49494
- Arun, S., Liu, L., and Donmez, G. (2016). Mitochondrial biology and neurological diseases. *Curr. Neuropharmacol.* 14, 143–154. doi: 10.2174/1570159x13666150703154541
- Ashrafi, G., and Schwarz, T. L. (2013). The pathways of mitophagy for quality control and clearance of mitochondria. *Cell Death Differ.* 20, 31–42. doi: 10.1038/cdd.2012.81
- Ayuso, E., Mingozzi, F., Montane, J., Leon, X., Anguela, X. M., Haurigot, V., et al. (2010). High AAV vector purity results in serotype- and tissue-independent enhancement of transduction efficiency. *Gene Ther.* 17, 503–510. doi: 10.1038/gt.2009.157
- Balog, J., Mehta, S. L., and Vemuganti, R. (2016). Mitochondrial fission and fusion in secondary brain damage after CNS insults. *J. Cereb. Blood Flow Metab.* 36, 2022–2033. doi: 10.1177/0271678X16671528
- Barnhart, E. L. (2016). Mechanics of mitochondrial motility in neurons. *Curr. Opin. Cell Biol.* 38, 90–99. doi: 10.1016/j.ccb.2016.02.022
- Barsoum, M. J., Yuan, H., Gerencser, A. A., Liot, G., Kushnareva, Y., Graber, S., et al. (2006). Nitric oxide-induced mitochondrial fission is regulated by dynamin-related GTPases in neurons. *EMBO J.* 25, 3900–3911. doi: 10.1038/sj.emboj.7601253
- Bertholet, A. M., Delerue, T., Millet, A. M., Moulis, M. F., David, C., Daloyau, M., et al. (2016). Mitochondrial fusion/fission dynamics in neurodegeneration and neuronal plasticity. *Neurobiol. Dis.* 90, 3–19. doi: 10.1016/j.nbd.2015.10.011
- Bisicchia, E., Latini, L., Cavallucci, V., Sasso, V., Nicolini, V., Molinari, M., et al. (2017). Autophagy inhibition favors survival of rubrospinal neurons after spinal cord hemisection. *Mol. Neurobiol.* 54, 4896–4907. doi: 10.1007/s12035-016-0031-z
- Bradke, F., Fawcett, J. W., and Spira, M. E. (2012). Assembly of a new growth cone after axotomy, the precursor to axon regeneration. *Nat. Rev. Neurosci.* 13, 183–193. doi: 10.1038/nrn3176
- Brennan-Minnella, A. M., Arron, S. T., Chou, K. M., Cunningham, E., and Cleaver, J. E. (2016). Sources and consequences of oxidative damage from mitochondria and neurotransmitter signaling. *Environ. Mol. Mutagen.* 57, 322–330. doi: 10.1002/em.21995
- Campbell, D. S., and Holt, C. E. (2001). Chemotropic responses of retinal growth cones mediated by rapid local protein synthesis and degradation. *Neuron* 32, 1013–1026. doi: 10.1016/s0896-6273(01)00551-7
- Cartoni, R., Norsworthy, M. W., Bei, F., Wang, C., Li, S., Zhang, Y., et al. (2016). The Mammalian-specific protein armcx1 regulates mitochondrial transport during axon regeneration. *Neuron* 92, 1294–1307. doi: 10.1016/j.neuron.2016.10.060
- Chakrabarti, R., Ji, W. K., and Stan, R. V. (2018). INF2-mediated actin polymerization at the ER stimulates mitochondrial calcium uptake, inner membrane constriction and division. *J. Cell Biol.* 217, 251–268. doi: 10.1083/jcb.201709111
- Chen, T. W., Wardill, T. J., Sun, Y., Pulver, S. R., Renninger, S. L., Baohan, A., et al. (2013). Ultrasensitive fluorescent proteins for imaging neuronal activity. *Nature* 499, 295–300. doi: 10.1038/nature12354
- Cherubini, M., and Gines, S. (2017). Mitochondrial fragmentation in neuronal degeneration. Toward an understanding of HD striatal susceptibility. *Biochem. Biophys. Res. Commun.* 483, 1063–1068. doi: 10.1016/j.bbrc.2016.08.042
- Cho, B., Cho, H. M., Jo, Y., Kim, H. D., Song, M., Moon, C., et al. (2017). Constriction of the mitochondrial inner compartment is a priming event for mitochondrial division. *Nat. Commun.* 8:15754. doi: 10.1038/ncomms15754
- Cho, B., Choi, S. Y., Cho, H. M., Kim, H. J., and Sun, W. (2013). Physiological and pathological significance of dynamin-related protein 1 (drp1)-dependent mitochondrial fission in the nervous system. *Exp. Neurobiol.* 22, 149–157. doi: 10.5607/en.2013.22.3.149
- Cho, H. M., Ryu, J. R., Jo, Y., Seo, T. W., Choi, Y. N., Kim, J. H., et al. (2019). Drp1-Zip1 interaction regulates mitochondrial quality surveillance system. *Mol. Cell* 73, e8.364–e8.376. doi: 10.1016/j.molcel.2018.11.009
- Courchet, J., Lewis, T. L. Jr., Lee, S., Courchet, V., Liou, D. Y., Aizawa, S., et al. (2013). Terminal axon branching is regulated by the LKB1-NUAK1 kinase pathway via presynaptic mitochondrial capture. *Cell* 153, 1510–1525. doi: 10.1016/j.cell.2013.05.021
- Eckert, M. J., and Martin, M. J. (2017). Trauma: spinal cord injury. *Surg. Clin. North Am.* 97, 1031–1045. doi: 10.1016/j.suc.2017.06.008
- Fawcett, J. W., and Verhaagen, J. (2018). Intrinsic determinants of axon regeneration. *Dev. Neurobiol.* 78, 890–897. doi: 10.1002/dneu.22637
- Fitch, M. T., and Silver, J. (2008). CNS injury, glial scars and inflammation: inhibitory extracellular matrices and regeneration failure. *Exp. Neurol.* 209, 294–301. doi: 10.1016/j.expneurol.2007.05.014
- Fonteriz, R., Matesanz-Isabel, J., Arias-Del-Val, J., Alvarez-Illera, P., Montero, M., and Alvarez, J. (2016). Modulation of calcium entry by mitochondria. *Adv. Exp. Med. Biol.* 898, 405–421. doi: 10.1007/978-3-319-26974-0_17
- Friedman, J. R., Lackner, L. L., West, M., DiBenedetto, J. R., Nunnari, J., and Voeltz, G. K. (2011). ER tubules mark sites of mitochondrial division. *Science*, 334, 358–362. doi: 10.1126/science.1207385
- Gallo, G. (2004). Myosin II activity is required for severing-induced axon retraction in *in vitro*. *Exp. Neurol.* 189, 112–121. doi: 10.1016/j.expneurol.2004.05.019
- Galloway, C. A., Lee, H., and Yoon, Y. (2012). Mitochondrial morphology-emerging role in bioenergetics. *Free Radic. Biol. Med.* 53, 2218–2228. doi: 10.1016/j.freeradbiomed.2012.09.035
- Galluzzi, L., Bravo-San Pedro, J. M., Blomgren, K., and Kroemer, G. (2016). Autophagy in acute brain injury. *Nat. Rev. Neurosci.* 17, 467–484. doi: 10.1038/nrn.2016.51
- Golpich, M., Amini, E., Mohamed, Z., Azman Ali, R., Mohamed Ibrahim, N., and Ahmadiani, A. (2017). Mitochondrial dysfunction and biogenesis in neurodegenerative diseases: pathogenesis and treatment. *CNS Neurosci. Ther.* 23, 5–22. doi: 10.1111/cns.12655
- Gunter, K. K., and Gunter, T. E. (1994). Transport of calcium by mitochondria. *J. Bioenerg. Biomembr.* 26, 471–485. doi: 10.1007/BF00762732
- Han, S. M., Baig, H. S., and Hammarlund, M. (2016). Mitochondria localize to injured axons to support regeneration. *Neuron* 92, 1308–1323. doi: 10.1016/j.neuron.2016.11.025
- He, M., Ding, Y., Chu, C., Tang, J., Xiao, Q., and Luo, Z. G. (2016). Autophagy induction stabilizes microtubules and promotes axon regeneration after spinal cord injury. *Proc. Natl. Acad. Sci. U S A* 113, 11324–11329. doi: 10.1073/pnas.1611282113
- Hill, C. E. (2017). A view from the ending: axonal dieback and regeneration following SCI. *Neurosci. Lett.* 652, 11–24. doi: 10.1016/j.neulet.2016.11.002
- Hill, C. E., Beattie, M. S., and Bresnahan, J. C. (2001). Degeneration and sprouting of identified descending supraspinal axons after contusive spinal cord injury in the rat. *Exp. Neurol.* 171, 153–169. doi: 10.1006/exnr.2001.7734
- Hu, C., Huang, Y., and Li, L. (2017). Drp1-dependent mitochondrial fission plays critical roles in physiological and pathological progresses in mammals. *Int. J. Mol. Sci.* 18:144. doi: 10.3390/ijms18010144
- Ingerman, E., Perkins, E. M., Marino, M., Mears, J. A., McCaffery, J. M., Hinshaw, J. E., et al. (2005). Dnm1 forms spirals that are structurally tailored to fit mitochondria. *J. Cell Biol.* 170, 1021–1027. doi: 10.1083/jcb.2005.06078
- Islam, M. T. (2017). Oxidative stress and mitochondrial dysfunction-linked neurodegenerative disorders. *Neurol. Res.* 39, 73–82. doi: 10.1080/01616412.2016.1251711
- Jin, Y., McEwen, M. L., Nottingham, S. A., Maragos, W. F., Dragicevic, N. B., Sullivan, P. G., et al. (2004). The mitochondrial uncoupling agent 2,4-dinitrophenol improves mitochondrial function, attenuates oxidative damage and increases white matter sparing in the contused spinal cord. *J. Neurotrauma* 21, 1396–1404. doi: 10.1089/neu.2004.21.1396
- Kageyama, Y., Zhang, Z., and Sesaki, H. (2011). Mitochondrial division: molecular machinery and physiological functions. *Curr. Opin. Cell Biol.* 23, 427–434. doi: 10.1016/j.ccb.2011.04.009
- Karbowski, M. (2010). Mitochondria on guard: role of mitochondrial fusion and fission in the regulation of apoptosis. *Adv. Exp. Med. Biol.* 687, 131–142. doi: 10.1007/978-1-4419-6706-0_8

- Kasahara, A., and Scorrano, L. (2014). Mitochondria: from cell death executioners to regulators of cell differentiation. *Trends Cell Biol.* 24, 761–770. doi: 10.1016/j.tcb.2014.08.005
- Knight, Z. A., and Shokat, K. M. (2007). Chemically targeting the PI3K family. *Biochem. Soc. Trans.* 35, 245–249. doi: 10.1042/BST0350245
- Knoferle, J., Koch, J. C., Ostendorf, T., Michel, U., Planchamp, V., Vutova, P., et al. (2010). Mechanisms of acute axonal degeneration in the optic nerve *in vivo*. *Proc. Natl. Acad. Sci. U S A* 107, 6064–6069. doi: 10.1073/pnas.0909794107
- Kong, D., and Yamori, T. (2008). Phosphatidylinositol 3-kinase inhibitors, promising drug candidates for cancer therapy. *Cancer Sci.* 99, 1734–1740. doi: 10.1111/j.1349-7006.2008.00891.x
- Korobova, F., Ramabhadran, V., and Higgs, H. N. (2013). An actin-dependent step in mitochondrial fission mediated by the ER-associated formin INF2. *Science* 339, 464–467. doi: 10.1111/j.1349-7006.2008.00891.x
- Krols, M., van Isterdael, G., Asselbergh, B., Kremer, A., Lippens, S., Timmerman, V., et al. (2016). Mitochondria-associated membranes as hubs for neurodegeneration. *Acta Neuropathol.* 131, 505–523. doi: 10.1007/s00401-015-1528-7
- Kuroiwa, T., Misumi, O., Nishida, K., Yagisawa, F., Yoshida, Y., Fujiwara, T., et al. (2008). Vesicle, mitochondrial, and plastid division machineries with emphasis on dynamin and electron-dense rings. *Int. Rev. Cell Mol. Biol.* 271, 97–152. doi: 10.1016/S1937-6448(08)01203-3
- Lackner, L. L., and Nunnari, J. (2010). Small molecule inhibitors of mitochondrial division, tools that translate basic biological research into medicine. *Chem. Biol.* 17, 578–583. doi: 10.1016/j.chembiol.2010.05.016
- Lane, R. K., Hilsabeck, T., and Rea, S. L. (2015). The role of mitochondrial dysfunction in age-related diseases. *Biochim. Biophys. Acta* 1847, 1387–1400. doi: 10.1016/j.bbabi.2015.05.021
- Li, G., Cao, Y., Shen, F., Wang, Y., Bai, L., Guo, W., et al. (2016). Mdivi-1 inhibits astrocyte activation and astroglial scar formation and enhances axonal regeneration after spinal cord injury in rats. *Front. Cell. Neurosci.* 10:241. doi: 10.3389/fncel.2016.00241
- Liu, Y., Keefe, K., Tang, X., Lin, S., and Smith, G. M. (2014). Use of self-complementary adeno-associated virus serotype 2 as a tracer for labeling axons: implications for axon regeneration. *PLoS One* 9:e87447. doi: 10.1371/journal.pone.0087447
- Luo, Y., Hoffer, A., Hoffer, B., and Qi, X. (2015). Mitochondria: a therapeutic target for Parkinson's disease. *Int. J. Mol. Sci.* 16, 20704–20730. doi: 10.3390/ijms160920704
- Maday, S. (2016). Mechanisms of neuronal homeostasis: autophagy in the axon. *Brain Res.* 1649, 143–150. doi: 10.1016/j.brainres.2016.03.047
- Maday, S., and Holzbaur, E. L. (2016). Compartment-specific regulation of autophagy in primary neurons. *J. Neurosci.* 36, 5933–5945. doi: 10.1523/JNEUROSCI.4401-15.2016
- Matlib, M. A., Zhou, Z., Knight, S., Ahmed, S., Choi, K. M., Krause-Bauer, J., et al. (1998). Oxygen-bridged dinuclear ruthenium amine complex specifically inhibits Ca²⁺ uptake into mitochondria *in vitro* and *in situ* in single cardiac myocytes. *J. Biol. Chem.* 273, 10223–10231. doi: 10.1074/jbc.273.17.10223
- McEwen, M. L., Sullivan, P. G., and Springer, J. E. (2007). Pretreatment with the cyclosporin derivative, NIM811, improves the function of synaptic mitochondria following spinal cord contusion in rats. *J. Neurotrauma* 24, 613–624. doi: 10.1089/neu.2006.9969
- Mears, J. A., Lackner, L. L., Fang, S., Ingerman, E., Nunnari, J., and Hinshaw, J. E. (2011). Conformational changes in Dnm1 support a contractile mechanism for mitochondrial fission. *Struct. Mol. Biol.* 18, 20–26. doi: 10.1038/nsmb.1949
- Molino, D., Zemirli, N., Codogno, P., and Morel, E. (2017). The journey of the autophagosome through mammalian cell organelles and membranes. *J. Mol. Biol.* 429, 497–514. doi: 10.1016/j.jmb.2016.12.013
- Narayanareddy, B. R., Vartiainen, S., Hariri, N., O'Dowd, D. K., and Gross, S. P. (2014). A biophysical analysis of mitochondrial movement, differences between transport in neuronal cell bodies versus processes. *Traffic* 15, 762–771. doi: 10.1111/tra.12171
- Nasr, P., Sullivan, P. G., and Smith, G. M. (2008). Mitochondrial imaging in dorsal root ganglion neurons following the application of inducible adenoviral vector expressing two fluorescent proteins. *J. Neurosci. Methods* 172, 185–194. doi: 10.1016/j.jneumeth.2008.04.023
- Otera, H., Ishihara, N., and Mihara, K. (2013). New insights into the function and regulation of mitochondrial fission. *Biochim. Biophys. Acta* 1833, 1256–1268. doi: 10.1016/j.bbamcr.2013.02.002
- Pacheco, A., Merianda, T. T., Twiss, J. L., and Gallo, G. (2020). Mechanism and role of the intra-axonal Calreticulin translation in response to axonal injury. *Exp. Neurol.* 323:113072. doi: 10.1016/j.expneurol.2019.113072
- Patel, S. P., Sullivan, P. G., Lyttle, T. S., and Rabchevsky, A. G. (2010). Acetyl-L-carnitine ameliorates mitochondrial dysfunction following contusion spinal cord injury. *J. Neurochem.* 114, 291–301. doi: 10.1111/j.1471-4159.2010.06764.x
- Patel, S. P., Sullivan, P. G., Pandya, J. D., and Rabchevsky, A. G. (2009). Differential effects of the mitochondrial uncoupling agent, 2,4-dinitrophenol, or the nitroxide antioxidant, Tempol, on synaptic or nonsynaptic mitochondria after spinal cord injury. *J. Neurosci. Res.* 87, 130–140. doi: 10.1002/jnr.21814
- Paxinos, G., and Charles, W. (2007). *The Rat Brain in Stereotaxic Coordinates*. New York, NY: Academic Press.
- Pitts, K. R., Yoon, Y., Krueger, E. W., and McNiven, M. A. (1999). The dynamin-like protein DLP1 is essential for normal distribution and morphology of the endoplasmic reticulum and mitochondria in mammalian cells. *Mol. Biol. Cell* 10, 4403–4417. doi: 10.1091/mbc.10.12.4403
- Pradeep, H., Sharma, B., and Rajanikant, G. K. (2014). Drp1 in ischemic neuronal death, an unusual suspect. *Curr. Med. Chem.* 21, 2183–2189. doi: 10.2174/0929867321666131228203513
- Reddy, P. H. (2014). Increased mitochondrial fission and neuronal dysfunction in Huntington's disease, implications for molecular inhibitors of excessive mitochondrial fission. *Drug. Discov. Today* 19, 951–955. doi: 10.1016/j.drudis.2014.03.020
- Reddy, P. H., Reddy, T. P., Manczak, M., Calkins, M. J., Shirendeb, U., and Mao, P. (2011). Dynamin-related protein 1 and mitochondrial fragmentation in neurodegenerative diseases. *Brain Res. Rev.* 67, 103–118. doi: 10.1016/j.brainresrev.2010.11.004
- Ribas, V. T., and Lingor, P. (2015). Autophagy in degenerating axons following spinal cord injury, evidence for autophagosome biogenesis in retraction bulbs. *Neural Regen. Res.* 10, 198–200. doi: 10.4103/1673-5374.152367
- Ribas, V. T., Schnepf, B., Challagundla, M., Koch, J. C., Bahr, M., and Lingor, P. (2015). Early and sustained activation of autophagy in degenerating axons after spinal cord injury. *Brain Pathol.* 25, 157–170. doi: 10.1111/bpa.12170
- Sainath, R., Ketschek, A., Grandi, L., and Gallo, G. (2017). CSPGs inhibit axon branching by impairing mitochondria-dependent regulation of actin dynamics and axonal translation. *Dev. Neurobiol.* 77, 454–473. doi: 10.1002/dneu.22420
- Saxton, W. M., and Hollenbeck, P. J. (2012). The axonal transport of mitochondria. *J. Cell Sci.* 125, 2095–2104. doi: 10.1242/jcs.053850
- Schwarz, T. L. (2013). Mitochondrial trafficking in neurons. *Cold Spring Harb. Perspect. Biol.* 5:a011304. doi: 10.1101/cshperspect.a011304
- Sesaki, H., Adachi, Y., Kageyama, Y., Itoh, K., and Iijima, M. (2014). *in vivo* functions of Drp1: lessons learned from yeast genetics and mouse knockouts. *Biochim. Biophys. Acta* 1842, 1179–1185. doi: 10.1016/j.bbabi.2013.11.024
- Sheng, Z. H. (2014). Mitochondrial trafficking and anchoring in neurons: new insight and implications. *J. Cell Biol.* 204, 1087–1098. doi: 10.1083/jcb.201312123
- Smith, G., and Gallo, G. (2017). To mdivi-1 or not to mdivi-1, Is that the question. *Dev. Neurobiol.* 77, 1260–1268. doi: 10.1002/dneu.22519
- Spillane, M., Ketschek, A., Merianda, T. T., Twiss, J. L., and Gallo, G. (2013). Mitochondria coordinate sites of axon branching through localized intra-axonal protein synthesis. *Cell Rep.* 5, 1564–1575. doi: 10.1016/j.celrep.2013.11.022
- Steketee, M. B., Moysidis, S. N., Weinstein, J. E., Kreymerman, A., Silva, J. P., Iqbal, S., et al. (2012). Mitochondrial dynamics regulate growth cone motility, guidance and neurite growth rate in perinatal retinal ganglion cells *in vitro*. *Invest. Ophthalmol. Vis. Sci.* 53, 7402–7411. doi: 10.1167/iovs.12-10298
- Sullivan, P. G., Krishnamurthy, S., Patel, S. P., Pandya, J. D., and Rabchevsky, A. G. (2007). Temporal characterization of mitochondrial bioenergetics after spinal cord injury. *J. Neurotrauma* 24, 991–999. doi: 10.1089/neu.2006.0242

- Tao, K., Matsuki, N., and Koyama, R. (2014). AMP-activated protein kinase mediates activity-dependent axon branching by recruiting mitochondria to axon. *Dev. Neurobiol.* 74, 557–573. doi: 10.1002/dneu.22149
- Thomas, G. M., Hayashi, T., Chiu, S. L., Chen, C. M., and Haganir, R. L. (2012). Palmitoylation by DHHC5/8 targets GRIP1 to dendritic endosomes to regulate AMPA-R trafficking. *Neuron* 73, 482–496. doi: 10.1016/j.neuron.2011.11.021
- Vanderluit, J. L., McPhail, L. T., Fernandes, K. J., Kobayashi, N. R., and Tetzlaff, W. (2003). *In vivo* application of mitochondrial pore inhibitors blocks the induction of apoptosis in axotomized neonatal facial motoneurons. *Cell Death Differ.* 10, 969–976. doi: 10.1038/sj.cdd.4401258
- Verma, P., Chierzi, S., Codd, A. M., Campbell, D. S., Meyer, R. L., Holt, C. E., et al. (2005). Axonal protein synthesis and degradation are necessary for efficient growth cone regeneration. *J. Neurosci.* 25, 331–342. doi: 10.1523/JNEUROSCI.3073-04.2005
- Winkle, C. C., Taylor, K. L., Dent, E. W., Gallo, G., Greif, K. F., and Gupton, S. L. (2016). Beyond the cytoskeleton: the emerging role of organelles and membrane remodeling in the regulation of axon collateral branches. *Dev. Neurobiol.* 76, 1293–1307. doi: 10.1002/dneu.22398
- Wu, Q., Luo, C. L., and Tao, L. Y. (2017). Dynamin-related protein 1 (Drp1) mediating mitophagy contributes to the pathophysiology of nervous system diseases and brain injury. *Histol. Histopathol.* 32, 551–559. doi: 10.14670/HH-11-841
- Wu, Q., Xia, S. X., Li, Q. Q., Gao, Y., Shen, X., Ma, L., et al. (2016). Mitochondrial division inhibitor 1 (Mdivi-1) offers neuroprotection through diminishing cell death and improving functional outcome in a mouse model of traumatic brain injury. *Brain Res.* 1630, 134–143. doi: 10.1016/j.brainres.2015.11.016
- Zhang, C. W., Hang, L., Yao, T. P., and Lim, K. L. (2015). Parkin regulation and neurodegenerative disorders. *Front. Aging Neurosci.* 7:248. doi: 10.3389/fnagi.2015.00248
- Zhou, B., Yu, P., Lin, M. Y., and Sun, T. (2016). Facilitation of axon regeneration by enhancing mitochondrial transport and rescuing energy deficits. *J. Cell Biol.* 214, 103–119. doi: 10.1083/jcb.201605101
- Zhou, Z., Matlib, M. A., and Bers, D. M. (1998). Cytosolic and mitochondrial Ca²⁺ signals in patch clamped mammalian ventricular myocytes. *J. Physiol.* 507, 379–403. doi: 10.1111/j.1469-7793.1998.379bt.x

Conflict of Interest: The authors declare that the research was conducted in the absence of any commercial or financial relationships that could be construed as a potential conflict of interest.

Copyright © 2021 Kedra, Lin, Pacheco, Gallo and Smith. This is an open-access article distributed under the terms of the Creative Commons Attribution License (CC BY). The use, distribution or reproduction in other forums is permitted, provided the original author(s) and the copyright owner(s) are credited and that the original publication in this journal is cited, in accordance with accepted academic practice. No use, distribution or reproduction is permitted which does not comply with these terms.



Axonal Transport and Local Translation of mRNA in Neurodegenerative Diseases

Seiichi Nagano^{1,2} and Toshiyuki Araki^{2*}

¹ Department of Neurotherapeutics, Osaka University Graduate School of Medicine, Osaka, Japan, ² Department of Peripheral Nervous System Research, National Institute of Neuroscience, National Center of Neurology and Psychiatry, Tokyo, Japan

OPEN ACCESS

Edited by:

James N. Sleigh,
University College London,
United Kingdom

Reviewed by:

Alessio Vagnoni,
King's College London,
United Kingdom
Claudia Fallini,
University of Rhode Island,
United States

*Correspondence:

Toshiyuki Araki
taraki@ncnp.go.jp

Specialty section:

This article was submitted to
Brain Disease Mechanisms,
a section of the journal
Frontiers in Molecular Neuroscience

Received: 20 April 2021

Accepted: 25 May 2021

Published: 14 June 2021

Citation:

Nagano S and Araki T (2021)
Axonal Transport and Local
Translation of mRNA
in Neurodegenerative Diseases.
Front. Mol. Neurosci. 14:697973.
doi: 10.3389/fnmol.2021.697973

Since neurons have long neurites including axons, it is crucial for the axons to transport many intracellular substances such as proteins and mitochondria in order to maintain their morphology and function. In addition, mRNAs have also been shown to be transported within axons. RNA-binding proteins form complexes with mRNAs, and regulate transport of the mRNAs to axons, as well as locally translate them into proteins. Local translation of mRNAs actively occurs during the development and damage of neurons, and plays an important role in axon elongation, regeneration, and synapse formation. In recent years, it has been reported that impaired axonal transport and local translation of mRNAs may be involved in the pathogenesis of some neurodegenerative diseases. In this review, we discuss the significance of mRNA axonal transport and their local translation in amyotrophic lateral sclerosis/frontotemporal dementia, spinal muscular atrophy, Alzheimer's disease, and fragile X syndrome.

Keywords: axonal transport, local translation, mRNA, amyotrophic lateral sclerosis, frontotemporal dementia, spinal muscular atrophy, Alzheimer's disease, fragile X syndrome

INTRODUCTION

Neurodegenerative diseases chronically affect neurons in a specific network of the central or peripheral nervous system. Aging is one of the risk factors for the occurrence of these diseases, and the number of patients is increasing year by year with the increasing elderly population (Heemels, 2016). The detailed etiology of these diseases is still undetermined, and there are currently no curative therapeutics. Therefore, it is extremely important to clarify the pathogenic mechanism of these diseases, and to develop new treatment strategies based on identified mechanisms.

It has been suggested that in some of these neurodegenerative diseases, the function of neurons is impaired due to abnormal aggregation/deposition of the causative proteins inside or outside the neurons. For example, in amyotrophic lateral sclerosis (ALS) and frontotemporal dementia (FTD), changes in the localization of transactive responsive-DNA binding protein 43 (TDP-43) (Arai et al., 2006; Neumann et al., 2006) and fused in sarcoma (FUS) (Kwiatkowski et al., 2009; Vance et al., 2009), as well as formation of inclusion bodies containing these proteins are seen in neurons. It is also known that in some ALS/FTD cases, mRNA and abnormally translated dipeptide repeat protein by repeat-associated non-ATG translation are deposited in neurons due to abnormal expansion of the hexanucleotide repeat sequence in the untranslated region of the *C9orf72* gene (DeJesus-Hernandez et al., 2011; Renton et al., 2011; Mori et al., 2013). Alzheimer's disease is

characterized by the formation of amyloid plaques from extracellular accumulation of amyloid β and neurofibrillary tangles due to aggregation of tau protein in neurons (Serý et al., 2013).

In other neurodegenerative diseases, the pathogenic mechanism is assumed to be due to functional decline or loss of the causative gene. In spinal muscular atrophy (SMA), deletion or missense mutations of the survival of motor neuron 1 (*SMN1*) gene causes loss of functional SMN protein, resulting in damage of motor neurons (Fallini et al., 2012). In fragile X syndrome (FXS), abnormal trinucleotide repeat expansion in the untranslated region of the fragile X mental retardation 1 (*FMR1*) gene reduces fragile X mental retardation protein (FMRP) production, resulting in autism spectrum-like symptoms (Maurin et al., 2014).

In all of these diseases, it is speculated that impaired axonal transport in neurons, especially axonal transport of mRNAs and local translation in axons, are involved in the pathogenesis. Transport and translation of mRNAs in axons are thought to play an important role in maintaining the viability of neurons (Khalil et al., 2018). This review outlines the physiological significance of axonal transport of mRNAs, and explains the pathogenic mechanism of neurodegenerative diseases due to its disruption by providing examples of typical diseases.

PHYSIOLOGICAL ROLE OF MRNA TRANSPORT IN NEURONAL AXONS

Neurons have neurites consisting of axons and dendrites, which are morphological features characterizing neurons apart from other cells. At the tip of the axon, a growth cone exists during the development of neurons. After maturation, a pre-synapse structure is made to form synapses with other neurons or effector receptors to support to mutual communication. In order to maintain its morphology and function, neurons constantly transport proteins involved in cytoskeleton and synapse formation or essential intracellular substances, such as mitochondria to neurites (Hirokawa et al., 2009). The transport is actively carried out during neurogenesis and regeneration after neuronal injury for axonal elongation/branching and formation of growth cones/synapses. In addition, the transport is also necessary to maintain normal functions in mature neurons.

In recent years, it has been shown that mRNAs are also transported to axons and locally translated onsite into proteins to maintain axonal morphology and function (Holt et al., 2019). Two types of axonal transport are known: fast axonal transport (50–400 mm/day) and slow axonal transport (<8 mm/day). Generally, organelles such as mitochondria are carried by fast axonal transport, whereas cytoskeletal proteins and some soluble proteins are moved via slow transport (Maday et al., 2014). However, even the fast axonal transport is not sufficient for neuronal functions, including synaptic neogenesis or remodeling during long-term potentiation, axonal regeneration after neuronal injury. To enable immediate protein supply at the axon terminal, mRNAs may need to be transported

and stored in axons in advance, then locally translated into proteins when necessary.

It is known that factors necessary for protein translation, such as ribosomes, tRNAs, and translation initiation factors are all localized within axons (Kar et al., 2013), and that these translation apparatuses work together to perform local translation. When brain-derived neurotrophic factor (BDNF) or netrin-1, which promotes axon elongation, growth cone and synapse formation, and remodeling, is applied to the axons of cultured neurons, local protein synthesis increases, suggesting that local translation is an important factor in these phenomena (Cagnetta et al., 2018). BDNF binds to its receptor, tropomyosin-related kinase B (TrkB) and activates various intracellular signaling cascades to release mRNAs from RNA granules and promote their local translation (Leal et al., 2014). Deleted in colorectal carcinoma (DCC), a receptor for netrin-1, binds to translation initiation factors and ribosomes directly inside cells, and then promotes local translation in axons by signaling netrin-1 (Tcherkezian et al., 2010).

Ribosomes in axons were originally considered to be transported from cell bodies in neurons or other cells, such as glial cells, after being assembled in the nucleolus (Court et al., 2008). However, it has recently been reported that some ribosomes are assembled in axons in order to maintain their function, from locally translated components such as ribosome proteins as described later (Shigeoka et al., 2019; Nagano et al., 2020). It is thought that neurons have a translation control mechanism specialized for axons, other than the one in cell bodies.

Vesicles, such as endosomes and lysosomes, and mitochondria are crucial to maintain local translation in axons. RNA granules are transferred to axons on lysosomes tethered by annexin A11 (ANXA11), an RNA granule-associated phosphoinositide-binding protein (Liao et al., 2019). Mitochondria are recruited to branching sites of axons following translational machinery to provide energy supply for local translation (Spillane et al., 2013). Furthermore, late endosomes regulate overall protein synthesis in axons by association with both RNA granules and ribosomes, and by controlling mitochondrial function through translation of the related mRNAs (Cioni et al., 2019).

SIGNIFICANCE OF AXONAL DEGENERATION IN NEURODEGENERATIVE DISEASES

It is controversial which is more critical for triggering neuronal cell death in neurodegenerative diseases: changes in neuronal cell bodies (neuronopathy) or changes in axons (axonopathy). Nonetheless, there are many reports that indicate changes in axons or synapses occur during the early stage of the diseases. In ALS and SMA, morphological and functional abnormalities of the neuromuscular junctions between lower motor neurons and skeletal muscles, are detected in model mice that have not yet developed motor symptoms, as well as in patients with mild symptoms (Fallini et al., 2012; Moloney et al., 2014). In Alzheimer's disease (AD), abnormally aggregated A β oligomers

inside and outside of neurons have been shown to suppress long-term potentiation at synapses or alter the synaptic structure (Viola and Klein, 2015). In addition, changes suggestive of impaired axonal transport, such as axonal swelling and tau deposition in axons, have been observed in pre-symptomatic model mice and early symptomatic patients (Stokin et al., 2005).

MRNA TRANSPORT AND LOCAL TRANSLATION IN AXONS IN NEURODEGENERATIVE DISEASES

As mentioned above, local translation in axons plays an important role in maintaining a healthy state of neurons. Therefore, it is presumed that if the local translation is disrupted, the function and viability of neurons will be impaired. In fact, several neurodegenerative diseases have been suggested to impair the local translation function, and are considered to be involved in the pathophysiology of various neurodegenerative disease models. In the following, we review dysfunctions of local translation in some typical neurodegenerative diseases.

Amyotrophic Lateral Sclerosis/Frontotemporal Dementia

Amyotrophic lateral sclerosis is an intractable disease in which impairment of upper and lower motor neurons cause muscle weakness and atrophy of skeletal muscles throughout the body. FTD is accompanied with personality changes, behavioral abnormalities, aphasia, etc., due to degeneration of cerebral cortical neurons in the frontal and temporal lobes. Mutations of causative genes, especially those of RNA-binding proteins, have been identified in some cases of these diseases, including TDP-43 (*TARDBP*), *FUS*, heterogeneous nuclear ribonucleoprotein A1 (*hnRNPA1*), *hnRNPA2/B1*. As a frequent mutation in ALS/FTD, abnormal expansion of the GGGGCC repeat sequence in the untranslated region of the *C9orf72* gene is also observed (Mejzini et al., 2019).

In addition to the cases caused by these gene mutations, many sporadic ALS/FTD cases of unknown genetic factors show TDP-43 disappearance from the nuclei and abnormal depositions in the cytoplasm of neurons, indicating that these diseases form a common pathological spectrum in terms of TDP-43 pathology (Arai et al., 2006; Neumann et al., 2006). Similar localization abnormalities are also observed in other RNA-binding proteins such as *FUS* (Kwiatkowski et al., 2009; Vance et al., 2009). These phenomena imply that disturbance of RNA metabolism due to functional abnormality of RNA-binding proteins is involved in the pathogenesis of ALS/FTD.

Physiologically, TDP-43 and *FUS* are mainly localized in the nucleus and control gene translation and splicing of transcribed pre-mRNAs. In addition, these proteins shuttle between the nucleus and cytoplasm to regulate export out of the nucleus, transfer into the cytoplasm, and translation of mature mRNAs (Ederle and Dormann, 2017).

mRNAs can form granular structures in the cytoplasm called RNA granules in association with RNA-binding proteins

(Khalil et al., 2018). mRNAs are transferred to a required site in RNA granules where translation is suppressed, and when protein synthesis is needed, they are released from the RNA granules and incorporated into translation machinery, such as ribosomes. RNA granules consist of: stress granules that temporarily suppress the translation of mRNAs during stress such as starvation, P-bodies that work to degrade mRNAs, and neuronal RNA granules that transport mRNAs to neurites such as axons and dendrites (Anderson and Kedersha, 2009). These RNA granules contain common RNA-binding proteins and are supposed to have similar structures to each other. A single RNA granule includes multiple RNA-binding proteins to incorporate specific mRNA having an affinity for these proteins.

Transactive responsive-DNA binding protein 43 and *FUS* are constituents of stress granules, which regulate the translation of mRNAs (Aulas and Vande Velde, 2015). In addition, these proteins also form neuronal RNA granules and are involved in the transport of mRNAs to axons (Alami et al., 2014; López-Erauskin et al., 2018). Both TDP-43 and *FUS* have a highly hydrophobic amino acid sequence region called low complexity domain (LCD), and multiple molecules of RNA-binding proteins associate with this region to form a non-membranous structure called a liquid droplet. It generates surfaced vesicles and contributes to the formation of RNA granules. Most of the *TARDBP* and *FUS* gene mutations found in familial ALS/FTD are distributed in the LCD of TDP-43, and in the nuclear localization signal (NLS) site required for nuclear localization of *FUS*. These mutations are thought to be involved in diseases by changing the intracellular localization and enhancing aggregation of the proteins. Mutant TDP-43 and *FUS* show disturbance of stress granule dynamics (Aulas and Vande Velde, 2015). In addition, neuronal RNA granules containing TDP-43 dynamically change in morphology and assembly in axons, and the number of mature granules decreases by inhibition of hydrophobic binding (Gopal et al., 2017). It has also been reported that in mutant TDP-43 the neuronal RNA granules formed are unstable, and anterograde axonal transport is reduced (Alami et al., 2014).

Previous reports have identified some molecules to be TDP-43-dependent for axonal transport. For instance, neurofilament-L (*NEFL*) and microtubule associated protein 1B (*MAP1B*) mRNAs are reported to be transported to axons by TDP-43 (Godena et al., 2011; Alami et al., 2014). *Drosophila* lacking the TDP-43 gene show abnormal synaptic structure due to a decrease in MAP1B protein at synapses (Coyne et al., 2014). *FUS* transports *FOSB* mRNA in axons, dysregulation of which causes abnormal axonal branching (Akiyama et al., 2019). It has also been shown that TDP-43 and *FUS* transport mRNAs to neurites by binding to a three-dimensional structure called G-quadruplex (Ishiguro et al., 2016; Imperatore et al., 2020). In order to survey target mRNAs for axonal transport by TDP-43, we screened mRNAs downregulated in axons by RNAi-mediated TDP-43 down-regulation, and identified mRNAs of translation-related factors including multiple cytoplasmic ribosomal proteins and some translation elongation factors as a major targets of TDP-43-dependent axonal transport (Nagano et al., 2020).

Ribosomal proteins compose ribosomes, which are intracellular apparatuses that together with ribosomal RNA

translate proteins from mRNAs. mRNAs of translation-related proteins, including different subunits of ribosomal proteins, are abundant in neuronal axons (Bigler et al., 2017; Rotem et al., 2017), suggesting that the axonal transport of the mRNAs has functional significance. Ribosomal protein mRNAs have been shown to be translated in axons and to play an important role in axonal ribosome assembly (Shigeoka et al., 2019; Nagano et al., 2020). From the results above, it is conceivable that the impairment of axonal protein translation by decreased axonal transport of ribosomal protein mRNAs may lead to the degeneration of motor neurons in ALD/FTD. Furthermore, we have found that the RNA-binding protein La, which is a known antigen of autoantibodies detected in systemic lupus erythematosus and Sjögren's syndrome (Maraia et al., 2017), is co-localized with TDP-43 and ribosomal protein mRNA in axons. A detailed analysis of the regulatory mechanism of local translation by TDP-43 and La is anticipated.

Recent reports have shown findings similar to our study. Ribosomal protein mRNAs have been identified as mRNAs with decreased stability in fibroblasts and iPS cell-derived motor neurons in sporadic and *C9orf72* mutated ALS patients (Tank et al., 2018). Briese et al. (2020) showed that mRNAs of translation-related proteins including ribosomal proteins are identified as targets for TDP-43-dependent axonal transport in motor neurons, and TDP-43 regulates their local translation. Other reports also showed that mice overexpressing TDP-43 localized in the cytoplasm or mutant FUS have a decrease in overall protein translation in neurons including axons, postulating their involvement in the pathogenesis of ALS/FTD (López-Erauskin et al., 2018; Charif et al., 2020).

Approximately half of FTD cases do not show TDP-43 pathology, but instead such cases tau shows abnormal phosphorylation (Šimić et al., 2016). Also, mutations in the tau (*MAPT*) gene have been identified in juvenile FTD (Hutton et al., 1998). Tau binds to cytoskeletal protein microtubules and contributes to the morphology maintenance of neurons including axons. Abnormally phosphorylated tau undergoes structural changes that reduce its binding to microtubules, and form aggregates and deposits in somatodendritic or axonal compartments (Combs et al., 2019). Microtubules serve as tracks for axonal transport via motor proteins such as kinesin. Therefore, in tauopathy, it is possible that axonal transport of various molecules, including mRNAs, is impaired, which likely disrupts local translation.

Spinal Muscular Atrophy

Spinal muscular atrophy is a hereditary disorder that causes degeneration of lower motor neurons (Bharucha-Goebel and Kaufmann, 2017). It is classified into types I thru IV according to the age of onset; and the earlier the onset is, the more serious motor symptoms manifest. Pathologically, a decrease in motor neuron axons and morphological changes in the neuromuscular junction are observed at an early stage (Ling et al., 2012; Courtney et al., 2019), and axonal degeneration plays a central role in disease progression. In most SMA cases, deletion of the *SMN1* gene destabilizes its translation product SMN, causing a deficiency in SMN protein expression (Fallini et al., 2012). *SMN2*

gene is a paralog of *SMN1* gene, and *SMN2* differs from *SMN1* by only five nucleotides at the 3' end of the gene. Most *SMN2* transcripts are spliced to skip exon 7 due to a single nucleotide change from *SMN1* in the exon. By that, only about 10% are the full-length transcript to produce a stable protein. The copy number of the *SMN2* gene varies between patients. Most severe type I patients have only 1 or 2 copies of *SMN2*; and the symptoms become milder with an increase of *SMN2* copy number because the *SMN2* gene transcript can help supplement the deficiency of SMN protein to some extent (Calucho et al., 2018).

Survival of motor neuron is ubiquitously expressed throughout the body, but SMA has a particularly profound effect on lower motor neurons. SMN is mostly located in the nucleus and together with gem-associated proteins (Gemins) assembles small nuclear ribonucleoproteins (snRNP) (Fallini et al., 2012) and forms a complex called spliceosome, which executes pre-mRNA splicing (Pellizzoni, 2007). SMN is also localized in axons (Todd et al., 2010) and regulates axonal transport of mRNAs, as well as their translation by interacting with cytoskeletal proteins and RNA-binding proteins (Fallini et al., 2012). SMN binds to actin-binding proteins profilins, and modulates actin polymerization (Giesemann et al., 1999; Sharma et al., 2005). SMN in axons forms a ribonucleoprotein complex with components different from snRNP, suggesting that SMN have a function independent of splicing regulation in snRNP (Fallini et al., 2011). HuD, the neuron-specific RNA-binding protein assembled into RNA granules, controls axonal transport of mRNAs and axon elongation in cooperation with SMN (Akten et al., 2011; Hao le et al., 2017). In addition, it has been reported that axons have a short isoform different from the canonical SMN which acts on polarity formation in neurons (Pletto et al., 2018). The dysfunction of the molecules may define specific changes in motor neurons due to *SMN1* expression deficiency.

Localization of β -actin (*ACTB*) mRNA is reduced in axons of SMN-deficient motor neurons (Rossoll et al., 2003). β -actin is a major skeletal protein that acts on morphological maintenance and dynamics of growth cones and synapses. In addition to axonal targeting of *ACTB* mRNA, SMN also regulates its local translation in growth cones, which is known to be impaired in SMN-deficient motor neurons (Rossoll et al., 2003; Rathod et al., 2012).

Growth-associated protein 43 (*GAP43*) mRNA is also transported and translated in axons under the control of SMN (Fallini et al., 2016). *GAP43* is highly expressed in growth cones and binds to phospholipids in the cell membrane. This protein signals to maintain cytoskeletal morphology (Hartl and Schneider, 2019). Axonal transport of *GAP43* and *ACTB* mRNAs influence each other, and their local translation affects axon elongation and branching, respectively (Donnelly et al., 2013).

Candidate plasticity-related gene 15 (*CPG15*) is highly expressed in developing spinal motor neurons, and promotes axon branching and neuromuscular junction formation. *CPG15* mRNA is transported to axons with the assistance of SMN and translated locally. Overexpression of *CPG15* mRNA rescues SMN deficiency motor axon defects, indicating that localization of *CPG15* mRNA in axons is an important determinant of axon architecture (Akten et al., 2011).

There are other RNA-binding proteins as well, which function in conjunction with SMN. Heterogeneous nuclear ribonucleoprotein R (hnRNP R) binds to both *ACTB* mRNA and SMN (Glinka et al., 2010). Furthermore, HuD is involved in axonal transport of *GAP43* and *CPG15* mRNAs (Akten et al., 2011; Hao et al., 2017). These RNA-binding proteins are thought to regulate the axonal transport and translation of target mRNAs in cooperation with SMN.

Decreased expression of SMN has been shown to result in reduced overall translation in growth cones (Fallini et al., 2016). This may suggest that the axonal transport and local translation of mRNA regulated by SMN are involved not only in the above-mentioned mRNAs, but also in the metabolic regulation of many mRNAs, or that mRNAs that directly affect the translation function.

Other Neurodegenerative Diseases

Alzheimer's disease causes memory deficits, behavioral changes, and personality changes due to cognitive impairment, and is the most common causative disease of dementia. Pathologically, amyloid β ($A\beta$) is produced by processing from amyloid precursor protein (APP) and extracellularly deposited as amyloid plaques. These plaques and hyperphosphorylated tau which is characterized by intracellular accumulation as neurofibrillary tangles are hallmarks of the disease (Serý et al., 2013). One of the $A\beta$ isoforms, $A\beta_{1-42}$, has the most potent aggregating property. Mutations in *APP*, presenilin 1 (*PSEN1*) and *PSEN2* genes have been identified in familial AD patients, and these mutations are responsible for increased processing of $A\beta_{1-42}$ (Selkoe and Hardy, 2016).

Brain-derived neurotrophic factor mRNA and BDNF protein are reduced in the brains of AD patients and model mice (Tanila, 2017). *In vitro*, $A\beta$ reduces BDNF signaling by inhibiting the proteolytic production of BDNF from pro-BDNF

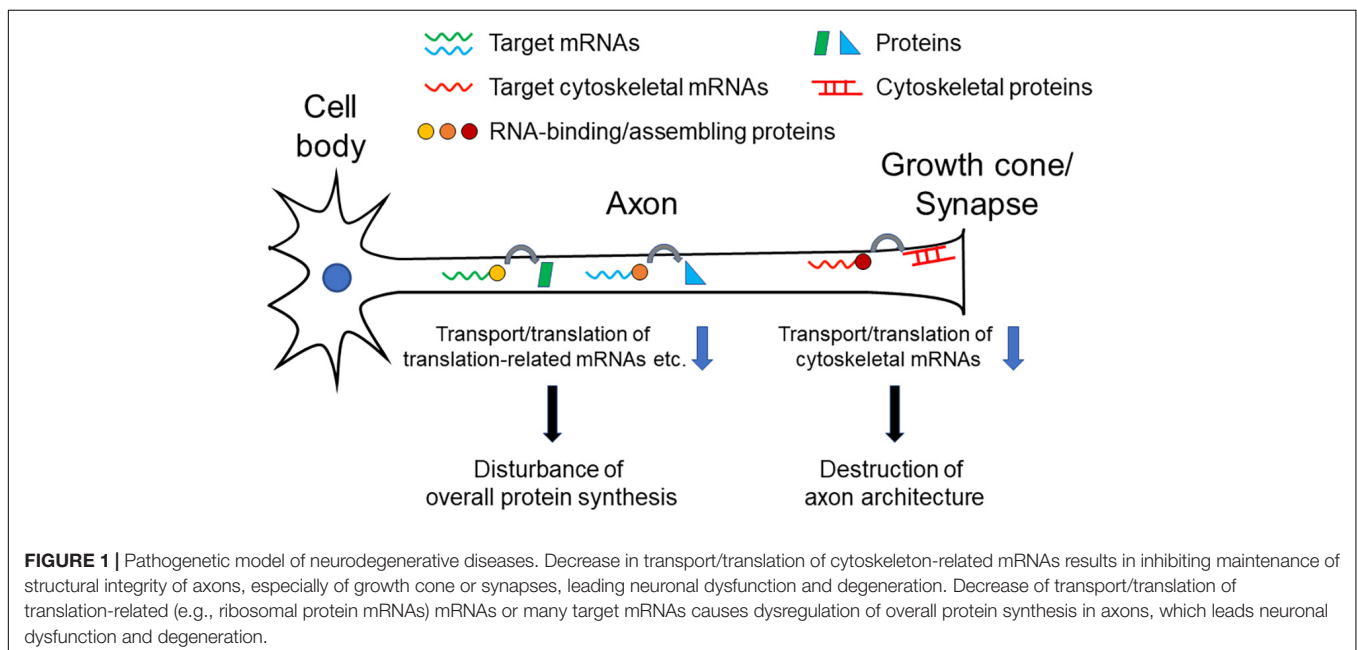
(Zheng et al., 2010), and by suppressing the retrograde axonal transport of the BDNF-TrkB complex (Poon et al., 2013).

On the other hand, local treatment of $A\beta_{1-42}$ on axons has been shown to increase translation from some of the mRNAs within axons (Baleriola et al., 2014). Among them, the transcription factor *ATF4* mRNA is locally translated in axons, and then ATF4 protein is retrogradely transported into the nucleus to increase the expression of C/EBP homologous protein (CHOP), a key molecule of the unfolded protein response pathway, thereby causing neurodegeneration. *ATF4* mRNA and protein are both increased in axons of brain lesions in patients with AD, supporting the notion obtained from cultured neuron experiments.

Furthermore, tau binds to TIA1, one of the RNA-binding proteins in stress granules, and in doing so controls the formation of stress granules and regulates protein translation. Conversely, TIA1 promotes tau aggregation and neurotoxicity (Vanderweyde et al., 2016). In addition, increased expression of G3BP1 and IMP1, which are RNA-binding proteins that bind to *MAPT* mRNA, change the isoform expression pattern of *MAPT* mRNA and protein, increase the formation of neuronal RNA granules, and promote axonal elongation (Moschner et al., 2014).

It is also known that TDP-43 pathology exists in 20–50% of AD patients (Chang et al., 2016). Although it is not yet clear how this change is involved in the pathogenesis of AD, it is quite possible that the dysfunction of TDP-43 is modifying the AD pathology by impairing local translation in neurons with a mechanism similar to ALS/FTD disease models.

Fragile X syndrome is a disease that causes various physical abnormalities, intellectual disability, and psychiatric symptoms. Abnormal expansion of the CGG repeat sequence in the 5' untranslated region of the *FMR1* gene causes methylation of the promoter of the gene, which decreases the expression of the



FMRP at the transcription level for emergence of the disease (Hagerman et al., 2017).

Fragile X mental retardation protein is an RNA-binding protein having a ribonucleoprotein K homology (KH) domain and an arginine-glycine-glycine repeat (RGG) domain, which function to suppress the overall translation of proteins via binding to the RGG domain to G-quadruplexes of mRNAs (Schaeffer et al., 2001), or binding to ribosomes between large and small subunits (Chen et al., 2014).

The mechanism of translation suppression by FMRP has been vigorously investigated primarily in dendrites, specifically in postsynaptic spines (Thelen and Kye, 2020; Lu et al., 2021). However, FMRP is also present in axons and forms a complex with molecules involved in RNA interference (RNAi) such as Dicer, and suppresses the expression of *RHOA* mRNA in distal axons, which causes collapse of growth cones (Hengst et al., 2006). It has also been shown that FMRP transports *MAP1B* and calmodulin (*CALMI*) mRNA into axons, and regulates their local translation via microRNA to act on axon elongation (Wang et al., 2015).

General View

As we overviewed here, different RNA-binding or RNA-assembly protein abnormalities are reported to be associated with neurodegenerative disorders, and the corresponding target mRNAs have been identified in each of the proteins. Notably, many of the target mRNAs are cytoskeleton-related protein transcripts that reside in growth cones and synapses. These data suggest that axonal transport and local translation of these mRNAs are important for the morphological and functional formation and maintenance of growth cones and synapses. Dysfunction of the transport and translation of these mRNAs causes degeneration of axon terminals, which disconnects the neural network to cause symptoms of each disease (Figure 1).

REFERENCES

- Akiyama, T., Suzuki, N., Ishikawa, M., Fujimori, K., Sone, T., Kawada, J., et al. (2019). Aberrant axon branching via Fos-B dysregulation in FUS-ALS motor neurons. *EBioMedicine* 45, 362–378. doi: 10.1016/j.ebiom.2019.06.013
- Akten, B., Kye, M. J., Hao le, T., Wertz, M. H., Singh, S., Nie, D., et al. (2011). Interaction of survival of motor neuron (SMN) and HuD proteins with mRNA cpg15 rescues motor neuron axonal deficits. *Proc. Natl. Acad. Sci. U.S.A.* 108, 10337–10342. doi: 10.1073/pnas.1104928108
- Alami, N. H., Smith, R. B., Carrasco, M. A., Williams, L. A., Winborn, C. S., Han, S. S. W., et al. (2014). Axonal transport of TDP-43 mRNA granules is impaired by ALS-causing mutations. *Neuron* 81, 536–543. doi: 10.1016/j.neuron.2013.12.018
- Al-Chalabi, A., Andersen, P. M., Nilsson, P., Chioza, B., Andersson, J. L., Russ, C., et al. (1999). Deletions of the heavy neurofilament subunit tail in amyotrophic lateral sclerosis. *Hum. Mol. Genet.* 8, 157–164. doi: 10.1093/hmg/8.2.157
- Anderson, P., and Kedersha, N. (2009). RNA granules: post-transcriptional and epigenetic modulators of gene expression. *Nat. Rev. Mol. Cell Biol.* 10, 430–436. doi: 10.1038/nrm2694
- Arai, T., Hasegawa, M., Akiyama, H., Ikeda, K., Nonaka, T., Mori, H., et al. (2006). TDP-43 is a component of ubiquitin-positive tau-negative inclusions in frontotemporal lobar degeneration and amyotrophic lateral sclerosis. *Biochem. Biophys. Res. Commun.* 351, 602–611. doi: 10.1016/j.bbrc.2006.10.093

Impairment of such functions may also gradually affect neuronal viability, resulting in chronically progressive neurodegeneration. Furthermore, *TUBA4A* and *NEFH* are listed as the causative genes of some ALS cases (Al-Chalabi et al., 1999; Smith et al., 2014), which also indicates the importance of cytoskeletal proteins in the pathogenesis of the disease.

The integrity of ribosomes in axons to maintain local protein synthesis capability may also be a critical factor for maintaining neuronal health. As we discussed above, RNA-binding and RNA-assembling proteins can regulate transport and translation of many different mRNAs in axons, rather than limited specific targets. In addition to our finding that TDP-43 targets translation-related mRNAs for axonal transport, change of overall translation efficiency is detected in axons as a result of TDP-43, FUS, and SMN dysfunction (Rossoll et al., 2003; López-Erauskin et al., 2018; Nagano et al., 2020). Protein synthesizing activity in axons and synapses is indispensable not only for rapid neuronal responses, but also for maintaining structural integrity and electrical conductivity of axons (Figure 1).

CONCLUSION

Axonal transport and local translation of mRNAs play an important role in maintaining the survival of neurons, and their failure to do so is greatly involved in the development of many neurodegenerative diseases. By improving the function of mRNA metabolism in axons, it will be possible to develop new therapeutic strategies for these neurodegenerative diseases.

AUTHOR CONTRIBUTIONS

SN and TA wrote the manuscript. Both authors contributed to the article and approved the submitted version.

- Aulas, A., and Vande Velde, C. (2015). Alterations in stress granule dynamics driven by TDP-43 and FUS: a link to pathological inclusions in ALS? *Front. Cell. Neurosci.* 9:423. doi: 10.3389/fncel.2015.00423
- Baleriola, J., Walker, C. A., Jean, Y. Y., Cray, J. F., Troy, C. M., Nagy, P. L., et al. (2014). Axonally synthesized ATF4 transmits a neurodegenerative signal across brain regions. *Cell* 158, 1159–1172. doi: 10.1016/j.cell.2014.07.001
- Bharucha-Goebel, D., and Kaufmann, P. (2017). Treatment advances in spinal muscular atrophy. *Curr. Neurol. Neurosci. Rep.* 17:91. doi: 10.1007/s11910-017-0798-y
- Bigler, R. L., Kamande, J. W., Dumitru, R., Niedringhaus, M., and Taylor, A. M. (2017). Messenger RNAs localized to distal projections of human stem cell derived neurons. *Sci. Rep.* 7:611. doi: 10.1038/s41598-017-00676-w
- Briese, M., Saal-Bauerschubert, L., Lüningschrör, P., Moradi, M., Dombert, B., Surrey, V., et al. (2020). Loss of Tdp-43 disrupts the axonal transcriptome of motoneurons accompanied by impaired axonal translation and mitochondria function. *Acta Neuropathol. Commun.* 8:116. doi: 10.1186/s40478-020-00987-6
- Cagnetta, R., Frese, C. K., Shigeoka, T., Krijgsveld, J., and Holt, C. E. (2018). Rapid cue-specific remodeling of the nascent axonal proteome. *Neuron* 99, 29–46. doi: 10.1016/j.neuron.2018.06.004
- Calucho, M., Bernal, S., Alías, L., March, F., Venceslá, A., Rodríguez-Álvarez, F. J., et al. (2018). Correlation between SMA type and SMN2 copy number revisited: An analysis of 625 unrelated Spanish patients and a compilation of 2834 reported cases. *Neuromuscul. Disord.* 28, 208–215. doi: 10.1016/j.nmd.2018.01.003

- Chang, X. L., Tan, M. S., Tan, L., and Yu, J. T. (2016). The role of TDP-43 in Alzheimer's disease. *Mol. Neurobiol.* 53, 3349–3359. doi: 10.1007/s12035-015-9264-5
- Charif, S. E., Luchelli, L., Vila, A., Blaustein, M., and Igaz, L. M. (2020). Cytoplasmic expression of the ALS/FTD-related protein TDP-43 decreases global translation both *in vitro* and *in vivo*. *Front. Cell. Neurosci.* 14:594561. doi: 10.3389/fncel.2020.594561
- Chen, E., Sharma, M. R., Shi, X., Agrawal, R. K., and Joseph, S. (2014). Fragile X mental retardation protein regulates translation by binding directly to the ribosome. *Mol. Cell* 54, 407–417. doi: 10.1016/j.molcel.2014.03.023
- Cioni, J. M., Lin, J. Q., Holtermann, A. V., Koppers, M., Jakobs, M. A. H., Azizi, A., et al. (2019). Late endosomes act as mRNA translation platforms and sustain mitochondria in axons. *Cell* 176, 56–72. doi: 10.1016/j.cell.2018.11.030
- Combs, B., Mueller, R. L., Morfini, G., Brady, S. T., and Kanaan, N. M. (2019). Tau and axonal transport misregulation in tauopathies. *Adv. Exp. Med. Biol.* 1184, 81–95. doi: 10.1007/978-981-32-9358-8_7
- Court, F. A., Hendriks, W. T., MacGillavry, H. D., Alvarez, J., and van Minnen, J. (2008). Schwann cell to axon transfer of ribosomes: toward a novel understanding of the role of glia in the nervous system. *J. Neurosci.* 28, 11024–11029. doi: 10.1523/JNEUROSCI.2429-08.2008
- Courtney, N. L., Mole, A. J., Thomson, A. K., and Murray, L. M. (2019). Reduced P53 levels ameliorate neuromuscular junction loss without affecting motor neuron pathology in a mouse model of spinal muscular atrophy. *Cell Death Dis.* 10:515. doi: 10.1038/s41419-019-1727-6
- Coyne, A. N., Siddegowda, B. B., Estes, P. S., Johannesmeyer, J., Kovalik, T., Daniel, S. G., et al. (2014). Futsch/MAP1B mRNA is a translational target of TDP-43 and is neuroprotective in a *Drosophila* model of amyotrophic lateral sclerosis. *J. Neurosci.* 34, 15962–15974. doi: 10.1523/JNEUROSCI.2526-14.2014
- DeJesus-Hernandez, M., Mackenzie, I. R., Boeve, B. F., Boxer, A. L., Baker, M., Rutherford, N. J., et al. (2011). Expanded GGGGCC hexanucleotide repeat in noncoding region of C9ORF72 causes chromosome 9p-linked FTD and ALS. *Neuron* 72, 245–256. doi: 10.1016/j.neuron.2011.09.011
- Donnelly, C. J., Park, M., Spillane, M., Yoo, S., Pacheco, A., Gomes, C., et al. (2013). Axonally synthesized β -actin and GAP-43 proteins support distinct modes of axonal growth. *J. Neurosci.* 33, 3311–3322. doi: 10.1523/JNEUROSCI.1722-12.2013
- Ederle, H., and Dormann, D. (2017). TDP-43 and FUS en route from the nucleus to the cytoplasm. *FEBS Lett.* 591, 1489–1507. doi: 10.1002/1873-3468.12646
- Fallini, C., Bassell, G. J., and Rossoll, W. (2012). Spinal muscular atrophy: the role of SMN in axonal mRNA regulation. *Brain Res.* 1462, 81–92. doi: 10.1016/j.brainres.2012.01.044
- Fallini, C., Donlin-Asp, P. G., Rouanet, J. P., Bassell, G. J., and Rossoll, W. (2016). Deficiency of the survival of motor neuron protein impairs mRNA localization and local translation in the growth cone of motor neurons. *J. Neurosci.* 36, 3811–3820. doi: 10.1523/JNEUROSCI.2396-15.2016
- Fallini, C., Zhang, H., Su, Y., Silani, V., Singer, R. H., Rossoll, W., et al. (2011). The survival of motor neuron (SMN) protein interacts with the mRNA-binding protein HuD and regulates localization of poly(A) mRNA in primary motor neuron axons. *J. Neurosci.* 31, 3914–3925. doi: 10.1523/JNEUROSCI.3631-10.2011
- Giesemann, T., Rathke-Hartlieb, S., Rothkegel, M., Bartsch, J. W., Buchmeier, S., Jockusch, B. M., et al. (1999). A role for polyproline motifs in the spinal muscular atrophy protein SMN. Profilins bind to and colocalize with smn in nuclear gems. *J. Biol. Chem.* 274, 37908–37914. doi: 10.1074/jbc.274.53.37908
- Glinka, M., Herrmann, T., Funk, N., Havlicek, S., Rossoll, W., Winkler, C., et al. (2010). The heterogeneous nuclear ribonucleoprotein-R is necessary for axonal beta-actin mRNA translocation in spinal motor neurons. *Hum. Mol. Genet.* 19, 1951–1966. doi: 10.1093/hmg/ddq073
- Godena, V. K., Romano, G., Romano, M., Appocher, C., Klima, R., Buratti, E., et al. (2011). TDP-43 regulates *Drosophila* neuromuscular junctions growth by modulating Futsch/MAP1B levels and synaptic microtubules organization. *PLoS One* 6:e17808. doi: 10.1371/journal.pone.0017808
- Gopal, P. P., Nirschl, J. J., Klinman, E., and Holzbaur, E. L. (2017). Amyotrophic lateral sclerosis-linked mutations increase the viscosity of liquid-like TDP-43 RNP granules in neurons. *Proc. Natl. Acad. Sci. U.S.A.* 114, E2466–E2475. doi: 10.1073/pnas.1614462114
- Hagerman, R. J., Berry-Kravis, E., Hazlett, H. C., Bailey, D. B. Jr., Moine, H., Kooy, R. F., et al. (2017). Fragile X syndrome. *Nat. Rev. Dis. Primers* 3:17065. doi: 10.1038/nrdp.2017.65
- Hao le, T., Duy, P. Q., An, M., Talbot, J., Iyer, C. C., Wolman, M., et al. (2017). HuD and the survival motor neuron protein interact in motoneurons and are essential for motoneuron development, function, and mRNA regulation. *J. Neurosci.* 37, 11559–11571. doi: 10.1523/JNEUROSCI.1528-17.2017
- Hartl, M., and Schneider, R. (2019). A unique family of neuronal signaling proteins implicated in oncogenesis and tumor suppression. *Front. Oncol.* 9:289. doi: 10.3389/fonc.2019.00289
- Heemels, M. T. (2016). Neurodegenerative diseases. *Nature* 539:179. doi: 10.1038/539179a
- Hengst, U., Cox, L. J., Macosko, E. Z., and Jaffrey, S. R. (2006). Functional and selective RNA interference in developing axons and growth cones. *J. Neurosci.* 26, 5727–5732. doi: 10.1523/JNEUROSCI.5229-05.2006
- Hirokawa, N., Noda, Y., Tanaka, Y., and Niwa, S. (2009). Kinesin superfamily motor proteins and intracellular transport. *Nat. Rev. Mol. Cell Biol.* 10, 682–696. doi: 10.1038/nrm2774
- Holt, C. E., Martin, K. C., and Schuman, E. M. (2019). Local translation in neurons: visualization and function. *Nat. Struct. Mol. Biol.* 26, 557–566. doi: 10.1038/s41594-019-0263-5
- Hutton, M., Lendon, C. L., Rizzu, P., Baker, M., Froelich, S., Houlden, H., et al. (1998). Association of missense and 5'-splice-site mutations in tau with the inherited dementia FTDP-17. *Nature* 393, 702–705. doi: 10.1038/31508
- Imperatore, J. A., McAninch, D. S., Valdez-Sinon, A. N., Bassell, G. J., and Mihailescu, M. R. (2020). FUS recognizes G quadruplex structures within neuronal mRNAs. *Front. Mol. Biosci.* 7:6. doi: 10.3389/fmolb.2020.00006
- Ishiguro, A., Kimura, N., Watanabe, Y., Watanabe, S., and Ishihama, A. (2016). TDP-43 binds and transports G-quadruplex-containing mRNAs into neurites for local translation. *Genes Cells* 21, 466–481. doi: 10.1111/gtc.12352
- Kar, A. N., MacGibben, M. A., Gervasi, N. M., Gioio, A. E., and Kaplan, B. B. (2013). Intra-axonal synthesis of eukaryotic translation initiation factors regulates local protein synthesis and axon growth in rat sympathetic neurons. *J. Neurosci.* 33, 7165–7174. doi: 10.1523/JNEUROSCI.2040-12.2013
- Khalil, B., Morderer, D., Price, P. L., Liu, F., and Rossoll, W. (2018). mRNP assembly, axonal transport, and local translation in neurodegenerative diseases. *Brain Res.* 1693, 75–91. doi: 10.1016/j.brainres.2018.02.018
- Kwiatkowski, T. J. Jr., Bosco, D. A., Leclerc, A. L., Tamrazian, E., Vanderburg, C. R., Russ, C., et al. (2009). Mutations in the FUS/TLS gene on chromosome 16 cause familial amyotrophic lateral sclerosis. *Science* 323, 1205–1208. doi: 10.1126/science.1166066
- Leal, G., Comprido, D., and Duarte, C. B. (2014). BDNF-induced local protein synthesis and synaptic plasticity. *Neuropharmacology* 76, 639–656. doi: 10.1016/j.neuropharm.2013.04.005
- Liao, Y. C., Fernandopulle, M. S., Wang, G., Choi, H., Hao, L., Drerup, C. M., et al. (2019). RNA granules hitchhike on lysosomes for long-distance transport, using annexin A11 as a molecular tether. *Cell* 179, 147–164. doi: 10.1016/j.cell.2019.08.050
- Ling, K. K. Y., Gibbs, R. M., Feng, Z., and Ko, C. P. (2012). Severe neuromuscular denervation of clinically relevant muscles in a mouse model of spinal muscular atrophy. *Hum. Mol. Genet.* 21, 185–195. doi: 10.1093/hmg/ddr453
- López-Erauskin, J., Tadokoro, T., Baughn, M. W., Myers, B., McAlonis-Downes, M., Chillón-Marinas, C., et al. (2018). ALS/FTD-linked mutation in FUS suppresses intra-axonal protein synthesis and drives disease without nuclear loss-of-function of FUS. *Neuron* 100, 816–830. doi: 10.1016/j.neuron.2018.09.044
- Lu, J. X., Wang, Y., Zhang, Y. J., Shen, M. F., Li, H. Y., Yu, Z. Q., et al. (2021). Axonal mRNA localization and local translation in neurodegenerative disease. *Neural Regen. Res.* 16, 1950–1957. doi: 10.4103/1673-5374.308074
- Maday, S., Twelvetrees, A. E., Moughamian, A. J., and Holzbaur, E. L. (2014). Axonal transport: cargo-specific mechanisms of motility and regulation. *Neuron* 84, 292–309. doi: 10.1016/j.neuron.2014.10.019
- Maraia, R. J., Mattijssen, S., Cruz-Gallardo, I., and Conte, M. R. (2017). The La and related RNA-binding proteins (LARPs): structures, functions, and evolving perspectives. *Wiley Interdiscip. Rev. RNA* 8:e1430. doi: 10.1002/wrna.1430
- Maurin, T., Zongaro, S., and Bardoni, B. (2014). Fragile X syndrome: from molecular pathology to therapy. *Neurosci. Biobehav. Rev.* 46, 242–255. doi: 10.1016/j.neubiorev.2014.01.006

- Mejzini, R., Flynn, L. L., Pitout, I. L., Fletcher, S., Wilton, S. D., and Akkari, P. A. (2019). ALS genetics, mechanisms, and therapeutics: where are we now? *Front. Neurosci.* 13:1310. doi: 10.3389/fnins.2019.01310
- Moloney, E. B., de Winter, F., and Verhaagen, J. (2014). ALS as a distal axonopathy: molecular mechanisms affecting neuromuscular junction stability in the presymptomatic stages of the disease. *Front. Neurosci.* 8:252. doi: 10.3389/fnins.2014.00252
- Mori, K., Weng, S. M., Arzberger, T., May, S., Rentzsch, K., Kremmer, E., et al. (2013). The C9orf72 GGGGCC repeat is translated into aggregating dipeptide-repeat proteins in FTL/ALS. *Science* 339, 1335–1338. doi: 10.1126/science.1232927
- Moschner, K., Sündermann, F., Meyer, H., da Graca, A. P., Appel, N., Paululat, A., et al. (2014). RNA protein granules modulate tau isoform expression and induce neuronal sprouting. *J. Biol. Chem.* 289, 16814–16825. doi: 10.1074/jbc.M113.541425
- Nagano, S., Jinno, J., Abdelhamid, R. F., Jin, Y., Shibata, M., Watanabe, S., et al. (2020). TDP-43 transports ribosomal protein mRNA to regulate axonal local translation in neuronal axons. *Acta Neuropathol.* 140, 695–713. doi: 10.1007/s00401-020-02205-y
- Neumann, M., Sampathu, D. M., Kwong, L. K., Truax, A. C., Micsenyi, M. C., Chou, T. T., et al. (2006). Ubiquitinated TDP-43 in frontotemporal lobar degeneration and amyotrophic lateral sclerosis. *Science* 314, 130–133. doi: 10.1126/science.1134108
- Pellizzoni, L. (2007). Chaperoning ribonucleoprotein biogenesis in health and disease. *EMBO Rep.* 8, 340–345. doi: 10.1038/sj.embor.7400941
- Pletto, D., Capra, S., Finardi, A., Colciaghi, F., Nobili, P., Battaglia, G. S., et al. (2018). Axon outgrowth and neuronal differentiation defects after a-SMN and FL-SMN silencing in primary hippocampal cultures. *PLoS One* 13:e0199105. doi: 10.1371/journal.pone.0199105
- Poon, W. W., Carlos, A. J., Aguilar, B. L., Berchtold, N. C., Kawano, C. K., Zograbyan, V., et al. (2013). β -Amyloid (A β) oligomers impair brain-derived neurotrophic factor retrograde trafficking by down-regulating ubiquitin C-terminal hydrolase, UCH-L1. *J. Biol. Chem.* 288, 16937–16948. doi: 10.1074/jbc.M113.463711
- Rathod, R., Havlicek, S., Frank, N., Blum, R., and Sendtner, M. (2012). Laminin induced local axonal translation of β -actin mRNA is impaired in SMN-deficient motoneurons. *Histochem. Cell Biol.* 138, 737–748. doi: 10.1007/s00418-012-0989-1
- Renton, A. E., Majounie, E., Waite, A., Simón-Sánchez, J., Rollinson, S., Gibbs, J. R., et al. (2011). A hexanucleotide repeat expansion in C9ORF72 is the cause of chromosome 9p21-linked ALS-FTD. *Neuron* 72, 257–268. doi: 10.1016/j.neuron.2011.09.010
- Rossoll, W., Jablonka, S., Andreassi, C., Kröning, A. K., Karle, K., Monani, U. R., et al. (2003). Smn, the spinal muscular atrophy-determining gene product, modulates axon growth and localization of beta-actin mRNA in growth cones of motoneurons. *J. Cell Biol.* 163, 801–812. doi: 10.1083/jcb.200304128
- Rotem, N., Magen, I., Ionescu, A., Gershoni-Emek, N., Altman, T., Costa, C. J., et al. (2017). ALS along the axons – expression of coding and noncoding RNA differs in axons of ALS models. *Sci. Rep.* 7:44500. doi: 10.1038/srep44500
- Schaeffer, C., Bardoni, B., Mandel, J. L., Ehresmann, B., Ehresmann, C., and Moine, H. (2001). The fragile X mental retardation protein binds specifically to its mRNA via a purine quartet motif. *EMBO J.* 20, 4803–4813. doi: 10.1093/emboj/20.17.4803
- Selkoe, D. J., and Hardy, J. (2016). The amyloid hypothesis of Alzheimer's disease at 25 years. *EMBO Mol. Med.* 8, 595–608. doi: 10.15252/emmm.201606210
- Serý, O., Povová, J., Míšek, I., Pešák, L., and Janout, V. (2013). Molecular mechanisms of neuropathological changes in Alzheimer's disease: a review. *Folia Neuropathol.* 51, 1–9. doi: 10.5114/fn.2013.34190
- Sharma, A., Lambrechts, A., Hao le, T., Le, T. T., Sewry, C. A., Ampe, C., et al. (2005). A role for complexes of survival of motor neurons (SMN) protein with gemins and profilin in neurite-like cytoplasmic extensions of cultured nerve cells. *Exp. Cell Res.* 309, 185–197. doi: 10.1016/j.yexcr.2005.05.014
- Shigeoka, T., Koppers, M., Wong, H. H., Lin, J. Q., Cagnetta, R., Dwivedy, A., et al. (2019). On-site ribosome remodeling by locally synthesized ribosomal proteins in axons. *Cell Rep.* 29, 3605–3619. doi: 10.1016/j.celrep.2019.11.025
- Šimić, G., Babić Leko, M., Wray, S., Harrington, C., Delalle, I., Jovanov-Milošević, N., et al. (2016). Tau protein hyperphosphorylation and aggregation in Alzheimer's disease and other tauopathies, and possible neuroprotective strategies. *Biomolecules* 6:6. doi: 10.3390/biom6010006
- Smith, B. N., Ticozzi, N., Fallini, C., Gkazi, A. S., Topp, S., Kenna, K. P., et al. (2014). Exome-wide rare variant analysis identifies TUBA4A mutations associated with familial ALS. *Neuron* 84, 324–331. doi: 10.1016/j.neuron.2014.09.027
- Spillane, M., Ketschek, A., Merianda, T. T., Twiss, J. L., and Gallo, G. (2013). Mitochondria coordinate sites of axon branching through localized intraxonal protein synthesis. *Cell Rep.* 5, 1564–1575. doi: 10.1016/j.celrep.2013.11.022
- Stokin, G. B., Lillo, C., Falzone, T. L., Brusch, R. G., Rockenstein, E., Mount, S. L., et al. (2005). Axonopathy and transport deficits early in the pathogenesis of Alzheimer's disease. *Science* 307, 1282–1288. doi: 10.1126/science.1105681
- Tanila, H. (2017). The role of BDNF in Alzheimer's disease. *Neurobiol. Dis.* 97, 114–118. doi: 10.1016/j.nbd.2016.05.008
- Tank, E. M., Figueroa-Romero, C., Hinder, L. M., Bedi, K., Archbold, H. C., Li, X., et al. (2018). Abnormal RNA stability in amyotrophic lateral sclerosis. *Nat. Commun.* 9:2845. doi: 10.1038/s41467-018-05049-z
- Tcherkezian, J., Brittis, P. A., Thomas, F., Roux, P. P., and Flanagan, J. G. (2010). Transmembrane receptor DCC associates with protein synthesis machinery and regulates translation. *Cell* 141, 632–644. doi: 10.1016/j.cell.2010.04.008
- Thelen, M. P., and Kye, M. J. (2020). The role of RNA binding proteins for local mRNA translation: implications in neurological disorders. *Front. Mol. Biosci.* 6:161. doi: 10.3389/fmolb.2019.00161
- Todd, A. G., Morse, R., Shaw, D. J., Stebbings, H., and Young, P. J. (2010). Analysis of SMN-neurite granules: core cajal body components are absent from SMN-cytoplasmic complexes. *Biochem. Biophys. Res. Commun.* 397, 479–485. doi: 10.1016/j.bbrc.2010.05.139
- Vance, C., Rogelj, B., Hortobágyi, T., De Vos, K. J., Nishimura, A. L., Sreedharan, J., et al. (2009). Mutations in FUS, an RNA processing protein, cause familial amyotrophic lateral sclerosis type 6. *Science* 323, 1208–1211. doi: 10.1126/science.1165942
- Vanderweyde, T., Apicco, D. J., Youmans-Kidder, K., Ash, P. E. A., Cook, C., Lummertz da Rocha, E., et al. (2016). Interaction of tau with the RNA-binding protein TIA1 regulates tau pathophysiology and toxicity. *Cell Rep.* 15, 1455–1466. doi: 10.1016/j.celrep.2016.04.045
- Viola, K. L., and Klein, W. L. (2015). Amyloid β oligomers in Alzheimer's disease pathogenesis, treatment, and diagnosis. *Acta Neuropathol.* 129, 183–206. doi: 10.1007/s00401-015-1386-3
- Wang, B., Pan, L., Wei, M., Wang, Q., Liu, W. W., Wang, N., et al. (2015). FMRP-mediated axonal delivery of miR-181d regulates axon elongation by locally targeting Map1b and Calm1. *Cell Rep.* 13, 2794–2807. doi: 10.1016/j.celrep.2015.11.057
- Zheng, Z., Sabirzhanov, B., and Keifer, J. (2010). Oligomeric amyloid- β inhibits the proteolytic conversion of brain-derived neurotrophic factor (BDNF), AMPA receptor trafficking, and classical conditioning. *J. Biol. Chem.* 285, 34708–34717. doi: 10.1074/jbc.M110.150821

Conflict of Interest: The authors declare that the research was conducted in the absence of any commercial or financial relationships that could be construed as a potential conflict of interest.

Copyright © 2021 Nagano and Araki. This is an open-access article distributed under the terms of the Creative Commons Attribution License (CC BY). The use, distribution or reproduction in other forums is permitted, provided the original author(s) and the copyright owner(s) are credited and that the original publication in this journal is cited, in accordance with accepted academic practice. No use, distribution or reproduction is permitted which does not comply with these terms.



The Curious Anti-Pathology of the *Wld^s* Mutation: Paradoxical Postsynaptic Spine Growth Accompanies Delayed Presynaptic Wallerian Degeneration

Oswald Steward^{1,2,3,4,5*}, Jennifer M. Yonan^{1,2} and Paula M. Falk⁵

¹ Reeve-Irvine Research Center, University of California, Irvine, Irvine, CA, United States, ² Department of Anatomy & Neurobiology, University of California, Irvine, Irvine, CA, United States, ³ Department of Neurobiology and Behavior, University of California, Irvine, Irvine, CA, United States, ⁴ Department of Neurosurgery, University of California, Irvine, Irvine, CA, United States, ⁵ Department of Neuroscience, University of Virginia, Charlottesville, VA, United States

OPEN ACCESS

Edited by:

Dianna E. Willis,
Burke-Cornell Medical Research
Institute, United States

Reviewed by:

Andrea Loreto,
University of Cambridge,
United Kingdom
Rochelle Marie Hines,
University of Nevada, Las Vegas,
United States

*Correspondence:

Oswald Steward
osteward@uci.edu

Specialty section:

This article was submitted to
Molecular Signalling and Pathways,
a section of the journal
Frontiers in Molecular Neuroscience

Received: 03 July 2021

Accepted: 20 August 2021

Published: 10 September 2021

Citation:

Steward O, Yonan JM and
Falk PM (2021) The Curious
Anti-Pathology of the *Wld^s* Mutation:
Paradoxical Postsynaptic Spine
Growth Accompanies Delayed
Presynaptic Wallerian Degeneration.
Front. Mol. Neurosci. 14:735919.
doi: 10.3389/fnmol.2021.735919

The *Wld^s* mutation, which arose spontaneously in C57Bl/6 mice, remarkably delays the onset of Wallerian degeneration of axons. This remarkable phenotype has transformed our understanding of mechanisms contributing to survival vs. degeneration of mammalian axons after separation from their cell bodies. Although there are numerous studies of how the *Wld^s* mutation affects axon degeneration, especially in the peripheral nervous system, less is known about how the mutation affects degeneration of CNS synapses. Here, using electron microscopy, we explore how the *Wld^s* mutation affects synaptic terminal degeneration and withering and re-growth of dendritic spines on dentate granule cells following lesions of perforant path inputs from the entorhinal cortex. Our results reveal that substantial delays in the timing of synapse degeneration in *Wld^s* mice are accompanied by paradoxical hypertrophy of spine heads with enlargement of post-synaptic membrane specializations (PSDs) and development of spinules. These increases in the complexity of spine morphology are similar to what is seen following induction of long-term potentiation (LTP). Robust and paradoxical spine growth suggests yet to be characterized signaling processes between amputated but non-degenerating axons and their postsynaptic targets.

Keywords: nicotinamide adenyltransferase 1 (NMNAT1), ubiquitination factor U4B, denervation, reinnervation, dentate gyrus, entorhinal cortex, perforant path

INTRODUCTION

The remarkable phenotype of delayed Wallerian degeneration in mice carrying the *Wld^s* mutation has dramatically revised our understanding of mechanisms contributing to survival vs. degeneration of mammalian axons after separation from their cell bodies. The *Wld^s* mutation occurred spontaneously in a colony of C57Bl/6J mice at the Olac breeding colony in Bicester England, and was discovered because of its signature effect—axons that are separated from their cell bodies appear intact at the light and electron microscopic level for many days, and are able to conduct action potentials for up to 2 weeks (Lunn et al., 1989; Perry et al., 1990, 1991).

Herein, we use the term “orphaned axons” to refer to axons that have been separated from their parental cell body that survive. The prolonged viability of orphaned axons in *Wld^s* mutant mice is in dramatic contrast to the situation in normal mice, where amputated axons exhibit signs of degeneration within hours. The dramatic survival of orphaned axons in *Wld^s* mice motivated studies to identify and target the relevant molecular pathways to abrogate axonal degeneration in various neurodegenerative diseases (Fischer et al., 2005; Gillingwater et al., 2006; Coleman and Freeman, 2010).

Early genetic studies revealed that the mutant *Wld^s* gene is dominant (Perry et al., 1990), indicating a gain of function. Subsequent studies revealed that the mutant locus encodes a fusion protein made up of the amino terminal 70 amino acids (N70) fragment of ubiquitination factor U4B, the complete coding region of NAD⁺ synthesizing enzyme nicotinamide adenyltransferase 1 (NMNAT1), and an 18 amino acid linking region (Mack et al., 2001). Enzymatically active NMNAT1 is critical for the axon survival phenotype (Avery et al., 2009). Although the mutant protein accumulates in the nucleus, studies involving fusion of the *Wld^s* protein with axonally transported proteins reveal that axonal targeting is both necessary and sufficient to confer protection against Wallerian degeneration (Babetto et al., 2010). Insights into mechanisms came from subsequent studies revealing that NMNAT2, a rapidly turning over protein related to NMNAT1, is a natural survival factor for axons and that axonal delivery of the *Wld^s* protein with enzymatically active NMNAT1 can substitute for NMNAT2 to maintain axonal NAD levels after injury and promote axonal survival [for a recent review, see (Coleman and Hoke, 2020)].

A deeper understanding of the mechanisms underlying axonal degeneration came as a result of the discovery of the pro-axon degeneration molecule SARM1 [for a review, see (Figley and DiAntonio, 2020)]. Initial studies revealed that loss of the protein SARM1 in flies or mice conferred protection against axon degeneration similar to that of the *Wld^s* mutation. Subsequent studies revealed that SARM1 degrades NAD and that this NADase activity is essential for SARM1 to promote degeneration. A relationship between SARM1 and NMNAT was revealed by the finding that in healthy axons, NMNAT2 protects axons from SARM1-mediated degeneration, and loss of NMNAT2 as a result of injury activates SARM1, triggering degeneration. Moreover, over-expression of and axonal targeting of NMNAT1 blocks injury-induced SARM1 activation and NAD degradation critical for axon degeneration (Sasaki et al., 2016). Together, these studies revealed that axon degeneration is an active process regulated by the balance of action of pro- and anti-degenerative molecular pathways. These findings reveal potential targets for therapeutic interventions to prevent or delay axon degeneration in various neurodegenerative diseases (Coleman and Hoke, 2020; Figley and DiAntonio, 2020).

Although numerous studies reveal how the *Wld^s* mutation affects axon degeneration, especially in the peripheral nervous system, less is known about how the mutation affects degeneration of synapses in the mammalian CNS. In this regard, electron microscopic studies can provide important clues about cell biological mechanisms. One

electron microscopic study (Gillingwater et al., 2006) reported that degeneration of cortico-striate synapses after cortical lesions was dramatically delayed in *Wld^s* mice, but orphaned synapses began to exhibit ultrastructural changes similar to degenerating synapses in control mice by 8–10 days post-lesion. Gillingwater et al. (2006) did not assess the fate of synaptic terminals in *Wld^s* mice at time points after 10 days post-lesion.

Although no unique features of orphaned presynaptic terminals in *Wld^s* were detected by Gillingwater et al. (2006), a notable finding was an increased incidence of large, complex spines with multiple segmented postsynaptic densities (PSDs). It was suggested that these complex synaptic profiles reflected an enhanced plastic response at both injured and uninjured synapses, but exactly what this involves was not defined. Also, because this study did not assess time points beyond 10 days post-lesion, it was unknown whether spine alterations were transient or permanent.

To further explore how the *Wld^s* mutation affects CNS synapse degeneration, spine morphology and synaptic plasticity, here we use electron microscopy to characterize synaptic degeneration and replacement on dentate granule cells following lesions of perforant path inputs from the entorhinal cortex. This model of post-lesion synaptic plasticity has been extensively studied in rats (Matthews et al., 1976a,b; Steward and Vinsant, 1983) and mice (Perederiy et al., 2013). In wild type rats and mice, loss and reformation of synapses is accompanied by withering and re-growth of dendrites and loss and re-appearance of dendritic spines (Caceres and Steward, 1983; Steward et al., 1988a). Electron microscopic studies indicate that loss of spines actually involves a collapse or withdrawal of the spine into the parent dendrite (Steward and Vinsant, 1983). This model of lesion-induced synapse turnover provides a unique opportunity to explore whether there are unique ultrastructural features of synaptic terminals on orphaned CNS axons and how the mutation affects structural adjustments of denervated postsynaptic neurons. Of particular interest is whether loss and regrowth of dendritic spines occurs with the same delay as the onset of terminal degeneration in *Wld^s* mice, or whether the mutation also confers a degree of protection on the post-synaptic side, preventing or delaying spine atrophy.

Our quantitative electron microscopic analysis addresses two questions: (1) What is the timing of degeneration of orphaned synaptic terminals in *Wld^s* mice? (2) What changes occur in spines contacted by orphaned synapses, but are not exhibiting signs of degeneration?

Our results provide a thorough characterization of the timing of synapse degeneration in *Wld^s* mice and identify previously uncharacterized early ultrastructural changes prior to the time that orphaned synapses begin to exhibit typical signs of Wallerian degeneration. In addition, we document striking alterations in the structure of dendritic spines contacted by synapses of orphaned axons including dramatic hypertrophy of spine heads, enlargement and segmentation post-synaptic membrane specializations (PSDs), and development of spinules. These increases in

the complexity of spine morphology are very similar to what is seen following intense synaptic activity and induction of LTP [for a recent review, see (Petralia et al., 2021)]. Robust and paradoxical spine growth during the time period when spines in WT mice are withering and retracting suggests yet to be characterized signaling processes between orphaned axons and their postsynaptic targets.

MATERIALS AND METHODS

Experimental Animals and Surgical Procedures

C57Bl/6 mice were purchased from Jackson Labs. *Wld^s* mice were obtained from our local breeding colony, originally established from *Wld^s* mice on a C57Bl/6 background obtained from Jackson labs. All procedures were approved by the Institutional Animal Care and Use Committee (IACUC) of the University of Virginia.

Entorhinal Cortex Lesions

For surgery, adult male mice (3–6 months of age) were anesthetized with Avertin (2.5 μg tribromoethanol per 10 g of body weight). The fur was removed from the area overlying the posterior cortex, and the scalp was incised. The skull overlying the entorhinal area was removed and the posterior portion of the cerebral hemisphere was removed by gentle aspiration. The scalp was sutured and mice were allowed to survive for 4, 8, 12, and 16 days post-lesion. The extent of the lesion was assessed by histological analysis. Damage sometimes extended slightly into the mesencephalon and diencephalon, but when lesions extended into the hippocampus or dentate gyrus, the animals were excluded. Quantitative analyses were carried out on mice with acceptable lesions (at least 3 mice per genotype per timepoint).

Tissue Preparation

Mice were perfused transcardially with 2% paraformaldehyde/2% glutaraldehyde in 0.13 M cacodylate buffer, pH 7.2. Brains were blocked by a coronal cut approximately 2.5 mm posterior to bregma. Coronal sections were cut by hand from the rostral block containing the dorsal hippocampus, and sample blocks were dissected from the dorsal blade of the dentate gyrus approximately 1.5–2.0 mm posterior to bregma. The posterior portion of the brain containing the entorhinal cortex was embedded in egg yolk and sectioned in the horizontal plane; sections were stained for Cresyl violet for lesion assessment.

Blocks containing the dentate gyrus were osmicated and embedded in plastic. Thin sections were cut using an LKB ultramicrotome perpendicular to the layer of the granule cell bodies in order to obtain sections that extend from the cell body layer to the zone containing the tips of the dendrites (the outer molecular layer of the dentate gyrus). Sections were taken at 1 μm and stained with toluidine blue to aid with mapping in the EM; sections cut at approximately 600 \AA were mounted on grids and stained with uranyl acetate/lead citrate.

Quantitative Electron Microscopic Analyses

We evaluated synapse degeneration and replacement using quantitative electron microscopic techniques as in our previous studies in rats (Steward and Vinsant, 1983). Sample images were taken at 8,000 \times magnification in the middle molecular layer of the dentate gyrus so as to sample a region encompassing approximately 2,000 μm^2 of neuropil. From these collections of images, we counted intact synapses and degenerating synapses. Intact synapses were defined as appositions between a presynaptic process with at least three synaptic vesicles and a postsynaptic element with a definable postsynaptic density (PSD). Degenerating synapses were identified as presynaptic terminals with apposed PSD exhibiting either electron dense or electron lucent forms of degeneration. Data are expressed as intact synapses and degenerating synapses/100 μm^2 of neuropil.

Here, we express data as synapses/100 μm^2 of neuropil rather than using more sophisticated stereological techniques (such as the physical bisector technique) because this allows data to be compared across labs and with data from previous studies in rats and mice (Matthews et al., 1976a,b; Steward and Vinsant, 1983). Although stereological techniques are preferred when determining absolute synapse numbers, they are not essential for measurements of changes in relative numbers of synapses over time (for example, as in the present study) providing that the size of the elements being counted is relatively constant over time. In this regard, our previous study in rats revealed no changes in the size of presynaptic terminals or synapses over time post-injury (Steward and Vinsant, 1983).

Image Manipulation

One electron micrograph was manipulated to cover a scratch (Figure 4C). Some EM images are colorized to highlight key structures.

RESULTS

Aspiration lesions of the entorhinal cortex are somewhat variable because they are done without stereotaxic guidance. Accordingly, for the electron microscopic (EM) analysis, we selected cases in which the lesion destroyed most of the entorhinal cortex (both medial and lateral divisions) with little or no damage to the posterior hippocampus. Figure 1A illustrates an example of the lesion. Cases where lesions were incomplete or where there was damage to the posterior hippocampus were excluded.

From the collection of cases with acceptable lesions, at least 3 mice of each strain were prepared for EM at each timepoint post-lesion. One μm sections from the block were stained with toluidine blue to aid in mapping in the electron microscope (Figure 1B). The area of the molecular layer containing degenerating axons and synapses was easily identifiable in the toluidine blue-stained sections (Figure 1B). In the electron microscope, the section was mapped by recording stage coordinates, the layer of granule cells was identified and the location of the hippocampal fissure was identified. Non-overlapping sample images were taken at 8,000 \times in the middle

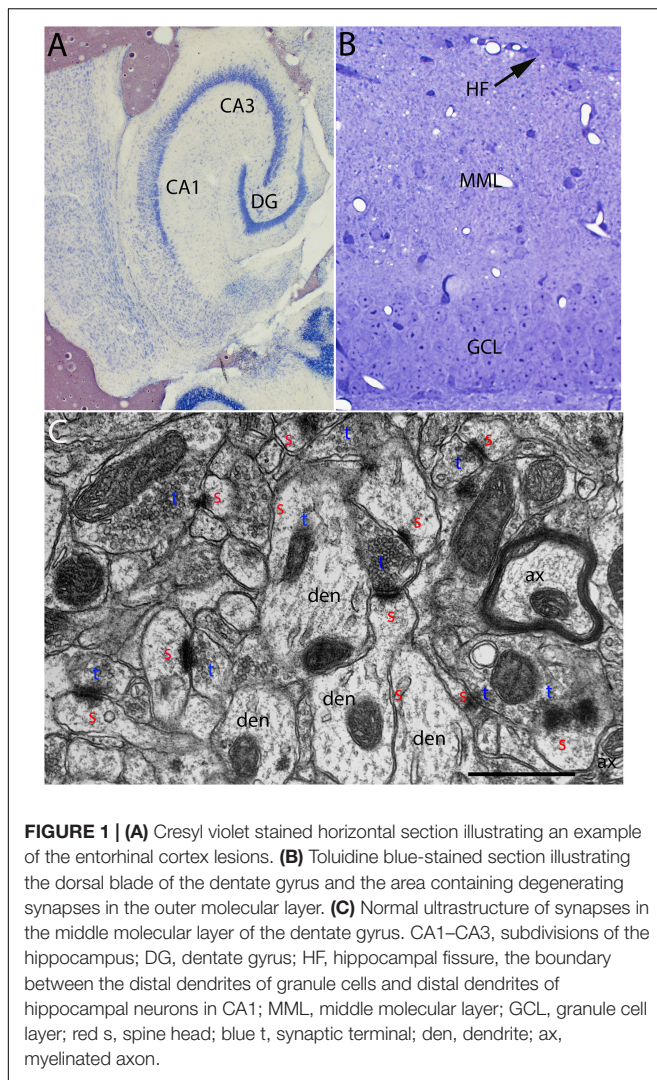


FIGURE 1 | (A) Cresyl violet stained horizontal section illustrating an example of the entorhinal cortex lesions. **(B)** Toluidine blue-stained section illustrating the dorsal blade of the dentate gyrus and the area containing degenerating synapses in the outer molecular layer. **(C)** Normal ultrastructure of synapses in the middle molecular layer of the dentate gyrus. CA1–CA3, subdivisions of the hippocampus; DG, dentate gyrus; HF, hippocampal fissure, the boundary between the distal dendrites of granule cells and distal dendrites of hippocampal neurons in CA1; MML, middle molecular layer; GCL, granule cell layer; red s, spine head; blue t, synaptic terminal; den, dendrite; ax, myelinated axon.

portion of the molecular layer of the dorsal blade of the dentate gyrus avoiding large blood vessels and flaws in the section (knife marks for example).

Normal Ultrastructure in Un-Operated Mice

The ultrastructural appearance of synapses in the molecular layer of the dentate gyrus in un-operated mice was not noticeably different from what has been previously described in rats (see **Figure 1C**). Also, the ultrastructural appearance of synapses in *Wld^s* was unremarkable and was not noticeably different than control C57Bl/6 mice. Counts of synapses in uninjured mice revealed that synapse density was comparable in the two strains ($43.3 \pm 6/100 \mu\text{m}^2$ in C57Bl/6 mice, $40.6 \pm 2.4/100 \mu\text{m}^2$ in *Wld^s* mice).

4 Days Post-lesion

At 4 days post-lesion, most synapses in the denervated zone exhibited clear signs of degeneration in C57Bl/6 mice. Most

presynaptic terminals exhibited the typical dark-dense form of degeneration in which the contents of the terminal appeared electron dense and compressed; synaptic vesicles are not seen in these types of degenerating terminals (**Figure 2A**). A small number of synapses (average of 1.5% of the total number of degenerating synapses) exhibited the lucent form of degeneration in which the contents of the presynaptic terminal appear washed out with synaptic vesicles floating in empty space (**Figure 2B**). The lucent form of terminal degeneration is common at 2 days post-lesion but is less common by 4 days (Steward and Vinsant, 1983). Scattered amongst the degenerating synapses were a few normal-appearing synapses (for quantification, see below). Quantitative analyses revealed that the number of intact synapses per $100 \mu\text{m}^2$ decreased to about 10% of un-operated controls, and

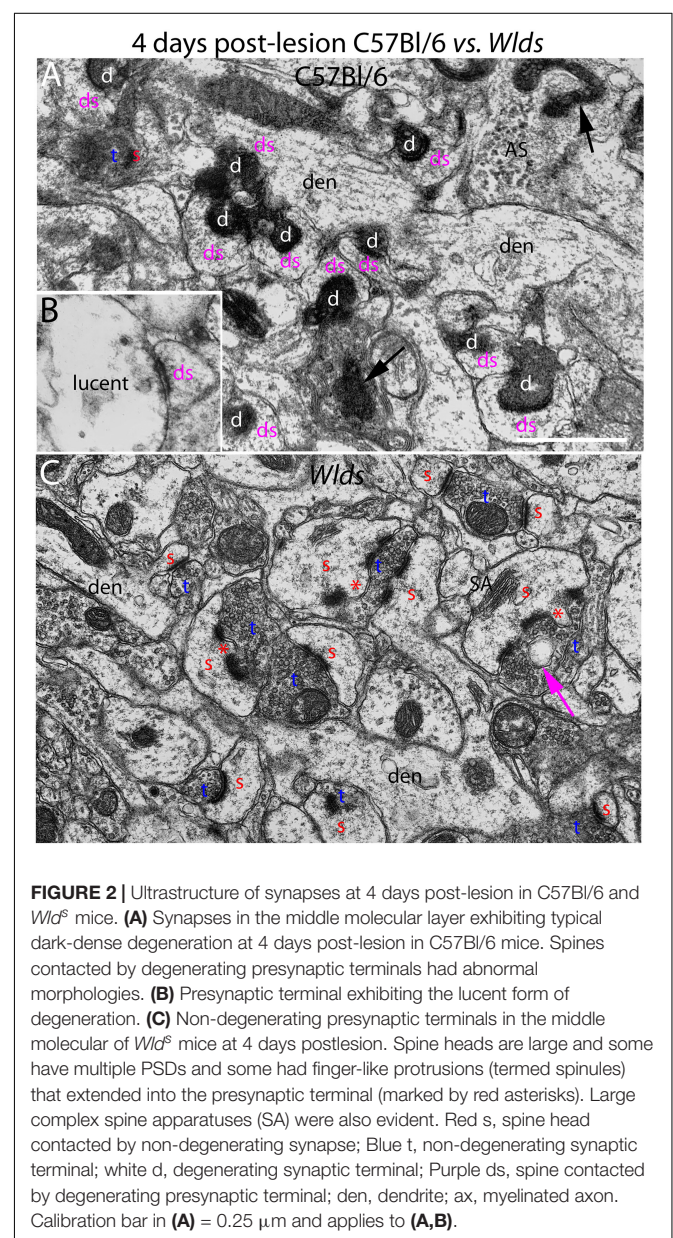
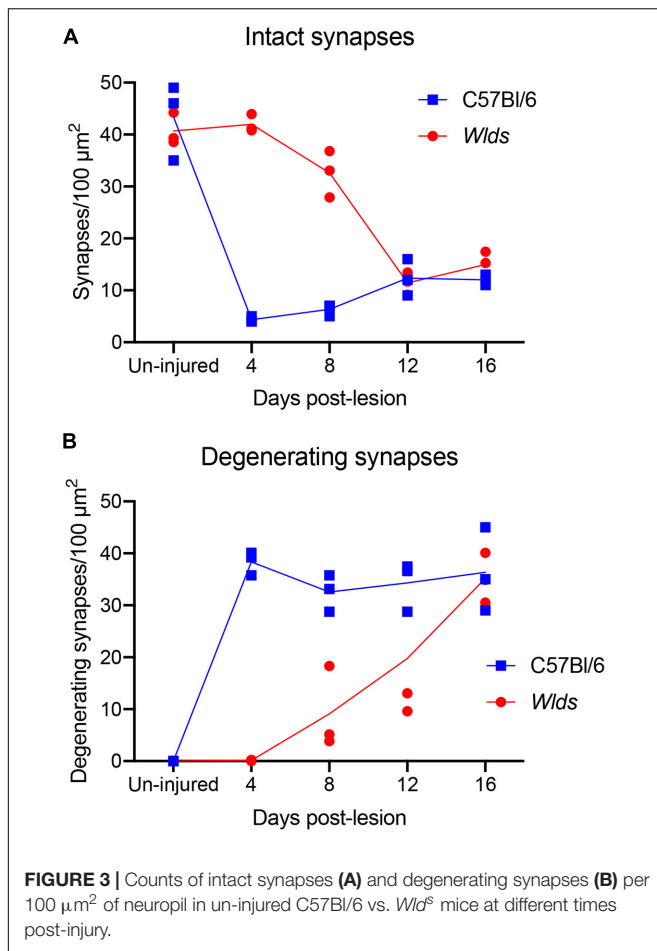


FIGURE 2 | Ultrastructure of synapses at 4 days post-lesion in C57Bl/6 and *Wld^s* mice. **(A)** Synapses in the middle molecular layer exhibiting typical dark-dense degeneration at 4 days post-lesion in C57Bl/6 mice. Spines contacted by degenerating presynaptic terminals had abnormal morphologies. **(B)** Presynaptic terminal exhibiting the lucent form of degeneration. **(C)** Non-degenerating presynaptic terminals in the middle molecular of *Wld^s* mice at 4 days postlesion. Spine heads are large and some have multiple PSDs and some had finger-like protrusions (termed spinules) that extended into the presynaptic terminal (marked by red asterisks). Large complex spine apparatuses (SA) were also evident. Red s, spine head contacted by non-degenerating synapse; Blue t, non-degenerating synaptic terminal; white d, degenerating synaptic terminal; Purple ds, spine contacted by degenerating presynaptic terminal; den, dendrite; ax, myelinated axon. Calibration bar in **(A)** = $0.25 \mu\text{m}$ and applies to **(A,B)**.

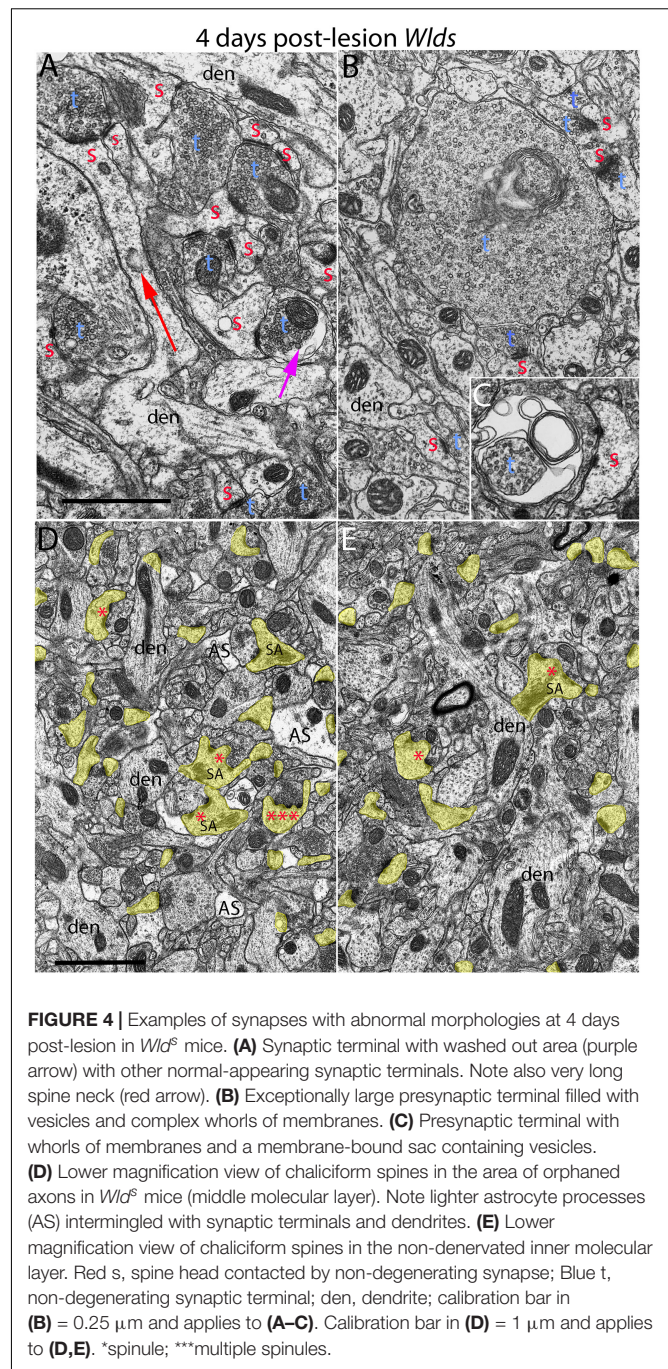


the number of degenerating synapses corresponded closely to the number of intact synapses that were lost (Figure 3).

Most spines contacted by degenerating presynaptic terminals had abnormal morphologies. Spine heads were cup-shaped, and spine necks were more amorphous in form in comparison to normal spines. Some degenerating synapses were on irregularly shaped mounds along the dendritic shaft that contained flocculent material similar in appearance to what is seen in spine heads (Figure 2A). The shape and general appearance of these mounds strongly suggests that these were spines that had collapsed or withdrawn into the dendrite. In contrast to dendrites in un-operated mice, which have a generally regular diameter, dendrites in the area of degeneration had an irregular, varicose, lumpy appearance.

A few empty PSD's were seen at 4 days post-lesion (PSD's that were not apposed by either an intact or degenerating presynaptic terminal). Some of these may be synapses that are sectioned off-center so that the presynaptic element is out of the plane of section, but others represent synapses from which the presynaptic terminal has been removed. Some empty PSD's were apposed by a glial process or slip of membrane, which we interpret as the remnant of the degenerated presynaptic terminal.

In striking contrast, in *Wld^s* mice at 4 days postlesion, there were virtually no profiles exhibiting the dark-dense form



of degeneration (Figures 2C, 4); indeed, only one presynaptic terminal exhibiting electron dense degeneration was seen in all the photomicrographs that were analyzed. Counts revealed that the number of intact synapses per 100 μm² remained comparable to un-operated *Wld^s* mice (Figure 3).

Although no terminals exhibited typical dark-dense degeneration, a few synapses had unusual morphologies that might represent early stages of degeneration. Some had washed out areas in the presynaptic terminal (Figure 4A, purple arrow) or empty vacuoles (Figure 2C, purple arrow);

a few terminals had washed out areas with complex whorls of membranes, and sometimes membrane-bound sacs containing vesicles (Figure 4C). There were also a few profiles that appeared to be exceptionally large presynaptic terminals filled with synaptic vesicles (Figure 4B). Although uncommon (approximately one per 2,000 μm^2), the appearance of these was quite striking.

The most obvious qualitative difference in the appearance of the neuropil in *Wld^s* mice at 4 days postlesion was that there were many spines exhibiting a very complex morphology with large chaliciform heads. Many spines had segmented PSDs (Figure 2C), often with finger-like protrusions (termed spinules) extending into the presynaptic terminal between the multiple PSDs (marked by red asterisks in Figure 2C). Unusually large, complex spine apparatuses were also evident (Figures 2C, 4D, SA). Figure 4D is a lower magnification view with spine heads colored yellow to illustrate the numerous spines with chaliciform heads in *Wld^s* mice. Spines with complex chaliciform heads, multiply segmented PSDs, spinules and large complex spine apparatuses were evident in the denervated zone in all *Wld^s* mice examined at 4 days postlesion. Indeed, these were such a distinguishing feature of the denervated neuropil of *Wld^s* mice that it was impossible to be blind as to the identification of micrographs from mutant mice. Spines with abnormal morphologies were even more evident at 8 days post-lesion (below).

A previous study reported spines with similar complex morphologies in the striatum 8–10 days after cortical lesions in *Wld^s* mice (Gillingwater et al., 2006). Of note, such complex spines were contacted by both degenerating and non-degenerating synapses. A caveat, however, is that synapses scored as “non-degenerating” that contact complex spines may be orphaned axons that not yet have begun to exhibit degenerative changes.

To further explore whether complex spine morphology is unique to synapses from orphaned axons that will eventually degenerate, we took advantage of the precise lamination of inputs to dentate granule cells. With complete lesions of the entorhinal cortex, approximately 95% of the synapses in the outer 2/3 of the molecular layer degenerate. However, proximal dendrites of dentate granule cells are innervated by commissural/associational axons, whose synapses do not degenerate. Assessment of spines in this zone revealed that some complex spines with chalice-shaped heads, spinules, segmented PSDs and large spine apparatuses were in fact present. To estimate the relative numbers of spines with unusual morphologies in the non-denervated inner molecular layer (IML) vs. the denervated outer molecular layer (OML), we collected sample micrographs at 3,000 \times from each zone (area of each image = 50 μm^2) and counted spines with spinules or segmented PSDs. These counts revealed that although complex spines were present in the inner molecular layer, they were less common than in the denervated zone (3.27/100 μm^2 in the IML vs. 9.56/100 μm^2 in the OML).

Although spines in *Wld^s* mice exhibited changes indicating growth, dendrites appeared generally comparable to un-operated

mice, and did not have the varicose appearance of dendrites contacted by degenerating terminals in WT C57Bl/6 mice.

8 Days Post-lesion

At 8 days post-lesion the overall appearance of degenerating synapses in C57Bl/6 control mice was similar to what was seen at 4 days post lesion except that all degenerating terminals were dark and dense and none exhibited the electron lucent form of degeneration seen occasionally at 4 days (Figures 5A,B). Counts revealed that the number of degenerating synapses was comparable to 4 days whereas the number of intact synapses was slightly higher (Figure 3), indicating the early stage of reinnervation.

Of note, degenerating presynaptic terminals frequently contacted multiple spine heads. Degenerating terminals in contact with multiple spine heads has previously been described

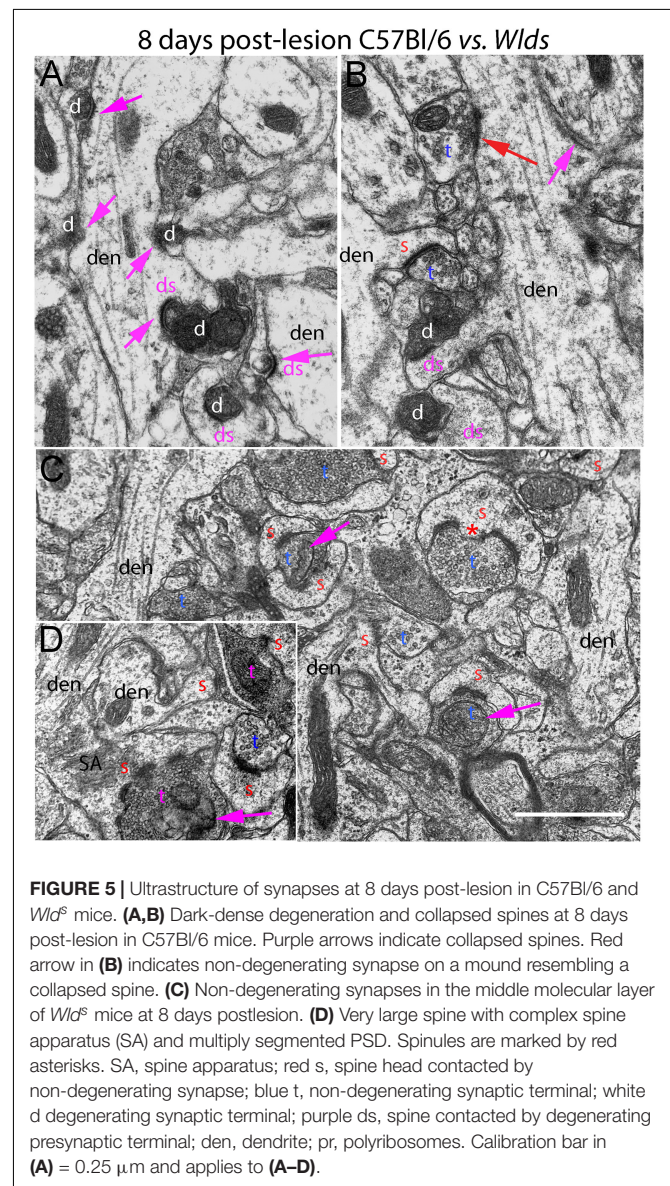


FIGURE 5 | Ultrastructure of synapses at 8 days post-lesion in C57Bl/6 and *Wld^s* mice. (A,B) Dark-dense degeneration and collapsed spines at 8 days post-lesion in C57Bl/6 mice. Purple arrows indicate collapsed spines. Red arrow in (B) indicates non-degenerating synapse on a mound resembling a collapsed spine. (C) Non-degenerating synapses in the middle molecular layer of *Wld^s* mice at 8 days postlesion. (D) Very large spine with complex spine apparatus (SA) and multiply segmented PSD. Spinules are marked by red asterisks. SA, spine apparatus; red s, spine head contacted by non-degenerating synapse; blue t, non-degenerating synaptic terminal; white d degenerating synaptic terminal; purple ds, spine contacted by degenerating presynaptic terminal; den, dendrite; pr, polyribosomes. Calibration bar in (A) = 0.25 μm and applies to (A–D).

in rats (Steward and Vinsant, 1983). Our interpretation is that this configuration arises because presynaptic axons contract as they degenerate, pulling attached spines closer together.

As described previously in rats, some dark dense degenerating presynaptic terminals with attached spine heads were surrounded by astrocytes, identified as such by the characteristic appearance of the cytoplasm (electron lucent with few organelles, occasional glycogen granules, and intermediate filaments). It is likely that spine heads that appear to be engulfed by an astrocyte are still connected with the main dendrite via a spine neck that extends out of the plane of section.

As at 4 days, spines contacted by degenerating presynaptic terminals in C57Bl/6 mice had abnormal morphologies (cup-shaped heads and short amorphous spine necks) or had the appearance of fully collapsed spines (Figures 5A,B). Empty PSDs were more common at 8 days post-lesion than at 4 days, but were still relatively uncommon. Dendritic shafts had a varicose appearance as at 4 days.

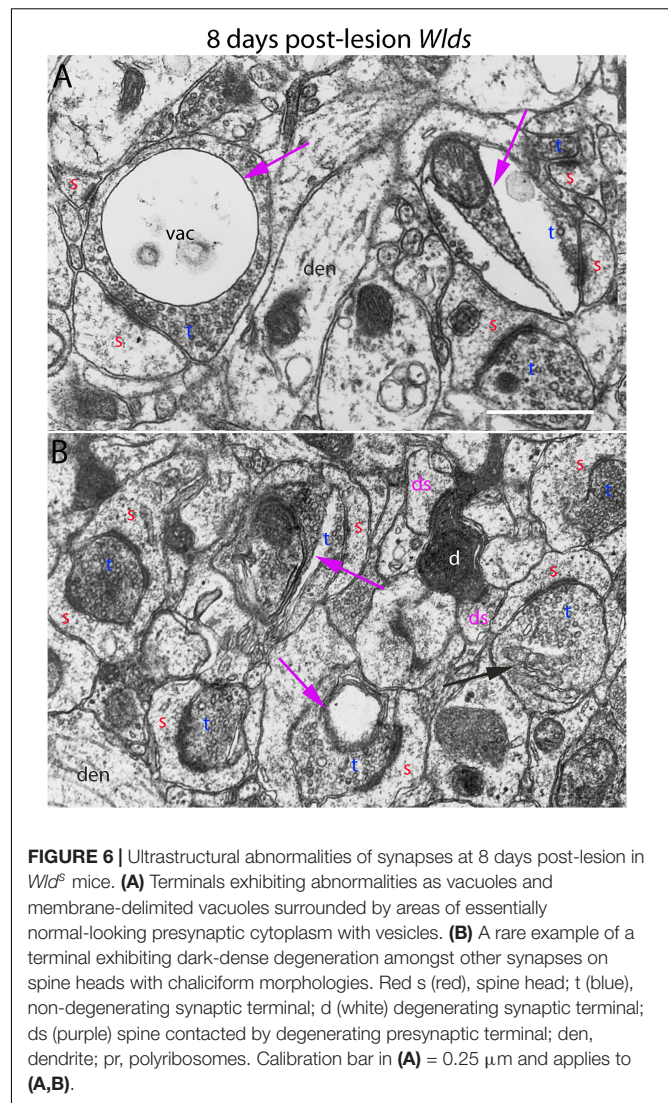
Some normal-appearing presynaptic terminals were scattered amongst the degenerating synapses, and some of these contacted mounds on the dendrite, inviting the speculation that they were new connections onto collapsed spines that had been cleared of degeneration debris (red arrow, Figure 5B).

At 8 days post-lesion in *Wld^s* mice, most presynaptic terminals still appeared relatively normal (Figures 5C, 6), but some terminals did exhibit abnormal morphologies. Some terminals that looked relatively normal otherwise contained unusual looking membrane structures that were not readily identifiable as typical organelles (Figure 5C, purple arrows). Some terminals exhibited abnormalities with some similarity to the lucent form of degeneration in WT mice. In contrast to typical lucent degeneration, however, where the entire terminal appears swollen and washed out, some terminals *Wld^s* mice had large membrane-delimited vacuoles surrounded by areas of essentially normal-looking presynaptic cytoplasm with vesicles (Figure 6A, vac) or washed out regions along with areas containing cytoplasm and vesicles (right side, Figure 6A). These profiles were unlike anything seen in WT C57BL/6 mice and as such, were another distinguishing feature of *Wld^s* mice. Still other terminals had a dark cytoplasm with embedded vesicles that could represent an early stage in the transition to dark-dense degeneration. Very few presynaptic terminals exhibited typical dark-dense degeneration, however (Figure 6B).

In contrast to the denervated spines in C57Bl/6 mice, in *Wld^s* mice, there were very few profiles resembling collapsed spines. Instead, as at 4 days post-lesion, spines with hypertrophied caliciform heads were prominent. Some spines exhibited even more dramatic hypertrophy than at 4 days post-lesion, exhibiting complex heads bearing multiple PSDs, spinules extending into the presynaptic terminal and an elaborate spine apparatus at the base. Figure 5D illustrates a spine with 6 separate PSD segments and a large spine apparatus (SA).

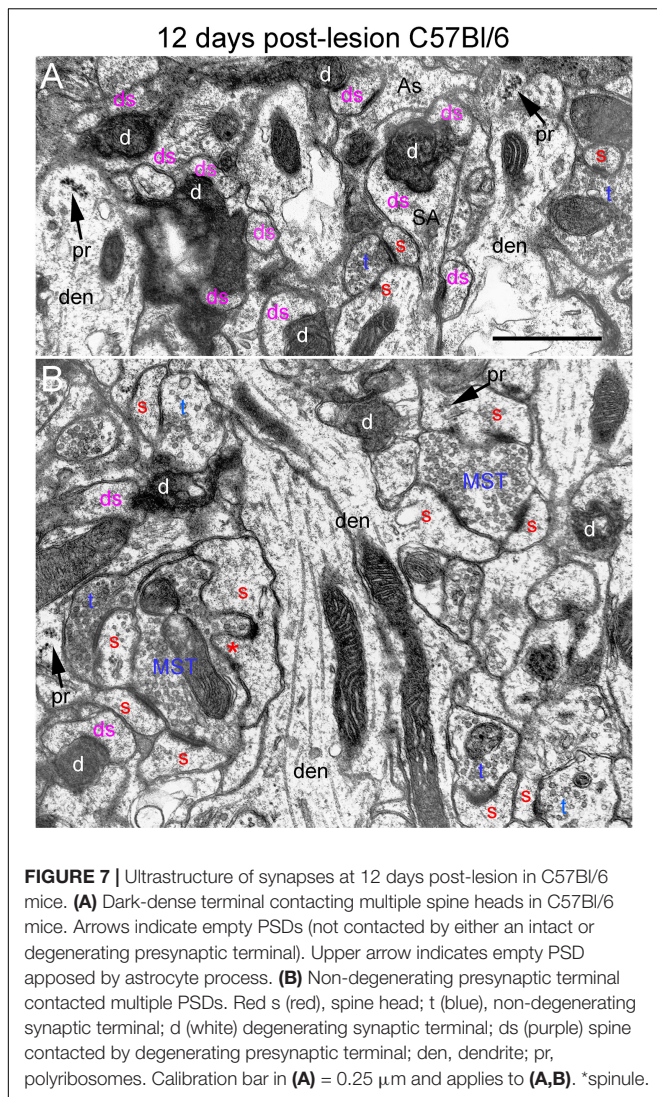
12 Days Post-lesion

At 12 days postlesion, the denervated zone of control C57Bl/6 mice still contained large numbers of synaptic terminals exhibiting dark-dense degeneration. Counts revealed that the



number of degenerating synapses was comparable to 4 and 8 days. As at 8 days, many of the dark-dense terminals contacted multiple spine heads forming nests of denervated spine heads with a degenerating terminal at the center (Figure 7A). Empty PSDs (not contacted by either an intact or degenerating presynaptic terminal) were also evident (Figure 7A); some of these were apposed by astrocyte processes.

Qualitatively, it was clear that there were a larger number of non-degenerating synapses than at 8 days. Indeed, the number of intact synapses was about twofold higher than at 8 days (Figure 3) indicating formation of new synapses between 8 and 12 days. A distinguishing feature of the neuropil at 12 days post-injury was that many of the non-degenerating presynaptic terminals contacted multiple PSDs (Figure 7B). Multiple synapse terminals (MSTs) are a common feature of reinnervating axons in this model (Steward et al., 1988b), and a possible explanation for this configuration is that sprouting axons grow into the nests of denervated spine heads where they form multiple synaptic connections.

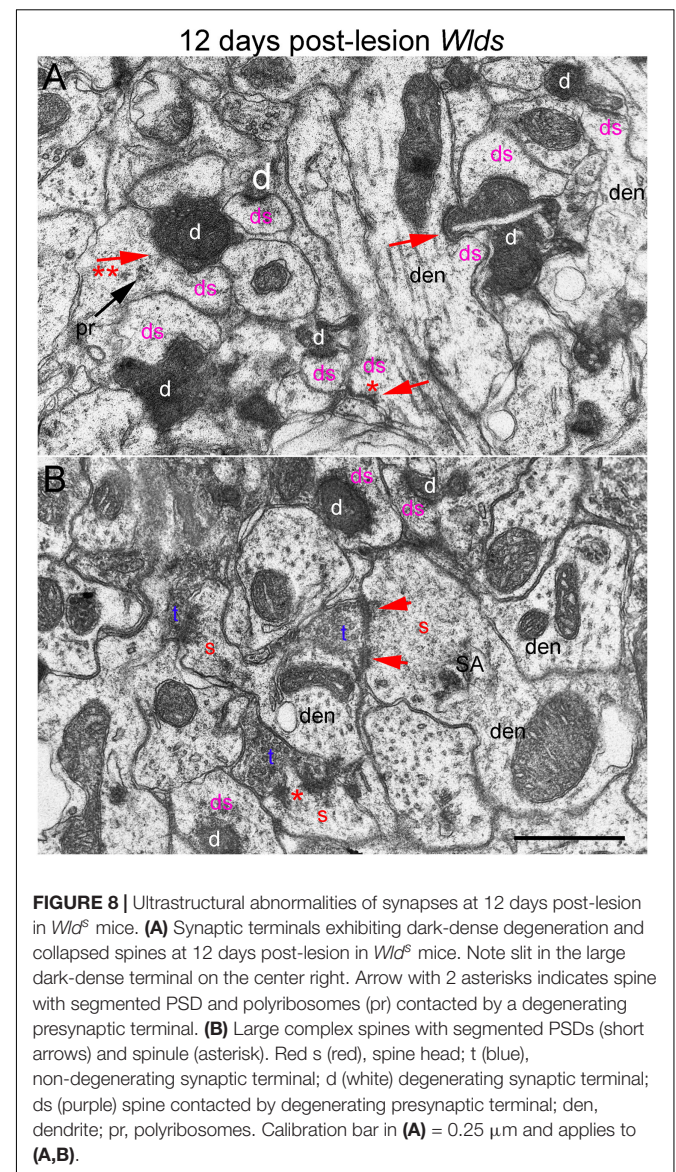


To determine the extent of increases in multiple synapse terminals, we counted presynaptic terminals contacting 2 or more PSDs and expressed the counts as numbers of MSTs per 1,000 μm^2 of neuropil. Confirming our qualitative impression, the number of MSTs was in fact almost threefold higher at 12 days post lesion than at 4 days (see below for additional quantitative analyses).

Spines contacted by degenerating presynaptic terminals continued to exhibit the atrophic morphologies described above. Spine necks were irregular in shape and many had the morphology of collapsed spines, indicating spine atrophy, and in some cases collapse or withdrawal of the spine into the parent dendrite. However, some non-degenerating synapses were on spines with a morphology similar to un-injured mice (**Figure 7B**) suggesting restoration of spine morphology with reinnervation. Polyribosome clusters were evident in dendrites and sometimes spine heads, consistent with previous studies documenting increases in spine-associated polyribosomes during reinnervation (Steward, 1983).

In *Wld^s* mice at 12 days postlesion, degenerating synaptic terminals were more numerous than at 8 days, although there were still not as many as in C57Bl/6 mice (**Figure 3**). Degenerating terminals exhibited dark-dense degeneration (**Figure 8**), but the terminals weren't as dark and dense as in WT mice and synaptic vesicles and mitochondria could still be discerned in the dark dense presynaptic cytoplasm. Some terminals exhibiting dark-dense degeneration had the long slits that were frequently seen in terminals of *Wld^s* mice at 8 days. Counts revealed decreases in the number of intact synapses in comparison to 8 days post-lesion to a level that was comparable to WT C57Bl/6 mice (**Figure 3**).

Most spines contacted by degenerating presynaptic terminals were short and stubby and there were some profiles suggestive of collapse or withdrawal of the spine into the dendrite (**Figure 8A**, arrows; asterisk indicates a collapsed spine that is not contacted



by either an intact or degenerating presynaptic terminal). Thus, although the initial response at 4–8 days post-lesion in *Wld^s* mice is paradoxical hypertrophy of spines contacted by terminals of orphaned axons, spine atrophy does eventually occur in parallel with the onset of degeneration of orphaned presynaptic terminals.

Large complex spines with segmented PSDs were still present at 12 days post-lesion (Figure 8B), but these were less complex and less numerous than at 8 days and also had a more amorphous appearance than at 4 and 8 days suggesting that they were beginning to undergo atrophy and collapse. Also, most of the large complex spines that were present were contacted by presynaptic terminals that were not exhibiting degenerative changes.

16 Days Post-lesion

At 16 days postlesion, the denervated zone of control C57Bl/6 mice appeared qualitatively similar to what was seen at 12 days post-lesion with large numbers of synaptic terminals exhibiting dark-dense degeneration (not shown). Counts revealed that the numbers of degenerating and intact synapses were comparable to those at 12 days (Figure 3), suggesting minimal removal of degenerating synapses or additional formation of new synapses.

In *Wld^s* mice at 16 days postlesion, synaptic terminals in the denervated portion of the molecular layer exhibited dark-dense degeneration in numbers that were comparable to C57Bl/6 mice (Figure 9 and for counts, see Figure 3). Empty PSDs were also present (Figure 9 indicated by asterisk). The number of non-degenerating synaptic terminals was comparable to C57Bl/6. Some of these were MSTs (Figure 9B). As was the case at 4 days post-lesion in C57Bl/6 mice, some degenerating presynaptic terminals contacted multiple spine heads (Figure 9A, upper right, Figure 9B, lower middle).

Non-degenerating synaptic terminals that appeared entirely normal were intermixed with dark-dense synaptic terminals; some of these intact terminals were MSTs (Figure 9B). Counts revealed that the number of non-degenerating terminals was comparable to C57Bl/6 and slightly higher than the number at 12 days post-lesion in *Wld^s* mice (Figure 3).

Quantification of Synapse Parameters

We carried out additional analyses to quantify changes in synapse parameters (Figure 10). First, to quantify multiple synapse terminals (MSTs), we counted presynaptic terminals contacting 2 or more PSDs and expressed the values as counts per 1,000 μm^2 of neuropil (Figure 10). In C57Bl/6 mice, the number of MSTs decreased at 4 days post-lesion to about 5% of the values in uninjured mice in parallel with the decreases in the number of intact synapses, then increased gradually over the post-lesion interval in parallel with re-appearance of non-degenerating synapses. In *Wld^s* mice, however, the number of MSTs was higher at 4 days post-lesion than in uninjured mice, increased further at 8 days. Numbers of MSTs decreased at 12 days to about 50% of unoperated control in parallel with the appearance of degenerating presynaptic terminals, and then increased again at 16 days post-lesion to an average comparable to un-operated mice (although with considerable variability between cases). Statistical analysis

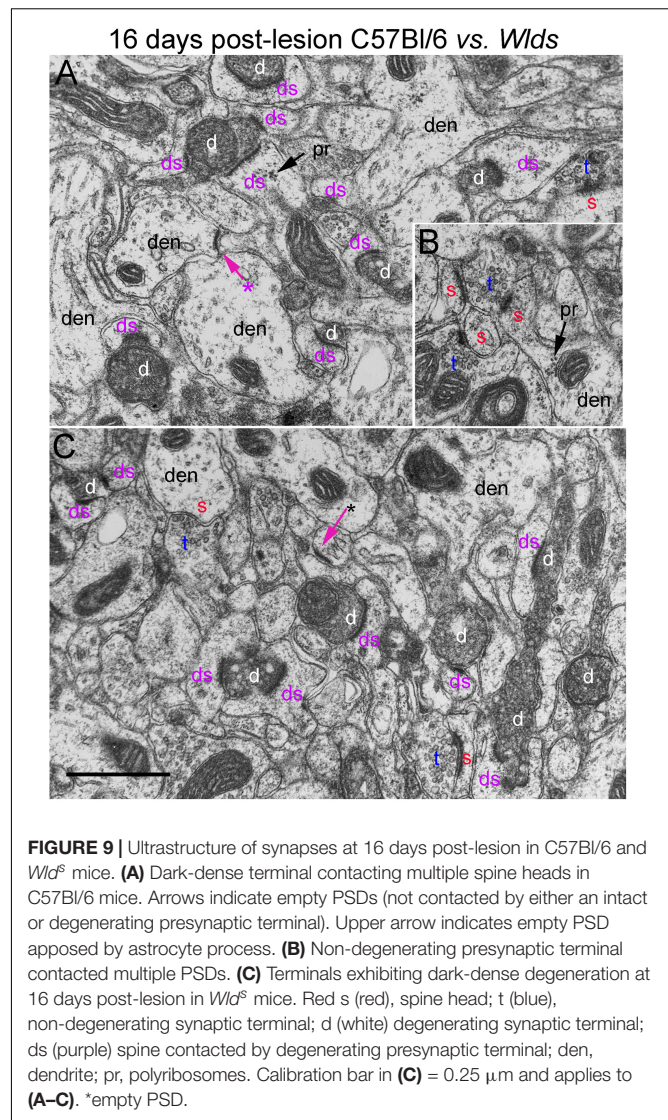


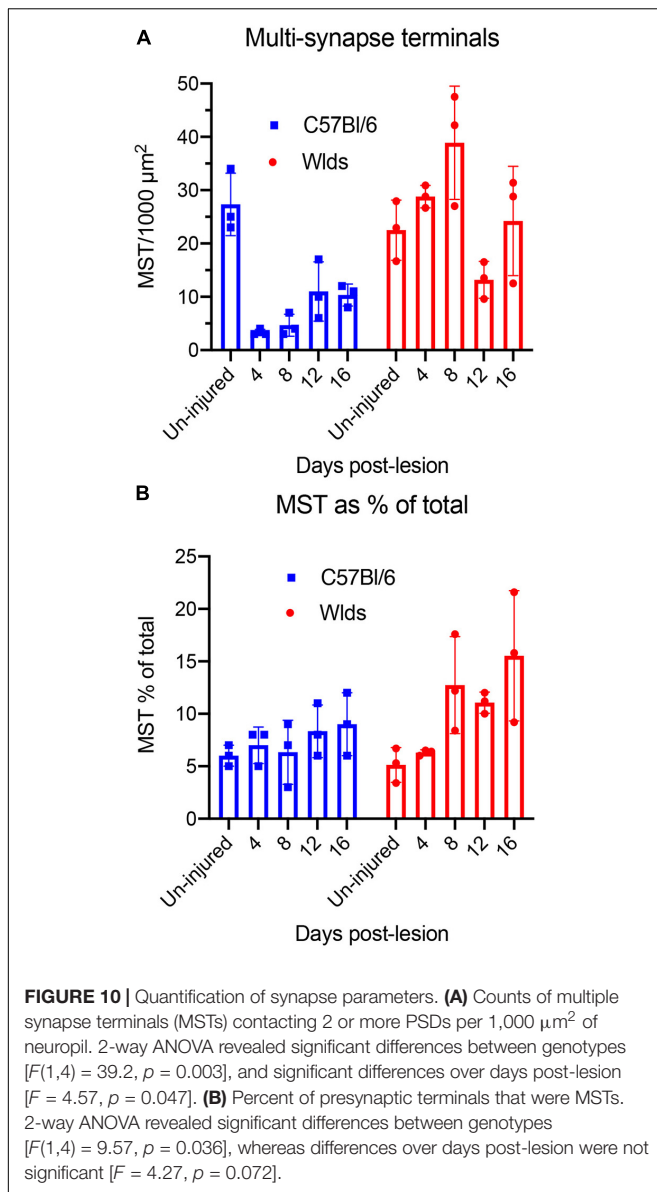
FIGURE 9 | Ultrastructure of synapses at 16 days post-lesion in C57Bl/6 and *Wld^s* mice. **(A)** Dark-dense terminal contacting multiple spine heads in C57Bl/6 mice. Arrows indicate empty PSDs (not contacted by either an intact or degenerating presynaptic terminal). Upper arrow indicates empty PSD apposed by astrocyte process. **(B)** Non-degenerating presynaptic terminal contacted multiple PSDs. **(C)** Terminals exhibiting dark-dense degeneration at 16 days post-lesion in *Wld^s* mice. Red (s), spine head; t (blue), non-degenerating synaptic terminal; d (white) degenerating synaptic terminal; ds (purple) spine contacted by degenerating presynaptic terminal; den, dendrite; pr, polyribosomes. Calibration bar in **(C)** = 0.25 μm and applies to **(A–C)**. *empty PSD.

by 2-way ANOVA revealed significant differences between genotypes [$F(1,4) = 39.2, p = 0.003$], and significant differences over days post-lesion [$F = 4.57, p = 0.047$].

We also calculated the percent of presynaptic terminals that were MSTs (Figure 10B). In uninjured mice of both strains, about 6% of the presynaptic terminals were MSTs. In C57Bl/6 mice, MSTs increased slightly to about 8% of control values by 16 days. In *Wld^s* mice, the percent of presynaptic terminals that were MSTs increased to approximately threefold higher than control by 16 days. Statistical analysis by 2-way ANOVA revealed significant differences between genotypes [$F(1,4) = 9.57, p = 0.036$], whereas differences over days post-lesion were not significant [$F = 4.27, p = 0.072$].

DISCUSSION

The goal of this study was to further explore the curious phenotypes of the *Wld^s* mutation. Although the mutation was



discovered over 3 decades ago and the mutant protein has been identified as a fusion protein made up of the amino terminal 70 amino acids (N70) fragment of ubiquitination factor U4B, the complete coding region of NAD⁺ synthesizing enzyme nicotinamide adenyltransferase 1 (NMNAT1), and an 18 amino acid linking region, the cell biology that underlies the signature phenotype remains mysterious. Most previous studies have focused on Wallerian degeneration of axons, particularly in the peripheral nervous system, but to our knowledge, there have been only two previous studies focusing on consequences of the mutation on degeneration of CNS synapses (Gillingwater et al., 2006; Wright et al., 2010).

Here, we were particularly interested in the timing and nature of degeneration of presynaptic terminals of orphaned axons and on the postsynaptic side, how atrophy of postsynaptic spines is affected. Electron microscopy can provide insights into cell

biological mechanisms, and provide hints about whether the mutation mainly affects axon degeneration or also confers a degree of protection on the post-synaptic side, preventing or delaying spine atrophy or causing other un-predicted alterations in spines. Accordingly, our quantitative electron microscopic analysis focused on: (1) The timing of degeneration of orphaned synaptic terminals in *Wld^s* mice; (2) changes in spines contacted by orphaned synapses, and especially whether in this model of lesion-induced synapse plasticity, spines in *Wld^s* mice exhibited the remarkable changes in ultrastructure previously reported in the striatum following cortical lesion (Gillingwater et al., 2006); (3) ultrastructural signs of reinnervation.

Timing of Degeneration of Orphaned Synaptic Terminals

A previous study of consequences of the mutation on degeneration of CNS synapses (Gillingwater et al., 2006) documented delayed onset of degenerative changes in corticostriate synapses after cortical injury. However, this study did not assess time points beyond 10 days post-injury. Also, a technical caveat of this previous study was that in the quantitative analysis of synapse numbers over time, counts were expressed as numbers of synapses observed during a 15 min observation period on the electron microscope. Expressing data in this way does not allow comparisons across labs because the counts depend on how much area was assessed during the 15 min scans.

Our results demonstrate that onset of degeneration of presynaptic terminals of the perforant path is similarly delayed by many days in *Wld^s* mice. There are minimal signs of degenerative changes in presynaptic terminals at 4 days post-injury at a time when amputated axons in WT rats and mice exhibit full-blown degeneration. Even at 8 days post-lesion, most presynaptic terminals of orphaned axons in *Wld^s* mice still appear relatively normal, although some exhibit ultrastructural abnormalities that might represent previously uncharacterized early degenerative changes including large, elongated membrane bound areas with empty lumens and atypical membrane structures. Typical presynaptic degeneration does eventually occur, however. At 12 days, some terminals exhibit dark-dense degeneration, although many terminals still appear relatively normal but at 16 days post-injury, synaptic terminals of orphaned axons exhibit the full extent of degeneration seen in WT C57Bl/6 mice.

The fact that typical signs of synaptic degeneration do eventually occur in *Wld^s* mice suggests that the mutation does not alter the actual mechanisms of synapse degeneration, and instead maintains the synapse in a viable state. It is unknown how such synaptic terminals of orphaned axons operate physiologically. The presence of large numbers of synaptic vesicles suggests that orphaned terminals may remain capable of packaging neurotransmitter, but it is unknown whether the terminals actually release neurotransmitter onto the postsynaptic neuron when there is no cell body to generate action potentials. Indeed, the physiology of orphaned axons and their terminals is essentially un-explored, except that peripheral nerve axons do remain capable of propagating action potentials when stimulated electrically (Perry et al., 1991).

Mechanisms Underlying Spine Hypertrophy

Presynaptic degeneration of amputated axons in WT C57Bl/6 mice is accompanied by withering and collapse of spines as previously described in rats (Steward and Vinsant, 1983). In striking contrast, spines contacted by synapses of orphaned axons exhibited dramatic hypertrophy and remodeling of post-synaptic membrane specializations (PSDs). Hypertrophy was evident at 4 days post-lesion before the onset degenerative changes in orphaned presynaptic terminals and was most dramatic at 8 days. By 12 days, spines began to exhibit collapse and withering. The dramatic hypertrophy and PSD remodeling indicates a robust and paradoxical spine growth in *Wld^s* mice during the time period when denervated spines in WT mice are withering and retracting. Similar dramatic spine hypertrophy was reported by Gillingwater et al. (2006) in their study of cortico-striate synapse degeneration, and our findings extend the story by showing that the spine hypertrophy is transient.

Trans-Synaptic Signaling From Orphaned Axons

The remarkable hypertrophy of spines on neurons contacted by terminals of orphaned axons suggests that orphaned presynaptic terminals must somehow signal to the postsynaptic neuron. The nature of the signaling is unknown, however. The alterations in spine morphology including transformation from simple to caliciform morphology, PSD segmentation and appearance of spinules are remarkably similar to alterations that occur as a result of induction of long-term potentiation of perforant path synapses (Desmond and Levy, 1983, 1988). Very similar changes have been reported as a result of other interventions that induce intense synaptic activity (Petralia et al., 2021). These alterations are paradoxical in the present setting because the spines exhibiting this transformation are contacted by orphaned axons that have been separated from their cell bodies. Orphaned axons appear morphologically intact and do contain large numbers of synaptic vesicles, so it is conceivable that they continue to release neurotransmitter. However, action potentials are normally generated at the cell body or initial segment, which was removed by the aspiration lesion. If spine changes are induced by intense presynaptic activity, then the activity must somehow be generated intrinsically in the orphaned axons. To our knowledge, there have been no studies of spontaneous action potential generation by orphaned axons before they begin to degenerate. If this is the mechanism, it would represent another remarkable consequence of the *Wld^s* mutation on axonal pathophysiology.

One possibility is that silencing of action potential-driven neurotransmitter release without degeneration is a signal for spine hypertrophy. This idea is counter to the prevailing concept that spines are maintained by synaptic activity and decreases in activity typically lead to decreases rather than increases in spine size. Another possibility is that surviving orphaned axons release neurotransmitter with different dynamics than normal, and that this abnormal release is the critical signal. A third possibility is that preserved terminals of orphaned axons in *Wld^s* mice

release some other molecule that triggers spine growth. These questions indicate that there are still many unknowns about the cell biological consequences of the *Wld^s* mutation.

The postsynaptic mechanisms underlying the dramatic hypertrophy of spines are unknown. Spine hypertrophy could be a manifestation of the *Wld^s* mutation on the intrinsic cell biology of the postsynaptic cell, altering its responses to impending degeneration of presynaptic axons. Alternatively, if the effect of the mutation is limited to delaying Wallerian degeneration of axons and their synaptic terminals, then postsynaptic hypertrophy could be due to some signal(s) from the orphaned axons during the time that they are protected from degeneration. Our results do not provide a definitive answer but do provide a basis for formulation of questions.

One question is whether hypertrophy is limited to spines contacted by preserved orphaned axons or whether it is a general postsynaptic response involving all spines including those contacted by un-injured axons. A previous study that assessed synaptic degeneration in the striatum up to 10 days after cortical lesions reported that very complex spines on striatal neurons contacted by both degenerating and non-degenerating synapses (Gillingwater et al., 2006). A caveat, however, is that synapses scored as non-degenerating that contact complex spines may be orphaned axons that not yet have begun to exhibit degenerative changes. In this case, the complex morphology seen in the study of cortico-striatal synapses may still be unique to synapses from orphaned axons that will eventually degenerate.

Definitive identification of spines contacted by synaptic terminals of orphaned axons is less of a complication in the present study because about 95% of the synapses in the outer molecular layer of the dentate gyrus derive from the ipsilateral entorhinal cortex, and thus will eventually degenerate following complete entorhinal cortex lesions. The inner molecular layer of the dentate gyrus contains synapses of the dentate commissural/associational system, which do not degenerate, and there is essentially no overlap in the terminal fields of these two afferent systems. Nevertheless, spines with complex morphology were evident in the non-denervated inner molecular layer of *Wld^s* mice supporting the conclusion that there is hypertrophy of non-denervated spines.

Although a limitation of the present study is the use of a single technical approach (electron microscopy), our findings do point to questions for future studies. For example, the dramatic hypertrophy of spines suggests some sort of *trans-synaptic* signaling that could be related to neurotransmitter release by orphaned axons or release of some other signaling molecule. It would be informative to create chimeras where presynaptic neurons were from one strain and postsynaptic neurons were from another. The question would be whether postsynaptic neurons from *Wld^s* mice exhibited spine hypertrophy when there was degeneration of synaptic contacts from WT mice. If future studies indicate that hypertrophy is not an intrinsic effect of the mutation on the postsynaptic neuron, then identification the *trans-synaptic* signal is of great interest and could suggest new ways to protect postsynaptic neurons from denervation-induced atrophy. It would also be of great interest to assess whether other unique ultrastructural features, especially spine

hypertrophy, were seen in other strains of mice with delayed Wallerian degeneration (SARM1 knockout mice for example).

Ultrastructural Signs of Reinnervation in *Wld^S* vs. C57Bl/6 Mice

In the model system of reinnervation of dentate granule cells following entorhinal cortex lesions, synapse replacement is reflected by loss and then replacement of non-degenerating synapses over time. There is no categorical marker or definitive morphology to identify new synapses, although tracing studies have demonstrated that some are multi-synapse terminals (Steward et al., 1988b). Defining synapse replacement in *Wld^S* mice is not straightforward because synapse loss is delayed, extending into the early phase of new synapse formation in WT C57Bl/6 mice between 4 and 8 days post-lesion. At 8 days post-lesion in *Wld^S* mice, most synapses that will eventually degenerate have not yet begun to exhibit degenerative changes. This mix of orphaned synapses that will eventually degenerate and new synapses compromises EM quantification of the time course of new synapse formation. By 12 days, the numbers of intact synapses and degenerating synapses in *Wld^S* mice are equivalent to what is seen in C57Bl/6 mice, and then numbers of intact synapses increase between 12 and 16 days. These data are consistent with previous studies of sprouting of different inputs to dentate granule cells after entorhinal cortex lesions. Sprouting of septal cholinergic axons is delayed and less extensive in *Wld^S* mice (Steward et al., 1988b; Shi and Stanfield, 1996). Sprouting of commissural axons is delayed to an even greater extent than sprouting of cholinergic axons with the first sign of sprouting being at 12 days post-lesion (Shi and Stanfield, 1996).

Implications for Searches for Naturally-Occurring Neuroprotective Mutations

The *Wld^S* mutation was discovered during studies of axonal pathophysiology, specifically Wallerian degeneration of peripheral nerve axons. It is highly unlikely that this spontaneous mutation would have been noticed otherwise because there are

to our knowledge no reports of any phenotype in un-injured mice with the *Wld^S* mutation. Discovery of the *Wld^S* mutation happened in much the same way as our discovery of other murine genetic backgrounds that confer protection against excitotoxic neurodegeneration (Schauwecker and Steward, 1997). The initial surprising discovery was an unexpected finding from studies of hippocampal degeneration following kainic acid-induced seizures, which revealed that a commonly used inbred strain (C57Bl/6) was highly resistant to kainic acid-induced neurodegeneration (Schauwecker and Steward, 1997). One wonders how many other naturally-occurring mutations have neuroprotective phenotypes that are only manifested in the context of pathophysiology.

DATA AVAILABILITY STATEMENT

The raw data supporting the conclusions of this article will be made available by the authors, without undue reservation, to any qualified researcher.

ETHICS STATEMENT

The animal study was reviewed and approved by Institutional Animal Care and Use Committee at the University of Virginia.

AUTHOR CONTRIBUTIONS

OS planned the study, analyzed the data, and wrote the manuscript. PF and JY prepared EM samples and contributed to writing the manuscript. All authors contributed to the article and approved the submitted version.

FUNDING

This study was supported by National Institutes of Health (NIH)-NS32280.

REFERENCES

- Avery, M. A., Sheehan, A. E., Kerr, K. S., Wang, J., and Freeman, M. R. (2009). *Wld^S* requires *Nmnat1* enzymatic activity and N16-VCP interactions to suppress Wallerian degeneration. *J. Cell Biol.* 184, 501–513. doi: 10.1083/jcb.200808042
- Babetto, E., Beirowski, B., Janeckova, L., Brown, R., Gilley, J., Thomson, D., et al. (2010). Targeting NMNAT1 to axons and synapses transforms its neuroprotective potency in vivo. *J. Neurosci.* 30, 13291–13304. doi: 10.1523/jneurosci.1189-10.2010
- Caceres, A., and Steward, O. (1983). Dendritic reorganization in the denervated dentate gyrus of the rat following entorhinal cortical lesions: A Golgi and electron microscopic analysis. *J. Comp. Neurol.* 214, 387–403.
- Coleman, M. P., and Freeman, M. R. (2010). Wallerian degeneration, *wld(s)*, and *nmnat*. *Annu. Rev. Neurosci.* 33, 245–267. doi: 10.1146/annurev-neuro-060909-153248
- Coleman, M. P., and Hoke, A. (2020). Programmed axon degeneration: from mouse to mechanism to medicine. *Nat. Rev. Neurosci.* 21, 183–196. doi: 10.1038/s41583-020-0269-3
- Desmond, N. L., and Levy, W. B. (1983). Synaptic correlates of associative potentiation/depression: an ultrastructural study in the hippocampus. *Brain Res.* 265, 21–30. doi: 10.1016/0006-8993(83)91329-x
- Desmond, N. L., and Levy, W. B. (1988). Synaptic interface surface area increases with long-term potentiation in the hippocampal dentate gyrus. *Brain Res.* 453, 308–314. doi: 10.1016/0006-8993(88)90171-0
- Figley, M. D., and DiAntonio, A. (2020). The SARM1 axon degeneration pathway: control of the NAD(+) metabolome regulates axon survival in health and disease. *Curr. Opin. Neurobiol.* 63, 59–66. doi: 10.1016/j.conb.2020.02.012
- Fischer, L. R., Culver, D. G., Davis, A. A., Tennant, P., Wang, M., Coleman, M., et al. (2005). The *Wld^S* gene modestly prolongs survival in the SOD1G93A fALS mouse. *Neurobiol. Dis.* 19, 293–300. doi: 10.1016/j.nbd.2005.01.008
- Gillingwater, T. H., Ingham, C. A., Parry, K. E., Wright, A. K., Haley, J. E., Wishart, T. M., et al. (2006). Delayed synaptic degeneration in the CNS of *Wld^S* mice after cortical lesion. *Brain* 129, 1546–1556. doi: 10.1093/brain/awl101
- Lunn, E. R., Perry, V. H., Brown, M. C., Rosen, H., and Gordon, S. (1989). Absence of Wallerian degeneration does not hinder regeneration in peripheral nerve. *Eur J Neurosci* 1, 27–33. doi: 10.1111/j.1460-9568.1989.tb00771.x

- Mack, T. G., Reiner, M., Beirowski, B., Mi, W., Emanuelli, M., Wagner, D., et al. (2001). Wallerian degeneration of injured axons and synapses is delayed by a Ube4b/Nmnat chimeric gene. *Nat. Neurosci.* 4, 1199–1206. doi: 10.1038/nn770
- Matthews, D. A., Cotman, C., and Lynch, G. (1976a). An electron microscopic study of lesion-induced synaptogenesis in the dentate gyrus of the adult rat. I. Magnitude and time course of degeneration. *Brain Res.* 115, 1–21. doi: 10.1016/0006-8993(76)90819-2
- Matthews, D. A., Cotman, C., and Lynch, G. (1976b). An electron microscopic study of lesion-induced synaptogenesis in the dentate gyrus of the adult rat. II. Reappearance of morphologically normal synaptic contacts. *Brain Res.* 115, 23–41. doi: 10.1016/0006-8993(76)90820-9
- Perederiy, J. V., Luikart, B. W., Washburn, E. K., Schnell, E., and Westbrook, G. L. (2013). Neural injury alters proliferation and integration of adult-generated neurons in the dentate gyrus. *J. Neurosci.* 33, 4754–4767. doi: 10.1523/jneurosci.4785-12.2013
- Perry, V. H., Brown, M. C., and Lunn, E. R. (1991). Very slow retrograde and wallerian degeneration in the CNS of C57BL/Ola mice. *Eur. J. Neurosci.* 3, 102–105. doi: 10.1111/j.1460-9568.1991.tb00815.x
- Perry, V. H., Lunn, E. R., Brown, M. C., Cahusac, S., and Gordon, S. (1990). Evidence that the rate of wallerian degeneration is controlled by a single autosomal dominant gene. *Eur. J. Neurosci.* 2, 408–413. doi: 10.1111/j.1460-9568.1990.tb00433.x
- Petralia, R. S., Yao, P. J., Kapogiannis, D., and Wang, Y. X. (2021). Invaginating structures in synapses - perspective. *Front. Synaptic Neurosci.* 13:685052. doi: 10.3389/fnsyn.2021.68505
- Sasaki, Y., Nakagawa, T., Mao, X., DiAntonio, A., and Milbrandt, J. (2016). NMNAT1 inhibits axon degeneration via blockade of SARM1-mediated NAD(+) depletion. *Elife* 5:e19749.
- Schauwecker, P. E., and Steward, O. (1997). Genetic determinants of susceptibility to excitotoxic cell death: implications for gene targeting approaches. *Proc. Natl. Acad. Sci. U.S.A.* 94, 4103–4108. doi: 10.1073/pnas.94.8.4103
- Shi, B., and Stanfield, B. B. (1996). Differential sprouting responses in axonal fiber systems in the dentate gyrus following lesions of the perforant path in WLDs mutant mice. *Brain Res.* 740, 89–101. doi: 10.1016/s0006-8993(96)00849-9
- Steward, O. (1983). Alterations in polyribosomes associated with dendritic spines during the reinnervation of the dentate Gyrus of the adult rat. *J. Neurosci.* 3, 177–188. doi: 10.1523/jneurosci.03-01-00177.1983
- Steward, O., and Vinsant, S. L. (1983). The process of reinnervation in the dentate of the adult rat: A quantitative electron microscopic analysis of terminal proliferation and reactive synaptogenesis. *J. Comp. Neurol.* 214, 370–386. doi: 10.1002/cne.902140403
- Steward, O., Caceres, A. O., and Reeves, T. M. (1988a). “Rebuilding synapses after injury: remodeling the postsynaptic cell’s receptive surface during reinnervation,” in *Neural Plasticity: A Lifespan Approach*, eds T. Petit and G. Ivy (New York, NY: Alan R. Liss), 143–158.
- Steward, O., Vinsant, S. L., and Davis, L. (1988b). The process of reinnervation in the dentate gyrus of adult rats: an ultrastructural study of changes in presynaptic terminals as a result of sprouting. *J. Comp. Neurol.* 267, 203–210. doi: 10.1002/cne.902670205
- Wright, A. K., Wishart, T. M., Ingham, C. A., and Gillingwater, T. H. (2010). Synaptic protection in the brain of WldS mice occurs independently of age but is sensitive to gene-dose. *PLoS One* 5:e15108. doi: 10.1371/journal.pone.0015108

Conflict of Interest: OS is a co-founder and has economic interests in the company “Axonis Inc.”, which holds a license on patents relating to axon regeneration.

The remaining authors declare that the research was conducted in the absence of any commercial or financial relationships that could be construed as a potential conflict of interest.

Publisher’s Note: All claims expressed in this article are solely those of the authors and do not necessarily represent those of their affiliated organizations, or those of the publisher, the editors and the reviewers. Any product that may be evaluated in this article, or claim that may be made by its manufacturer, is not guaranteed or endorsed by the publisher.

Copyright © 2021 Steward, Yonan and Falk. This is an open-access article distributed under the terms of the Creative Commons Attribution License (CC BY). The use, distribution or reproduction in other forums is permitted, provided the original author(s) and the copyright owner(s) are credited and that the original publication in this journal is cited, in accordance with accepted academic practice. No use, distribution or reproduction is permitted which does not comply with these terms.



MFN2 Deficiency Impairs Mitochondrial Transport and Downregulates Motor Protein Expression in Human Spinal Motor Neurons

Yongchao Mou^{1,2†}, Joshua Dein^{3†}, Zhenyu Chen^{1,2}, Mrunali Jagdale^{1,2} and Xue-Jun Li^{1,2*}

¹ Department of Biomedical Sciences, University of Illinois College of Medicine Rockford, Rockford, IL, United States,

² Department of Bioengineering, University of Illinois at Chicago, Chicago, IL, United States, ³ MD Program, University of Illinois College of Medicine Rockford, Rockford, IL, United States

OPEN ACCESS

Edited by:

James N. Sleight,
University College London,
United Kingdom

Reviewed by:

Wenting Guo,
VIB-KU Leuven Center for Brain and
Disease Research, Belgium
Peter Verstraelen,
University of Antwerp, Belgium

*Correspondence:

Xue-Jun Li
xjli23@uic.edu

[†] These authors have contributed
equally to this work and share first
authorship

Specialty section:

This article was submitted to
Molecular Signaling and Pathways,
a section of the journal
Frontiers in Molecular Neuroscience

Received: 18 June 2021

Accepted: 26 August 2021

Published: 16 September 2021

Citation:

Mou Y, Dein J, Chen Z, Jagdale M
and Li X-J (2021) MFN2 Deficiency
Impairs Mitochondrial Transport
and Downregulates Motor Protein
Expression in Human Spinal Motor
Neurons.
Front. Mol. Neurosci. 14:727552.
doi: 10.3389/fnmol.2021.727552

Charcot-Marie-Tooth (CMT) disease is one of the most common genetically inherited neurological disorders and CMT type 2A (CMT 2A) is caused by dominant mutations in the mitofusin-2 (*MFN2*) gene. *MFN2* is located in the outer mitochondrial membrane and is a mediator of mitochondrial fusion, with an essential role in maintaining normal neuronal functions. Although loss of *MFN2* induces axonal neuropathy, the detailed mechanism by which *MFN2* deficiency results in axonal degeneration of human spinal motor neurons remains largely unknown. In this study, we generated *MFN2*-knockdown human embryonic stem cell (hESC) lines using lentivirus expressing *MFN2* short hairpin RNA (shRNA). Using these hESC lines, we found that *MFN2* loss did not affect spinal motor neuron differentiation from hESCs but resulted in mitochondrial fragmentation and dysfunction as determined by live-cell imaging. Notably, *MFN2*-knockdown spinal motor neurons exhibited CMT2A disease-related phenotypes, including extensive perikaryal inclusions of phosphorylated neurofilament heavy chain (pNfH), frequent axonal swellings, and increased pNfH levels in long-term cultures. Importantly, *MFN2* deficit impaired anterograde and retrograde mitochondrial transport within axons, and reduced the mRNA and protein levels of kinesin and dynein, indicating the interfered motor protein expression induced by *MFN2* deficiency. Our results reveal that *MFN2* knockdown induced axonal degeneration of spinal motor neurons and defects in mitochondrial morphology and function. The impaired mitochondrial transport in *MFN2*-knockdown spinal motor neurons is mediated, at least partially, by the altered motor proteins, providing potential therapeutic targets for rescuing axonal degeneration of spinal motor neurons in CMT2A disease.

Keywords: human embryonic stem cell, spinal motor neuron, *MFN2*, *CMT2A*, mitochondrial transport

INTRODUCTION

Charcot-Marie-Tooth (CMT) disease is the most common genetically inherited group of motor and sensory neurodegenerative disorders, with a global prevalence of one in every 2,500 people (Skre, 1974; Saporta et al., 2011). The pathogenesis and clinical presentation of CMT are extremely variable and differ based on the individual and inciting genetic mutation, but the disease generally worsens over time as the affected spinal motor neurons degenerate, impairing the neuromuscular junction (Bombelli et al., 2014; Sleight et al., 2014; Spaulding et al., 2016). It is broadly classified into two subgroups, demyelinating (CMT1) and axonal (CMT2) subgroups (Saporta et al., 2011; Morena et al., 2019). In particular, the predominantly autosomal dominant CMT2A type is the most common form of axonal CMT and has been previously studied in clinical cases as well as animal and *in vitro* models. This subtype of CMT has a variable presentation, but has been associated with more severe phenotypes occurring earlier in life and presenting with a neuropathic phenotype characterized by muscular atrophy, areflexia, pes cavus, vibratory sense loss, and neuropathic pain (Zuchner et al., 2004; Reilly et al., 2011; Vielhaber et al., 2013). Numerous additional features may also be present, including optic atrophy, cognitive impairment, vocal cord paresis, and respiratory insufficiency (Stuppia et al., 2015). CMT2A has been most commonly associated with mutations in the *MFN2* gene, which codes for the GTPase dynamin-like protein, MFN2 (Zuchner et al., 2004; Stuppia et al., 2015; Bertholet et al., 2016).

MFN2 is ubiquitously expressed throughout the human body, including the outer mitochondrial membrane and endoplasmic reticulum in human spinal motor neurons (Burte et al., 2015). The exact mechanism underlying how MFN2 dysfunction contributes to CMT2A has not yet been elucidated. MFN2 is vital in mitochondrial functioning and dynamics, including mitochondrial fusion, transport, and mitophagy (Detmer and Chan, 2007; Stuppia et al., 2015). Fusion of mitochondria is an important, continuous cellular process that promotes the appropriate survival or elimination of damaged mitochondria. Along with mitofusin 1 (MFN1), MFN2 regulates the processes of fusion and fission, which are crucial to proper mitochondrial distribution and shape (Chen et al., 2003; Stuppia et al., 2015). Altered mitochondrial fission and fusion can impair mitophagy, the autophagic process of mitochondrial degradation, and mitochondrial transport, leading to cell death (Itoh et al., 2013). Neurons are highly polarized and need proper axonal transport to maintain their normal functions. One study showed the association between an *mfh2* non-sense mutation in Zebrafish and subsequent impairment in mitochondrial retrograde axonal transport on a cellular level in cultured neurons, as well as reduced motor functioning similar to the phenotypic presentation of CMT2A on an organism level (Chapman et al., 2013). Mutated *MFN2* has also been studied in human embryonic kidney (HEK) cells and neurons derived from human induced pluripotent stem cells (iPSCs) from a patient with CMT2A, revealing abnormal cellular clustering of mitochondria and impaired mitochondrial axonal trafficking (Baloh et al., 2007; Saporta et al., 2015; Rizzo et al., 2016). However, the mechanism

by which MFN2 deficiency results in axonal transport defects and axonopathy in human spinal motor neurons remains elusive.

Human pluripotent stem cells, including hESCs and iPSCs, have the capacity to generate any cell type in the human body including neuronal subtypes. These cells offer a unique way to study the cellular and biochemical changes underlying the etiology of various neurodegenerative diseases (Chamberlain et al., 2008; Wang et al., 2013; Xu et al., 2016). Human models of CMT2A have been created and studied on a cellular level using iPSCs from individuals with this disease (Saporta et al., 2015). To better elucidate the role of MFN2 in maintaining human motor neuron and mitochondrial function, we utilized the combination of lentiviral infection and RNA interference (RNAi) in hESC-based models to generate MFN2-knockdown hESC cell lines. These cells were then differentiated into human spinal motor neurons to study their associated mitochondrial function, axonal transport, and morphology. Our data reveal that MFN2 knockdown in human spinal motor neurons results in increased mitochondrial fragmentation and impaired function, including significantly altered morphology, reduced mitochondrial membrane potential, recapitulating CMT2A-specific mitochondrial defects. Using this hESC-based model, we found MFN2 deficiency downregulated motor proteins including KIF1A, KIF5A, and DYNC1H1 for anterograde and retrograde mitochondrial transport, which may contribute to the impaired axonal transport and axonal degeneration of human spinal motor neurons.

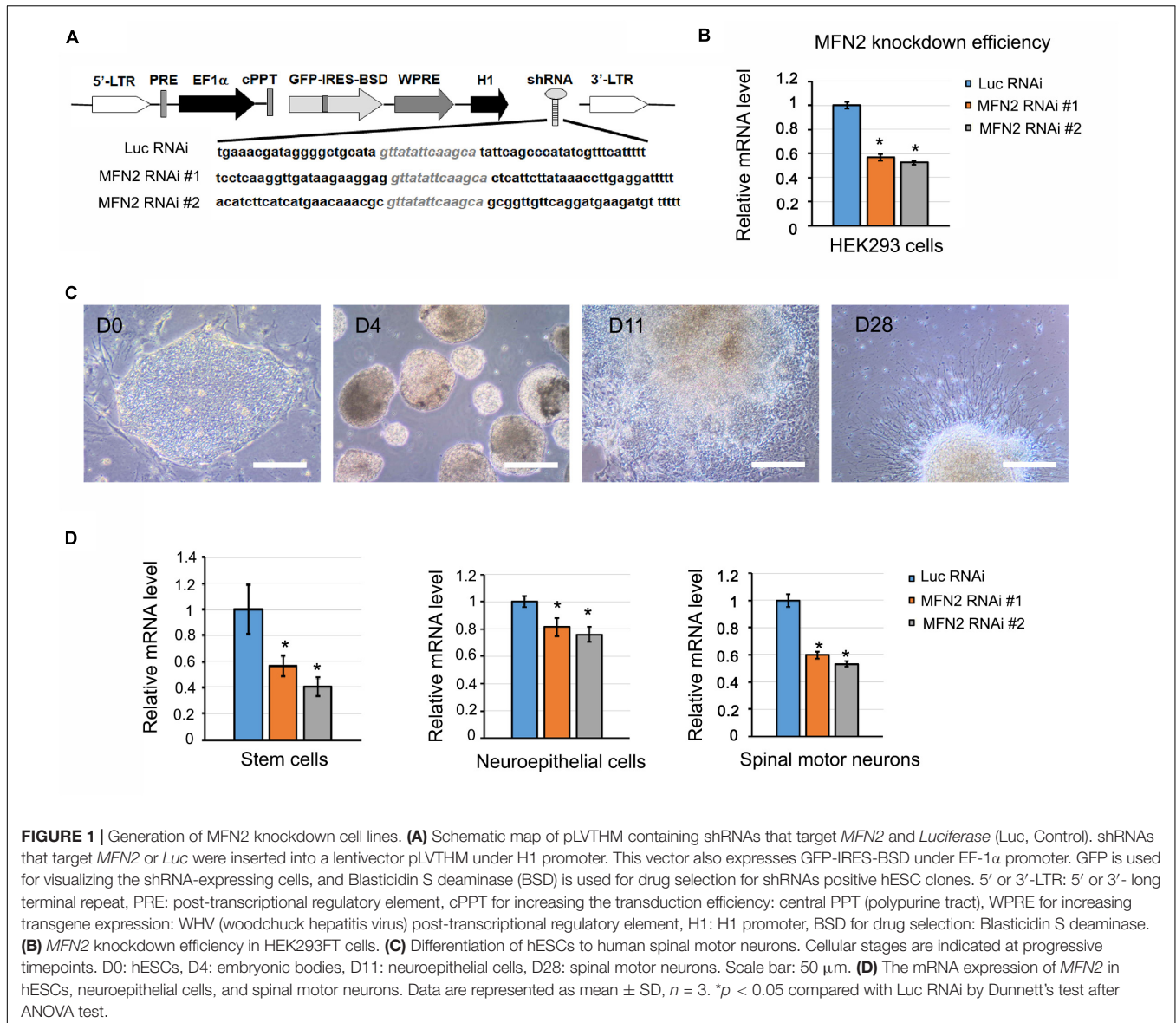
MATERIALS AND METHODS

Ethics Statement

All experiments involving hESCs were approved by the University of Illinois Embryonic Stem Cell Research Oversight Committee (ESCRO) and Institutional Biosafety Committee (IBC).

MFN2 Knockdown Efficiency Test in HEK293FT Cells

To knockdown MFN2 expression, MFN2 shRNA #1, MFN2 shRNA #2 and Luciferase shRNA (control) were cloned into pLVTHM vectors (Figure 1). The sequence for MFN2 RNAi #1: tcctcaagggtgataagaaggagggttatattcaagcactcattctataaaccttgaggattttt. MFN2 RNAi #2: acatctcatcatgaacaacgcggttatattcaagcagcg-gttgttcaggatgaagatgttttt. Luc RNAi (Control): tgaacgatagg-ggctgcatagttatattcaagcatattcagcccatatcgtttcatttt. Before lentivirus transduction was performed in hESCs, knockdown efficiency of MFN2 shRNA was examined in a human embryonic kidney cell line (HEK293FT). This transfection process was carried out using calcium phosphate precipitation. In short, HEK293FT cells plated on 6-well plates were first exposed to a transfection mix of 105 μ L ddH₂O, 15 μ L of 2M CaCl₂, and 120 μ L 2XHebs solution. In addition, 3.0 μ g MFN2 shRNA or Luciferase shRNA (control) vectors were added. Cells were then incubated in a transfection mix for 6–20 h at 37°C before changing the medium and culturing for 2 days. MFN2 knockdown efficiency was compared between MFN2 RNAi #1, MFN2 RNAi #2,



and Luciferase RNAi (Luc RNAi) using quantitative reverse transcription PCR (qRT-PCR).

Lentivirus Production and Transduction of hESCs

To generate MFN2 knockdown hESC cell lines, H9 hESCs were infected with pLVTHM lentiviruses (10^6 transducing units/ml) containing MFN2 shRNA #1 and MFN2 shRNA #2, as well as Luciferase shRNA (as controls). Briefly, to produce high-titer lentivirus, 10 μ g of pLVTHM-shRNA lentiviral transfer vector, 7.5 μ g of lentiviral vector psPAX2, and 5 μ g of pMD2.G (VSV-G envelope protein) were co-transfected into HEK293FT cells (Invitrogen) using the calcium phosphate method (Denton et al., 2018). For transduction with Luciferase and hMFN2 shRNA, H9 hESC pellets were incubated with lentivirus at 37°C for 30 min. The viruses and cell mixture were then transferred to irradiated

mouse embryonic fibroblasts (MEF) feeder layers overnight, and the medium was changed the next day. Blasticidin (BSD) was used to select for the transduced GFP-positive hESC clones. MFN2 knockdown efficiency was evaluated by testing mRNA expression using qPCR.

Spinal Motor Neuron Differentiation From hESCs

Spinal motor neurons were differentiated from hESCs according to our well-established protocol (Li et al., 2005, 2008). In short, MFN2 RNAi #1, MFN2 RNAi #2, and Luc RNAi hESC clones were cultured on MEF feeder layers in hESC media supplemented with 10 ng/mL bFGF. hESCs were dissociated and cultured in suspension in a neural induction medium (NIM) that included DMEM/F12 medium, 1x N2 supplement, and non-essential amino acids with DMH1 (2 μ M) and SB431542 (2 μ M) for 5 days.

During this time, medium was changed every other day. On day 7, the aggregates were attached and cultured in NIM with 0.1 μ M of retinoic acid (RA). At day 15–17, neuroepithelial cells were detached and cultured in suspension to form neurospheres in NIM with 1x B27, cAMP (1 μ M), RA (0.1 μ M), and purmorphamine (0.5 μ M). The medium was changed every other day. For terminal differentiation, neurospheres enriched with spinal motor neural progenitor cells were plated on the poly-ornithine and Matrigel-coated coverslips in neurobasal medium (Invitrogen) supplemented with 1x N2, 1x B27, cAMP (1 μ M), IGF-1 (10 ng/mL), brain-derived neurotrophic factor (BDNF, 10 ng/mL) and glial-derived neurotrophic factor (GDNF, 10 ng/mL). The medium was changed every other day until the desired day for measurement.

Western Blotting Assay

Total proteins from D42 spinal motor neurons were extracted using cell lysis buffer containing RIPA lysis buffer (Invitrogen) with 1x Halt Protease Inhibitor Cocktail (Thermo Fisher) and 1 mM phenylmethylsulfonyl fluoride (PMSF). The concentration of total proteins was measured using a Micro BCA Protein Assay Kit (Cat. #: 23235, Thermo Scientific). Total proteins were denatured with 4x Laemmli Sample Buffer (Bio-Rad, Cat. #: 1610747) at 100°C for 10 min. 15 μ g total proteins were loaded to 10% SDS-PAGE gel and transferred to a 0.2 μ m PVDF membrane at 200 mA for 3 h in a cold environment. Following the blocking with 3% bovine serum albumin (BSA) for 1 h at room temperature, the transferred PVDF membranes were incubated with primary antibodies at 4°C with shaking overnight. The primary antibodies used in this study include mouse IgG anti-MFN2 antibody (Sigma-Aldrich, WH0009927M3, 1:500), recombinant rabbit IgG anti-KIF1A antibody (Abcam, ab180153, 1:8,000), rabbit IgG anti-KIF5A antibody (Abcam, ab5628, 1:1,000), rabbit IgG anti-DYNC1H1 antibody (Proteintech, 13808-1-AP, 1:800), and mouse IgG anti- β -ACTIN (Sigma-Aldrich, A5316, 1:10,000). The PVDF membrane was washed with Tris-buffered-saline containing 0.1% tween-20 (TBST) three times and incubated with secondary antibodies donkey anti-mouse or rabbit HRP antibody (Santa Cruz, 1:5,000) for 1 h at room temperature. SuperSignal West Pico Plus chemiluminescent substrate kit (Thermo Scientific, Cat. #: 34579) was used to visualize the bands. The images were obtained by iBright Imaging Systems, and band intensity was quantified and normalized with β -ACTIN using ImageJ software (NIH).

Immunocytochemistry and Quantification of pNfH Inclusions and Neurite Swellings

Spinal motor neurons were fixed in 4% paraformaldehyde for 20 min and incubated with 0.2% Triton X-100 for 10 min at room temperature. After incubation with 10% donkey serum for 1 h, cells were incubated with primary antibodies at 4°C overnight. Secondary antibodies were used on the second day and incubated at room temperature for 30 min. Hoechst (1 mg/ml) was used to stain the nuclei. Primary antibodies used in this study include rabbit IgG anti-OLIG2 (Abcam,

Cat. #: AB109186, 1:1,000), mouse IgG anti-MNR2 (HB9) (Developmental Studies Hybridoma Bank, Cat. #: 81.5 C10, 1:50), mouse IgG anti-ISLET1/2 (Developmental Studies Hybridoma Bank, Cat. #:39.4D5, 1:100), mouse IgG anti-anti-Neurofilament H (NF-H or SMI32, Clone SMI32, Biolegend, Cat. #: SMI-32P, 1:500), rabbit IgG anti-TAU (Sigma, Cat. #: T6402, 1:200), and mouse IgG anti-phosphorylated neurofilament heavy chain (pNfH) (Millipore, Cat. #: MAB1592, 1:1,000). Donkey anti-rabbit Cy3, Donkey anti-mouse Cy3, Donkey anti-mouse Alexa Fluor 647, and Donkey anti-rabbit Alexa Fluor 647 were used as secondary antibodies. To compare between groups, at least three coverslips from each group were used for immunostaining as we described before (Li et al., 2009). At least five fields in each coverslip were imaged using an Olympus confocal microscope or Olympus IX83 microscope.

The pNfH aggregates in human spinal motor neural culture were analyzed following the previous method (Chen et al., 2014). A perikaryal inclusion was defined as an accumulation of immunoreactive staining against pNfH with intensities of threefold higher than that of their local distributions. Neurite swellings were defined as a beading of neurites with positive pNfH that was at least twice the diameter of the neurite. ImageJ (NIH) was used for quantifying these parameters. At least three coverslips from each group were used for immunostaining and at least five fields in each coverslip were imaged using an Olympus IX83 microscope.

Real-Time Quantitative PCR

D0 hESCs, D11 neuroepithelial cells, and D28 and D42 spinal motor neurons were collected. Total RNA samples were isolated using TRIzol (Invitrogen). 1 μ g of RNA was used to generate cDNA using the iScriptTM cDNA Synthesis Kit (Bio-Rad). MFN2 mRNA level was analyzed using the Taqman gene expression assay. Mitochondrial transport-associated motor protein gene expression was analyzed by the PowerUp SYBR Green Master Mix (Applied Biosystems) in the QuantStudio 6 Flex Real-Time PCR System (Applied Biosystems). PCR cycling conditions were 50°C for 2 min, 95°C for 3 min, 45 two-step cycles at 95°C for 15 s and 60°C for 60 s, followed by melt-curve stage at 95°C for 15 s, 60°C for 60 s, and 95°C for 15 s. Details of qRT-PCR primers are listed in **Supplementary Table 1**.

Mitochondrial Morphological Analysis and Transport by Live-Cell Imaging

To examine the mitochondrial transport, MFN2 RNAi #1, #2, and Luc RNAi spinal motor neurons were plated on poly-ornithine and Matrigel-coated 35 mm dishes (MatTek). D56-old spinal motor neurons were stained with 50 nM MitoTracker Red CMXRos (Invitrogen) for 3 min to visualize mitochondria and then incubated in imaging medium (pH to 7.4) containing 136 mM NaCl, 2.5 mM KCl, 2 mM CaCl₂, 1.3 mM MgCl₂, 10 mM HEPES, and 10 mM Glucose. Mitochondrial transport within axons was evaluated through live-cell imaging using an Olympus IX83 microscope equipped with an incubation chamber. Neurons were kept at 37°C with 5% CO₂ during imaging in the humid chamber. Pictures were captured every

5 s for 5 min. Quantifications were performed using ImageJ with Macros and Multiple Kymograph as described previously (Mou et al., 2020). Motile mitochondria were defined as average velocity $\geq 0.02 \mu\text{m/s}$ during the entire period (5 min). Mitochondria with an average velocity $< 0.02 \mu\text{m/s}$ were considered stationary (Rumora et al., 2018). The average anterograde and retrograde velocities were analyzed only in the motile mitochondria. Three dishes of spinal motor neurons per group and at least five fields per dish were imaged and analyzed.

The mitochondrial morphology was analyzed by ImageJ (NIH) according to our previously published method (Xu et al., 2016; Mou et al., 2020). In brief, axons were straightened, and the mitochondria were analyzed using the function of Analyze Particles in ImageJ, with mitochondrial area, perimeter, and length being plotted.

Mitochondrial Membrane Potential

Mitochondrial membrane potential (MMP) was measured based on a previous protocol (Joshi and Bakowska, 2011), and the fluorescent dye tetramethylrhodamine methyl ester (TMRM, Invitrogen) was used because it accumulates in mitochondria based on the MMP ($\Delta\psi\text{m}$). Spinal motor neurons were plated on 35 mm glass-bottomed dishes (MatTek). They were washed three times with 5 mM K^+ , 2 mM Ca^{2+} Tyrodes solution, then incubated with 10 nM TMRM in 2 mL Tyrodes solution for 45 min at room temperature in the dark. Live-cell imaging was performed using an Olympus microscope. The fluorescence exposure time and microscope setting were optimized using Luc RNAi neurons, and the same settings were used for all other groups in this study. Five random fields of each dish were tracked and analyzed using ImageJ (NIH). The average pixel intensity of TMRM labeling in each field was measured, followed by background subtraction.

Phosphorylated Neurofilament Heavy Chain ELISA

The neuron culture medium were collected and concentrated using Amicon Ultra-2 mL Centrifugal Filter Unit (Millipore Sigma). pNfH levels in medium were determined using a commercialized ELISA kit (Cat. #: ELISA-pNF-h-V1, EnCor Biotechnology Inc., United States). In brief, 50 μL of media were added into each well of the ELISA plates and incubated at 4°C overnight. 100 μL of detection antibody solution was added and incubated for 2 h at room temperature, followed by several washes with TBST. The following steps were carried out according to the manufacturer's instruction and read at 450 nm. pNfH amount in each group was calculated using the standard curve. The pNfH level in the medium was normalized to the total protein of the cultured spinal motor neurons. At least three wells of spinal motor neurons in each group were measured respectively.

Statistical Analysis

Data were analyzed using Dunnett's test after ANOVA to determine if the MFN2 RNAi #1 and MFN2 RNAi #2

groups differed significantly from the Luc RNAi control group in this study. Dunnett's test utilized a significance level of $p < 0.05$.

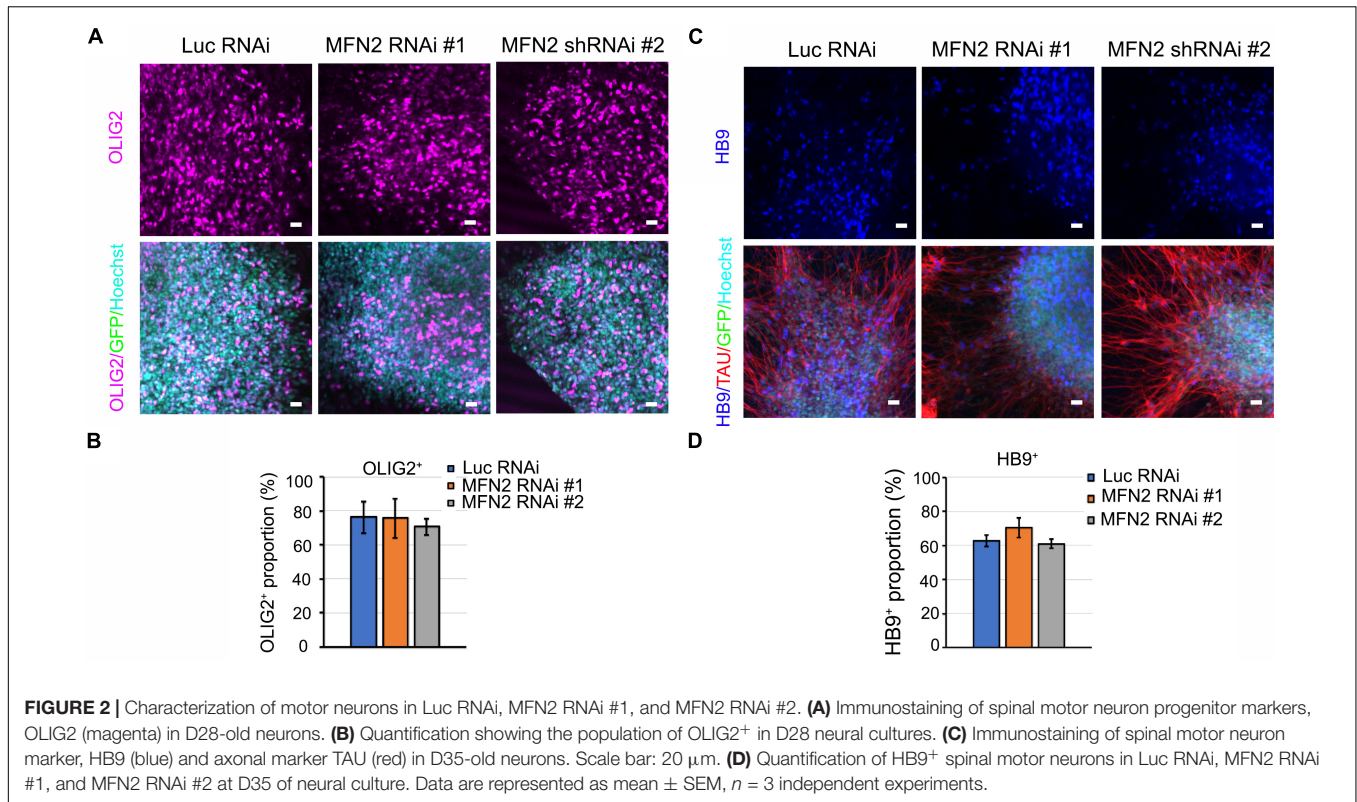
RESULTS

Generation of MFN2-Knockdown Human Embryonic Stem Cell Lines

To gain more insight into the role MFN2 plays in mitochondrial dynamics and human spinal motor neuron degeneration, we established MFN2-knockdown hESC lines to generate spinal motor neurons. This process started with a lentivirus containing shRNA sequences that specifically targeted and knocked down *MFN2* expression. Green fluorescence protein (GFP) in lentiviral vectors served as a marker indicating the positive transduction of lentivirus and consistent expression of *MFN2* shRNA in hESCs. We generated two MFN2-knockdown hESC lines (MFN2 RNAi #1 and #2) using lentivirus infection that expressed shRNA targeting *MFN2* (Figure 1A). The H9 line expressing shRNA targeting luciferase (Luc RNAi), a gene which is not expressed in mammalian cells, was generated as a control. Before lentivirus infection was performed in hESCs, knockdown efficiency of the MFN2-shRNA was examined in HEK cells and MFN2 knockdown efficiency was compared between MFN2 RNAi #1, MFN2 RNAi #2, and Luc RNAi using qRT-PCR. Two shRNA constructs were created and resulted in 44% and 47% reductions in *MFN2* mRNA levels in HEK cells compared to the control, respectively (Figure 1B). We then generated hESC lines expressing Luc RNAi, MFN2 RNAi #1, and MFN2 RNAi #2 using lentiviral transduction. To determine the role of MFN2 in spinal motor neurons, which are specifically affected in CMT2A, MFN2-knockdown hESC lines were differentiated into spinal motor neurons using a well-established method (Li et al., 2005, 2008). Throughout the duration of this differentiation process, four stages were observed at different timepoints. These included stem cell clones at D0, embryonic bodies at D4, neuroepithelial cells with rosettes at D11, and spinal motor neurons at D28 after plating on Matrigel-coated coverslips (Figure 1C). Significantly decreased expression of *MFN2* was observed in three stages of the differentiation process, including stem cells, neuroepithelial cells, and spinal motor neurons (Figure 1D). MFN2 protein levels were determined in spinal motor neurons by western blotting, indicating the significant reduction of MFN2 in MFN2 RNAi #1 and #2 compared with Luc RNAi (Figures 6B,C). These data revealed that the employed lentiviral model was able to effectively knockdown *MFN2* in hESCs and their derivatives, providing a tool for modeling CMT2A disease.

Effect of MFN2 on Spinal Motor Neuron Differentiation

After the effectiveness of our lentivirus model was demonstrated in hESCs, we sought to determine whether reduced *MFN2* expression affects the differentiation process from hESCs to

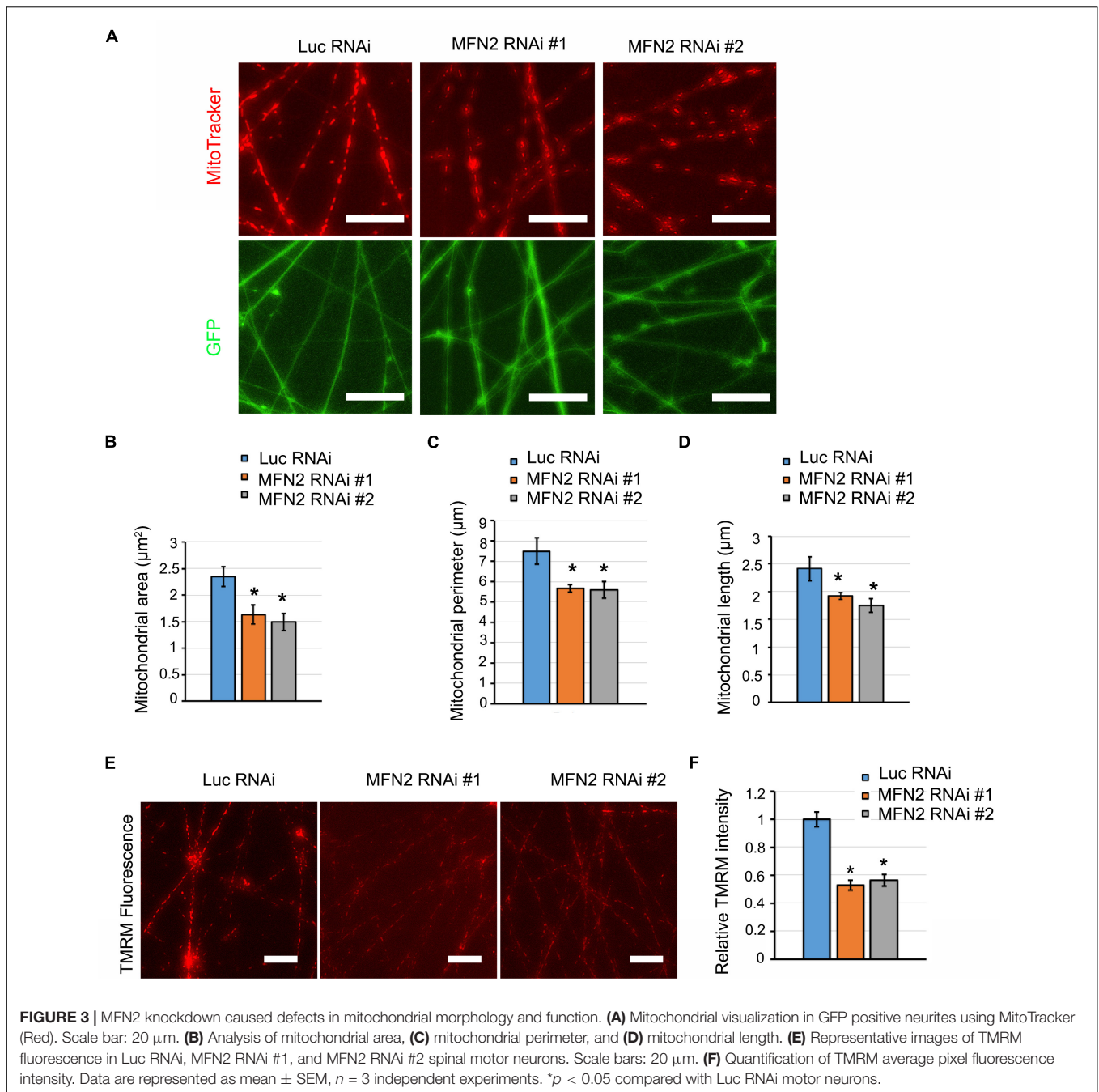


spinal motor neurons. Motor neuron markers for different stages of the differentiation process were measured by immunostaining, including OLIG2 for the spinal motor neuroprogenitor stage and HB9 for the spinal motor neuron stage. At day 28 of the differentiation process, OLIG2 expression in nuclei were observed in about 70% of the cells tested, revealing that most hESCs had differentiated toward the spinal motor neuron lineage and entered the spinal motor neuroprogenitor stage (Figure 2A). GFP in the lentiviral vector indicated the successful expression of shRNA in hESCs (Figure 2A). There was no significant difference between the percentage of cells staining positive for OLIG2 between the MFN2 RNAi #1 and #2 compared with Luc RNAi (Figure 2B). This indicated that MFN2 knockdown may not affect the initial differentiation from hESCs to spinal motor neuron progenitor cells. Further, we determined whether MFN2 knockdown affected the final differentiation into spinal motor neurons by staining the post-mitotic motor neuron marker HB9, and TAU, the axonal marker, at day 35 of the differentiation process (Figure 2C). At this point, about 60% of the spinal motor neurons demonstrated HB9-positivity. There was no significant difference between the percentage of cells staining positive for HB9, indicating that MFN2 knockdown may not affect the differentiation from hESCs to spinal motor neurons (Figure 2D). Furthermore, spinal motor neurons from Luc RNAi and MFN2 RNAi hESC lines were visualized by ISLET1/2 and SMI32, which are additional motor neuron markers (Supplementary Figures 1A,B). These markers did not show obvious alterations after MFN2 knockdown. These data suggest that MFN2 knockdown did not significantly

alter the specification and initial differentiation of motor neurons at day 35.

Altered Mitochondrial Morphology and Function in MFN2-Knockdown Spinal Motor Neurons

MFN2 encoding mitofusin-2, regulates mitochondrial fusion to maintain normal mitochondrial morphology and function (Chen et al., 2003). MFN2 mutation or loss of function results in CMT2A, leading to mitochondrial impairment and axonal neuropathy of dorsal root ganglion neurons (Misko et al., 2012). To determine whether MFN2 deficit causes mitochondrial impairments in human spinal motor neurons, we analyzed mitochondrial morphology by visualizing mitochondria with MitoTracker (Figure 3A). In MFN2-RNAi neurons, mitochondria appeared to be both smaller and shorter compared with Luc-RNAi neurons. Mitochondrial area, perimeter, and length were significantly decreased in MFN2-RNAi human neurons compared with Luc RNAi neurons (Figures 3B–D), indicating that MFN2 loss led to altered mitochondrial morphology and increased mitochondrial fragmentation. Altered mitochondrial morphology may interfere with mitochondrial functions. We further tested mitochondrial membrane potential (MMP) in MFN2 RNAi spinal motor neurons using TMRM (Figure 3E). A significantly decreased MMP was observed in MFN2 RNAi human spinal motor neurons compared with Luc RNAi group (Figure 3F). These data indicate MFN2 is important for maintaining



normal mitochondrial morphology and function, and MFN2 loss induced mitochondrial fragments and led to reduced mitochondrial health.

MFN2 Knockdown Induced Axonal Degeneration of Spinal Motor Neurons

Mitochondria play a central role in maintaining neural function. Impairment of mitochondria can be a stimulus that leads to axonal degeneration (Court and Coleman, 2012). Neurofilament is a structural component of axonal cytoskeleton in neurons, and hyper-phosphorylation of neurofilament is considered one

of the main triggers of its subsequent aggregation in degenerated neurons (Sihag et al., 2007). In some subtypes of CMT disease, neurofilament assembly and transport is linked to degeneration of neurons (Brownlee et al., 2002; Tradewell et al., 2009). pNfH, together with bundled aggregated neurofilament, is a histopathological hallmark for a variety of neurodegenerative diseases (Beck et al., 2012). We have observed that MFN2 deficiency caused mitochondrial defects and dysfunction. We then examined whether MFN2 deficit led to axonal degeneration in spinal motor neurons. In long-term culture of spinal motor neurons, we observed extensive perikaryal inclusions of pNfH

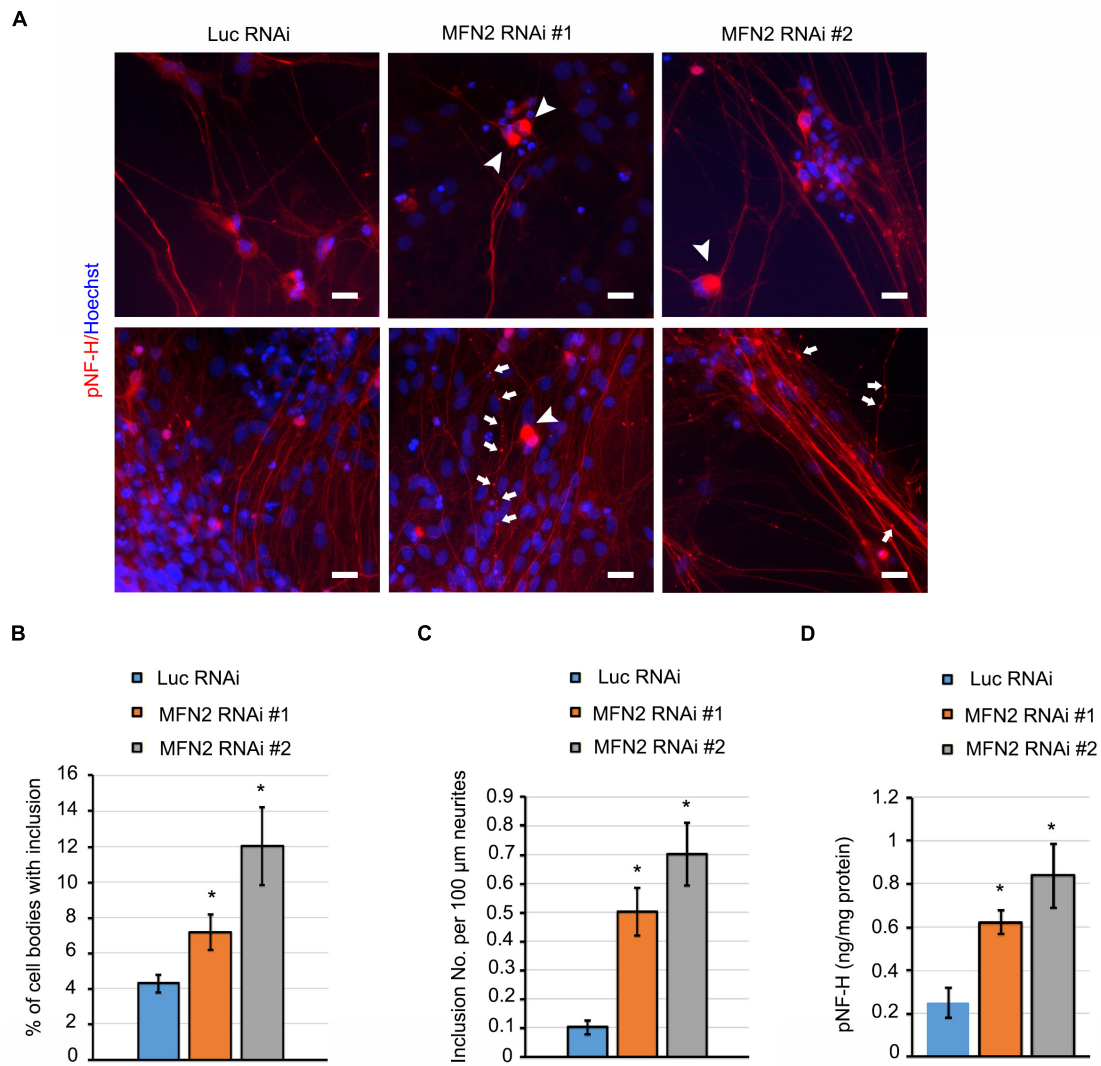


FIGURE 4 | MFN2 deficit induced pNfH inclusion in cell bodies and neurites of spinal motor neurons. **(A)** Immunofluorescent images of pNfH (Red) in spinal motor neurons. Arrowheads indicate pNfH inclusions in the cell bodies; arrow indicates pNfH inclusions in neurites. Scale bar: 20 μ m. **(B)** Quantification of cell bodies with inclusion in MFN2 RNAi #1, MFN2 RNAi #2, and Luc RNAi spinal motor neurons. **(C)** Quantification of inclusion numbers per 100 μ m neurites in MFN2 RNAi #1, MFN2 RNAi #2, and Luc RNAi spinal motor neurons. **(D)** ELISA quantification of pNfH level in conditioned cell culture media (normalized to protein). Data are represented as mean \pm SEM, $n = 3$ independent experiments. * $p < 0.05$ compared with Luc RNAi spinal motor neurons.

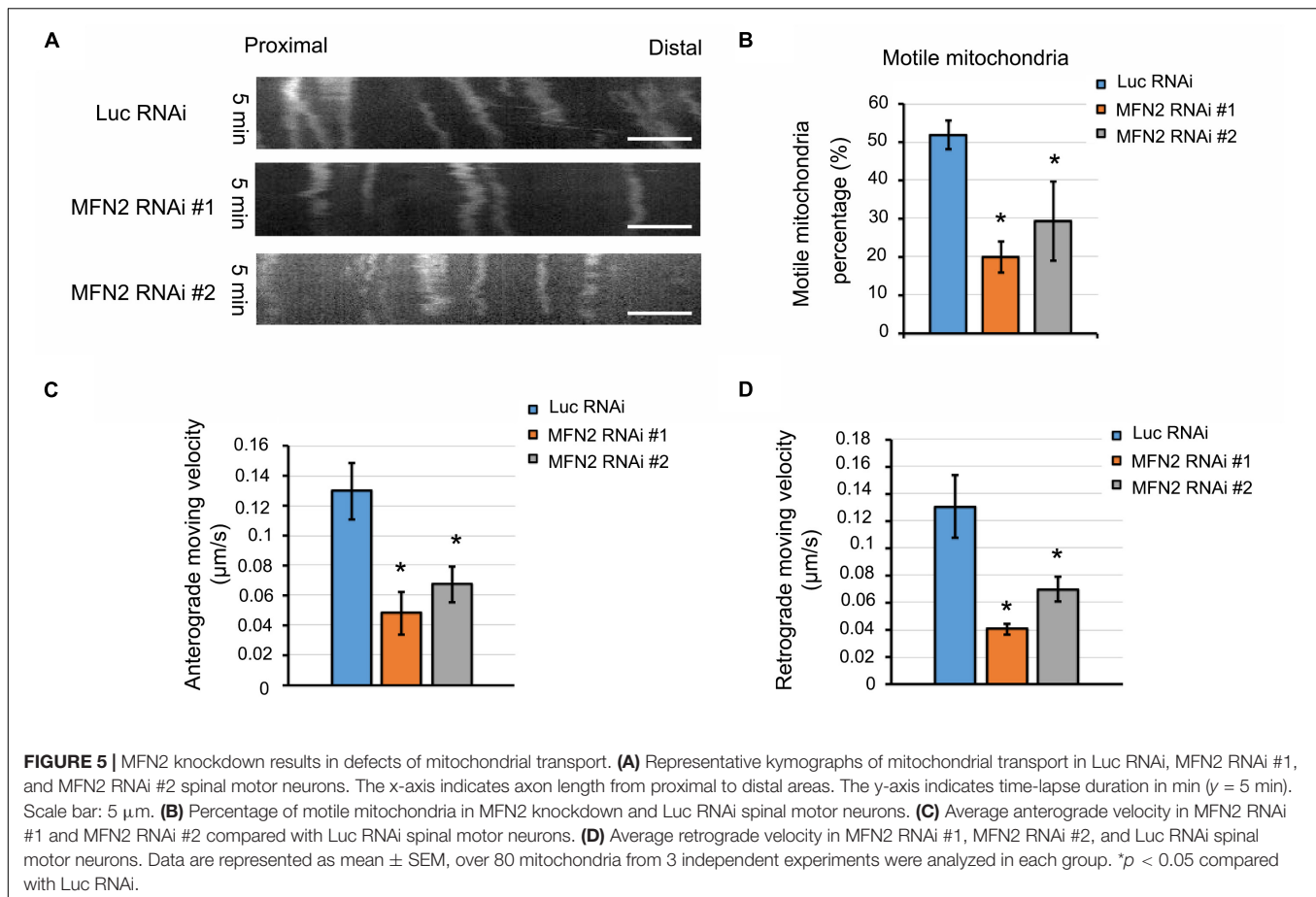
in MFN2 RNAi spinal motor neurons (**Figure 4A**). In addition, frequent scattered, dilated swellings and beadings with the aggregation of pNfH can be clearly visualized in neurites of MFN2 RNAi spinal motor neurons (**Figure 4A**). The numbers of pNfH inclusions in cell bodies and neurites of MFN2 RNAi spinal motor neurons are significantly increased compared to those in the Luc RNAi group (**Figures 4B,C**), implicating MFN2 loss in the subsequent axonal degeneration.

In the process of neurodegeneration, axonal remodeling results in the release of a variety of neurofilaments, including pNfH into extracellular fluids, a process which is widely considered as one of the biomarkers of neurodegenerative diseases (Rosengren et al., 1996). In spinal motor neuron culture medium, pNfH level was significantly elevated in MFN2 RNAi

group compared with the Luc RNAi group (**Figure 4D**). These data showed MFN2 loss resulted in the accumulation of pNfH in perikaryon and neurites of spinal motor neurons as well as the increased release of pNfH in the extracellular medium, highlighting that loss of MFN2 contributed to the degeneration of spinal motor neurons.

MFN2 Deficit Impaired Mitochondrial Transport by Interfering With Motor Protein Expression in Spinal Motor Neurons

One potential etiology behind the axonal degeneration in CMT disease is the dysregulated mitochondrial positioning due

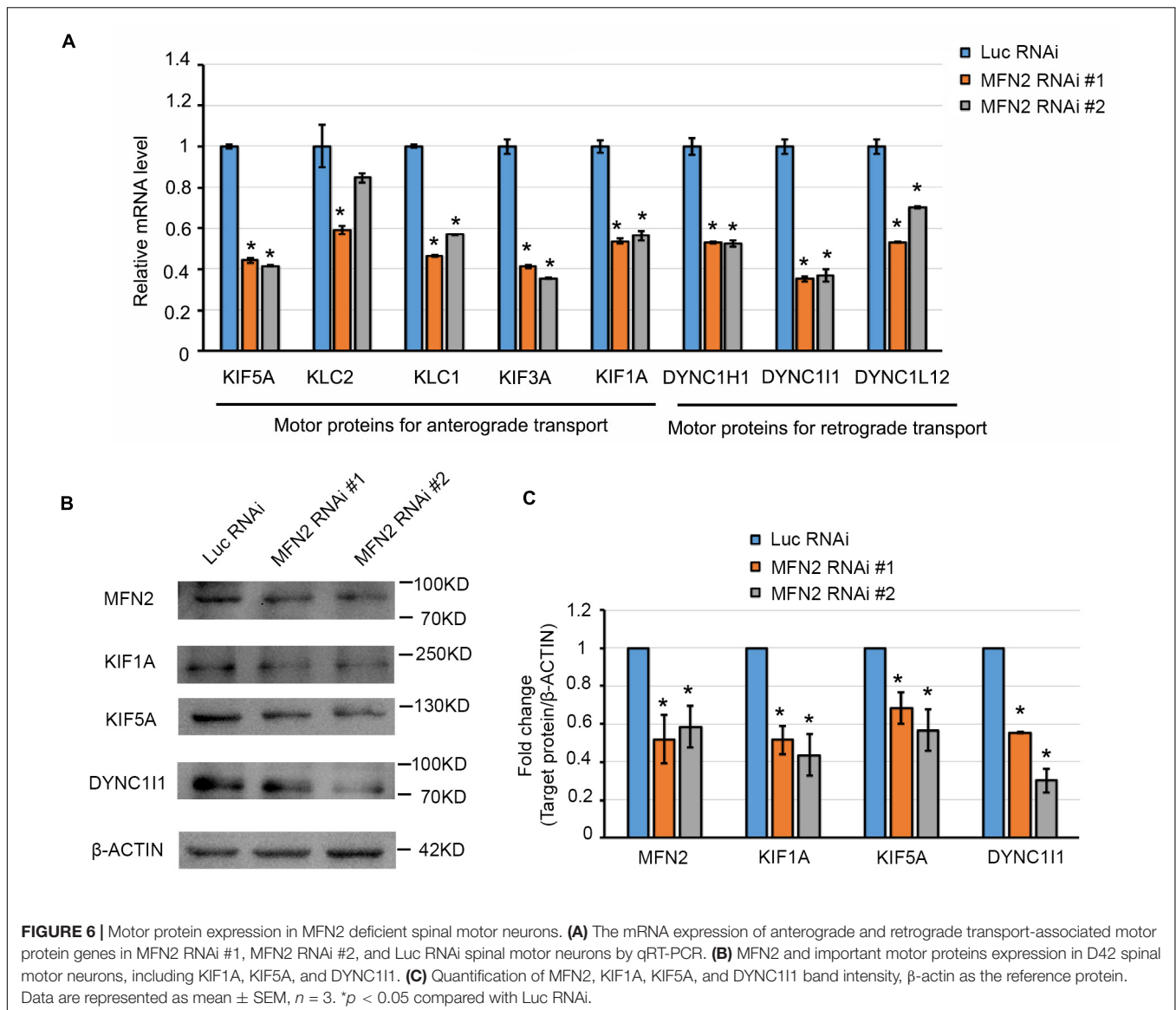


to interrupted transport within axons (Correia et al., 2016). To further elucidate whether MFN2 affects mitochondrial trafficking within axons of spinal motor neurons, we observed mitochondrial transport along axons with live-cell imaging. Kymographs of mitochondrial transport were generated and analyzed by ImageJ (Figure 5A). In the Luc RNAi group, extensive motile mitochondria were clearly observed, and most of the observed mitochondria (70–80% in 5 min) in the MFN2 RNAi neurons remained stationary or barely moving within axons (Figure 5A). Subsequent quantification indicated significant reductions of motile mitochondria in human spinal motor neurons with MFN2 loss compared to controls (Figure 5B). Importantly, both anterograde and retrograde velocity of mitochondria in MFN2-knockdown spinal motor neurons were dramatically reduced, implying MFN2 is necessary for mitochondrial trafficking and its deficit impaired both anterograde and retrograde mitochondrial transport within axons (Figures 5C,D). Motor-based anterograde and retrograde mitochondrial transport along axons is primarily driven by kinesin and dynein, respectively (Pilling et al., 2006). We thus examined the mRNA expression of anterograde and retrograde mitochondrial transport-associated motor proteins in MFN2 RNAi spinal motor neurons (Figure 6A). Interestingly, both kinesin (*KIF5A*, *KLC1*, *KIF3A*, and *KIF1A*) and dynein (*DYNC1H1*, *DYNC1H1*, and *DYNC-L12*) gene

expression was significantly decreased in human spinal motor neurons with MFN2 loss. The protein levels of *KIF1A*, *KIF5A*, and *DYNC1H1* expression were significantly decreased in MFN2 RNAi #1 and #2 compared with Luc RNAi spinal motor neurons, suggesting that MFN2 deficiency dramatically reduced axonal transport machinery proteins (Figures 6B,C). Our data suggest MFN2 deficiency in spinal motor neurons impairs mitochondrial transport in both the anterograde and retrograde directions along axons through decreased motor protein expression.

DISCUSSION

MFN2 deficiency results in CMT2A, a disease that is characterized by axonal neuropathy of peripheral neurons. Using animal models or animal-derived neurons, it has been shown that MFN2 is necessary for mitochondrial fusion and maintenance of normal mitochondrial morphology and distribution (Misko et al., 2012; Bergamin et al., 2016; El Fissi et al., 2018; Rocha et al., 2018). In this study, using a human spinal motor neuron model, we demonstrate that MFN2 loss does not affect the initial differentiation of human spinal motor neurons from pluripotent stem cells, but does result in later mitochondrial fragmentation and dysfunction



in these neurons. In addition, MFN2 deficit increases the inclusions of pNfH in cell bodies and neurites of spinal motor neurons, suggesting that MFN2 loss leads to the degeneration of human spinal motor neurons. Importantly, MFN2 deficiency significantly reduces the expression of both kinesin and dynein genes, resulting in decreased anterograde and retrograde mitochondrial motility within axons. Our study demonstrates that loss of MFN2 in human spinal motor neurons leads to axonal degeneration as well as defects in motor-based mitochondrial transport along axons by altering motor proteins expression.

MFN2 plays an essential role in mitochondrial fusion (Chen et al., 2003), endoplasmic reticulum-mitochondria tethering (Filadi et al., 2015; Larrea et al., 2019), and reactive oxygen species (ROS) production (Pich et al., 2005; van Hameren et al., 2019). Proper mitochondrial morphology and positioning allows for local metabolic and energetic needs within axons to be

met, which is critical to properly regulate the formation of neuromuscular junctions (Franco et al., 2020). MFN2, located in the mitochondrial outer membrane, regulates mitochondrial fusion to maintain mitochondrial morphology by balancing the process of mitochondrial fission. In vertebrates, both MFN1 and MFN2 are non-redundant and have been shown to be essential in mitochondrial outer membrane fusion, although they are highly homologous and share similar protein domain architecture (Sloat et al., 2019). In our study, MFN2 deficit caused smaller and shorter mitochondria and impaired mitochondrial function, which is consistent with mitochondrial phenotypes observed in CMT2A patient-specific motor neurons (Van Lent et al., 2021). These data confirm that MFN2 plays an essential role in maintaining mitochondrial morphology and function and highlight that its loss leads to altered mitochondrial dynamics and trafficking in human spinal motor neuron axons.

Mutation or loss-of-function of MFN2 causes axonal degeneration and motor deficit in patients (Kijima et al., 2005; Verhoeven et al., 2006). Neurofilament level in biofluid is one of the extremely sensitive biomarkers for many neurological diseases (Khalil et al., 2018). Interestingly, one specific subtypes (CMT2E) is caused by mutations in neurofilament L (Sasaki et al., 2006). Aggregation of pNfH in neurons and its subsequent release into extracellular fluid was increased in MFN2 RNAi neurons, implicating the process of axonal degeneration in our human CMT2A disease models. Although the exact mechanism leading to perikaryal inclusion and aggregation of neurofilament in neurites of MFN2-knockdown spinal motor neurons is not clear, a number of possible explanations have been proposed, including hyperphosphorylation, oxidative stress, or protease activity due to mitochondrial defects (Sihag et al., 2007; Court and Coleman, 2012). The degeneration of spinal motor neurons in our study, as indicated by the aggregation of pNfH in neurites, is consistent with the neurofilament aggregation seen in CMT2A dorsal root ganglion neurons, and abnormal mitochondrial distribution in axons was induced by Mfn2 mutants (Misko et al., 2012). In a transgenic mouse model using the CAMKII promoter to knockout neuronal Mfn2, knockout of Mfn2 in the cortex caused cytoskeleton alterations, including increased MAP2 distribution in cell bodies and hyperphosphorylated Tau in cortical neurons, indicating the importance of Mfn2 in maintaining normal axon structure and function (Jiang et al., 2018). It has been shown that MFN2 loss and mutation induced mitochondria-associated oxidative stress by dysregulating the oxidative phosphorylation (OXPHOS) system in neurons and non-neuron cells (Pich et al., 2005; Jiang et al., 2018; Yao et al., 2019). Mitochondria-linked oxidative stress could modify the post-translation of cytoskeletal proteins and enhance the degradation of microtubule-associated proteins, thereby disturbing normal cytoskeletal networks in neuronal and non-neuronal cells (Kwei et al., 1993; Pang et al., 1996; Akulinin and Dahlstrom, 2003). Pathologically altered mitochondrial distribution may be one of the underlying mechanisms contributing to axonal degeneration in our CMT2A models. Additionally, defective mitochondrial transport could cause the accumulation of mitochondrial fragments in axons, leading to axonal swellings and neuropathy (Sheng and Cai, 2012).

Alterations of other pathways in CMT diseases may contribute to the axonopathy of motor neurons, including post-translational modifications, oxidative stress-activated pathways, and neuroinflammatory responses (Hofer and Wenz, 2014; Fernandez-Lizarbe et al., 2019; Cassereau et al., 2020). Changes to post-translational modifications in CMT diseases have emerged as a critical pathway, including phosphorylation, acetylation, and ubiquitination (Park et al., 2010; d'Ydewalle et al., 2011; Benoy et al., 2018). Targeting these potential pathways or regulating MFN2 activity have showed the possibility of ameliorating CMT disease, including PI3K-Akt signaling pathway, histone deacetylase 6 (HDAC6), and MFN2 agonists (d'Ydewalle et al., 2011; Benoy et al., 2018;

Rocha et al., 2018; Van Lent et al., 2021). An imbalanced PI3K-Akt signaling pathway has been found in CMT2A spinal motor neurons and CMT rodent models (Fledrich et al., 2014; Van Lent et al., 2021). A dual leucine kinase (DLK, also known as MAP3K12) inhibitor, GNE-8505 was able to increase the mitochondrial aspect ratio and basal respiration that was reduced in MFN2^{R94Q} spinal motor neurons (Van Lent et al., 2021). HDAC6 is another potential target for rescuing CMT disease. Pharmacological inhibition of HDAC6 rescued axonal transport by increasing alpha-tubulin acetylation and the CMT phenotype of CMT mice with a small heat-shock protein gene (*HSPB1*) mutation (d'Ydewalle et al., 2011). These studies indicate a potentially important role for both post-translational modification and stress-related pathways in CMT diseases.

Given that MFN2 reduction impaired both anterograde and retrograde mitochondrial transport within axons in spinal motor neurons, we further examined how MFN2 loss induced defects in mitochondrial transport. Mfn2 was found to be necessary for mitochondrial transport through its physical interaction with Miro/Milton complexes, which link mitochondria to kinesin motors. In addition, Mfn2 mutant caused slower anterograde and retrograde mitochondrial transport (Misko et al., 2010). The reduced physical interaction between MFN2 and Miro/Milton/kinesin complex could be one of the reasons for interrupted mitochondrial transport in CMT2A spinal motor neurons. Interestingly, our study revealed that the expression of a variety of motor proteins is important for both anterograde and retrograde mitochondrial transport and were significantly reduced in MFN2-knockdown spinal motor neurons. The coordination between kinesin and dynein motors determines the bidirectional trafficking within axons. The reduced kinesin and dynein induced by loss of MFN2 may be another reason for slower mitochondrial trafficking. Although the mechanism of MFN2 deficiency leading to reduced expression of kinesin and dynein-related genes awaits further investigation, our study reveals that MFN2 deficiency in human motor neurons impairs motor protein expression and axonal transport, leading to axonal degeneration and serving as potential therapeutic targets for CMT2A.

DATA AVAILABILITY STATEMENT

The original contributions presented in the study are included in the article/**Supplementary Material**, further inquiries can be directed to the corresponding author/s.

ETHICS STATEMENT

All experiments involving hESCs were approved by the University of Illinois Embryonic Stem Cell Research

Oversight Committee (ESCRO) and Institutional Biosafety Committee (IBC).

AUTHOR CONTRIBUTIONS

X-JL conceived and supervised the study. YM and JD performed MFN2 knockdown stem cell lines generation, stem cell differentiation, mitochondrial transport, and axonal degeneration analysis experiments. ZC performed MFN2 shRNA design and tested gene knockdown efficiency. MJ did the immunostaining and imaging of axonal degeneration. YM, JD, and ZC collected and analyzed data. YM, JD, and X-JL wrote the manuscript with comments

from ZC and MJ. All authors read and approved the final manuscript.

FUNDING

This study is supported by the Blazer foundation.

SUPPLEMENTARY MATERIAL

The Supplementary Material for this article can be found online at: <https://www.frontiersin.org/articles/10.3389/fnmol.2021.727552/full#supplementary-material>

REFERENCES

- Akulinin, V. A., and Dahlstrom, A. (2003). Quantitative analysis of MAP2 immunoreactivity in human neocortex of three patients surviving after brain ischemia. *Neurochem. Res.* 28, 373–378. doi: 10.1023/a:1022401922669
- Baloh, R. H., Schmidt, R. E., Pestronk, A., and Milbrandt, J. (2007). Altered axonal mitochondrial transport in the pathogenesis of charcot-marie-tooth disease from mitofusin 2 mutations. *J. Neurosci.* 27, 422–430. doi: 10.1523/jneurosci.4798-06.2007
- Beck, R., Deek, J., and Safinya, C. R. (2012). Structures and interactions in 'bottlebrush' neurofilaments: the role of charged disordered proteins in forming hydrogel networks. *Biochem. Soc. Trans.* 40, 1027–1031. doi: 10.1042/bst20120101
- Benoy, V., Van Helleputte, L., Prior, R., D'ydewalle, C., Haec, W., Geens, N., et al. (2018). HDAC6 is a therapeutic target in mutant GARS-induced charcot-marie-tooth disease. *Brain* 141, 673–687. doi: 10.1093/brain/awx375
- Bergamin, G., Cieri, D., Vazza, G., Argenton, F., and Mostacciolo, M. L. (2016). Zebrafish Tg(hb9:MTS-Kaede): a new in vivo tool for studying the axonal movement of mitochondria. *Biochim. Biophys. Acta.* 1860, 1247–1255. doi: 10.1016/j.bbagen.2016.03.007
- Bertholet, A. M., Delerue, T., Millet, A. M., Moulis, M. F., David, C., Daloyau, M., et al. (2016). Mitochondrial fusion/fission dynamics in neurodegeneration and neuronal plasticity. *Neurobiol. Dis.* 90, 3–19. doi: 10.1016/j.nbd.2015.10.011
- Bombelli, F., Stojkovic, T., Dubourg, O., Echaniz-Laguna, A., Tardieu, S., Larcher, K., et al. (2014). Charcot-marie-tooth disease type 2A: from typical to rare phenotypic and genotypic features. *JAMA Neurol.* 71, 1036–1042. doi: 10.1001/jamaneurol.2014.629
- Brownlees, J., Ackerley, S., Grierson, A. J., Jacobsen, N. J., Shea, K., Anderton, B. H., et al. (2002). Charcot-marie-tooth disease neurofilament mutations disrupt neurofilament assembly and axonal transport. *Hum. Mol. Genet.* 11, 2837–2844. doi: 10.1093/hmg/11.23.2837
- Burte, F., Carelli, V., Chinnery, P. F., and Yu-Wai-Man, P. (2015). Disturbed mitochondrial dynamics and neurodegenerative disorders. *Nat. Rev. Neurol.* 11, 11–24. doi: 10.1038/nrneuro.2014.228
- Cassereau, J., Chevrollier, A., Codron, P., Goizet, C., Gueguen, N., Verny, C., et al. (2020). Oxidative stress contributes differentially to the pathophysiology of Charcot-Marie-Tooth disease type 2K. *Exp. Neurol.* 323:113069. doi: 10.1016/j.expneurol.2019.113069
- Chamberlain, S. J., Li, X. J., and Lalande, M. (2008). Induced pluripotent stem (iPS) cells as in vitro models of human neurogenetic disorders. *Neurogenetics* 9, 227–235. doi: 10.1007/s10048-008-0147-z
- Chapman, A. L., Bennett, E. J., Ramesh, T. M., De Vos, K. J., and Grierson, A. J. (2013). Axonal transport defects in a mitofusin 2 loss of function model of charcot-marie-tooth disease in zebrafish. *PLoS One* 8:e67276. doi: 10.1371/journal.pone.0067276
- Chen, H., Detmer, S. A., Ewald, A. J., Griffin, E. E., Fraser, S. E., and Chan, D. C. (2003). Mitofusins Mfn1 and Mfn2 coordinately regulate mitochondrial fusion and are essential for embryonic development. *J. Cell Biol.* 160, 189–200. doi: 10.1083/jcb.200211046
- Chen, H., Qian, K., Du, Z., Cao, J., Petersen, A., Liu, H., et al. (2014). Modeling ALS with iPSCs reveals that mutant SOD1 misregulates neurofilament balance in motor neurons. *Cell Stem Cell* 14, 796–809. doi: 10.1016/j.stem.2014.02.004
- Correia, S. C., Perry, G., and Moreira, P. I. (2016). Mitochondrial traffic jams in Alzheimer's disease—pinpointing the roadblocks. *Biochim. Biophys. Acta* 1862, 1909–1917. doi: 10.1016/j.bbadis.2016.07.010
- Court, F. A., and Coleman, M. P. (2012). Mitochondria as a central sensor for axonal degenerative stimuli. *Trends Neurosci.* 35, 364–372. doi: 10.1016/j.tins.2012.04.001
- Denton, K., Mou, Y., Xu, C. C., Shah, D., Chang, J., Blackstone, C., et al. (2018). Impaired mitochondrial dynamics underlie axonal defects in hereditary spastic paraplegias. *Hum. Mol. Genet.* 27, 2517–2530. doi: 10.1093/hmg/ddy156
- Detmer, S. A., and Chan, D. C. (2007). Complementation between mouse Mfn1 and Mfn2 protects mitochondrial fusion defects caused by CMT2A disease mutations. *J. Cell Biol.* 176, 405–414. doi: 10.1083/jcb.200611080
- d'Ydewalle, C., Krishnan, J., Chiheb, D. M., Van Damme, P., Irobi, J., Kozikowski, A. P., et al. (2011). HDAC6 inhibitors reverse axonal loss in a mouse model of mutant HSPB1-induced charcot-marie-tooth disease. *Nat. Med.* 17, 968–974. doi: 10.1038/nm.2396
- El Fissi, N., Rojo, M., Aouane, A., Karatas, E., Poliacikova, G., David, C., et al. (2018). Mitofusin gain and loss of function drive pathogenesis in drosophila models of CMT2A neuropathy. *EMBO Rep.* 19:e45241.
- Fernandez-Lizarbe, S., Civera-Tregon, A., Cantarero, L., Herrero, I., Juarez, P., Hoenicka, J., et al. (2019). Neuroinflammation in the pathogenesis of axonal Charcot-Marie-Tooth disease caused by lack of GDAP1. *Exp. Neurol.* 320:113004. doi: 10.1016/j.expneurol.2019.113004
- Filadi, R., Greotti, E., Turacchio, G., Luini, A., Pozzan, T., and Pizzo, P. (2015). Mitofusin 2 ablation increases endoplasmic reticulum-mitochondria coupling. *Proc. Natl. Acad. Sci. U.S.A.* 112, E2174–E2181.
- Fledrich, R., Stassart, R. M., Klink, A., Rasch, L. M., Prukop, T., Haag, L., et al. (2014). Soluble neuregulin-1 modulates disease pathogenesis in rodent models of charcot-marie-tooth disease 1A. *Nat. Med.* 20, 1055–1061. doi: 10.1038/nm.3664
- Franco, A., Dang, X., Walton, E. K., Ho, J. N., Zablocka, B., Ly, C., et al. (2020). Burst mitofusin activation reverses neuromuscular dysfunction in murine CMT2A. *Elife* 9:e61119.
- Hofer, A., and Wenz, T. (2014). Post-translational modification of mitochondria as a novel mode of regulation. *Exp. Gerontol.* 56, 202–220. doi: 10.1016/j.exger.2014.03.006
- Itoh, K., Nakamura, K., Iijima, M., and Sesaki, H. (2013). Mitochondrial dynamics in neurodegeneration. *Trends Cell Biol.* 23, 64–71.
- Jiang, S., Nandy, P., Wang, W., Ma, X., Hsia, J., Wang, C., et al. (2018). Mfn2 ablation causes an oxidative stress response and eventual neuronal death in the hippocampus and cortex. *Mol. Neurodegener.* 13:5. doi: 10.1007/978-3-662-22516-5_2
- Joshi, D. C., and Bakowska, J. C. (2011). Determination of mitochondrial membrane potential and reactive oxygen species in live rat cortical neurons. *J. Vis. Exp.* 51:2704.
- Khalil, M., Teunissen, C. E., Otto, M., Piehl, F., Sormani, M. P., Gatteringer, T., et al. (2018). Neurofilaments as biomarkers in neurological disorders. *Nat. Rev. Neurol.* 14, 577–589.

- Kijima, K., Numakura, C., Izumino, H., Umetsu, K., Nezu, A., Shiiki, T., et al. (2005). Mitochondrial GTPase mitofusin 2 mutation in charcot-marie-tooth neuropathy type 2A. *Hum. Genet.* 116, 23–27. doi: 10.1007/s00439-004-1199-2
- Kwei, S., Jiang, C., and Haddad, G. G. (1993). Acute anoxia-induced alterations in MAP2 immunoreactivity and neuronal morphology in rat hippocampus. *Brain Res.* 620, 203–210. doi: 10.1016/0006-8993(93)90157-i
- Larrea, D., Pera, M., Gonnelli, A., Quintana-Cabrera, R., Akman, H. O., Guardia-Laguarta, C., et al. (2019). MFN2 mutations in charcot-marie-tooth disease alter mitochondria-associated ER membrane function but do not impair bioenergetics. *Hum. Mol. Genet.* 28, 1782–1800. doi: 10.1093/hmg/ddz008
- Li, X. J., Du, Z. W., Zarnowska, E. D., Pankratz, M., Hansen, L. O., Pearce, R. A., et al. (2005). Specification of motoneurons from human embryonic stem cells. *Nat. Biotechnol.* 23, 215–221.
- Li, X. J., Hu, B. Y., Jones, S. A., Zhang, Y. S., Lavaute, T., Du, Z. W., et al. (2008). Directed differentiation of ventral spinal progenitors and motor neurons from human embryonic stem cells by small molecules. *Stem Cells* 26, 886–893. doi: 10.1634/stemcells.2007-0620
- Li, X. J., Zhang, X., Johnson, M. A., Wang, Z. B., Lavaute, T., and Zhang, S. C. (2009). Coordination of sonic hedgehog and WNT signaling determines ventral and dorsal telencephalic neuron types from human embryonic stem cells. *Development* 136, 4055–4063. doi: 10.1242/dev.036624
- Misko, A., Jiang, S., Węgorzewska, I., Milbrandt, J., and Baloh, R. H. (2010). Mitofusin 2 is necessary for transport of axonal mitochondria and interacts with the Miro/Milton complex. *J. Neurosci.* 30, 4232–4240. doi: 10.1523/jneurosci.6248-09.2010
- Misko, A. L., Sasaki, Y., Tuck, E., Milbrandt, J., and Baloh, R. H. (2012). Mitofusin2 mutations disrupt axonal mitochondrial positioning and promote axon degeneration. *J. Neurosci.* 32, 4145–4155. doi: 10.1523/jneurosci.6338-11.2012
- Morena, J., Gupta, A., and Hoyle, J. C. (2019). Charcot-marie-tooth: from molecules to therapy. *Int. J. Mol. Sci.* 20:3419. doi: 10.3390/ijms20143419
- Mou, Y., Mukte, S., Chai, E., Dein, J., and Li, X. J. (2020). Analyzing mitochondrial transport and morphology in human induced pluripotent stem cell-derived neurons in hereditary spastic paraplegia. *J. Vis. Exp.* doi: 10.3791/60548
- Pang, Z., Umberger, G. H., and Geddes, J. W. (1996). Neuronal loss and cytoskeletal disruption following intrahippocampal administration of the metabolic inhibitor malonate: lack of protection by MK-801. *J. Neurochem.* 66, 474–484. doi: 10.1046/j.1471-4159.1996.66020474.x
- Park, Y. Y., Lee, S., Karbowski, M., Neutzner, A., Youle, R. J., and Cho, H. (2010). Loss of MARCH5 mitochondrial E3 ubiquitin ligase induces cellular senescence through dynamin-related protein 1 and mitofusin 1. *J. Cell Sci.* 123, 619–626. doi: 10.1242/jcs.061481
- Pich, S., Bach, D., Briones, P., Liesa, M., Camps, M., Testar, X., et al. (2005). The charcot-marie-tooth type 2A gene product, Mfn2, up-regulates fuel oxidation through expression of OXPHOS system. *Hum. Mol. Genet.* 14, 1405–1415. doi: 10.1093/hmg/ddi149
- Pilling, A. D., Horiuchi, D., Lively, C. M., and Saxton, W. M. (2006). Kinesin-1 and dynein are the primary motors for fast transport of mitochondria in drosophila motor axons. *Mol. Biol. Cell* 17, 2057–2068. doi: 10.1091/mbc.e05-06-0526
- Reilly, M. M., Murphy, S. M., and Laura, M. (2011). Charcot-marie-tooth disease. *J. Peripher. Nerv. Syst.* 16, 1–14.
- Rizzo, F., Ronchi, D., Salani, S., Nizzardo, M., Fortunato, F., Bordoni, A., et al. (2016). Selective mitochondrial depletion, apoptosis resistance, and increased mitophagy in human charcot-marie-tooth 2A motor neurons. *Hum. Mol. Genet.* 25, 4266–4281. doi: 10.1093/hmg/ddw258
- Rocha, A. G., Franco, A., Krezel, A. M., Rumsey, J. M., Alberti, J. M., Knight, W. C., et al. (2018). MFN2 agonists reverse mitochondrial defects in preclinical models of charcot-marie-tooth disease type 2A. *Science* 360, 336–341. doi: 10.1126/science.aao1785
- Rosengren, L. E., Karlsson, J. E., Karlsson, J. O., Persson, L. I., and Wikkelso, C. (1996). Patients with amyotrophic lateral sclerosis and other neurodegenerative diseases have increased levels of neurofilament protein in CSF. *J. Neurochem.* 67, 2013–2018. doi: 10.1046/j.1471-4159.1996.67052013.x
- Rumora, A. E., Lentz, S. I., Hinder, L. M., Jackson, S. W., Valesano, A., Levinson, G. E., et al. (2018). Dyslipidemia impairs mitochondrial trafficking and function in sensory neurons. *FASEB J.* 32, 195–207. doi: 10.1096/fj.201700206r
- Saporta, A. S., Sottile, S. L., Miller, L. J., Feely, S. M., Siskind, C. E., and Shy, M. E. (2011). Charcot-marie-tooth disease subtypes and genetic testing strategies. *Ann. Neurol.* 69, 22–33. doi: 10.1002/ana.22166
- Saporta, M. A., Dang, V., Volfson, D., Zou, B., Xie, X. S., Adebola, A., et al. (2015). Axonal charcot-marie-tooth disease patient-derived motor neurons demonstrate disease-specific phenotypes including abnormal electrophysiological properties. *Exp. Neurol.* 263, 190–199. doi: 10.1016/j.expneurol.2014.10.005
- Sasaki, T., Gotow, T., Shiozaki, M., Sakaue, F., Saito, T., Julien, J. P., et al. (2006). Aggregate formation and phosphorylation of neurofilament-L Pro22 charcot-marie-tooth disease mutants. *Hum. Mol. Genet.* 15, 943–952. doi: 10.1093/hmg/ddl011
- Sheng, Z. H., and Cai, Q. (2012). Mitochondrial transport in neurons: impact on synaptic homeostasis and neurodegeneration. *Nat. Rev. Neurosci.* 13, 77–93. doi: 10.1038/nrn3156
- Sihag, R. K., Inagaki, M., Yamaguchi, T., Shea, T. B., and Pant, H. C. (2007). Role of phosphorylation on the structural dynamics and function of types III and IV intermediate filaments. *Exp. Cell Res.* 313, 2098–2109. doi: 10.1016/j.yexcr.2007.04.010
- Skre, H. (1974). Genetic and clinical aspects of charcot-marie-tooth's disease. *Clin. Genet.* 6, 98–118.
- Sleigh, J. N., Grice, S. J., Burgess, R. W., Talbot, K., and Cader, M. Z. (2014). Neuromuscular junction maturation defects precede impaired lower motor neuron connectivity in charcot-marie-tooth type 2D mice. *Hum. Mol. Genet.* 23, 2639–2650. doi: 10.1093/hmg/ddt659
- Sloat, S. R., Whitley, B. N., Engelhart, E. A., and Hoppins, S. (2019). Identification of a mitofusin specificity region that confers unique activities to Mfn1 and Mfn2. *Mol. Biol. Cell* 30, 2309–2319. doi: 10.1091/mbc.e19-05-0291
- Spaulding, E. L., Sleigh, J. N., Morelli, K. H., Pinter, M. J., Burgess, R. W., and Seburn, K. L. (2016). Synaptic deficits at neuromuscular junctions in two mouse models of charcot-marie-tooth type 2d. *J. Neurosci.* 36, 3254–3267. doi: 10.1523/jneurosci.1762-15.2016
- Stuppia, G., Rizzo, F., Riboldi, G., Del Bo, R., Nizzardo, M., Simone, C., et al. (2015). MFN2-related neuropathies: clinical features, molecular pathogenesis and therapeutic perspectives. *J. Neurol. Sci.* 356, 7–18. doi: 10.1016/j.jns.2015.05.033
- Tradewell, M. L., Durham, H. D., Mushynski, W. E., and Gentil, B. J. (2009). Mitochondrial and axonal abnormalities precede disruption of the neurofilament network in a model of charcot-marie-tooth disease type 2E and are prevented by heat shock proteins in a mutant-specific fashion. *J. Neuropathol. Exp. Neurol.* 68, 642–652. doi: 10.1097/nen.0b013e3181a5deeb
- van Hameren, G., Campbell, G., Deck, M., Berthelot, J., Gautier, B., Quintana, P., et al. (2019). In vivo real-time dynamics of ATP and ROS production in axonal mitochondria show decoupling in mouse models of peripheral neuropathies. *Acta Neuropathol. Commun.* 7:86.
- Van Lent, J., Verstraelen, P., Asselbergh, B., Adriaenssens, E., Mateiu, L., Verbist, C., et al. (2021). Induced pluripotent stem cell-derived motor neurons of CMT type 2 patients reveal progressive mitochondrial dysfunction. *Brain* 10:awab226.
- Verhoeven, K., Claeys, K. G., Zuchner, S., Schroder, J. M., Weis, J., Ceuterick, C., et al. (2006). MFN2 mutation distribution and genotype/phenotype correlation in charcot-marie-tooth type 2. *Brain* 129, 2093–2102. doi: 10.1093/brain/awl126
- Vielhaber, S., Debska-Vielhaber, G., Peeva, V., Schoeler, S., Kudin, A. P., Minin, I., et al. (2013). Mitofusin 2 mutations affect mitochondrial function by mitochondrial DNA depletion. *Acta Neuropathol.* 125, 245–256. doi: 10.1007/s00401-012-1036-y
- Wang, Z. B., Zhang, X., and Li, X. J. (2013). Recapitulation of spinal motor neuron-specific disease phenotypes in a human cell model of spinal muscular atrophy. *Cell Res.* 23, 378–393. doi: 10.1038/cr.2012.166
- Xu, C. C., Denton, K. R., Wang, Z. B., Zhang, X., and Li, X. J. (2016). Abnormal mitochondrial transport and morphology as early pathological changes in human models of spinal muscular atrophy. *Dis. Model. Mech.* 9, 39–49.
- Yao, C. H., Wang, R., Wang, Y., Kung, C. P., Weber, J. D., and Patti, G. J. (2019). Mitochondrial fusion supports increased oxidative phosphorylation during cell proliferation. *Elife* 8:e41351.

Zuchner, S., Mersiyanova, I. V., Muglia, M., Bissar-Tadmouri, N., Rochelle, J., Dadali, E. L., et al. (2004). Mutations in the mitochondrial GTPase mitofusin 2 cause charcot-marie-tooth neuropathy type 2A. *Nat. Genet.* 36, 449–451. doi: 10.1038/ng1341

Conflict of Interest: The authors declare that the research was conducted in the absence of any commercial or financial relationships that could be construed as a potential conflict of interest.

Publisher's Note: All claims expressed in this article are solely those of the authors and do not necessarily represent those of their affiliated organizations, or those of

the publisher, the editors and the reviewers. Any product that may be evaluated in this article, or claim that may be made by its manufacturer, is not guaranteed or endorsed by the publisher.

Copyright © 2021 Mou, Dein, Chen, Jagdale and Li. This is an open-access article distributed under the terms of the Creative Commons Attribution License (CC BY). The use, distribution or reproduction in other forums is permitted, provided the original author(s) and the copyright owner(s) are credited and that the original publication in this journal is cited, in accordance with accepted academic practice. No use, distribution or reproduction is permitted which does not comply with these terms.



Bioenergetic Requirements and Spatiotemporal Profile of Nerve Growth Factor Induced PI3K-Akt Signaling Along Sensory Axons

Rajiv Sainath¹ and Gianluca Gallo^{1,2*}

¹ Shriners Hospitals Pediatric Research Center, Lewis Katz School of Medicine, Temple University, Philadelphia, PA, United States, ² Department of Neural Sciences, Lewis Katz School of Medicine, Temple University, Philadelphia, PA, United States

OPEN ACCESS

Edited by:

Dianna E. Willis,
Burke-Cornell Medical Research
Institute, United States

Reviewed by:

Lars Klimaschewski,
Innsbruck Medical University, Austria
Naoya Yamashita,
Kanagawa Institute of Technology,
Japan

*Correspondence:

Gianluca Gallo
Tue86088@temple.edu

Specialty section:

This article was submitted to
Molecular Signaling and Pathways,
a section of the journal
Frontiers in Molecular Neuroscience

Received: 16 June 2021

Accepted: 23 August 2021

Published: 24 September 2021

Citation:

Sainath R and Gallo G (2021)
Bioenergetic Requirements
and Spatiotemporal Profile of Nerve
Growth Factor Induced PI3K-Akt
Signaling Along Sensory Axons.
Front. Mol. Neurosci. 14:726331.
doi: 10.3389/fnmol.2021.726331

Nerve Growth Factor (NGF) promotes the elaboration of axonal filopodia and branches through PI3K-Akt. NGF activates the TrkA receptor resulting in an initial transient high amplitude burst of PI3K-Akt signaling followed by a maintained lower steady state, hereafter referred to as initiation and steady state phases. Akt initially undergoes phosphorylation at T308 followed by phosphorylation at S473, resulting in maximal kinase activation. We report that during the initiation phase the localization of PI3K signaling, reported by visualizing sites of PIP3 formation, and Akt signaling, reflected by Akt phosphorylation at T308, correlates with the positioning of axonal mitochondria. Mitochondrial oxidative phosphorylation but not glycolysis is required for Akt phosphorylation at T308. In contrast, the phosphorylation of Akt at S473 is not spatially associated with mitochondria and is dependent on both oxidative phosphorylation and glycolysis. Under NGF steady state conditions, maintenance of phosphorylation at T308 shows dual dependence on oxidative phosphorylation and glycolysis. Phosphorylation at S473 is more dependent on glycolysis but also requires oxidative phosphorylation for maintenance over longer time periods. The data indicate that NGF induced PI3K-Akt signaling along axons is preferentially initiated at sites containing mitochondria, in a manner dependent on oxidative phosphorylation. Steady state signaling is discussed in the context of combined contributions by mitochondria and the possibility of glycolysis occurring in association with endocytosed signalosomes.

Keywords: axon, PI3K, Akt, mitochondria, glycolysis

INTRODUCTION

Nerve growth factor (NGF) regulates multiple aspects of the development of sensory neurons including morphology. NGF rapidly promotes the elaboration of the growth cone and induces the formation of axon collateral branches through the promotion of actin filament polymerization and microtubule tip dynamics (Gallo and Letourneau, 2000; Niewiadomska et al., 2011; Pacheco and Gallo, 2016; Armijo-Weingart and Gallo, 2017). NGF elicits its morphogenetic effects through the activation of the TrkA receptor that in turn activates multiple downstream signaling pathways (Huang and Reichardt, 2003; Reichardt, 2006). The PI3K-Akt signaling axis, downstream of

TrkA, mediates the NGF-induced formation of axon collateral branches through multiple cellular effects required for the initiation of axon branching. PI3K-Akt signaling is required for the promotion of axonal actin filament dynamics underlying the emergence of axonal filopodia, the activation of intra-axonal protein synthesis of actin regulatory proteins and the fission of axonal mitochondria (Ketschek and Gallo, 2010; Spillane et al., 2012, 2013; Armijo-Weingart et al., 2019). PI3K signaling also mediates the effects of NGF on microtubule growth and the hyperpolarization of mitochondria (Zhou et al., 2004; Verburg and Hollenbeck, 2008). The positioning of axonal mitochondria along axons determines sites where axon branches can form (Courchet et al., 2013; Spillane et al., 2013; Tao et al., 2014; Sainath et al., 2017a; Wong et al., 2017; Lewis et al., 2018; Smith and Gallo, 2018; Rangaraju et al., 2019) and in the context of NGF-induced branching also sites of preferential intra-axonal protein synthesis of required actin regulatory proteins (Spillane et al., 2013).

ATP is generated through two main sources; oxidative phosphorylation in the mitochondrion and glycolysis. Mitochondrial oxidative phosphorylation has been shown to be a required component of both regenerative and developmental axon extension (Patrón and Zinsmaier, 2016; Zhou et al., 2016; Sainath et al., 2017b; Sheng, 2017; Smith and Gallo, 2018). The targeting of mitochondria to growth cones promotes regeneration and the evacuation of mitochondria from growth cones is promoted by axon inhibitory signals (Morris and Hollenbeck, 1993; Han et al., 2016; Sainath et al., 2017b). Signals that promote axon extension and branching increase mitochondrial function and those that inhibit branching impair mitochondrial function (Verburg and Hollenbeck, 2008; Pacelli et al., 2015; Sainath et al., 2017a). Mitochondrial oxidative phosphorylation also regulates presynaptic transmission, at least in subsets of synapses wherein mitochondria are targeted. The role of glycolysis in axonal biology has received less attention than oxidative phosphorylation but it has been shown to regulate aspects of synaptic physiology (Ashrafi and Ryan, 2017). In developing central and peripheral nervous system neurons the contribution of glycolysis to net ATP levels is greatest during early embryogenesis and then wanes as oxidative phosphorylation becomes a more prominent source (reviewed in Gallo, 2020). Glycolytic enzymes are found throughout the axons of developing sensory neurons and glycolysis contributes to sensory axon extension and growth cone dynamics (Ketschek et al., 2021). Glycolytic enzymes associate with fast transport vesicles and “on board” glycolysis powers the transport of the vesicles while mitochondria transport depends on oxidative phosphorylation independent of glycolysis (Spillane et al., 2013; Zala et al., 2013; Hinckelmann et al., 2016). The contributions of mitochondrial oxidative phosphorylation and glycolysis in signaling by extracellular factors have not been addressed.

NGF-TrkA signaling involves extensive phosphorylation, endocytosis of receptors and transport of the ensuing signaling endosomes (signalosomes) (Huang and Reichardt, 2003; Reichardt, 2006; Marlin and Li, 2015), all processes requiring energetic input. Akt signaling has been reported to exhibit differential spatial and temporal profiles and subcellular domains of activation in response to epidermal growth factor

in non-neuronal cells (Miura et al., 2014). The subcellular localization of PI3K-Akt signaling and bioenergetic sources utilized during TrkA signaling are not known. In this manuscript we present evidence of different spatio-temporal contributions of mitochondrial oxidative phosphorylation and glycolysis in the initiation and maintenance of NGF-TrkA signaling along embryonic sensory axons focusing on the phosphorylation of the PI3K-Akt signaling axis.

MATERIALS AND METHODS

Neuron Culturing

Fertilized chicken eggs were obtained from Charles River Laboratories (#10100326). Dissociated primary embryonic day 7 chicken embryo neurons were prepared and cultured as previously detailed (Lelkes et al., 2005). Briefly, culturing was performed on coverslips coated with laminin (25 μ g/mL: Life Technologies, #23017-015) in F12H medium. Unless otherwise noted, F12H medium (Thermo Fisher Scientific, # 11765047) was supplemented with 20 ng/mL NGF (R&D Systems, #256-GF-100; see Lelkes et al., 2005 for complete supplement formulation). Experiments involving acute NGF treatment (20 ng/mL) were performed using cultures raised in the absence of NGF for 24 h, see the Results for a rationale and description of the experimental approach. For experiment involving inhibition of glycolysis, at the time of experimental treatment the medium was switched to either control DMEM medium lacking glucose (Gibco, #11966025) and supplemented with 10 mM D-glucose (Sigma, #G7021), 10 mM Hepes (Fisher BioReagents, #BP299-100), 1% PSF (penicillin-streptomycin mixture; Thermo Fisher Scientific, #BW17745E) and 1 mM NaPyruvate (Gibco, #11360-070) or GIM (Glycolysis Inhibition Medium) prepared using the same formulation but replacing D-glucose with 10 mM 2-deoxyglucose (Sigma, #D8375). Antimycin-A was Sigma (#A8674). Neurons were cultured for 24 h prior to use in experiments.

Immunocytochemistry

Dissociated neurons were fixed with 4% paraformaldehyde (Electron Microscopy Sciences Cat# 15710) and 5% sucrose (Thermo Fisher Scientific Cat# S5-500) in PBS for 15 min at room temperature and blocked for 30 min with 10% Goat Serum (Sigma Cat# G9023) in PBS with 0.1% of Triton X-100 (Sigma Cat# 9002-93-1) (GST). Samples were incubated for 1 h with primary antibody against Phospho-Akt (Ser473) (Cell Signaling Technology Cat# 4060, RRID:AB_2315049), Phospho-Akt (Thr308) (Cell Signaling Technology Cat# 9275, RRID:AB_329828) and pan-AKT antibody (Abcam Cat# ab8805, RRID:AB_306791) diluted in GST (1:200) at room temperature and washed with PBS. Next, fluorescently labeled secondary antibody Anti-Rabbit IgG (whole molecule)-TRITC (Sigma-Aldrich Cat# T6778, RRID:AB_261740) and phalloidin Alexa 488 (1:20, Invitrogen Cat# A12379), were applied for an additional hour, at room temperature. To reveal axon morphology, in some experiments, axons were labeled with anti- α -tubulin conjugated to FITC (DM1A; 1:100, Sigma #F2168, RRID:AB_476967). After secondary antibody incubation, samples were washed with PBS

and deionized water and mounted with Vectashield mounting media (Vector Cat# H-1000). Examples of TrkA staining shown in **Figure 1A** are from extant data sets initially published in Ketschek and Gallo (2010), and the relevant methods and antibody information are contained therein. The images shown here were not previously published.

Plasmids and Transfection

The plasmids expressing PH-GFP and Mitochondrially targeted DsRed were prepared and used as described in Ketschek and Gallo (2010) and Spillane et al. (2013), respectively. Briefly, following dissociation the neuron suspension was transferred to a nucleofector cuvette containing 10 μ g of Plasmid DNA, and electroporated using an Amaxa Nucleofector (program G-13; Lonza) and chicken transfection solution (Lonza). The electroporated neuronal suspension was then immediately transferred to a tube containing culturing media as described above prior to plating.

Imaging

All imaging was performed using a Zeiss 200 M microscope equipped with an Orca-ER camera (Hamamatsu) in series with a PC workstation running Zeiss Axiovision software for image acquisition and analysis. Imaging of PH-GFP and mitochondrially targeted DsRed was performed as previously described in Ketschek and Gallo (2010) and Spillane et al. (2013), respectively. For live imaging, cultures were placed on a heated microscope stage (Zeiss temperable insert P with objective heater) for 10 min at a constant 39°C before and during imaging. Imaging was performed using a Zeiss Pan-Neofluar 100 X (1.3 numerical aperture). Time lapse imaging of PH-GFP and mitochondrially targeted DsRed were performed at 100x using 2 \times 2 binning, 5 s inter-frame intervals, and minimal light (100 W mercury lamp). Still images of immunocytochemical staining were similarly obtained using the 100 x objective and phase contrast to visualize the axons. Due to the permeabilization required for immunocytochemical processing the phase contrast images are subpar but are only used to note the location of the axon shaft and not used to obtain data. In all cases, camera acquisition parameters were set so as not to obtain pixel saturation.

Quantification of Akt Puncta and GFP-PH Microdomains

Puncta of phosphorylated Akt were manually counted along the distal 50 μ m of axons excluding the growth cone. **Supplementary Figure 1** shows an example and provides details of the line scan analysis used to determine puncta and their intensities. GFP-PH microdomains were analyzed as described in Ketschek and Gallo (2010) and follow the protocol for the analysis of axonal actin patches (Loudon et al., 2006) which show similar dynamics to PH-GFP microdomains (Ketschek and Gallo, 2010). The formation of a PIP3 microdomain was scored when the PH-GFP signal locally increased above a threshold of greater than 20% of the average cytoplasmic baseline signal wherein no local peaks were detected by line scan analysis, in the same way as shown for pAkt puncta in **Supplementary Figure 1**. The formation of a new

microdomain in the same location as a prior one was only scored when the local intensity of the initial rise in the PH-GFP signal fell back to below 20% of the average cytoplasmic baseline signal for at least one frame.

Statistical Analysis and Study Design

All data was analyzed using InStat software (GraphPad Software Inc.). Determination of the normalcy of data sets was performed using the Kolmogorov and Smirnov test. Normal data sets were analyzed using the Welch *t*-test for independent groups or the paired *t*-test for before-after treatment experimental designs. If non-normal data sets were present then non-parametric analysis was used (Mann-Whitney test). For multiple comparison tests within experimental designs parametric Bonferroni or non-parametric Dunn's *post hoc* tests were used according to the normalcy of the data sets. One or two tailed *p*-values are reported based on whether the hypothesis predicted the directionality of the expected difference in mean or median, respectively. Graphs were generated using Prism (GraphPad Software Inc.). For presentation purposes, normally distributed data sets are shown using the mean and SEM and non-normally distributed data sets are shown as individual data points with the median noted.

All immunocytochemical data sets were acquired from at least triplicate cultures generated from ganglia harvested from multiple chicken embryos. All immunocytochemical samples within an experiment (control and experimental groups) were processed in parallel and imaged on the same day using the exact same acquisition parameters. For live imaging experiments using a before-after NGF treatment paradigm, each data point was obtained from a single neuron in a single culture. The full data set is thus representative of multiple cultures from multiple days.

RESULTS

NGF-Induced PI3K Signaling Is Most Pronounced in Axon Segments Populated by Mitochondria

We have previously detailed that NGF induces the formation of localized actin filament patches that serve as precursors to the emergence of filopodia, and that actin patch formation is dependent on PI3K-Akt signaling and the sites of formation of actin patches colocalize with microdomains of phosphatidylinositol (3,4,5)-trisphosphate (PIP3) formation, the product of PI3K activity (Ketschek and Gallo, 2010). Sites of NGF-induced axonal actin patch and filopodia formation strongly correlate with the positioning of mitochondria along axons (Ketschek and Gallo, 2010; Spillane et al., 2013; Armijo-Weingart et al., 2019) and mitochondria respiration is required for actin patch formation and dynamics (Ketschek and Gallo, 2010; Sainath et al., 2017a). Therefore, we sought to determine if NGF-induced PIP3 microdomains along axons similarly correlate with sites populated by axonal mitochondria. To track PIP3 microdomain formation along axons we expressed the PIP3 binding pleckstrin homology (PH) domain of Akt tagged with GFP (Kontos et al., 1998) as in our prior work

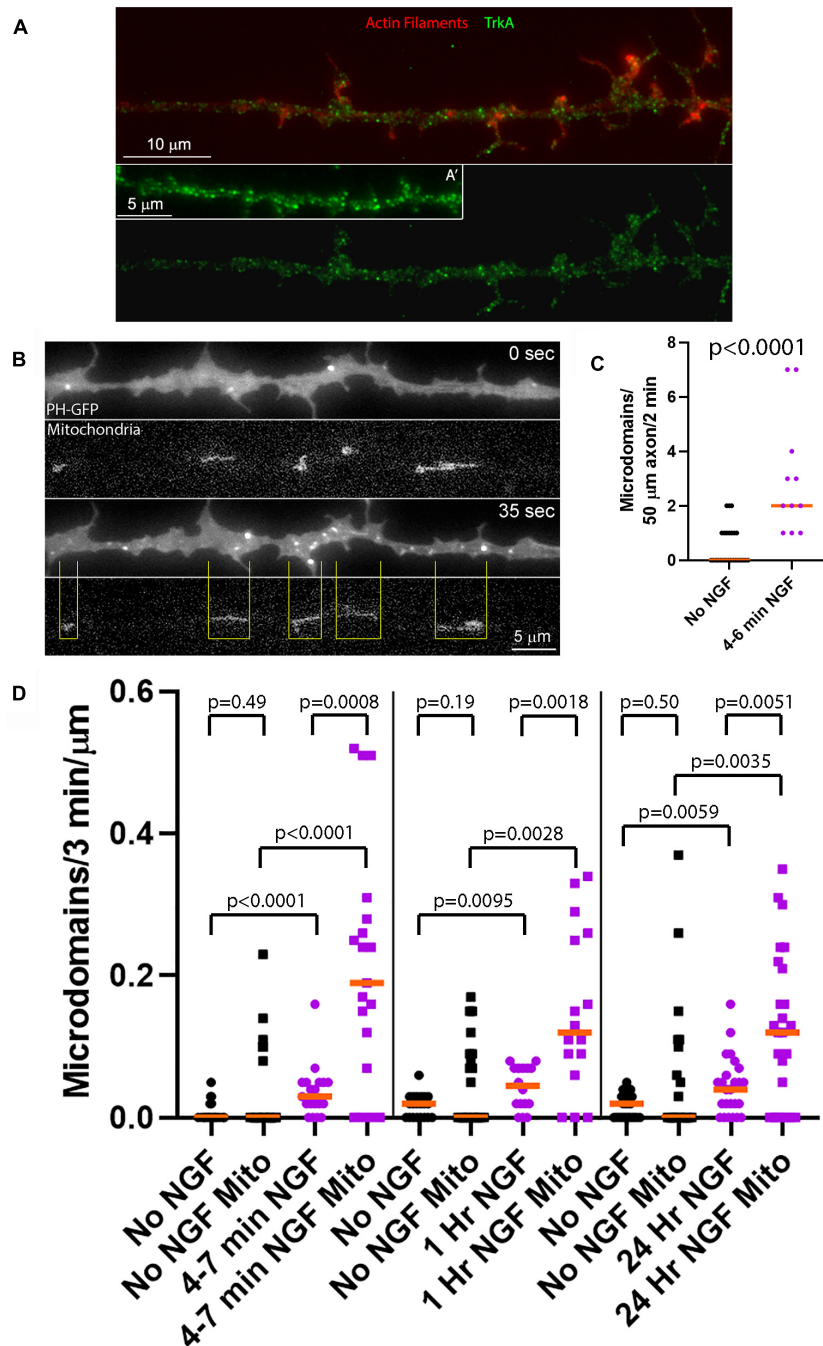


FIGURE 1 | NGF preferentially increases the rate of formation of PIP3 microdomains in axon segments populated by mitochondria. **(A)** Examples of the distribution of the TrkA receptor in the membranes of sensory axons as determined by immunostaining with an antibody to the extracellular domain of TrkA under non-permeabilized conditions as in Gallo et al. (1997) and Ketschek and Gallo (2010). **(A')** shows an example of an additional axon. Actin filaments were visualized using phalloidin. **(B)** Example of an NGF treated axon (4–7 min) expressing PH-GFP and with mitochondria labeled using mitochondrially targeted DsRed. At 0 s, representative of 4 min after NGF treatment, a few microdomains are visible as reflected by localized accumulation of PH-GFP. At 35 s a burst of microdomain formation has occurred. The yellow lines denote the positioning of mitochondria relative to the microdomains and define axon segments populated by mitochondria. Note that the majority of microdomains are formed in axon segments populated by mitochondria. **(C)** Quantification of the rate of microdomain formation per unit length/unit time of axon at 4–6 min after NGF treatment. Mann-Whitney test. **(D)** Analysis of the rate of microdomain formation in axon segments populated by mitochondria (Mito) and those lacking mitochondria as a function of time after NGF treatment. For each time point after NGF treatment (4–7 min, 1 and 24 h) time matched no NGF treatment control groups are shown. The rate of microdomain formation is normalized to the unit length of micron as mitochondria differ in length and the segments not populated by mitochondria similarly vary in length. The top row of p -values (shorter brackets) report on within NGF treatment group comparing axon segments populated by mitochondria to those that did not. The rest of the p -values report on comparisons within axon segments populated by mitochondria or not and between NGF treatment conditions. Mann-Whitney tests throughout.

(PH-GFP; Ketschek and Gallo, 2010). We acknowledge that PI3K activity results in the generation of PIP3 that following dephosphorylation by polyphosphate 5-phosphatases results in the formation of PtdIns (3,4)P₂ (Eramo and Mitchell, 2016) and both lipids are bound by the PH-domain of Akt (Lemmon et al., 2002). In the following text, we, however, use the terminology of PIP3 microdomains as in our prior work (Ketschek and Gallo, 2010) to refer to initial step in PI3K lipid phosphorylation based signaling. We have previously shown that pharmacological inhibition of PI3K suppresses detection of PIP3 microdomains reported by PH-GFP (Ketschek and Gallo, 2010). The term PIP3 microdomains thus refers to sites of PI3K activity.

In order to study the effects of acute treatment with NGF on a population of neurons responsive to NGF but naïve to NGF treatment, we cultured embryonic day 7 chicken embryo sensory neurons in the absence of NGF for 24 h on laminin coated substrata. Acute treatment with NGF means that cultures were raised for 24 h in no NGF conditions prior to treatment with NGF for the specified time period. This is a culturing model system wherein only the NGF responsive TrkA expressing population of neurons in sensory ganglia is able to survive and extend axons (Guan et al., 2003). We have used this experimental model system throughout our prior work addressing the effects of acute NGF treatment (Ketschek and Gallo, 2010; Spillane et al., 2012, 2013; Silver et al., 2014) and previously shown that NGF induces Akt phosphorylation and downstream phosphorylation of S6 in axons (Silver et al., 2014). Neurotrophins induce strong activation of Trk receptors and PI3K activity by 2–5 min of treatment (Kaplan et al., 1991; Soltoff et al., 1992). As previously described, TrkA receptors in the plasma membrane, detected with an antibody to the extracellular domain of TrkA in non-permeabilized samples, are widely distributed along the axonal population used in this study appearing as puncta all along the length of the axon (Figure 1A; Gallo et al., 1997; Ketschek and Gallo, 2010). At 4–6 min of NGF treatment increased the rate of PIP3 microdomain formation per unit length of distal axon (Figures 1B,C). Analysis of PIP3 microdomains along the axons of neurons with fluorescently labeled mitochondria showed that at 4–7 min after NGF treatment there was an increase in the rate of formation of PIP3 microdomains within axon segments populated by mitochondria, and also those not containing mitochondria, relative to axons not treated with NGF (Figures 1B,D). Axon segments populated by mitochondria were defined as the stretch of the axon encompassed between the distal and proximal ends of mitochondria (Figure 1B). However, after NGF treatment axon segments populated by mitochondria generated microdomains at median rates approximately 530% greater than those lacking mitochondria. Thus, these observations indicate that axon segments populated by mitochondria exhibit higher levels of PI3K signaling during the initial response to NGF treatment than those that do not contain mitochondria.

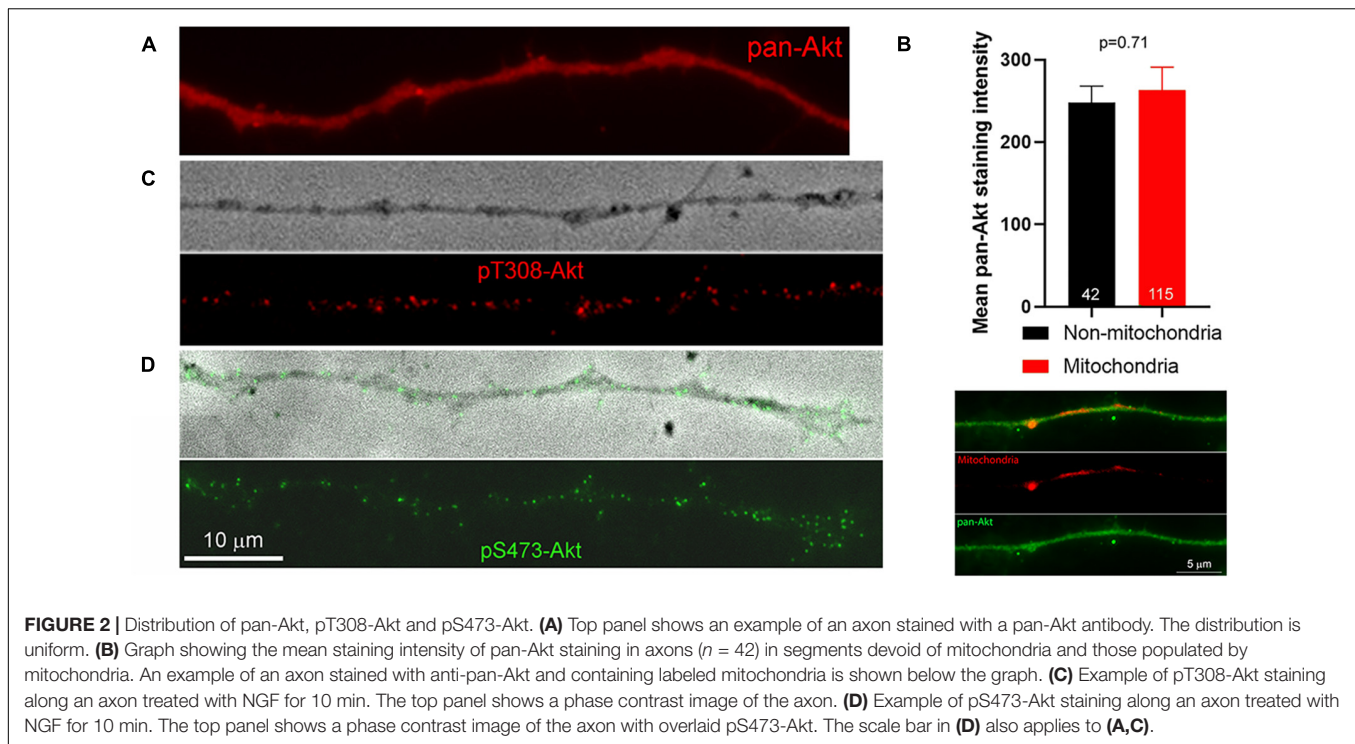
We next addressed PIP3 microdomain formation at 1 and 24 h after treatment with NGF, reflective of the later stages of NGF signaling when the amplitude of signaling has decreased to a lower level than during the initial phase following acute treatment with NGF but remaining above baseline no NGF treatment levels (Kaplan et al., 1991; Soltoff et al., 1992). As observed during the

initial phase of signaling, in NGF treatment conditions segments of axons populated by mitochondria exhibited higher rates of PIP3 microdomain formation than those lacking mitochondria at both of these delayed time points (Figure 1D). Segments of axons not populated by mitochondria also exhibited increased rates of PIP3 microdomain formation (Figure 1D). At 1 and 24 h of NGF treatment, starting at 24 h of culturing in no NGF, the median rates of microdomain formation in axon segments populated by mitochondria relative to those not populated by mitochondria were elevated by 167 and 200%, respectively (Figure 1D), in contrast to the initial 530% difference at 4–7 min of treatment and consistent with decreased NGF signaling at these later stages. The data indicate that NGF signaling at later stages continues to elicit higher net levels of PI3K activity resulting in increased rates of PIP3 microdomain formation and that the effect of NGF is most pronounced at sites populated by mitochondria. In the absence of NGF signaling there was no difference in the median rate of microdomain formation as a function of mitochondria positioning (Figure 1D), although at all-time points axonal segments populated by mitochondria tended to exhibit maximal values in a range greater than those not containing mitochondria.

Phosphorylation of Akt at T308 but Not S473 Localizes With Axon Segments Populated by Mitochondria

PIP3 generated through the activity of PI3K results in the targeting of Akt to the membrane through the binding of the PH domain of Akt to PIP3, and subsequent phosphorylation of Akt at T308 and S473 by PDK1 and mTORC2, respectively (Fayard et al., 2010). Full activation of Akt kinase activity is accomplished by di-phosphorylation at both residues, although Akt phosphorylated only at T308 exhibits some enhancement of kinase activity. As there are no biosensors for tracking the phosphorylation state of Akt, we used immunocytochemistry to gain insights into the spatio-temporal profile of Akt activation along axons in response to NGF (as previously used to measure increases and decreases in net levels of phosphorylated Akt along axons, Silver et al., 2014). We first considered the distribution of Akt, independent of its phosphorylation, in axons. Akt was uniformly distributed along the axons of neurons cultured in NGF and we did not observe any preferential association of Akt in axon segments populated by mitochondria (Figures 2A,B). The staining pattern for both pT308-Akt and pS473-Akt along the axons of neurons cultured in NGF was punctate, indicative of localized sites of phosphorylation (Figures 2C,D).

The localization and degree of pT308-Akt and pS473-Akt labeling in the axons of neurons expressing mitochondrially targeted DsRed (as in Spillane et al., 2013) was then determined during the first 14 min of NGF-induced signaling. The relative levels of pT308-Akt signaling, reflected in the density of puncta per unit length of axon, increased by 2 min of NGF treatment and reached a peak within 6 min of treatment (Figure 3A). Analysis of the staining intensity of puncta of pT308-Akt did not reveal any difference after NGF treatment (Supplementary Figure 1). Hereafter, the density of puncta per micron of axon of



phosphorylated Akt is thus used as the main metric for tracking the levels and position of phosphorylated pT308-Akt.

Axon segments populated by mitochondria accounted for the majority of the increase in density of pT308-Akt puncta during the initial 14 min of signaling (**Figures 3B,C** and **Supplementary Figure 2A**) and the density of pT308-Akt puncta in axon segments populated by mitochondria was highest at 6 min after NGF (**Figure 3B** and **Supplementary Figure 2A**). Considering that in these sensory axons mitochondria occupy approximately 15% of the area (Ketschek and Gallo, 2010), the localization of 60–80% of pT308-Akt puncta in axon segments populated by mitochondria represents a strong localization to these sub-axonal domains (**Figure 3C**). Both axon segments populated by mitochondria or devoid of mitochondria exhibited an increase in the density of pT308-Akt puncta as soon as 2 min after NGF treatment (**Figures 3D,E**), but the peak in signaling observed in axon segments populated by mitochondria was not evident in segments not containing mitochondria (**Figure 3E**). The density of pT308-Akt puncta was also elevated in axon segments populated by mitochondria in the absence of NGF treatment (**Figure 3F**), indicating that even in the absence of NGF sites populated by mitochondria exhibit elevated levels of pT308-Akt. In no NGF conditions approximately 23–35% of pT308-Akt puncta colocalized with mitochondria at all-time points (**Figure 3C**), closer to but greater than the percentage of area covered by mitochondria (15%).

NGF treatment increased the density of pS473-Akt puncta within axons (**Figures 2D, 3G** show an example of axonal pS473-Akt staining). The increase in the density of pS473-Akt puncta became detectable at 8 min after NGF treatment, following the peak in pT308-Akt levels (**Figure 3A**). Analysis of the staining

intensity of puncta of pS473-Akt did not reveal any difference after NGF treatment (**Supplementary Figure 1**), and thus as with pT308-Akt the density of pS473-Akt puncta was used as the main metric throughout. The density of pS473-Akt puncta following NGF treatment did not exhibit differences between axon segments populated by mitochondria and those not containing mitochondria (**Figure 3H**). Similarly, in the absence of NGF treatment there was no difference in the density of pS473-Akt puncta in axon segments populated by mitochondria and those not containing mitochondria (**Figure 3H**). The data thus indicate that phosphorylation of Akt at T308 in axons commences as soon as 2 min after NGF treatment and that axon segments populated by mitochondria experience higher levels of T308 phosphorylation. In contrast, the subsequent phosphorylation at S473, following the peak in T308 phosphorylation, does not correlate with mitochondria positioning along axons.

Oxidative Phosphorylation (OxP) but Not Glycolysis Is Required for the Initial Phosphorylation of Akt at T308

In embryonic neurons both OxP and glycolysis contribute to ATP levels with relative contributions varying between neurons (reviewed in Gallo, 2020). In the population of neurons used in the current study, measurement of the ATP/ADP ratio showed that OxP [inhibited using antimycin-A (AA)] and glycolysis (inhibited by exchanging to medium containing no glucose and supplemented with 2-deoxyglucose to inhibit glycolysis and with pyruvate to maintain mitochondrial respiratory function, Glycolysis Inhibition Medium; GIM) both contribute approximately equally to the ATP/ADP ratio and

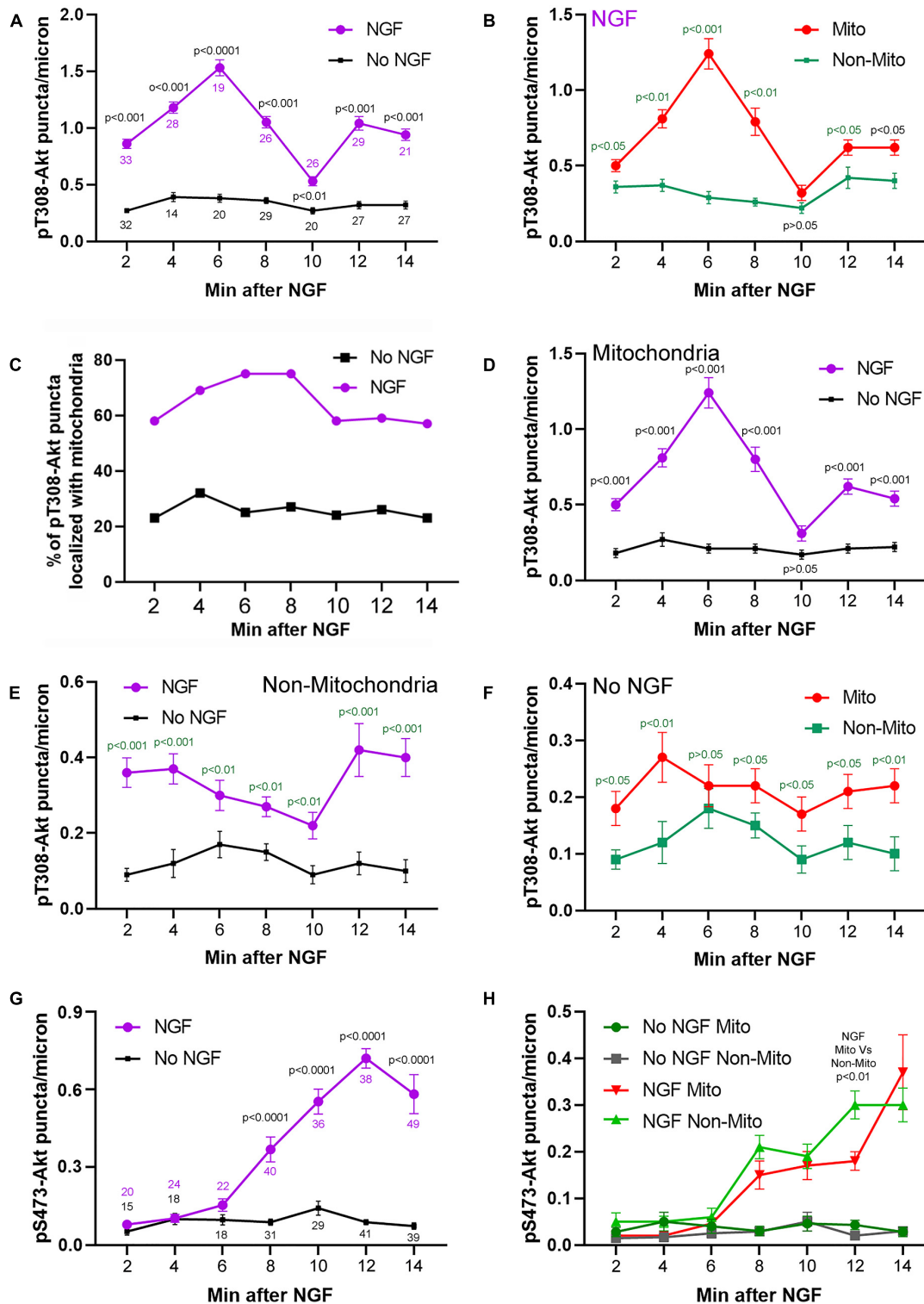


FIGURE 3 | Time course and relationship of pT308-Akt and pS473-Akt to mitochondria positioning during the early phase (2–14 min) of NGF treatment. **(A)** Levels of pT308-Akt along the distal 50 mm of axon as a function of time after treatment with NGF or vehicle (no NGF). Throughout the figure data are expressed as the number of puncta/micron. Sample sizes (n = number of axons) at each time point are shown color coded for the respective group. **(B–F)** Provide further analysis of this data set. **(B)** Density of pT308-Akt puncta after treatment with NGF in axon segments populated by mitochondria (Mito) and those not containing mitochondria (Non-Mito). These data are extracted from the NGF treatment group in **(A)**. **(C)** Percent of pT308-Akt puncta that localized with mitochondria as a function of time (Continued)

FIGURE 3 | (Continued)

after NGF treatment and no NGF conditions. These data are extracted from the NGF treatment group in **(A)**. **(D)** Comparison of the density of puncta of pT308-Akt in axon segments populated by mitochondria between NGF and no NGF treatment conditions. These data are extracted from the groups in **(A)**. **(E)** Comparison of the density puncta of pT308-Akt in axons segments not containing mitochondria as a function of time after NGF and no NGF treatment conditions. These data are extracted from the groups in **(A)**. **(F)** Comparison of the density of pT308-Akt puncta in the no NGF treatment condition in axon segments populated by mitochondria and those not containing mitochondria. These data are extracted from the no NGF treatment group in **(A)**. **(G)** Analysis of the levels of pS473-Akt in axons, as in **(A)**, as a function of time after treatment with NGF or no NGF. Sample sizes (n = number of axons) at each time point are shown color coded for the respective group. **(H)** Analysis of the density of puncta of pS473-Akt in axon segments populated by mitochondria and those not containing mitochondria in both the NGF and no NGF treatment conditions. These data are extracted from the NGF treatment group in **(G)**. Throughout the figure, time matched *post hoc* comparisons are shown.

inhibition of both has additive effects (Ketschek et al., 2021). While mitochondria occupy specific sites along the axon glycolytic enzymes show relatively even distributions within axons (**Supplementary Figure 3**).

The higher density of T308-Akt puncta associated with mitochondria led us to test the hypothesis that mitochondrial OxP might be required for this initial step of Akt signaling. Inhibition of OxP using AA (10 min pretreatment prior to NGF) blocked the NGF induced increase in the density of pT308-Akt puncta within distal axons (**Figures 4A,B**). Similarly, AA also blocked the NGF-induced increase in the density of pS473-Akt puncta (**Figure 4B** and **Supplementary Figure 4A**). Analysis of the spatial relationship of pT308-Akt puncta in relation to mitochondria showed that at 15 min of NGF treatment axon segments populated by mitochondria exhibited approximately 60% greater density of pT308-Akt puncta than those not containing mitochondria (**Supplementary Figures 5A,C**), consistent with the differences noted at 10–12 min of NGF treatment (**Figure 3B**). Consideration of the effects of AA treatment on the density of pT308-Akt puncta as a function of mitochondria positioning along axons showed that AA treatment suppressed the levels of pT308-Akt similarly in axon segments populated by or devoid of mitochondria (**Supplementary Figures 5B,C**).

In contrast, inhibition of glycolysis, using GIM exchange 15 min prior to NGF treatment did not block the NGF-induced increase in the density of pT308-Akt puncta along axons (**Figure 4C** and **Supplementary Figure 4B**), although GIM suppresses the ATP/ADP ratio by 15 min after treatment (Ketschek et al., 2021). GIM treatment alone decreased the baseline density of pT308-Akt puncta in the absence of NGF treatment. However, the magnitude of the increase in the density of pT308-Akt puncta after NGF treatment in GIM relative to the GIM treatment alone baseline was comparable to that in control medium (**Figure 4C**), indicating the magnitude of the response to NGF treatment in GIM does not differ from that in control medium, in sharp contrast to treatment with AA (**Figure 4A**). Similar to the treatment of GIM on the density of pT308-Akt puncta in the absence of NGF, GIM treatment decreased the density of pS473-Akt puncta along axons (**Figure 4D**). In contrast to pT308-Akt, GIM prevented the NGF-induced increase in the density of pS473-Akt puncta after 15 min of treatment (**Figure 4D**), a time point when the density of pS473-Akt puncta in response to NGF treatment have risen considerably (**Figure 3G**). The data thus indicate that the increases in phosphorylation of Akt the T308 and S473 induced by acute treatment with NGF

require OxP, but S473 and not T308 phosphorylation also requires glycolysis.

Bioenergetic Requirements of Steady State NGF Phosphorylation of Akt

After an initial high amplitude signaling period the levels of PI3K and Akt activity decline to a maintained steady state while in the continued presence of NGF (Kaplan et al., 1991; Soltoff et al., 1992). Here the term steady state refers to neurons cultured in the continuous presence of NGF from the time of culturing and used in experiments at 24 h of culturing. To assess the contribution of OxP to the maintenance of steady state levels of T308-Akt signaling we determined the effects of a 30 and 60 min treatment with AA on neurons cultured for 24 h in NGF. A 30 min treatment with AA decreased the density of pT308-Akt puncta along axons by approximately 50% (**Figure 5A** and **Supplementary Figure 6A**). The effect of AA treatment on the density of pT308-Akt puncta along axons was evident by 10 min of AA treatment and AA resulted in a greater suppression of the density of pT308-Akt puncta than the absence of NGF treatment (**Figure 5B**). Unexpectedly, by 60 min the density of pT308-Akt puncta had returned to baseline levels (**Figure 5A** and **Supplementary Figure 6A**). Inhibition of glycolysis by exchange of the medium with GIM resulted in a decrease in the density of pT308-Akt puncta along axons at both 30 and 60 min of treatment (**Figure 5C** and **Supplementary Figure 6B**). To determine if the return to baseline at 60 min of treatment with AA might be due to compensation through glycolysis we treated with GIM in the context of the same experimental design as in **Figure 5A**. Co-treatment with AA and GIM blocked the return of the density of pT308-Akt puncta to baseline levels following a 60 min AA treatment (**Figure 5D** and **Supplementary Figure 6B**). In GIM and AA treated samples measurements of the density of pT308-Akt puncta were lower than the GIM treatment condition alone (**Figure 5D** and **Supplementary Figure 6B**).

Inhibition of OxP using a 30 min treatment with AA did not alter the density of pS473-Akt puncta in axons (**Figure 5E** and **Supplementary Figure 7A**). However, a 60 min treatment resulted in an approximately 67% decrease (**Figure 5E** and **Supplementary Figure 7A**). Treatment with GIM for 30 or 60 min both decreased the density of pS473-Akt puncta along axons by approximately 75% (**Figure 5F** and **Supplementary Figure 7B**). These data indicate that the maintenance of pS473-Akt signaling in axons is more dependent on glycolytic function than OxP, but that both contribute to the maintenance of pS473-Akt signaling over a period of 1 h.

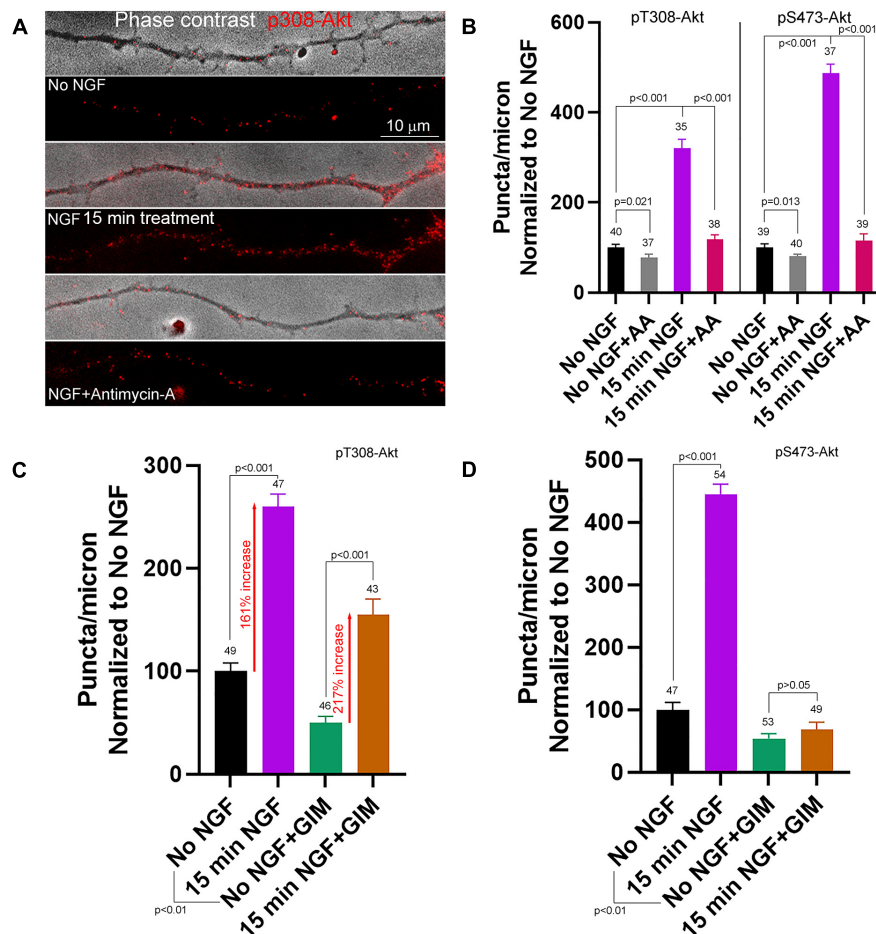


FIGURE 4 | Contributions of oxidative phosphorylation and glycolysis to the early phase of NGF driven pT308-Akt and pS473-Akt phosphorylation. **(A)** Examples of pT308-Akt staining in axons (shown in overlay with phase contrast images) with 15 min treatments of no NGF, NGF or NGF with antimycin-A (AA). **(B)** Quantification of the density of pT308-Akt and pS473-Akt puncta following treatment with AA under no NGF and NGF 15 min treatment conditions. **(C)** Effects of inhibition of glycolysis using glycolysis inhibition medium (GIM) or control medium exchange on the density pT308-Akt puncta. GIM decreased the baseline density of pT308-Akt puncta in the absence of NGF, but NGF treatment elevated the density to a similar fold increase with both GIM and control medium (percent increase relative to the corresponding baseline is denoted). **(D)** GIM treatment alone decreased the baseline density of pS473-Akt puncta in no NGF treatment conditions and blocked the NGF induced increase in the density of pS473-Akt puncta.

DISCUSSION

The relative contributions of mitochondrial OxP and glycolysis to the bioenergetics of axonal NGF signaling have not been previously addressed. In the experimental model system used in this study, mitochondria in distal sensory axons occupy specific domains and cover approximately 15% of the length of the axon (Ketschek and Gallo, 2010) while glycolytic enzymes are present in a mostly uniform distribution throughout axons (Supplementary Figure 3; Ketschek et al., 2021). We have previously reported evidence for local roles of mitochondrial OxP in regulating aspects axonal biology. Axonal segments populated by mitochondria are preferential sites for intra-axonal protein synthesis (Spillane et al., 2013; Sainath et al., 2017a) and also for the formation of axonal actin filament patches and the filopodia that emerge from these patches (Ketschek and Gallo, 2010; Sainath et al., 2017a), and mitochondrial OxP is required for

mitochondria associated protein synthesis, actin patch/filopodia formation and the emergence of axon branches in response to NGF treatment (Ketschek and Gallo, 2010; Spillane et al., 2013; Sainath et al., 2017a). The data presented in this report add to these prior observations by showing that sites of NGF induced PI3K signaling (here termed PIP3 microdomains as in Ketschek and Gallo, 2010) and the subsequent downstream phosphorylation of Akt at T308, during the initial high amplitude signaling induced by NGF, are also preferentially associated with axon segments populated by mitochondria. Mitochondrial OxP, but not glycolysis, is required for the initiation of pT308-Akt signaling. In contrast to sites of PI3K activation and pT308-Akt, the activation of Akt through S473 phosphorylation was not found to be associated with mitochondria. The data also indicate that the net increase in Akt activity induced by NGF is due to an increase in localized sites of Akt phosphorylation, presenting as puncta in immunocytochemistry, without effects on the amount

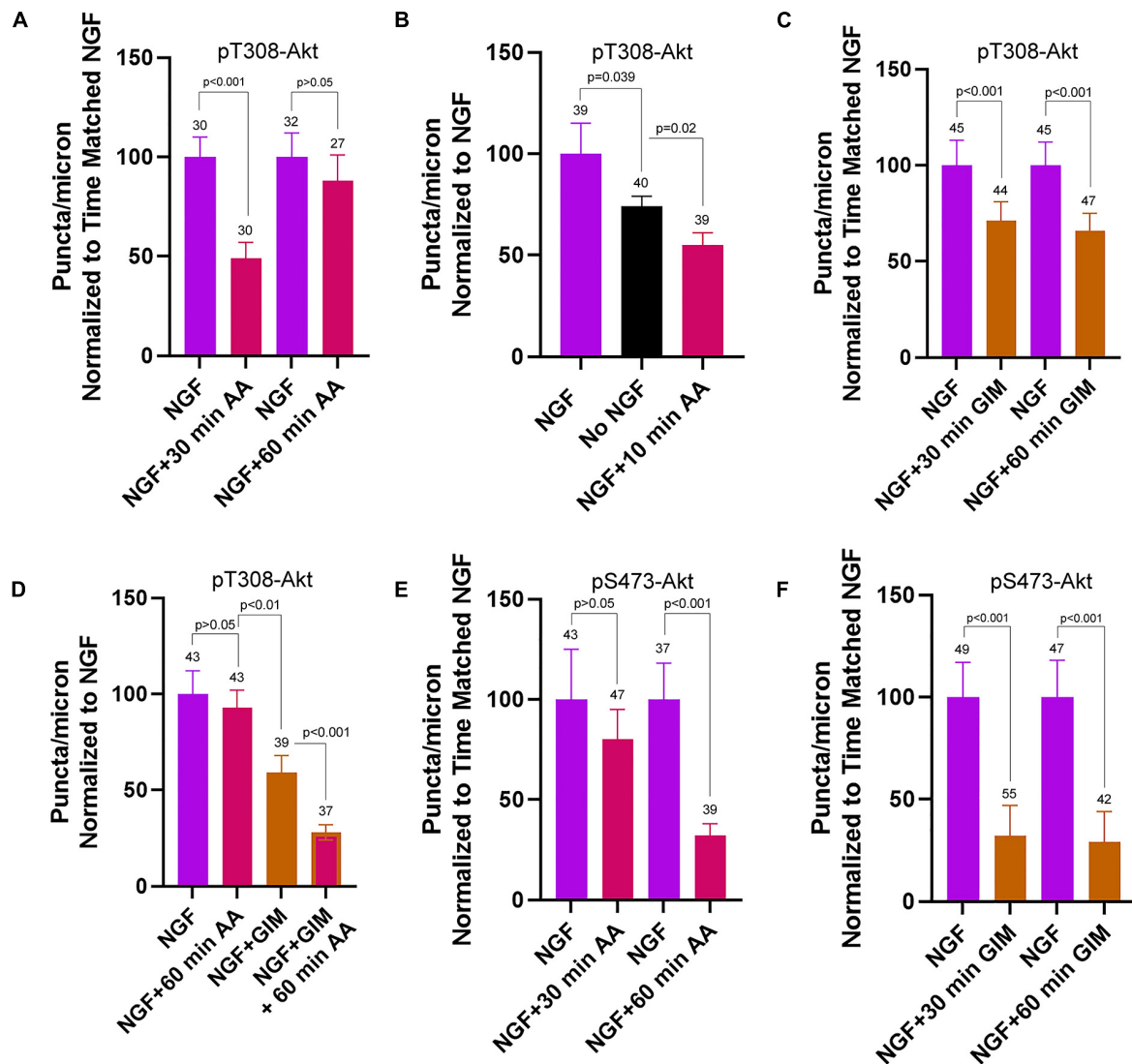


FIGURE 5 | Contributions of oxidative phosphorylation and glycolysis to steady state NGF (24 h treatment) driven pT308-Akt and pS473-Akt phosphorylation. **(A)** Effects of a 30 and 60 min treatment with antimycin-A on the density of pT308-Akt puncta in axons. A 30 min treatment decreased the density that, however, restored to the time matched control levels by 60 min. **(B)** A 10 min treatment with AA decreased the density of pT308-Akt puncta to a similar extent as a 30 min treatment **(A)**, and below those present in no NGF conditions. **(C)** GIM treatment for 30 and 60 min similarly decreased the density of pT308-Akt puncta. **(D)** The restoration of the density of pT308-Akt puncta to baseline after a 60 min treatment with AA is prevented by cotreatment with GIM. **(E)** Treatment with AA decreases the density of pS473-Akt puncta after a 60 min treatment but not a 30 min treatment. **(F)** Both 30 and 60 min treatments with GIM similarly decrease the density of pS473-Akt puncta.

of phosphorylation at each site (as reflected by no changes in the intensity of the staining of individual sites/puncta of both pT308-Akt and pS473-Akt). The sites of PI3K activation and puncta of pT308-Akt likely correspond to clusters of TrkA receptors in the membrane, but this issue was not directly investigated. Thus, the data indicate that along sensory axons NGF increases the density of sites of initial Akt activation, reflected by pT308-Akt puncta, preferentially along axon segments populated by mitochondria. The suppression of pT308-Akt puncta by AA treatment at 15 min after NGF treatment along axon segments populated by mitochondria and those not containing mitochondria may reflect

the redistribution of mitochondria that ensues during the first 10 min of NGF treatment (Armijo-Weingart et al., 2019) or the intracellular distribution of pT03-Akt puncta during this period. Consistent with the first suggestion, motile mitochondria can regulate aspects of synaptic function as they undergo transport (Sun et al., 2013), and thus may similarly regulate pT308-Akt. The relationship between motile mitochondria and sites of pT308-Akt will require further consideration.

Overall, the data suggest a hypothetical working model for the spatio-temporal initiation and spread of Akt signaling along axons, and the maintenance of the steady state during

prolonged NGF signaling (summarized in visual form in **Supplementary Figure 8**). The data indicate that the initial phosphorylation of Akt at T308 occurs most prominently in axon segments populated by mitochondria which provide the required ATP through OxP. We suggest that this phosphorylation likely occurs at the plasma membrane or during early stages of endocytosis of TrkA-NGF couplets (Marlin and Li, 2015). Following phosphorylation at T308, Akt is considered to be associated with the ensuing NGF-TrkA signaling endosomes (Marlin and Li, 2015). We suggest that signaling endosomes recruit glycolytic enzymes that then serve to provide ATP for the phosphorylation of Akt at S473, as previously shown for the role of glycolysis in “on board” powering of the transport of axonal vesicles that also carry markers for endosomes (Zala et al., 2013; Hinckelmann et al., 2016). Thus, impairment of endocytosis would prevent the endosome associated phosphorylation of Akt at S473. Interestingly, the endocytosis of TrkA is dependent on PI3K signaling (York et al., 2000) as are other forms of receptor endocytosis (Bhattacharya et al., 2016). Some forms of endocytosis are dependent on actin filament dynamics (Chakrabarti et al., 2021) and PI3K-Akt signaling along axons in response to NGF promotes localized polymerization of actin patches preferentially in axonal segments populated by mitochondria (Ketschek and Gallo, 2010). Thus, the failure to phosphorylate Akt at T308 when OxP is suppressed is likely to also prevent TrkA endocytosis, and as shown by the data also the subsequent phosphorylation at S473. A prior example for internalization dependent activation of a signaling pathway by NGF-TrkA signaling is the activation of Erk signaling which is dependent on TrkA endocytosis (Zhang et al., 2000; Rakhit et al., 2001; Boutilier et al., 2008). Under steady state NGF conditions, due to the recycling of TrkA receptors to the plasma membrane (Chen et al., 2005; Ascaño et al., 2009, 2012; Yu et al., 2011; Diering et al., 2013), the process described above for the initial stage of NGF signaling would repeat. This could account for the delayed suppression of the levels of pS473-Akt in axons after inhibition of OxP but the faster suppression by inhibition of glycolysis. These aspects of the hypothetical mechanism are discussed further below. The issue of retrograde signaling is not addressed as here we focus on local actions of NGF on axons.

In the experimental model system used in this study, in the absence of NGF axons are growing on a laminin coated substratum and laminin signals through integrin receptors to promote the extension of NGF-responsive axons in the absence of NGF (Guan et al., 2003). The low levels of PI3K-Akt signaling present prior to NGF treatment are likely due to integrin signaling (Guidetti et al., 2015), although this was not specifically addressed. However, a 10 min inhibition of OxP in steady state NGF conditions suppressed pT308-Akt levels below those present in axons not treated with NGF, indicating that there are additional sources of OxP dependent pT308-Akt puncta than those activated by NGF. Upon treatment with NGF, which also hyperpolarizes the mitochondrial membrane potential along axons (Verburg and Hollenbeck, 2008), there is an increase in sites of PIP3 microdomain formation that is greatest in axon segments populated by mitochondria. The hyperpolarization of mitochondrial membrane potential

by NGF requires PI3K signaling (Verburg and Hollenbeck, 2008). Thus, it is possible that a local feedforward loop is activated wherein NGF PI3K signaling promotes mitochondrial respiration that in turn promotes PI3K signaling locally within axon segments populated by mitochondria. PIP3 microdomains would then serve as scaffolds for the recruitment of Akt to the membrane and phosphorylation at T308 by PDK1. As the PIP3 microdomains are largely associated with mitochondria, the resulting phosphorylation of Akt at T308 is also similarly localized during the early phase of signaling.

In our investigation, the subsequent phosphorylation of Akt at S473 induced by NGF, presumably mediated by mTORC2, did not exhibit preferential localization with mitochondria and occurred with a similar temporal profile in axon segments populated by mitochondria and those not containing mitochondria. It is generally considered that mTORC2 is also localized to membranes through the binding of PI3K lipid products, but evidence indicates that the targeting may be at the plasma membrane or at endomembranes (Manning and Toker, 2017). The latter possibility is a better fit for the observation that S473 phosphorylation is not preferentially localized within axon segments populated by mitochondria and their associated PIP3 microdomains. NGF signaling induces the formation of signaling endosomes that then undergo intracellular redistribution (Marlin and Li, 2015). The data suggest the hypothesis that S473 phosphorylation may be occurring on signaling endosomes as they redistribute, but this possibility would need to be investigated empirically.

The imaging methods used in this study to address PIP3 localization have resolution limitations. The application of super resolution methods may reveal the presence of smaller PIP3 microdomains not visible using our approach. If the hypothesis that signaling endosomes are the sites of S473 Akt phosphorylation is valid, then super resolution imaging may be able to correlate endosomal markers with PI3K lipid products and phosphorylation of Akt at S473. However, inhibition of OxP also prevented S473 phosphorylation during the initial burst of NGF signaling. The requirement for OxP in S473 phosphorylation may be due to a requirement for OxP in the traffic mTORC2 to membranes, or inhibition of OxP may also be preventing the initial steps of TrkA activation upstream of PI3K signaling thereby shutting down subsequent signaling events, or in the endocytosis of TrkA receptors, issues not addressed in this study that will require future investigation.

Proteomic analysis of fast transport vesicles has found that glycolytic enzymes are associated with vesicles that also exhibit endosomal markers and that ATP production through glycolysis can occur on vesicles and powers their transport (Zala et al., 2013; Hinckelmann et al., 2016). Thus, glycolytic machinery is associated with endosomes. The observations that the initial NGF-induced S473 Akt phosphorylation is dependent on glycolysis and that suppression of glycolysis results in a faster decline in S473 levels than following suppression of OxP at steady state indicate a relationship between S473 phosphorylation and glycolysis. The data also suggest the hypothesis that S473 phosphorylation of Akt may occur on internalized Trk-NGF containing signalosomes.

Under conditions of steady state NGF signaling (treatment for 24 h) inhibition of OxP suppressed the levels of pT308-Akt by 30 min of treatment, but the levels recovered to baseline by 60 min, and the recovery required glycolysis. If the above consideration that OxP is required for the activation of NGF-TrkA signaling is valid, then under steady state conditions glycolysis may be able to compensate for the loss of OxP. This hypothetical compensatory mechanism has a precedence in the literature. Jang et al. (2016) report that under conditions of energy stress glycolytic enzymes are recruited to synaptic sites to compensate for decrease oxidative respiration or decreased mitochondrial numbers and function along neurites. Furthermore, Jang et al. (2016) also present evidence that glycolysis can power synaptic vesicle recycling when mitochondria function is impaired. The relevance of these observations to the current study is further emphasized by the prior demonstrations that sites of axonal filopodia and branch formation colocalize with mitochondria and accumulations of synaptic vesicles along axons (Courchet et al., 2013; Greif et al., 2013).

Inhibition of glycolysis also suppressed steady state pT308-Akt levels but by approximately 50% of the decrease observed with inhibition of OxP. These data indicate that although glycolysis is not required for the initial burst of pT308-Akt phosphorylation during the initial 15 min of NGF signaling, it does contribute to its maintenance during steady state signaling. The difference in the role of glycolysis will require further consideration but may reflect pools of internalized NGF-TrkA couplets in signalosomes, that may be more prevalent during steady state signaling than the initial phase of signaling, and these signalosomes may associate with the glycolytic apparatus as described for other fast transport vesicles (Zala et al., 2013; Hinckelmann et al., 2016). In contrast, the steady state levels of pS473-Akt dropped equally by approximately 75% with both a 30 and 60 min inhibition of glycolysis. The data thus indicate that the maintenance of pS473-Akt under steady state conditions of NGF signaling is more dependent on glycolysis, which we speculate may be occurring on internalized signalosomes.

In conclusion, this study indicates that OxP and glycolysis contribute differently to the activation of the PI3K-Akt signaling axis by NGF along sensory axons. The data suggest that the initial activation of PI3K and pT308-Akt signaling occurs preferentially

in axon segments populated by mitochondria, and that OxP is required for the initial phosphorylation of Akt at T308 independent of glycolysis. These initial observations suggest that additional work will be required to dissect the relative contributions of OxP and glycolysis to signaling along axons, and that the two bioenergetic sources may contribute differentially depending on the time frame, and possibly intracellular sites, of the signaling. Whether similar bioenergetic requirements may apply to other ligand-receptor signaling systems remains an open question.

DATA AVAILABILITY STATEMENT

The raw data supporting the conclusions of this article will be made available by the authors, without undue reservation.

ETHICS STATEMENT

The animal study was reviewed and approved by the Institutional Animal Care and Use Committee, Lewis Katz School of Medicine, Temple University.

AUTHOR CONTRIBUTIONS

GG designed the research, analyzed the data, and prepared the manuscript. RS designed, conducted the research, and analyzed the data. Both authors contributed to the article and approved the submitted version.

FUNDING

This work was supported by the NINDS NS095471 to GG.

SUPPLEMENTARY MATERIAL

The Supplementary Material for this article can be found online at: <https://www.frontiersin.org/articles/10.3389/fnmol.2021.726331/full#supplementary-material>

REFERENCES

- Armijo-Weingart, L., and Gallo, G. (2017). It takes a village to raise a branch: cellular mechanisms of the initiation of axon collateral branches. *Mol. Cell Neurosci.* 84, 36–47. doi: 10.1016/j.mcn.2017.03.007
- Armijo-Weingart, L., Ketschek, A., Sainath, R., Pacheco, A., Smith, G. M., and Gallo, G. (2019). Neurotrophins induce fission of mitochondria along embryonic sensory axons. *Elife* 8:e49494. doi: 10.7554/eLife.49494
- Ascaño, M., Bodmer, D., and Kuruvilla, R. (2012). Endocytic trafficking of neurotrophins in neural development. *Trends Cell Biol.* 22, 266–273. doi: 10.1016/j.tcb.2012.02.005
- Ascaño, M., Richmond, A., Borden, P., and Kuruvilla, R. (2009). Axonal targeting of Trk receptors via transcytosis regulates sensitivity to neurotrophin responses. *J. Neurosci.* 29, 11674–11685. doi: 10.1523/JNEUROSCI.1542-09.2009
- Ashrafi, G., and Ryan, T. A. (2017). Glucose metabolism in nerve terminals. *Curr. Opin. Neurobiol.* 45, 156–161. doi: 10.1016/j.conb.2017.03.007
- Bhattacharya, S., McElhanon, K. E., Gushchina, L. V., and Weisleder, N. (2016). Role of phosphatidylinositol-4,5-bisphosphate 3-kinase signaling in vesicular trafficking. *Life Sci.* 167, 39–45. doi: 10.1016/j.lfs.2016.10.018
- Boutillier, J., Ceni, C., Pagdala, P. C., Forgie, A., Neet, K. E., and Barker, P. A. (2008). Proneurotrophins require endocytosis and intracellular proteolysis to induce TrkA activation. *J. Biol. Chem.* 19, 12709–12716. doi: 10.1074/jbc.M710018200
- Chakrabarti, R., Lee, M., and Higgs, H. N. (2021). Multiple roles for actin in secretory and endocytic pathways. *Curr. Biol.* 31, R603–R618. doi: 10.1016/j.cub.2021.03.038
- Chen, Z. Y., Ieraci, A., Tanowitz, M., and Lee, F. S. (2005). A novel endocytic recycling signal distinguishes biological responses of Trk neurotrophin receptors. *Mol. Biol. Cell.* 16, 5761–5772. doi: 10.1091/mbc.e05-07-0651

- Courchet, J., Lewis, T. L. Jr., Lee, S., Courchet, V., Liou, D. Y., Aizawa, S., et al. (2013). Terminal axon branching is regulated by the LKB1-NUAK1 kinase pathway via presynaptic mitochondrial capture. *Cell* 153, 1510–1525. doi: 10.1016/j.cell.2013.05.021
- Diering, G. H., Numata, Y., Fan, S., Church, J., and Numata, M. (2013). Endosomal acidification by Na⁺/H⁺ exchanger NHE5 regulates TrkA cell-surface targeting and NGF-induced PI3K signaling. *Mol. Biol. Cell* 24, 3435–3448. doi: 10.1091/mbc.E12-06-0445
- Eramo, M. J., and Mitchell, C. A. (2016). Regulation of PtdIns(3,4,5)P3/Akt signalling by inositol polyphosphate 5-phosphatases. *Biochem. Soc. Trans.* 44, 240–252. doi: 10.1042/BST20150214
- Fayard, E., Xue, G., Parcellier, A., Bozulic, L., and Hemmings, B. A. (2010). “Protein kinase B (PKB/Akt), a key mediator of the PI3K signaling pathway,” in *Phosphoinositide 3-Kinase in Health and Disease. Current Topics in Microbiology and Immunology*, Vol. 346, eds C. Rommel, B. Vanhaesebroeck, and P. Vogt (Berlin: Springer). doi: 10.1007/82_2010_58
- Gallo, G. (2020). The bioenergetics of neuronal morphogenesis and regeneration: frontiers beyond the mitochondrion. *Dev. Neurobiol.* 80, 263–276. doi: 10.1002/dneu.22776
- Gallo, G., Lefcort, F. B., and Letourneau, P. C. (1997). The trkA receptor mediates growth cone turning toward a localized source of nerve growth factor. *J. Neurosci.* 17, 5445–5454. doi: 10.1523/JNEUROSCI.17-14-05445.1997
- Gallo, G., and Letourneau, P. C. (2000). Neurotrophins and the dynamic regulation of the neuronal cytoskeleton. *J. Neurobiol.* 44, 159–173. doi: 10.1002/1097-4695(200008)44:2<159::aid-neu6<3.0.co;2-h
- Greif, K. F., Asabere, N., Lutz, G. J., and Gallo, G. (2013). Synaptotagmin-1 promotes the formation of axonal filopodia and branches along the developing axons of forebrain neurons. *Dev. Neurobiol.* 73, 27–44. doi: 10.1002/dneu.22033
- Guan, W., Puthenveedu, M. A., and Condic, M. L. (2003). Sensory neuron subtypes have unique substratum preference and receptor expression before target innervation. *J. Neurosci.* 23, 1781–1791. doi: 10.1523/JNEUROSCI.23-05-01781.2003
- Guidetti, G. F., Canobbio, I., and Torti, M. (2015). PI3K/Akt in platelet integrin signaling and implications in thrombosis. *Adv. Biol. Regul.* 59, 36–52. doi: 10.1016/j.jbior.2015.06.001
- Han, S. M., Baig, H. S., and Hammarlund, M. (2016). Mitochondria localize to injured axons to support regeneration. *Neuron* 92, 1308–1323. doi: 10.1016/j.neuron.2016.11.025
- Hinckelmann, M. V., Virlogeux, A., Niehage, C., Poujol, C., Choquet, D., Hoflack, B., et al. (2016). Self-propelling vesicles define glycolysis as the minimal energy machinery for neuronal transport. *Nat. Commun.* 7:13233. doi: 10.1038/ncomms13233
- Huang, E. J., and Reichardt, L. F. (2003). Trk receptors: roles in neuronal signal transduction. *Annu. Rev. Biochem.* 72, 609–642. doi: 10.1146/annurev.biochem.72.121801.161629
- Jang, S., Nelson, J. C., Bend, E. G., Rodríguez-Laureano, L., Tueros, F. G., Cartagena, L., et al. (2016). Glycolytic enzymes localize to synapses under energy stress to support synaptic function. *Neuron* 90, 278–291. doi: 10.1016/j.neuron.2016.03.011
- Kaplan, D. R., Martin-Zanca, D., and Parada, L. F. (1991). Tyrosine phosphorylation and tyrosine kinase activity of the trk proto-oncogene product induced by NGF. *Nature* 350, 158–160.
- Ketschek, A., and Gallo, G. (2010). Nerve growth factor induces axonal filopodia through localized microdomains of phosphoinositide 3-kinase activity that drive the formation of cytoskeletal precursors to filopodia. *J. Neurosci.* 30, 12185–12197. doi: 10.1523/JNEUROSCI.1740-10.2010
- Ketschek, A., Sainath, R., Holland, S., and Gallo, G. (2021). The axonal glycolytic pathway is required for sensory axon extension and growth cone dynamics. *J. Neurosci.* 41, 6637–6651. doi: 10.1523/JNEUROSCI.0321-21.2021
- Kontos, C. D., Stauffer, T. P., Yang, W. P., York, J. D., Huang, L., Blonar, M. A., et al. (1998). Tyrosine 1101 of Tie2 is the major site of association of p85 and is required for activation of phosphatidylinositol 3-kinase and Akt. *Mol. Cell. Biol.* 18, 4131–4140. doi: 10.1128/MCB.18.7.4131
- Lelkes, P. I., Unsworth, B. R., Saporta, S., Cameron, D. F., and Gallo, G. (2005). “Chapter 14 culture of neuroendocrine and neuronal cells for tissue engineering,” in *Culture of Cells of Tissue Engineering*, ed. R. I. Freshney (Hoboken, NJ: John Wiley & Sons). doi: 10.1002/0471741817.ch14
- Leemans, M. A., Ferguson, K. M., and Abrams, C. S. (2002). Pleckstrin homology domains and the cytoskeleton. *FEBS Lett.* 513, 71–76. doi: 10.1016/s0014-5793(01)03243-4
- Lewis, T. L. Jr., Kwon, S. K., Lee, A., Shaw, R., and Polleux, F. (2018). MFF-dependent mitochondrial fission regulates presynaptic release and axon branching by limiting axonal mitochondria size. *Nat. Commun.* 9:5008. doi: 10.1038/s41467-018-07416-2
- Loudon, R. P., Silver, L. D., Yee, H. F. Jr., and Gallo, G. (2006). RhoA-kinase and myosin II are required for the maintenance of growth cone polarity and guidance by nerve growth factor. *J. Neurobiol.* 66, 847–867. doi: 10.1002/neu.20258
- Manning, B. D., and Toker, A. (2017). AKT/PKB signaling: navigating the network. *Cell* 169, 381–405. doi: 10.1016/j.cell.2017.04.001
- Marlin, M. C., and Li, G. (2015). Biogenesis and function of the NGF/TrkA signaling endosome. *Int. Rev. Cell. Mol. Biol.* 314, 239–257. doi: 10.1016/bs.ircmb.2014.10.002
- Miura, H., Matsuda, M., and Aoki, K. (2014). Development of a FRET biosensor with high specificity for Akt. *Cell Struct. Funct.* 39, 9–20. doi: 10.1247/csf.13018
- Morris, R. L., and Hollenbeck, P. J. (1993). The regulation of bidirectional mitochondrial transport is coordinated with axonal outgrowth. *J. Cell Sci.* 104, 917–927.
- Niewiadomska, G., Mietelska-Porowska, A., and Mazurkiewicz, M. (2011). The cholinergic system, nerve growth factor and the cytoskeleton. *Behav. Brain Res.* 221, 515–526. doi: 10.1016/j.bbr.2010.02.024
- Pacelli, C., Giguère, N., Bourque, M. J., Lévesque, M., Slack, R. S., and Trudeau, L. É. (2015). Elevated mitochondrial bioenergetics and axonal arborization size are key contributors to the vulnerability of dopamine neurons. *Curr. Biol.* 25, 2349–2360. doi: 10.1016/j.cub.2015.07.050
- Pacheco, A., and Gallo, G. (2016). Actin filament-microtubule interactions in axon initiation and branching. *Brain Res. Bull.* 126, 300–310. doi: 10.1016/j.brainresbull.2016.07.013
- Patrón, L. A., and Zinsmaier, K. E. (2016). Mitochondria on the road to power axonal regeneration. *Neuron* 92, 1152–1154. doi: 10.1016/j.neuron.2016.12.007
- Rakhit, S., Pyne, S., and Pyne, N. J. (2001). Nerve growth factor stimulation of p42/p44 mitogen-activated protein kinase in PC12 cells: role of G(i/o), G protein-coupled receptor kinase 2, beta-arrestin I, and endocytic processing. *Mol. Pharmacol.* 60, 63–70. doi: 10.1124/mol.60.1.63
- Rangaraju, V., Lewis, T. L. Jr., Hirabayashi, Y., Bergami, M., Motori, E., Cartoni, R., et al. (2019). Pleiotropic mitochondria: the influence of mitochondria on neuronal development and disease. *J. Neurosci.* 39, 8200–8208. doi: 10.1523/JNEUROSCI.1157-19.2019
- Reichardt, L. F. (2006). Neurotrophin-regulated signalling pathways. *Philos. Trans. R. Soc. Lond. B Biol. Sci.* 361, 1545–1564. doi: 10.1098/rstb.2006.1894
- Sainath, R., Armijo-Weingart, L., Ketschek, A., Xu, Z., Li, S., and Gallo, G. (2017b). Chondroitin sulfate proteoglycans negatively regulate the positioning of mitochondria and endoplasmic reticulum to distal axons. *Dev. Neurobiol.* 77, 1351–1370. doi: 10.1002/dneu.22535
- Sainath, R., Ketschek, A., Grandi, L., and Gallo, G. (2017a). CSPGs inhibit axon branching by impairing mitochondria-dependent regulation of actin dynamics and axonal translation. *Dev. Neurobiol.* 77, 454–473. doi: 10.1002/dneu.22420
- Sheng, Z. H. (2017). The interplay of axonal energy homeostasis and mitochondrial trafficking and anchoring. *Trends Cell Biol.* 27, 403–416. doi: 10.1016/j.tcb.2017.01.005
- Silver, L., Michael, J. V., Goldfinger, L. E., and Gallo, G. (2014). Activation of PI3K and R-Ras signaling promotes the extension of sensory axons on inhibitory chondroitin sulfate proteoglycans. *Dev. Neurobiol.* 74, 918–933. doi: 10.1002/dneu.22174
- Smith, G. M., and Gallo, G. (2018). The role of mitochondria in axon development and regeneration. *Dev. Neurobiol.* 78, 221–237. doi: 10.1002/dneu.22546
- Soltoff, S. P., Rabin, S. L., Cantley, L. C., and Kaplan, D. R. (1992). Nerve growth factor promotes the activation of phosphatidylinositol 3-kinase and its association with the trk tyrosine kinase. *J. Biol. Chem.* 267, 17472–17477.

- Spillane, M., Ketschek, A., Donnelly, C. J., Pacheco, A., Twiss, J. L., and Gallo, G. (2012). Nerve growth factor-induced formation of axonal filopodia and collateral branches involves the intra-axonal synthesis of regulators of the actin-nucleating Arp2/3 complex. *J. Neurosci.* 32, 17671–17689. doi: 10.1523/JNEUROSCI.1079-12.2012
- Spillane, M., Ketschek, A., Merianda, T. T., Twiss, J. L., and Gallo, G. (2013). Mitochondria coordinate sites of axon branching through localized intra-axonal protein synthesis. *Cell Rep.* 5, 1564–1575. doi: 10.1016/j.celrep.2013.11.022
- Sun, T., Qiao, H., Pan, P. Y., Chen, Y., and Sheng, Z. H. (2013). Motile axonal mitochondria contribute to the variability of presynaptic strength. *Cell Rep.* 4, 413–419. doi: 10.1016/j.celrep.2013.06.040
- Tao, K., Matsuki, N., and Koyama, R. (2014). AMP-activated protein kinase mediates activity-dependent axon branching by recruiting mitochondria to axon. *Dev. Neurobiol.* 74, 557–573. doi: 10.1002/dneu.22149
- Verburg, J., and Hollenbeck, P. J. (2008). Mitochondrial membrane potential in axons increases with local nerve growth factor or semaphorin signaling. *J. Neurosci.* 28, 8306–8315. doi: 10.1523/JNEUROSCI.2614-08.2008
- Wong, H. H., Lin, J. Q., Ströhl, F., Roque, C. G., Cioni, J. M., Cagnetta, R., et al. (2017). RNA docking and local translation regulate site-specific axon remodeling in vivo. *Neuron* 95, 852–868.e8. doi: 10.1016/j.neuron.2017.07.016
- York, R. D., Molliver, D. C., Grewal, S. S., Stenberg, P. E., McCleskey, E. W., and Stork, P. J. (2000). Role of phosphoinositide 3-kinase and endocytosis in nerve growth factor-induced extracellular signal-regulated kinase activation via Ras and Rap1. *Mol. Cell Biol.* 20, 8069–8083. doi: 10.1128/MCB.20.21.8069-8083.2000
- Yu, T., Calvo, L., Anta, B., López-Benito, S., Southon, E., Chao, M. V., et al. (2011). Regulation of trafficking of activated TrkA is critical for NGF-mediated functions. *Traffic* 12, 521–534. doi: 10.1111/j.1600-0854.2010.01156.x
- Zala, D., Hinckelmann, M. V., Yu, H., Lyra da Cunha, M. M., Liot, G., Cordelières, F. P., et al. (2013). Vesicular glycolysis provides on-board energy for fast axonal transport. *Cell* 152, 479–491. doi: 10.1016/j.cell.2012.12.029
- Zhang, Y., Moheban, D. B., Conway, B. R., Bhattacharyya, A., and Segal, R. A. (2000). Cell surface Trk receptors mediate NGF-induced survival while internalized receptors regulate NGF-induced differentiation. *J. Neurosci.* 20, 5671–5678. doi: 10.1523/JNEUROSCI.20-15-05671.2000
- Zhou, B., Yu, P., Lin, M. Y., Sun, T., Chen, Y., and Sheng, Z. H. (2016). Facilitation of axon regeneration by enhancing mitochondrial transport and rescuing energy deficits. *J. Cell Biol.* 214, 103–119. doi: 10.1083/jcb.201605101
- Zhou, F. Q., Zhou, J., Dedhar, S., Wu, Y. H., and Snider, W. D. (2004). NGF-induced axon growth is mediated by localized inactivation of GSK-3beta and functions of the microtubule plus end binding protein APC. *Neuron* 42, 897–912. doi: 10.1016/j.neuron.2004.05.011

Conflict of Interest: The authors declare that the research was conducted in the absence of any commercial or financial relationships that could be construed as a potential conflict of interest.

Publisher's Note: All claims expressed in this article are solely those of the authors and do not necessarily represent those of their affiliated organizations, or those of the publisher, the editors and the reviewers. Any product that may be evaluated in this article, or claim that may be made by its manufacturer, is not guaranteed or endorsed by the publisher.

Copyright © 2021 Sainath and Gallo. This is an open-access article distributed under the terms of the Creative Commons Attribution License (CC BY). The use, distribution or reproduction in other forums is permitted, provided the original author(s) and the copyright owner(s) are credited and that the original publication in this journal is cited, in accordance with accepted academic practice. No use, distribution or reproduction is permitted which does not comply with these terms.



Neuronal Activity in the Sciatic Nerve Is Accompanied by Immediate Cytoskeletal Changes

Bossmat Yehuda¹, Tal Gradus Pery², Efrat Ophir¹, Tamar Blumenfeld-Katzir¹, Anton Sheinin³, Yael Alon¹, Noy Danino¹, Eran Perlson^{2,3} and Uri Nevo^{1,3*}

¹ Department of Biomedical Engineering, The Iby and Aladar Fleischman Faculty of Engineering, Tel Aviv University, Tel Aviv, Israel, ² Department of Physiology and Pharmacology, Sackler School of Medicine, Tel Aviv University, Tel Aviv, Israel, ³ Sagol School of Neuroscience, Tel Aviv University, Tel Aviv, Israel

Mechanical events and alterations in neuronal morphology that accompany neuronal activity have been observed for decades. However, no clear neurophysiological role, nor an agreed molecular mechanism relating these events to the electrochemical process, has been found. Here we hypothesized that intense, yet physiological, electrical activity in neurons triggers cytoskeletal depolymerization. We excited the sciatic nerve of anesthetized mice with repetitive electric pulses (5, 10, and 100 Hz) for 1 and 2 min and immediately fixed the excised nerves. We then scanned the excised nerves with high-resolution transmission electron microscopy, and quantified cytoskeletal changes in the resulting micrographs. We demonstrate that excitation with a stimulation frequency that is within the physiological regime is accompanied by a significant reduction in the density of cytoskeletal proteins relative to the baseline values recorded in control nerves. After 10 Hz stimulation with durations of 1 and 2 min, neurofilaments density dropped to 55.8 and 51.1% of the baseline median values, respectively. In the same experiments, microtubules density dropped to 23.7 and 38.5% of the baseline median values, respectively. These changes were also accompanied by a reduction in the cytoskeleton-to-cytoplasm contrast that we attribute to the presence of depolymerized electron-dense molecules in the lumen. Thus, we demonstrate with an *in vivo* model a link between electrical activity and immediate cytoskeleton rearrangement at the nano-scale. We suggest that this cytoskeletal plasticity reduces cellular stiffness and allows cellular homeostasis, maintenance of neuronal morphology and that it facilitates in later stages growth of the neuronal projections.

Keywords: biophysics, mechanics, neuronal plasticity, beading, Calpain

INTRODUCTION

Neuronal electrical activity is a cascade of biochemical events driven by the passive influx and efflux of ions through voltage-gated channels (Hodgkin and Huxley, 1952). Action potentials are accompanied also by mechanical events that occur in the immediate time scale. In the immediate temporal scale, nano-scale deformations are accompanying the action potential (Iwasa et al., 1980) and heat is released (Tasaki et al., 1989). These mechanical events are minute, but they cannot be explained solely by an electro-chemical view of action potentials. The exact molecular mechanism that leads to this mechanical wave is yet unclear. A physical model of propagation of

OPEN ACCESS

Edited by:

Pabitra Sahoo,
University of South Carolina,
United States

Reviewed by:

James C. Vickers,
University of Tasmania, Australia
Fernando Peña-Ortega,
National Autonomous University
of Mexico, Mexico

*Correspondence:

Uri Nevo
nevouiri@tauex.tau.ac.il

Specialty section:

This article was submitted to
Neuroplasticity and Development,
a section of the journal
Frontiers in Molecular Neuroscience

Received: 11 August 2021

Accepted: 04 October 2021

Published: 27 October 2021

Citation:

Yehuda B, Gradus Pery T,
Ophir E, Blumenfeld-Katzir T,
Sheinin A, Alon Y, Danino N, Perlson E
and Nevo U (2021) Neuronal Activity
in the Sciatic Nerve Is Accompanied
by Immediate Cytoskeletal Changes.
Front. Mol. Neurosci. 14:757264.
doi: 10.3389/fnmol.2021.757264

mechanical solitons was proposed by Heimburg and Jackson (2005). They describe how an action potential may lead to a phase transition of the lipid membrane, that reflects non-linear changes in multiple mechanical and thermodynamic properties (Heimburg and Jackson, 2005), including those described by Iwasa et al. (1980) and Tasaki et al. (1989). This phase transition propagates similar to an action potential, without being dispersed (soliton). Mussel and Schneider (2019) demonstrated theoretically that a propagating acoustic wave in the interface of a lipid membrane and the electrolytic extracellular medium can yield a pulse of electric potential that behaves similar to an action potential. The molecular mechanisms leading to these events are yet to be resolved, and so is their physiological role.

Electrical activity was shown to trigger cytoskeletal changes occurring in the long time scales. Alvarez (1979) demonstrated that a 2 h stimulation of the preganglionic cervical nerve in cats resulted in an increase in the density of microtubules. Hu et al. (2008) imaged cultured hippocampal neurons to show that increasing neuronal activity by repeated perfusion with high KCl medium, enhanced the invasion of microtubules into spines and lengthened the duration of these invasions. Mitsuyama et al. (2008) complemented this result with a similar model of acute hippocampal slices and showed that strong stimulation leads to elongation of microtubules into spines, thus enlarging their protrusions. Merriam et al. (2013) further established the role of Calcium, F-Actin, and Drebrin in regulating the growth of microtubules in spines in similar experiments.

In a set of separate experiments, it was shown that intense electrical activity may lead to beading of axons. In non-living physical systems, as fluids enclosed by a cylindrical membrane, beading is typically linked to a change in the mechanical forces acting on the cylinder. A stable cylindrical system reflects an equilibrium between the stiffness of the cylinder, its surface tension, and the pressure and volume of the enclosed fluid. Once the pressure increases, for example by fluid inflow, minimization of free energy favors an increase in the volume. Given a fixed surface area, volume can be maximized by deforming the cylinder into spheres (thereby the term “beading”). This can be facilitated by reduction of the stiffness of the cylinder (Clerk Maxwell, 1874). Similarly, in neurons, different conditions and manipulations lead to a dramatic segmentation of the neuronal projections into swollen sphere-like segments (beads) separated by long shrunken “necks” (Ochs et al., 1994). Beading was observed in a variety of neuronal pathologies and conditions related to cellular stress like ischemia (Murphy et al., 2008; Risher et al., 2010), spreading depression (Takano et al., 2007), and seizures (Zeng et al., 2007).

To complete this short review of activity related morphological changes, we should mention that, in even longer timescales, neuronal plasticity facilitates morphological changes related to neuronal growth and the formation of networks (Shefi et al., 2005).

All the above mentioned events are necessarily linked to cytoskeletal changes. Currently there is no model that links the mechanical events that occur in different spatio-temporal scales. A model of the relation between cytoskeletal dynamics and the cellular events should include the transition from short and less intense physiological activity to pathological stimulation, the

role of different cytoskeletal components linked to the above mentioned dynamics, and the way these affect different cellular structures, as axons, dendrites, and their growth cones.

We hypothesize that electrical activity affects the cytoskeleton immediately. We assume that activity triggers cytoskeletal depolymerization such that this effect serves a physiological role in reducing the neuronal stiffness thus facilitating the morphological changes that occur later. We present an *in vivo* experiment that is composed of electron-microscopy imaging and analysis of cytoskeletal changes in axons after electrical stimulation.

METHODS

Electrophysiology

Electrical stimulation was applied to exposed sciatic nerves in male ICR mice ($n = 17$, 3 weeks old, weight: 35–38 gr) under anesthetic influence, using a hook electrode (**Figures 1A,B**). Nerves were excited at a frequency of 5 Hz for 1 min, 10 Hz for 1 or 2 min, and 100 Hz for 2 min. These stimulation frequencies (5 and 10 Hz) were chosen to be mimic intense physiological activity that is observed in mice sciatic nerve (Heglund et al., 1974; Herbin et al., 2018). Stimulation was verified by tying the leg with the exposed nerve to a force transducer and recording the mechanical contractions, which were also visible to the naked eye. An example of the force transducer recording is presented in **Figure 2**. As the stimulation frequency was higher, the mechanical contraction of the leg was more rapid. When stimulating at 100 Hz for 2 min, the leg was stiff, and the contraction was continuous. The same methods were used to expose and fixate the nerves of the mice in the control group, without any electrical stimulation.

Fixation

Immediately after electrical stimulation, fixation was performed *in vivo* by constantly dripping 4% paraformaldehyde and 2.5% glutaraldehyde in a 0.1 M cacodylate buffer (pH 7.4) containing 3% sucrose (Karnovsky's fixative) onto the exposed nerves for 15–20 min, while the mice were kept anesthetized (**Figure 1C**). The nerves were then excised, and all samples were fixed by immersion in the same fixative, on a shaker, for 60 min at 24°C. Next, each nerve was divided into segments of 2–3 mm (three to four segments per nerve) and fixed further by immersion in the same fixative, first at 24°C for 2–3 h and then at 4°C for over 24 h. This fixation protocol was chosen because it produced the best results, preventing cell death before completion of the fixation. The mice were kept alive during the fixation stage by using a special heated sheet to keep them dry and warm.

Transmission Electron Microscopy

Tissues were rinsed four times, for 10 min each, in a cacodylate buffer and post-fixed and stained with 1% osmium tetroxide and 1.5% potassium ferricyanide in a 0.1 M cacodylate buffer for 1 h. Tissues were then washed four times in cacodylate buffer and dehydrated first in increasing concentrations of ethanol – 30, 50, 70, 80, 90, and 95% – for 10 min in each concentration; then

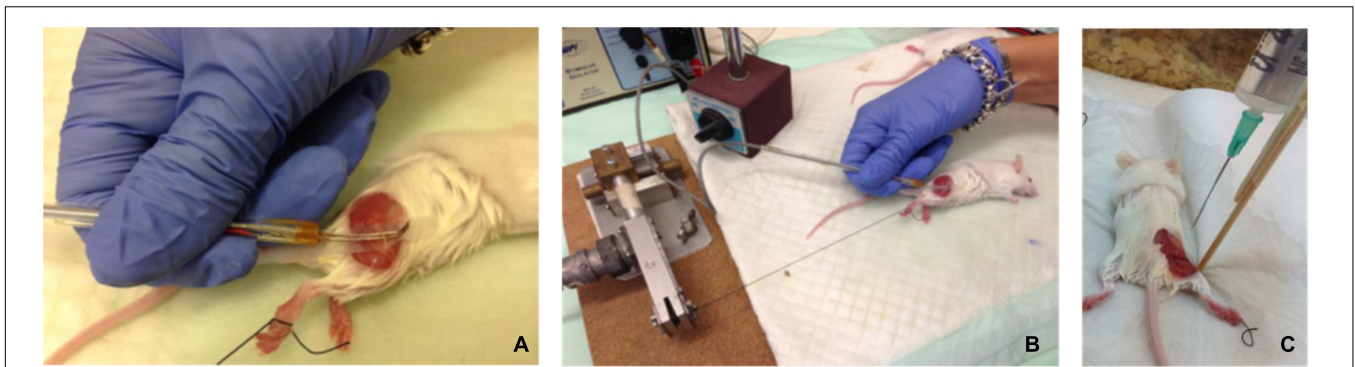


FIGURE 1 | (A,B) Electrophysiological setup – exposed mouse sciatic nerve excited by electrical stimulus, using a hook electrode. **(C)** Fixation was performed *in situ* by constantly dripping Karnovsky fixative onto the exposed sciatic nerve for 30–40 min, while the mice were kept anesthetized.

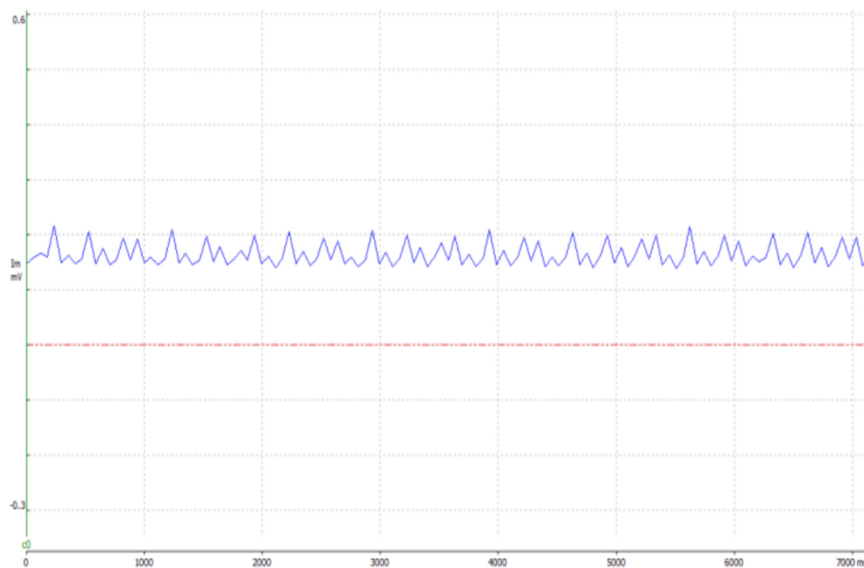


FIGURE 2 | An example presenting evidence of the electrical stimulation, in the 10 Hz test group, using WinWCP. The graph shows data obtained from the force transducer, to which the leg of the mouse was tied. When stimulating the sciatic nerve, the leg contracts, elevating the voltage.

three times in 100% anhydrous ethanol, for 20 min each time; and finally two times in propylene oxide, for 10 min each time. After dehydration, the tissues were infiltrated with increasing concentrations of Agar 100 resin in propylene oxide, consisting of 25, 50, 75, and 100% resin for 16 h for each concentration. The tissues were then embedded in fresh resin and placed in an oven at 60°C for 48 h for polymerization. Embedded tissues in blocks were sectioned with a diamond knife on a LKB III microtome, and ultrathin sections (80 nm) were collected on 200 mesh, thin bar copper grids. The sections were sequentially stained with uranyl acetate and lead citrate for 10 min each and viewed with a Tecnai 12 transmission electron microscopy (TEM) 100 kV (Phillips, Eindhoven, Netherlands), equipped with the MegaView II CCD camera and Analysis[®] version 3.0 software (Soft Imaging System GmbH, Münster, Germany).

Random areas in slices of specimens from each group were examined and scanned. Images were acquired at magnifications

of $\times 1,800$ (for observation of large sections of the nerve), $\times 9,700$ (for observation of a complete single projection transverse view), and $\times 37,000$ (for cytoskeleton filament analysis). In the highest resolution ($\times 37,000$) multiple consecutive micrograph need to be imaged, in order to cover the entire axial section of each axon. Altogether 124 axons were blindly chosen for imaging with the highest resolution: control- 32; 5 Hz 1 min- 15; 10 Hz 1 min- 13; 10 Hz 2 min- 39; 100 Hz 2 min- 25.

Image Processing

Transmission electron microscopy images were analyzed to detect differences in the density of neurofilaments and microtubules across the different groups. Quantifying the cytoskeleton changes between the different groups required separation of the cytoskeleton components. Because the images produced by TEM are gray level with a range of average values of intensities in different regions of the cytoplasm, a simple

threshold method did not achieve the best results. The method we used is detailed below and visually presented in **Figure 3**. Next, a set of parameters was chosen and extracted from the original images. Images were processed using MATLAB® and ImageJ®. The image analysis is mostly automatic, and yet, to validate its results, we compared its outcome to the results obtained manually by independent users.

- (1) All images (at a magnification of $\times 37,000$) were normalized by a linear factor. This step is designed to prevent a shift of the original image-intensities histogram due to microscope artifacts or different lighting conditions present when each image was scanned. When observing an image histogram, a significant peak containing many of the image pixels can be distinguished in the image histogram. This bin represents the gray level of the axoplasm. To overcome the TEM scan differences, this gray level was set to a common, fixed level in all images and, therefore, each image had a normalization factor with a different value.
- (2) The micrographs of each axon were combined using ImageJ software to create one complete axonal image, and its lumen was marked manually.
- (3) A binary image was necessary for quantifying the changes in the cytoskeleton. We classified the image into two populations: the axoplasm and the cytoskeleton and organelles. Each pixel classification was determined using a specific feature space composed of (a) its' normalized gray level and (b) the number of neighbors which were classified as lumen (from a 3×3 mask around each pixel). The data needed for assembling this space was collected from manually classified sub-micrographs of all experiment groups. Each pixel is represented as a feature vector. The feature space (in this case a plane) can be divided linearly into the two populations. With this feature space in place, each pixel in each new image is classified according to its properties, and a binary image is created according to this classification. Notice that a new image has no labeling therefore number of axoplasm neighbors cannot be calculated directly. To overcome this gap, a set of eight 3×3 masks was conducted (with all the possible divisions of axoplasm and cytoskeleton and organelles in it) and the classification was set according to the mask with minimal difference in gray level from the original image. An example of the classification method applied on a sub-image is presented in **Figure 4**.
- (4) Extraction of the organelles and noise. Extraction of organelles was accomplished by identifying all the elements in the binary image that contained twice as many pixels as microtubules.

Noise was removed by identifying all the elements in the binary image in which the number of pixels was half the number of pixels assessed for neurofilaments. In addition, other elements in the binary image were removed according to their roundness score. Roundness is defined as the normalized ratio between the circumference and the area of each object.

- (5) The characteristics of microtubules and neurofilaments were quantified using the number of pixels that were classified for each of these cytoskeletal proteins. The number of pixels for each of the cytoskeleton components was determined according to the known average size (Jia et al., 2011) and the micrograph resolution.

- (6) The following morphological features were quantified:

- Filament density normalized by cell size, separated into microtubules and neurofilaments.
- Nearest neighbor distance, which provides local measurements of the distribution of all the cytoskeleton components. This parameter is divided into the average value and a normalized histogram describing the distribution of values within the cells.
- Edge magnitude, which may indicate on the existence of cytoskeletal debris in the lumen, due to cytoskeleton depolymerization.

All data were expressed as the median value and the distribution of values between the first and third quartile with MATLAB®.

Statistical Analysis

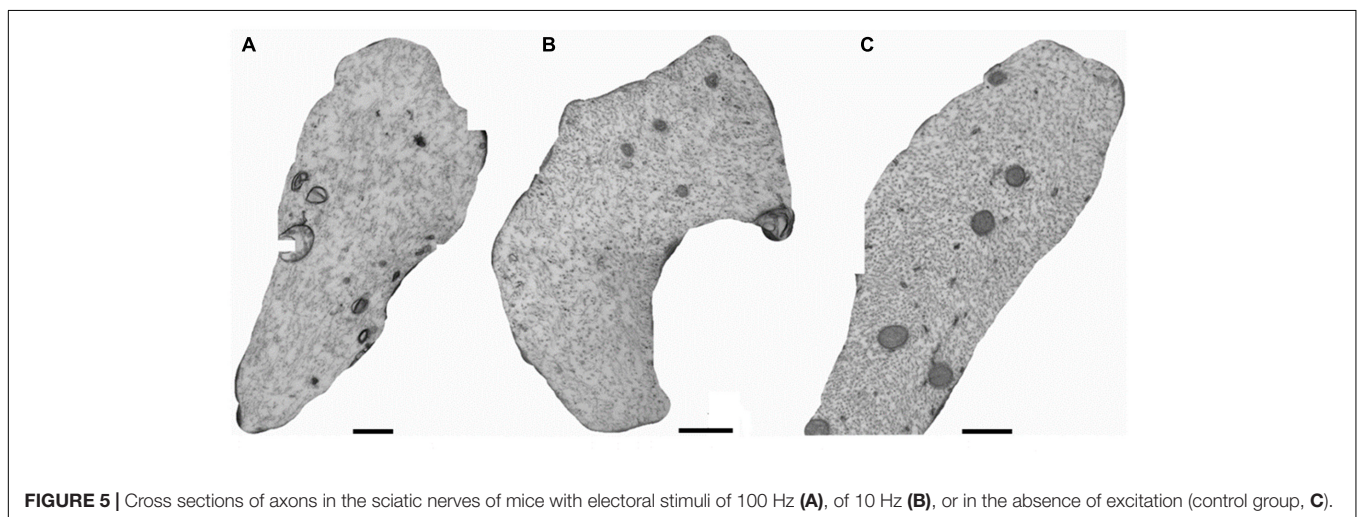
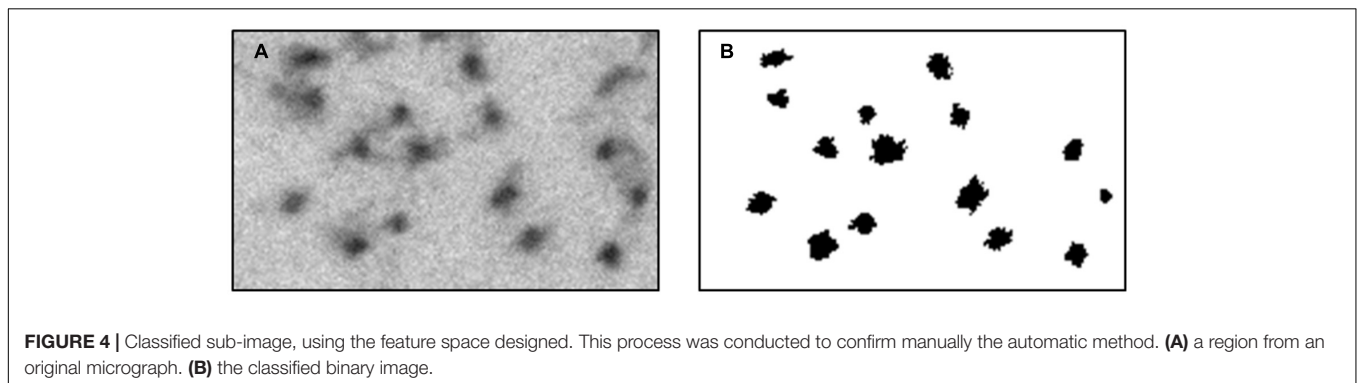
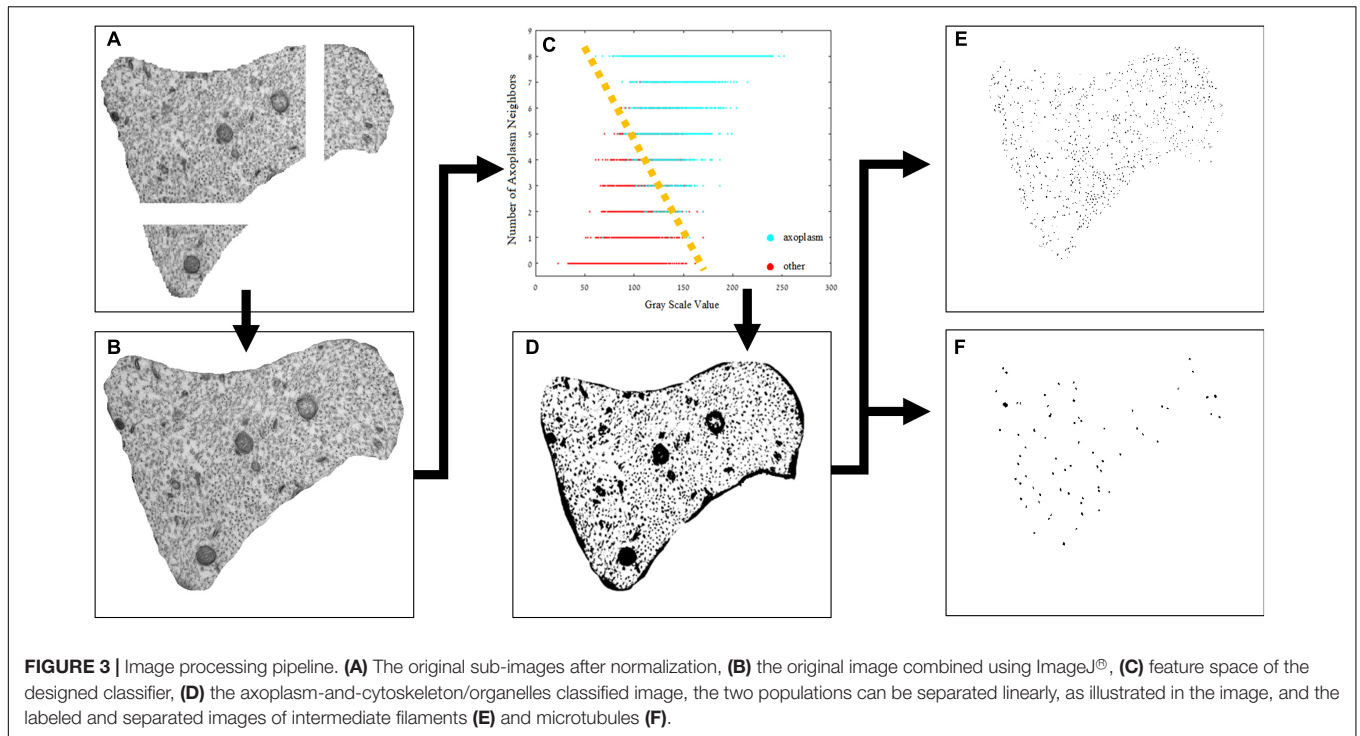
Normality of the distribution of each extracted parameter was tested using the Kolmogorov–Smirnov test. Most of the parameters were found to be distributed non-normally. To test the significance of differences across groups, we thus used the Kruskal–Wallis test, and whenever a statistical difference was found, we performed Mann–Whitney tests, with Bonferroni correction for multiple measurements, to find which are the groups that differ significantly.

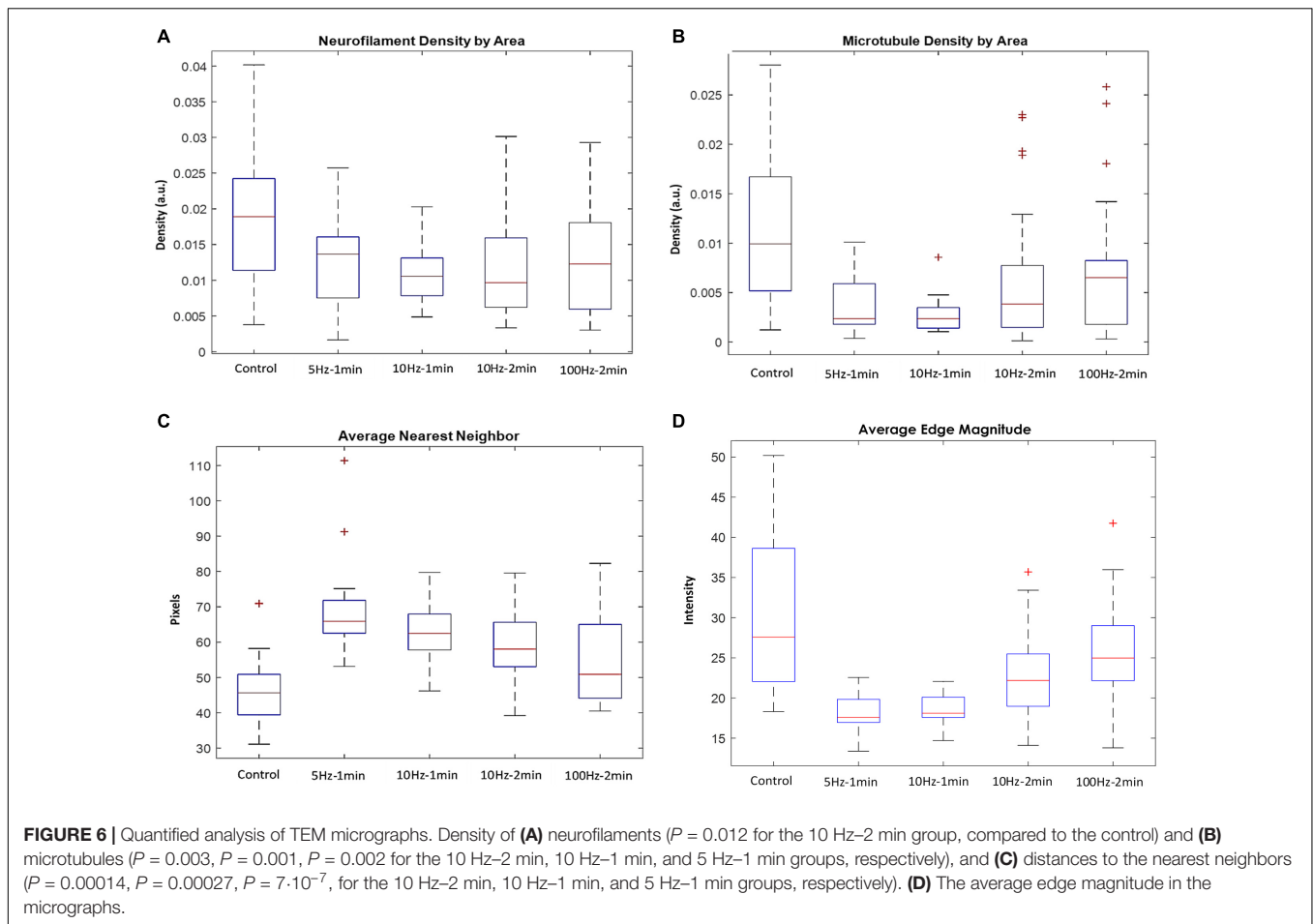
To test the correlations between the different factors (given non-normal distribution), we used the Spearman correlation and then corrected the *P*-values for multiple comparisons, using the Benjamini–Hochberg (BH) correction.

RESULTS

Representative micrographs of specific axons from the 100 Hz excitation (**Figure 5A**) and the 10 Hz (**Figure 5B**) excitation exhibit loss of densities of axial neurofilaments and microtubules from the lumen compared to the control non-excited group (**Figure 5C**).

A significant drop in the density of neurofilaments (**Figure 6A**) and microtubules (**Figure 6B**) was identified in the axon stimulated groups compared to the controls. For example, 10 Hz stimulations with durations of 1 and 2 min, resulted in neurofilaments density that dropped to 55.8 and 51.1% of the baseline median values, respectively. In the same experiments, microtubules density dropped to 23.7 and 38.5% of the baseline median values, respectively. Similar changes appear also in the 5 Hz stimulation group. However, results of the 100 Hz stimulation group had a much stronger variance, and the cytoskeletal densities dropped to more moderate values. The changes resulting due to stimulations with 10 and 5 Hz were statistically significant for both neurofilaments ($P = 0.012$ for





the 10 Hz–2 min group, compared to the control) and for the microtubules ($P = 0.003$, $P = 0.001$, $P = 0.002$ for the 10 Hz–2 min, 10 Hz–1 min, and 5 Hz–1 min groups, respectively). Changes in the distances to the nearest neighbors, compared to controls were also statistically significant ($P = 0.00014$, $P = 0.00027$, $P = 7 \cdot 10^{-7}$, for the 10 Hz–2 min, 10 Hz–1 min, and 5 Hz–1 min groups, respectively).

Furthermore, the average distance of both microtubules and neurofilaments from their nearest neighbors significantly increased in the stimulated axons compared to the control (**Figure 6C**), indicating that these changes are local, throughout the entire axonal sections, rather than the outcomes of specific regions that bias the calculated averages. Interestingly, the control group and the group excited with a 100 Hz stimulation display the highest variability in the densities of the microtubules and neurofilaments and the distance to the nearest neighbor. No statistical significance was found for the comparison of the 100 Hz stimulation group with the control group.

Quantifying the average magnitude of the edges in the micrographs (in between cytoskeletal objects and the lumen) links the electric activity to the presence of electron-dense molecules, such as cytoskeletal debris in the lumen. Indeed, the sharpness of the edges is attenuated in the micrographs of the excited nerves (**Figure 6D**). The highest variability within axons

of the same group was documented in the control group and the group of axons stimulated with 100 Hz. The substantial variability in these two groups is also reflected in the correlation between the densities of microtubules and neurofilaments within each axon, with more “outlayers” in the control and the 100 Hz groups (**Figure 7**) relative to the other stimulated groups. It should be noted that additional changes appear in the micrographs, especially in these of axons stimulated with a 100 Hz stimulation, on top of the quantified cytoskeletal changes. These include loss of mitochondria, loss of the integrity of the myelin sheath and intrusions appearing in the myelin sheath. Occurrence of changes in the benign stimulation frequencies (5 and 10 Hz) should be further studies.

DISCUSSION

We show with this *in vivo* model, that axon stimulation results in immediate rearrangements of the cytoskeleton, reducing the density of the cytoskeletal mesh. We suggest that the changes we identify in the density of neurofilaments and microtubules along the axons (**Figure 6**) result from activating a defined, highly regulated cytoskeleton cleavage process. We further suggest that this cleavage process is linked in a way that has never been related

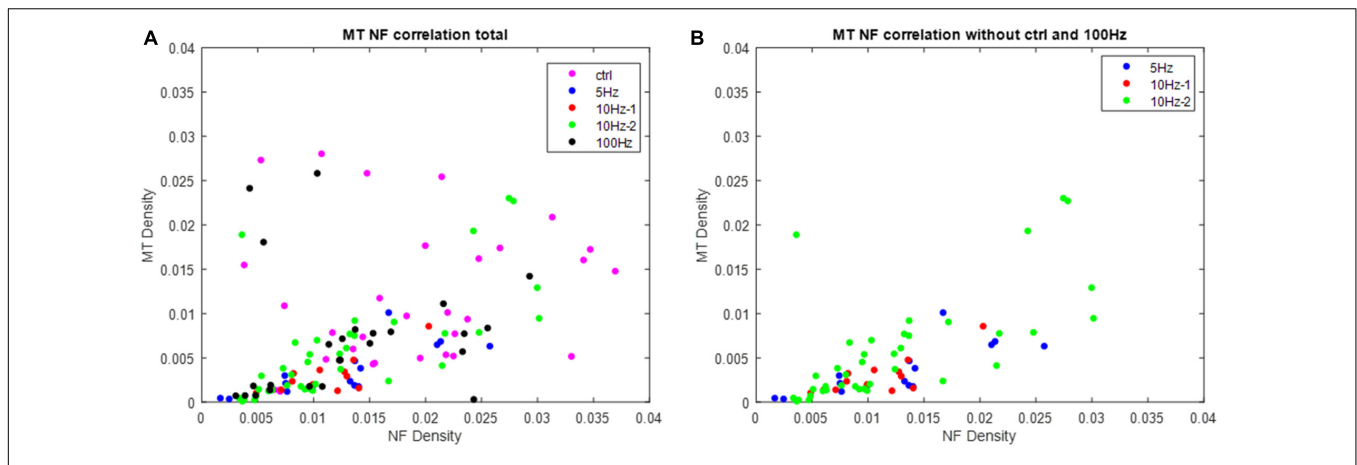


FIGURE 7 | The correlation between the densities of microtubules and neurofilaments. Each point represents a single axon. **(A)** Densities of microtubules and neurofilaments from all axons (group color coded). **(B)** Densities of microtubules and neurofilaments from the axons stimulated with 5 and 10 Hz stimulations. Notice the significant correlation in these groups and the reduction in densities relative to the control group ($P = 1 \cdot 10^{-3}$, $P = 0.034$, $P = 1 \cdot 10^{-7}$, for the 5 Hz–1 min, 10 Hz–1 min, and 10 Hz–2 min groups, respectively).

before to electrical activity. Action potentials are accompanied by an elevation in free calcium levels, both in the nerve cells and in their projections (Callewaert et al., 1996; Jia et al., 2011; Dana et al., 2019). It was further demonstrated in a model of neural axotomy that an elevation in free calcium levels induces activation of the Calpain protease that depolymerizes cytoskeletal proteins (Kamber et al., 2009). Moreover, depolymerization is pivotal in the creation of functional growth cones, following axotomy (Ziv and Spira, 1997). We suggest that a similar mechanism operates after electrical activity. Notice that Ca^{+2} concentration gradient across the cellular membrane exceeds these of other ions, since extracellular calcium concentration is $\times 10^4$ higher than that of the intracellular fluid (Jones and Keep, 1988). Once voltage gated channels open, the inflow of Ca^{+2} is very significant, and calcium transients can be detected even after a single action potential (Callewaert et al., 1996; Dana et al., 2019). Indeed, Hanemaaijer et al. (2020) demonstrated, with a model of pyramidal neurons, that single action potentials generate an immediate elevation in the calcium concentrations to near μM levels. The threshold for activation of $\mu\text{-Calpain}$ is Ca^{2+} concentration of 3–50 μM (Ma, 2013). Thus, these concentrations can be reached momentarily within a single train of action potentials and may trigger a proposed cascade of proteolytic activity – probably initiated in the cellular cortex – in a sub-second timescale. We suggest that in cases of repeated activity this depolymerization reduces the axonal stiffness. This initially results in axonal swelling and later on in beading. In even longer time-scales this activity-induced depolymerization facilitates a reduction of the stiffness that is a pre-requisite for growth. Our observation may thus reflect the first stage that can be followed later by axonal growth plasticity.

We observed changes in the density of microtubules that are opposite to some of the earlier results (Alvarez, 1979; Hu et al., 2008; Merriam et al., 2013). It is possible that the differences stem from differences in the experimental models used. However, it is also possible that we detected the initial outcome of the

stimulated activity, whereas some of the earlier observations are related to the late dynamics of the cytoskeleton. Given this interpretation, we assume that the process observed here is a reversible physiological process. In low level stimulation it facilitates growth. In more intense stimulation that involves an increased intracellular pressure, it facilitates volumetric extension of the axon, thereby preventing rupture of its membrane. In either case, in vital cells it should be followed by re-polymerization.

Note that the mechanical response described here is linked to “trains” of multiple spikes and not to single action potentials. In addition, the reversible effect of repolymerization most likely occurs in much longer timescales of minutes to hours. Thus, the process described and suggested here may be related to the observations of a propagating mechanical wave (Iwasa et al., 1980; Heimburg and Jackson, 2005; Mussel and Schneider, 2019), but is different from these observations.

As noted, our results demonstrate that the most substantial effect occurs in the 5/10 Hz–1 min stimulation groups. We speculate that the relative elevation in density in the 100 Hz stimulations may be linked to the beading of axons that creates shrunken segments with densely packed cytoskeletal proteins (Ochs et al., 1994). The elevation in the variability of the 100 Hz stimulation group also supports this, as the imaged axonal sections may include swollen or shrunken segments.

Additional experiments that will involve long term tracking of the cytoskeletal dynamics should further test the proposed mechanism of depolymerization by Ca^{+2} and Calpain and the proposed morphological kinetics that occur in different time scales.

Finally, we should highlight also the work of Lin and Cantiello (1993) and of Priel et al. (2006) that observed that cytoskeletal elements (actin and microtubules, respectively) act as “transmission lines” or non-linear transistors that amplify the conducted electrical signal in the neuron. If our view of the cytoskeletal dynamics is correct there is a possible link

between the de-polymerization and the adaptive nature of neuronal activity. This proposed link between Ca^{+2} triggered depolymerization and the results of Lin and Cantiello (1993) and of Priel et al. (2006) conforms with the observations that increase in Ca^{+2} level reduces firing frequency, and reduces the propagation velocity of action potentials (Lüscher et al., 1996).

To summarize, in this work we have demonstrated the immediate cytoskeletal changes that accompany neuronal excitation for the first time. Based on EM analysis, we suggest that electrical activity induced depolymerization of microtubules and neurofilaments. Awareness of this phenomenon may help expand our understanding of the biomechanical and chemical events during neuronal excitation. Our work may also have interesting neurophysiological implications on the understanding of the relationship between neuronal function and morphology as means of regulating adaptive neuronal activity, learning, and memory.

DATA AVAILABILITY STATEMENT

The original contributions presented in the study are included in the article/**Supplementary Material**, further inquiries can be directed to the corresponding author.

ETHICS STATEMENT

The animal study was reviewed and approved by the Institutional Animal Care and Use Committee (IACUC) of Tel Aviv University.

REFERENCES

- Alvarez, J. (1979). Microtubules in non-medullated fibres: effect of the action potential. *Neurosci. Lett.* 15, 15–17. doi: 10.1016/0304-3940(79)91521-0
- Callewaert, G., Eilers, J., and Konnerth, A. (1996). Axonal calcium entry during fast “sodium” action potentials in rat cerebellar Purkinje neurons. *J. Physiol.* 495, 641–647. doi: 10.1113/jphysiol.1996.sp021622
- Clerk Maxwell, J. (1874). Statique expérimentale et théorique des liquides soumis aux seules forces moléculaires. *Nature* 10, 119–121.
- Dana, H., Sun, Y., Mohar, B., Hulse, B. K., Kerlin, A. M., Hasseman, J. P., et al. (2019). High-performance calcium sensors for imaging activity in neuronal populations and microcompartments. *Nat. Methods* 16, 649–657. doi: 10.1038/s41592-019-0435-6
- Hanemaaijer, N. A., Popovic, M. A., Wilders, X., Grasman, S., Pavón Arocas, O., and Kole, M. H. (2020). Ca^{2+} entry through Na V channels generates submillisecond axonal Ca^{2+} signaling. *eLife* 9:e54566. doi: 10.7554/eLife.54566
- Heglund, N. C., Taylor, C. R., and McMahon, T. A. (1974). Scaling stride frequency and gait to animal size: mice to horses. *Science* 186, 1112–1113. doi: 10.1126/science.186.4169.1112
- Heimburg, T., and Jackson, A. D. (2005). On soliton propagation in biomembranes and nerves. *Proc. Natl. Acad. Sci. U.S.A.* 102, 9790–9795. doi: 10.1073/pnas.0503823102
- Herbin, M., Hommet, E., Hanotin-Dossot, V., Perret, M., and Hackert, R. (2018). Treadmill locomotion of the mouse lemur (*Microcebus murinus*); kinematic parameters during symmetrical and asymmetrical gaits. *J. Comp. Physiol. A Neuroethol. Sens. Neural Behav. Physiol.* 204, 537–547. doi: 10.1007/s00359-018-1256-2

AUTHOR CONTRIBUTIONS

UN initiated the study. UN, BY, EP, EO, and AS designed the experiments. BY, TG, EO, TB-K, and AS performed the experiments. BY, YA, ND, TB-K, UN, and EO performed the analysis. UN, BY, TB-K, and EP wrote the manuscript. All authors contributed to the article and approved the submitted version.

FUNDING

This study was funded by the Israeli Science Foundation (ISF), grant number 1585/17 to UN.

ACKNOWLEDGMENTS

We wish to thank Yael Friedmann of the Hebrew University of Jerusalem, for performing the electron microscopy preparation and acquisition, Aya Vituri of the Statistical Consulting Lab in TAU for aid in the statistical analysis and Liz Salak for editing the manuscript.

SUPPLEMENTARY MATERIAL

The Supplementary Material for this article can be found online at: <https://www.frontiersin.org/articles/10.3389/fnmol.2021.757264/full#supplementary-material>

- Hodgkin, A. L., and Huxley, A. F. (1952). The components of membrane conductance in the giant axon of *Loligo*. *J. Physiol.* 116, 473–496. doi: 10.1113/jphysiol.1952.sp004718
- Hu, X., Viesselmann, C., Nam, S., Merriam, E., and Dent, E. W. (2008). Activity-dependent dynamic microtubule invasion of dendritic spines. *J. Neurosci.* 28, 13094–13105. doi: 10.1523/JNEUROSCI.3074-08.2008
- Iwasa, K., Tasaki, I., and Gibbons, R. C. (1980). Swelling of nerve fibers associated with action potentials. *Science* 210, 338–339. doi: 10.1126/science.7423196
- Jia, H., Rochefort, N. L., Chen, X., and Konnerth, A. (2011). In vivo two-photon imaging of sensory-evoked dendritic calcium signals in cortical neurons. *Nat. Protoc.* 6, 28–35. doi: 10.1038/nprot.2010.169
- Jones, H. C., and Keep, R. F. (1988). Brain fluid calcium concentration and response to acute hypercalcaemia during development in the rat. *J. Physiol.* 402, 579–593. doi: 10.1113/jphysiol.1988.sp017223
- Kamber, D., Erez, H., and Spira, M. E. (2009). Local calcium-dependent mechanisms determine whether a cut axonal end assembles a retarded endbulb or competent growth cone. *Exp. Neurol.* 219, 112–125. doi: 10.1016/j.expneurol.2009.05.004
- Lin, E. C., and Cantiello, H. F. (1993). A novel method to study the electrodynamic behavior of actin filaments. Evidence for cable-like properties of actin. *Biophys. J.* 65, 1371–1378. doi: 10.1016/S0006-3495(93)81188-3
- Lüscher, C., Lipp, P., Lüscher, H. R., and Niggli, E. (1996). Control of action potential propagation by intracellular Ca^{2+} in cultured rat dorsal root ganglion cells. *J. Physiol.* 490(Pt 2), 319–324. doi: 10.1113/jphysiol.1996.sp021146
- Ma, M. (2013). Role of calpains in the injury-induced dysfunction and degeneration of the mammalian axon. *Neurobiol. Dis.* 60, 61–79. doi: 10.1016/j.nbd.2013.08.010
- Merriam, E. B., Millette, M., Lombard, D. C., Saengsawang, W., Fothergill, T., Hu, X., et al. (2013). Synaptic regulation of microtubule dynamics in dendritic

- spines by calcium, F-actin, and drebrin. *J. Neurosci.* 33, 16471–16482. doi: 10.1523/JNEUROSCI.0661-13.2013
- Mitsuyama, F., Niimi, G., Kato, K., Hirose, K., Mikoshiba, K., Okuya, M., et al. (2008). Redistribution of microtubules in dendrites of hippocampal CA1 neurons after tetanic stimulation during long-term potentiation. *Ital. J. Anat. Embryol.* 113, 17–27.
- Murphy, T. H., Li, P., Betts, K., and Liu, R. (2008). Two-photon imaging of stroke onset in vivo reveals that NMDA-receptor independent ischemic depolarization is the major cause of rapid reversible damage to dendrites and spines. *J. Neurosci.* 28, 1756–1772. doi: 10.1523/JNEUROSCI.5128-07.2008
- Mussel, M., and Schneider, M. F. (2019). It sounds like an action potential: unification of electrical, chemical and mechanical aspects of acoustic pulses in lipids. *J. R. Soc. Interface.* 16:20180743. doi: 10.1098/rsif.2018.0743
- Ochs, S., Pourmand, R., Jersild, R. A. Jr., and Potter, C. G. (1994). The beaded form of myelinated nerve fibers. *Neuroscience* 61, 361–372. doi: 10.1016/0306-4522(94)90237-2
- Priel, A., Ramos, A. J., Tuszynski, J. A., and Cantiello, H. F. (2006). A biopolymer transistor: electrical amplification by microtubules. *Biophys. J.* 90, 4639–4643. doi: 10.1529/biophysj.105.078915
- Risher, W. C., Ard, D., Yuan, J., and Kirou, S. A. (2010). Recurrent spontaneous spreading depolarizations facilitate acute dendritic injury in the ischemic penumbra. *J. Neurosci.* 30, 9859–9868.
- Shefi, O., Golebowicz, S., Ben-Jacob, E., and Ayali, A. (2005). A two-phase growth strategy in cultured neuronal networks as reflected by the distribution of neurite branching angles. *J. Neurobiol.* 62, 361–368. doi: 10.1002/neu.20108
- Takano, T., Tian, G. F., Peng, W., Lou, N., Lovatt, D., Hansen, A. J., et al. (2007). Cortical spreading depression causes and coincides with tissue hypoxia. *Nat. Neurosci.* 10, 754–762. doi: 10.1038/nn1902
- Tasaki, I., Kusano, K., and Byrne, P. M. (1989). Rapid mechanical and thermal changes in the garfish olfactory nerve associated with a propagated impulse. *Biophys. J.* 55, 1033–1040. doi: 10.1016/S0006-3495(89)82902-9
- Zeng, L. H., Xu, L., Rensing, N. R., Sinatra, P. M., Rothman, S. M., and Wong, M. (2007). Kainate seizures cause acute dendritic injury and actin depolymerization in vivo. *J. Neurosci.* 27, 11604–11613. doi: 10.1523/JNEUROSCI.0983-07.2007
- Ziv, N. E., and Spira, M. E. (1997). Localized and transient elevations of intracellular Ca²⁺ induce the dedifferentiation of axonal segments into growth cones. *J. Neurosci.* 17, 3568–3579. doi: 10.1523/JNEUROSCI.17-10-03568.1997
- Conflict of Interest:** The authors declare that the research was conducted in the absence of any commercial or financial relationships that could be construed as a potential conflict of interest.
- Publisher's Note:** All claims expressed in this article are solely those of the authors and do not necessarily represent those of their affiliated organizations, or those of the publisher, the editors and the reviewers. Any product that may be evaluated in this article, or claim that may be made by its manufacturer, is not guaranteed or endorsed by the publisher.
- Copyright © 2021 Yehuda, Gradus Pery, Ophir, Blumenfeld-Katzir, Sheinin, Alon, Danino, Perlson and Nevo. This is an open-access article distributed under the terms of the Creative Commons Attribution License (CC BY). The use, distribution or reproduction in other forums is permitted, provided the original author(s) and the copyright owner(s) are credited and that the original publication in this journal is cited, in accordance with accepted academic practice. No use, distribution or reproduction is permitted which does not comply with these terms.



Failure to Upregulate the RNA Binding Protein ZBP After Injury Leads to Impaired Regeneration in a Rodent Model of Diabetic Peripheral Neuropathy

James I. Jones¹, Christopher J. Costa¹, Caitlin Cooney¹, David C. Goldberg¹, Matthew Ponticciello¹, Melanie W. Cohen¹, Wilfredo Mellado¹, Thong C. Ma^{1,2} and Dianna E. Willis^{1,2*}

OPEN ACCESS

Edited by:

Guilherme Lucas,
University of São Paulo, Brazil

Reviewed by:

Hugo Leite-Almeida,
University of Minho, Portugal
Thiago Mattar Cunha,
University of São Paulo, Brazil
Felipe A. Court,
Universidad Mayor, Chile
Arthur W. English,
Emory University, United States

*Correspondence:

Dianna E. Willis
diw2004@med.cornell.edu

Specialty section:

This article was submitted to
Pain Mechanisms and Modulators,
a section of the journal
Frontiers in Molecular Neuroscience

Received: 21 June 2021

Accepted: 16 November 2021

Published: 07 December 2021

Citation:

Jones JI, Costa CJ, Cooney C, Goldberg DC, Ponticciello M, Cohen MW, Mellado W, Ma TC and Willis DE (2021) Failure to Upregulate the RNA Binding Protein ZBP After Injury Leads to Impaired Regeneration in a Rodent Model of Diabetic Peripheral Neuropathy. *Front. Mol. Neurosci.* 14:728163. doi: 10.3389/fnmol.2021.728163

¹Burke Neurological Institute, White Plains, NY, United States, ²Feil Family Brain & Mind Research Institute, Weill Cornell Medicine, New York, NY, United States

Most diabetes patients eventually suffer from peripheral nerve degeneration. Unfortunately, there is no treatment for the condition and its mechanisms are not well understood. There is, however, an emerging consensus that the inability of peripheral nerves to regenerate normally after injury contributes to the pathophysiology. We have previously shown that regeneration of peripheral axons requires local axonal translation of a pool of axonal mRNAs and that the levels and members of this axonal mRNA pool are altered in response to injury. Here, we show that following sciatic nerve injury in a streptozotocin rodent model of type I diabetes, this mobilization of RNAs into the injured axons is attenuated and correlates with decreased axonal regeneration. This failure of axonal RNA localization results from decreased levels of the RNA binding protein ZBP1. Over-expression of ZBP1 rescues the *in vitro* growth defect in injured dorsal root ganglion neurons from diabetic rodents. These results provide evidence that decreased neuronal responsiveness to injury in diabetes is due to a decreased ability to alter the pool of axonal mRNAs available for local translation, and may open new therapeutic opportunities for diabetic peripheral neuropathy.

Keywords: axon, regeneration, RNA-binding protein, ZBP, neuropathy, DPN

INTRODUCTION

Axonal injury in the peripheral nervous system (PNS) conditions neurons for more rapid axonal regeneration; these neurons show more rapid elongation after a subsequent injury (McQuarrie, 1978; Forman et al., 1980; McQuarrie and Grafstein, 1981; Lankford et al., 1998). Nerve injury is accompanied by a characteristic increase in the levels of many extracellular factors, such as neurotrophins and cAMP, which are known to enhance axonal growth. Neurons are large, polarized cells with morphologically and functionally distinct sub-cellular domains that are determined by the proteins that reside in these regions (Craig and Banker, 1994). mRNA sorting and localized

protein synthesis contribute to the targeting of proteins to specific sub-cellular domains of neurons, including the axonal compartment, which has the ability to locally generate new proteins. Indeed, studies from several groups, including our own, indicate that the capacity for intra-axonal protein synthesis is retained into adulthood (Koenig et al., 2000; Zheng et al., 2001; Hanz et al., 2003; Perlson et al., 2005; Verma et al., 2005; Willis et al., 2005, 2007; Gumy et al., 2011). Our results show that several hundred mRNAs extend into adult rodent dorsal root ganglion (DRG) axons and that the breadth of axonally synthesized proteins is much more complex than initially predicted (Willis et al., 2005, 2007; Gumy et al., 2011). We have also shown that regenerating axons of injury-conditioned (DRG) neurons are capable of local protein synthesis during rapid axonal regeneration (Willis et al., 2005, 2007). Together, the results of these studies indicate that localized protein synthesis plays a critical role in axonal regeneration.

Axonal protein synthesis can be regulated by extracellular stimuli such as chemotrophic signaling (Campbell and Holt, 2001, 2003; Brittis et al., 2002; Ming et al., 2002; Brunet et al., 2005; Piper et al., 2005; Wu et al., 2005). Some mRNAs are present in mature axons prior to any stimulation from the environment, and other mRNAs are upregulated only after specific extracellular cues. Among the triggers for axonal mRNA localization is injury. Following sciatic nerve injury, the mRNA encoding β -actin is increased in the axon. As is common for the sub-cellular localization of many mRNAs, the information ‘tagging’ an mRNA for axonal localization is inherent to its sequence (Bassell and Kelic, 2004). For β -actin, binding of the RNA-binding protein (RBP) ZBP1 to the “zipcode” element in its 3’UTR assembles this transcript into granules and directs its axonal localization (Zhang et al., 2001; Gu et al., 2002; Tiruchinapalli et al., 2003). The 3’UTR of rat β -actin mRNA, with its zipcode, is sufficient for regulated axonal transport in response to both attractive and repulsive axonal guidance cues (Willis et al., 2007) and the increased axonal levels of β -actin mRNA following injury is dependent on *cis*-elements and *trans*-acting factors interaction. Reduction in the availability of ZBP1 results in a decrease in the axonal levels of its cargo mRNAs, including β -actin (Donnelly et al., 2011). Regulation of the levels of ZBP1, then, is critical to the successful regeneration of axons following injury.

The induction of regeneration associated gene (RAG) expression by axon injury indicates an active process by which injured neurons sense axonal damage to activate an adaptive response. This can be achieved by the disruption of the retrograde flow of target-derived trophic signals (i.e., loss of NGF; Raivich et al., 1991; Gold et al., 1993), activation of existing or newly synthesized local (axonal) factors that are retrogradely transported (i.e., DLK, JNK, STAT3, CREB; Hanz et al., 2003; Cavalli et al., 2005; Cox et al., 2008; Ben-Yaakov et al., 2012; Shin et al., 2012), and depolarization of the axon due to the disruption of the plasma membrane (i.e., Ca^{2+} influx leading to cAMP elevation; Ghosh-Roy et al., 2010; Cho et al., 2013). Ultimately, the arrival of these signals to the cell body drives the transcriptional changes that initiate a regenerative response. Much of the focus of this transcriptional response has been on

RAGs that are known to enhance the intrinsic growth capacity of axons; however, given the functionally coordinated nature of this response, it seems likely that other upregulated genes, such as RBPs, are critical to the regeneration response. Failure of this response would be predicted to decrease axonal regeneration.

At least two-thirds of diabetic patients show symptoms of peripheral nerve damage, making peripheral neuropathy one of the most frequent and debilitating complications of diabetes mellitus. Whereas the mechanisms underlying diabetic peripheral neuropathy remain largely unknown, nerve biopsies from diabetic patients show evidence of axonal degeneration and incomplete regeneration, demyelination, and microangiopathy (Dyck and Giannini, 1996). Despite the high incidence, morbidity and mortality, and economic burden of diabetic peripheral neuropathy (DPN), the pathophysiology of this disorder remains unclear. Diabetes is a complex metabolic disorder and several different factors have been postulated to cause DPN. These include hyperglycemia and its metabolic consequences, oxidative stress, hypoxia due to accelerated vasculopathy, and alterations in neurotrophic factors (Vinik, 1999). None of these postulates are mutually exclusive. The most distal target fields of the long peripheral nervous system (PNS) axons are generally first affected in DPN. The sheer distance separating the nerve ending from the cell body coupled with the potential causes of DPN may render PNS neurons less resistant to trauma in diabetes. The pathology of DPN likely results from the combined contribution of axonal atrophy, demyelination, and reduced axonal regeneration (Yasuda et al., 2003; Sango et al., 2017). Recent studies clearly demonstrate a reduction in regeneration rates in both type 1 and type 2 diabetic patients compared to controls (Khoshnoodi et al., 2019), suggesting that DPN may result from delayed and incomplete regeneration and accumulating damage. Animal studies have recapitulated this delayed regeneration, demonstrating an increase in PTEN, a known inhibitor of axonal regeneration, in the nerves of diabetic mice (Pham et al., 2018). This reduced regeneration is also apparent in *in vitro* cultures of sensory neurons from diabetic animals (De Gregorio and Ezquer, 2021). The underlying cause of this delayed regeneration is unknown. Decreased axonal transport has been demonstrated in experimentally diabetic animals (Hellweg et al., 1994; Delcroix et al., 1997; Fernyhough et al., 1998). Here, we tested whether the failure to properly transport mRNAs into peripheral nerve axons following injury contributes to defective axonal regeneration. We show that following sciatic nerve injury, dorsal root ganglion (DRG) neurons fail to upregulate the levels of ZBP1, resulting in attenuation of axonal β -actin levels and decreased axonal regeneration.

MATERIALS AND METHODS

Cell Culture

Dissociated DRG cultures were prepared as previously described (Twiss et al., 2000). For fluorescent microscopy, neurons were cultured at low density on poly-lysine/laminin coated glass coverslips. For isolation of axons, neurons were cultured in microfluidic devices (Millipore), pre-coated with poly-

lysine/laminin. Axons were isolated and tested for purity by RT-PCR as previously described (Willis and Twiss, 2011).

Plasmid Construct

A fusion construct for ZBP1-mCherry was used, the production of which has been described previously (Farina et al., 2003; Huttelmaier et al., 2005; Donnelly et al., 2011).

Animal Surgeries and Procedures

Use of animals conformed to the Burke-Cornell Institutional Animal Care and Use Committees (IACUC) guidelines under approved protocols.

Modeling Diabetes

Diabetes was experimentally induced in rats by administering a single low dose of cytotoxic streptozotocin (STZ). In each experimental series, 150 g Sprague Dawley rats were food-deprived for 4–6 h prior to STZ injection. Animals were weighed and fresh STZ prepared at a final concentration of 50 mg/ml. A 1 ml insulin syringe containing 45 mg/kg was used to inject i.p. into each rat. Rats were supplied with 10% sucrose water as the sole water source for 48 h after STZ injection in order to protect them from the sudden hypoglycemic period that occurs after the lysis of the islet cells by STZ. Body weight and glucose levels were measured at 72 h after STZ injection and at subsequent 1-week intervals (nonfasting plasma glucose levels of >250 mg/dl is defined as diabetic hyperglycemia; STZ animal levels typically range from 300 to 550 mg/dl). For blood testing, the rats were restrained in a soft towel, leaving 3–5 cm at the tip of the tail exposed for blood collection. A lancet device was pressed against the surface of the skin near the tip of the exposed tail and blood analyzed using a LifeScan OneTouch Ultra Blood Glucose Meter.

Sciatic Nerve Injury

For injury-conditioning and morphological studies of regeneration, rodents were subjected to sciatic nerve crush at mid-thigh as previously described (Smith and Skene, 1997). Briefly, the sciatic nerves of anesthetized animals were exposed and the right nerve was crushed twice for 15 s each using #0 Dumont forceps; the left sciatic nerve was exposed but not otherwise manipulated. To harvest tissues for immunofluorescence (IF), deeply anesthetized rats were perfused transcardially with PBS followed by 4% paraformaldehyde. Tissues were post-fixed with 4% paraformaldehyde for 2–4 h, and then cryoprotected at 4°C overnight in 30% sucrose. The tissues were processed for cryosectioning.

Sensory Testing

Thermal sensation and mechanical sensation were assessed using a plantar infra-red analgesia meter and Dynamic Plantar Aesthesiometer (Ugo Basile), respectively. For mechanical allodynia measures, after rats were habituated to the apparatus, the Dynamic Plantar Aesthesiometer pushed a thin filament with increasing force against the plantar surface of a hind paw from beneath and the aesthesiometer recorded the latency for paw withdrawal. The force was increased from 0 to 5 g within 10 s (ramp 0.5 g/s) and is then held at 5 g for an additional 10 s. Baseline paw withdrawal latency time was calculated as the mean

of five consecutive stimulations with a 5-min interval between repetitions. For thermal hyperalgesia measurement, each hind paw was tested three times with a 10 min interval between repetitions and averaged.

Functional Measures of Sensorimotor Regeneration

CatWalk XT (Noldus) automated gait analysis system, which uses a high-speed camera to record the placement of paws as rats cross a glass-floored corridor, was used to assess motor function following sciatic nerve injury. Briefly, the test is performed in a darkened room to allow illumination of the platform. A high-speed camera records the animal from below the platform and captures the gait *via* localized areas of light. Contact with the floor refracts internally reflected light, which appears as an illumination of the paw. This system assessed parameters of gait, including footprint area, paw pressure, limb swing speed, and toe spread. The accompanying Catwalk XT software labels each paw and provides objective measurements of the aforementioned parameters. The experimenter is blinded to the treatment groups during gait analysis of numerical output from Catwalk XT software. Each animal is required to make three passes across the apparatus. Animals were allowed to return to their home cage before each run. Scores are reported as mean \pm SEM.

Analyses of RNAs

DRGs were placed in lysis buffer (*RNAqueous* kit, Ambion) and homogenized using a Bioruptor sonicator (Diagenode). RNA was isolated from cultured cells with a *microRNAqueous* kit (Ambion) and treated with DNase prior to analysis. One-hundred nanogram of total RNA was used as a template to generate cDNA libraries (iScript, Biorad) by reverse transcription. Gene expression was assayed by real time PCR using TaqMan FAM-labeled probes (Life Technologies) with VIC-labeled GAPDH included as endogenous controls.

Immunostaining

Tissue sections were immersion-fixed in 4% paraformaldehyde for 2–4 h, cryoprotected overnight in 30% sucrose at 4°C, and then cryosectioned. Sections were warmed to room temperature, washed in PBS, and incubated in 20 mM glycine for 30 min followed by 0.25 M NaBH₄ for 30 min. For cultures, coverslips were fixed in 4% paraformaldehyde for 20 min and then rinsed in PBS. IF was then performed as described (Willis et al., 2005) using chicken anti-NFH (1:1,000; Millipore) and Alexa555 goat anti-chicken (1:1,000; Invitrogen) antibodies.

Calculation of Axonal Regeneration *In vivo*

For analyses of crushed nerves, sections were immunostained for chicken anti-NFH as above. Matched exposure images were captured proximal and distal to the crush site. Montages of each nerve were constructed to encompass \pm 1.5 mm from the injury site. NF+ axons were counted in every fourth longitudinal section of the sciatic nerve using NeuroLucida (MBF Biosciences) and total counts were calculated using the line transect method at -1.0 , -0.5 , 0 , 0.5 , and 1.0 mm from the center of the crush site as previously described (Donnelly et al., 2011). Some images were evaluated using a “thresholding method”. For this, montage

images for axonal markers were processed for thresholding (0–50) using *ImageJ*, and the mean pixel intensity per area was then measured in 100 μm bins. The “regeneration front” was determined as the bin relative to the crush site where signal thresholds were 50% of the proximal intact nerve.

***In situ* Hybridization**

Fluorescence *in situ* hybridization (FISH)/IF to detect axonal mRNAs and proteins in cultured DRG neurons was performed with digoxigenin-labeled oligonucleotide probes as previously described (Willis et al., 2007). Epifluorescence image sets from individual experiments were matched for exposure, gain and offset. *ImageJ* was used to quantify FISH signals (pixels/ μm^2) in the cell body or the distal 200 μm of the axon. For FISH/IF of sciatic nerve sections, multiplex *in situ* hybridization was performed according to the manufacturer’s instructions (Advanced Cell Diagnostics #320850). Briefly, 16 μm -thick fresh frozen sections were fixed in 4% paraformaldehyde, treated with Proteinase K, and hybridized with β -actin specific probe (#316741). Sections were imaged by confocal microscopy (Zeiss LSM 510) and analyzed using FIJI software (National Institutes of Health) by an experimenter blind to the animal group. Four sciatic nerve sections from each animal were analyzed and averaged. Neurofilament staining was used to identify axons within the sciatic nerves and create a mask for quantification. Images were thresholded into a binary signal and the percent area of fluorescent signal was quantified.

Quantitation of Axon Length

DRG neurons were collected 7 days following sciatic nerve crush and grown in culture for 24 h. After 24 h, cultures were fixed with 4% paraformaldehyde and then processed for fluorescence immunocytochemistry with an anti- β III-tubulin antibody (1:500, rabbit monoclonal; Epitomics). Neurons were then imaged within each well of a 96-well plate using a flash cytometer (Trophos). Total neurite length/neuron and cell body diameter were quantified using the neurite outgrowth application in Metamorph (Molecular Devices). Representative higher magnification images were taken with an inverted epifluorescence microscope. For analyses of crushed nerves, cryosections were immunostained for neurofilament (NF) and imaged on an epifluorescence microscope. NF positive axons were counted in every fourth longitudinal section of the sciatic nerve using NeuroLucida (MBF Biosciences), and total counts were calculated using the line transect method at -1.0 , -0.5 , 0 , 0.5 , and 1.0 mm from the center of the crush site (Hill et al., 2001).

cAMP Measurement

The sciatic nerve was removed, frozen in liquid nitrogen, homogenized in ice-cold 0.1 M hydrochloric acid, and centrifuged at $13,000\times g$ for 50 min at 4°C . cAMP in the supernatant was determined by a direct cAMP ELISA kit (Enzo Life Sciences). The optical density was read at 405 nm using a Microplate Reader, and the cAMP concentration was normalized to total protein.

db-cAMP Treatment of DRG Cultures

DRG neurons cultured as above were treated with db-cAMP (2 mM), total RNA was isolated, and cDNA libraries synthesized for gene expression analysis as above. In parallel experiments, cell lysates were collected from which 20 μg of protein was separated by SDS-PAGE and analyzed by Western blot for ZBP1 protein expression (Cell Signaling #D33A2, 1:1,000).

Statistical Analysis

All statistical analyses were performed using GraphPad Prism software version 8 (GraphPad Software Inc). Data were plotted as mean \pm SEM unless otherwise indicated from at least three independent experiments from separate primary cultures. The specific statistical tests used are indicated in the figure legends.

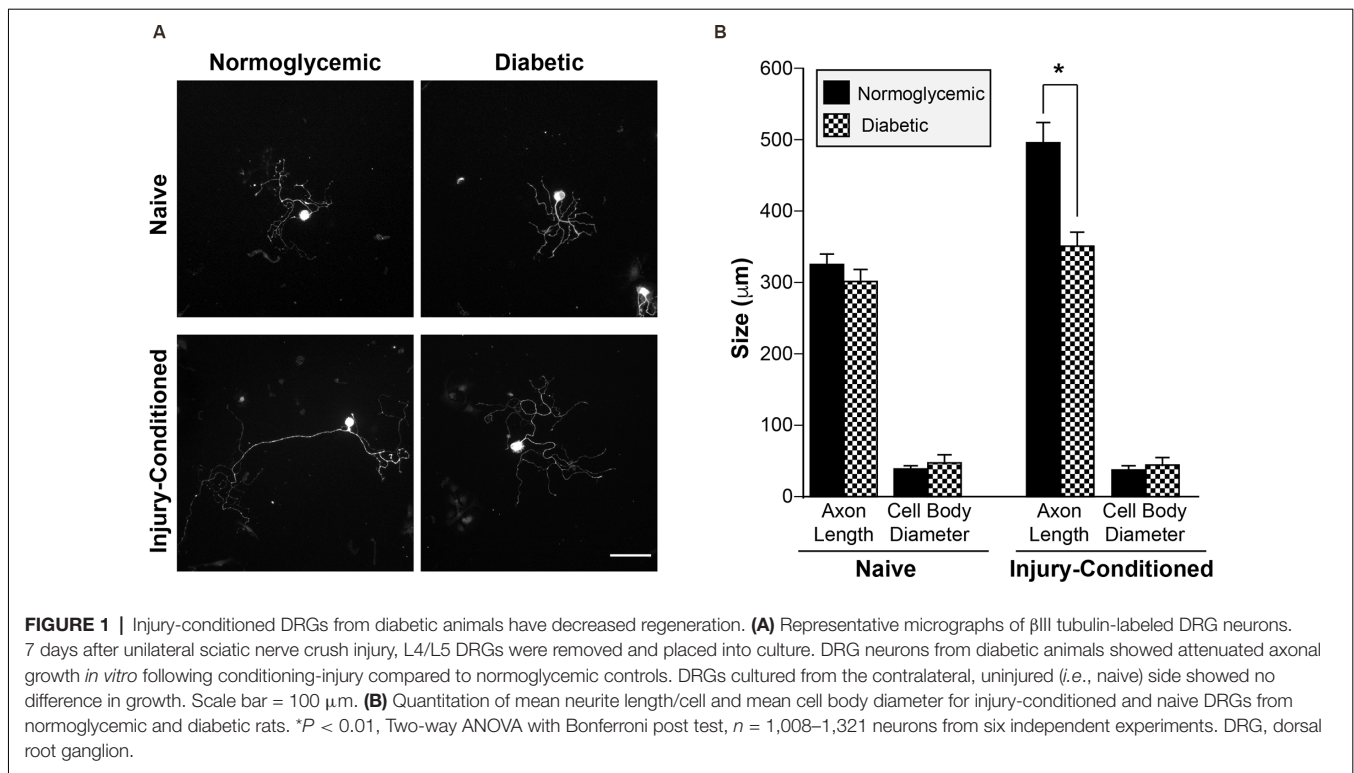
RESULTS

Adult Sensory Neurons From Diabetic Animals Grow Shorter Axons *In vitro* Following *In vivo* Injury Conditioning

In normoglycemic animals, an *in vivo* conditioning lesion to the sciatic nerve drives enhanced regeneration of the axons of subsequently cultured dorsal root ganglion (DRG) neurons *in vitro*. To determine whether sensory neurons from diabetic animals are able to generate a conditioning response enabling enhanced regeneration, we performed unilateral sciatic nerve crush injuries on control and diabetic animals. Seven days after crush, L4/L5 DRGs were removed and placed in culture to grow neurites for an additional 24 h. We refer to the processes of cultured DRG neurons as “axons” throughout the remainder of the text since MAP2 mRNA and protein are excluded from these processes and all processes from cultured DRGs are considered axonal in nature (Zheng et al., 2001; Donnelly et al., 2011). DRG neurons from diabetic and normoglycemic animals showed no differences in baseline axon growth *in vitro* in the absence of injury, whereas injury-conditioned DRGs from diabetic animals exhibited decreased axonal growth compared to normoglycemic rats (Figures 1A,B). This indicated that axonal growth *per se* was not deficient, but that the ability to mount the conditioning response that drives robust axonal regeneration was reduced. In addition, the size of the cell bodies in both naive and injury-conditioned DRGs did not differ in the normoglycemic and diabetic groups (Figures 1A,B). This suggests that the observed axon length differences are not due to changes in the overall composition of the DRG neuronal subtypes represented in our cultures and that the DRGs from diabetic animals do not exhibit gross morphological changes compared to control.

Delayed Recovery of Motor Function Following Injury Is Correlated With Altered Sensory Perception in Diabetic Animals

Mechanical allodynia and thermal hyperalgesia are common in the human diabetic population and in the STZ animal model. To confirm that our diabetic rats developed altered sensation, mechanical sensation thresholds were measured after induction of diabetes. Consistent with previous studies



characterizing diabetic neuropathy, our animals developed decreased mechanical withdrawal thresholds consistent with diabetic neuropathy at approximately 2 weeks after STZ injection (Figure 2A). Similar changes in thermal sensation were also observed (Figure 2B). To determine if altered peripheral sensitivity was accompanied by changes in the ability of the neurons to regenerate after injury, unilateral sciatic nerve crush injury was performed. CatWalk behavioral analysis revealed a delayed recovery of function following injury, with continued deficits in paw placement intensity up to 4 weeks following injury (Figure 2C). This delayed recovery of motor behavior correlated with decreased axonal regeneration *in vivo* following sciatic nerve injury. Histological examination of sciatic nerves following crush injury further demonstrates the reduction in the number of regenerating axons in diabetic animals compared to normoglycemic controls (Figures 2D–F). In diabetic rats, there were significantly fewer axons at points distal from the crush site compared to control animals. Taken together, these data support the conclusion that axon regeneration is decreased following injury in diabetic rats. This is consistent with a recent study from the Zigmond lab showing regenerative deficits in diabetic STZ mice (Niemi et al., 2017). It is important to note that the decrease in *in vivo* regeneration may also be consistent with the effect of the diabetic condition on Schwann cell redifferentiation and myelination.

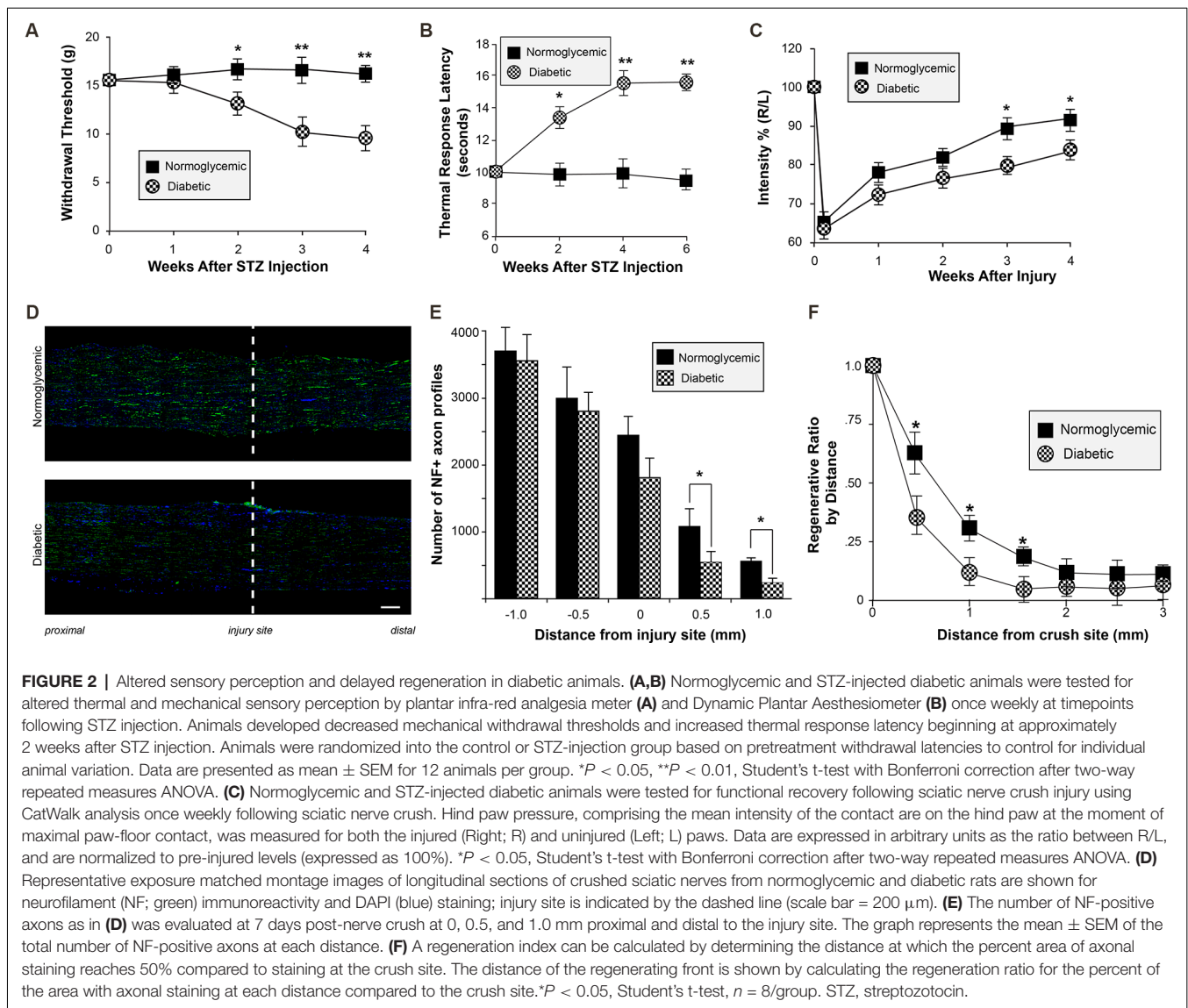
Reduced Levels of Axonal β -Actin mRNA in DRG Neurons From Diabetic Animals

To determine if the attenuated injury-conditioned regeneration is the result of a failure to properly localize mRNAs into the

axon for subsequent translation, we cultured DRG neurons in microfluidic devices in order to isolate axonal mRNAs (Figure 3A). In purity-verified axonal cultures from injury-conditioned diabetic DRGs, there were significantly lower axonal levels of β -actin mRNA (Figure 3B). In contrast, the levels of β -actin mRNA in axons from naive DRG neurons showed no difference between the diabetic and normoglycemic animals (Figure 3B). We confirmed this with quantitative fluorescent *in situ* hybridization (FISH) of DRGs cultures (Figures 3C,D) and sciatic nerves (Figures 3E,F) which also showed a significant reduction of axonal β -actin mRNA signal in diabetic animals compared to normoglycemic controls following injury-conditioning. Likewise, β -actin mRNA signal was not significantly different in naive axons, indicating that the diabetic animals failed to upregulate axonal β -actin mRNA in response to injury (Figure 3D). Decreased axonal levels of β -actin mRNA following injury in diabetic animals may be indicative of a global decrease in β -actin mRNA levels. We tested for this by performing quantitative FISH of DRG soma and found similar β -actin mRNA signals in each group following injury (not shown). This was further confirmed by real time PCR measurement of β -actin expression in RNA isolated from DRG cultures (not shown).

Levels of the β -Actin mRNA RNA-Binding Protein ZBP1 Are Attenuated in Diabetic Animals Following Injury

That the abundance of axonal level of β -actin mRNA levels was reduced following injury in diabetic animals, but total levels remained unchanged, suggested that axonal localization of β -



actin was attenuated. β -actin mRNA is transported through the activity of its RNA-binding protein ZBP1. To determine if the levels of ZBP1 are altered in diabetic animals, we measured the ZBP1 mRNA levels in DRGs from normoglycemic and diabetic animals at various times following sciatic nerve crush injury (Figure 4A). In normoglycemic animals, ZBP1 levels are low in uninjured DRGs and are increased approximately 3-fold by 7 days following an injury. By 14 days after an injury, the ZBP upregulation is reduced to a two-fold increase over uninjured. In diabetic animals, while the uninjured levels of ZBP1 are not significantly lower than the levels in uninjured DRGs from normoglycemic animals, injury-conditioning failed to upregulate ZBP1. We see a similar response in the ZBP1 protein levels (Figure 4B). This suggests that reduced ZBP1 following injury may limit the ability to transport cargo RNAs, such as β -actin mRNA, reducing regeneration in diabetic animals.

Limited Levels of ZBP1 Account for Reduced Axonal Levels of β -Actin mRNA and Decreased Axonal Growth in Diabetic DRGs

Since diabetic animals fail to upregulate the levels of ZBP1 following injury and exhibit decreased regeneration following injury, we investigated whether increasing ZBP1 could rescue axonal β -actin mRNA and facilitate axonal growth in DRG neurons cultured from diabetic animals. We transfected primary injury-conditioned DRG cultures with a ZBP1-mCherry fusion protein construct. After 2 days *in vitro* to allow for the expression of the construct, the ZBP1 transfection completely corrected the axonal β -actin mRNA deficit in DRGs from diabetic animals (Figure 5A). Similarly, the attenuation of growth in the cultures was corrected (Figures 5B,C).

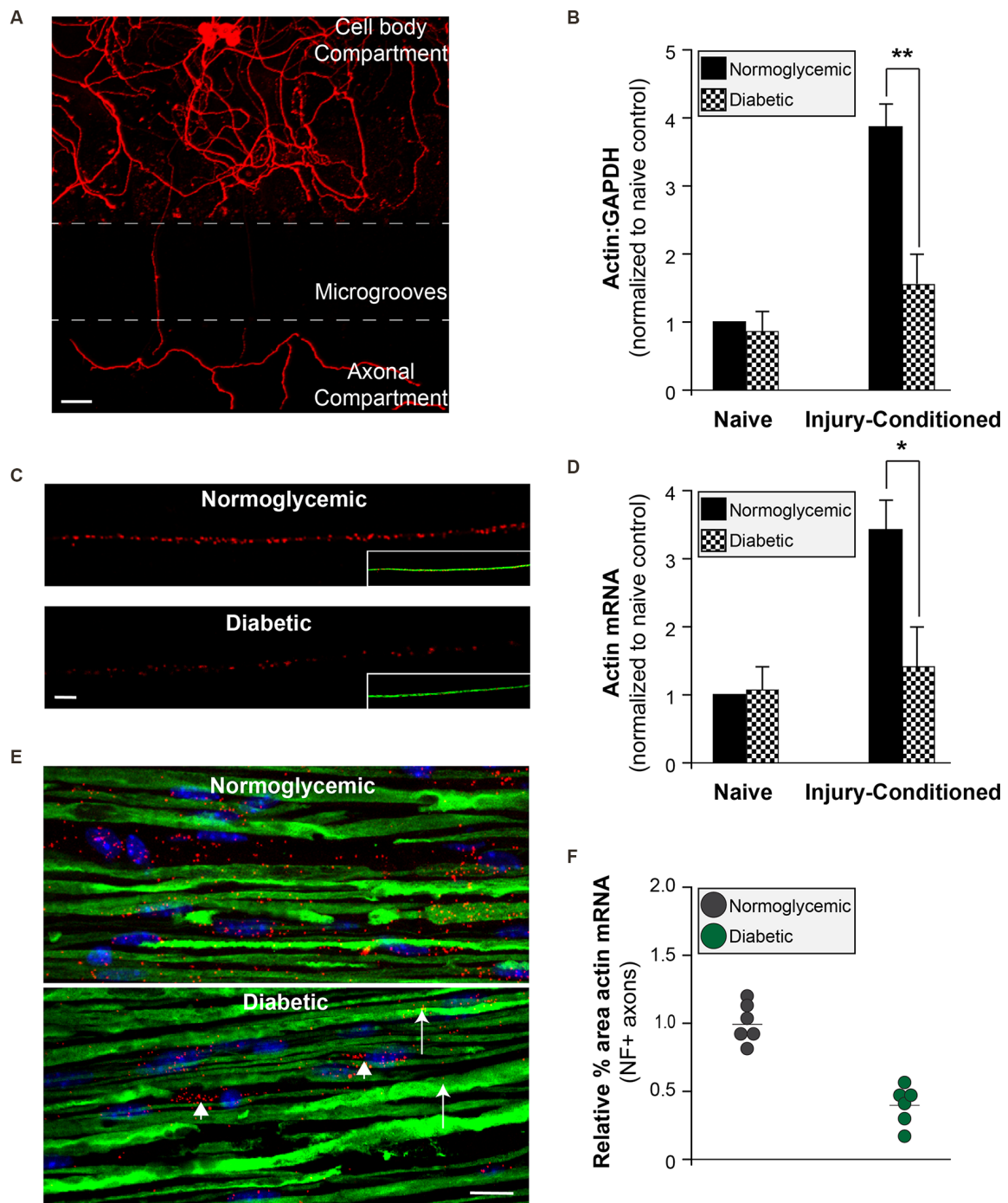
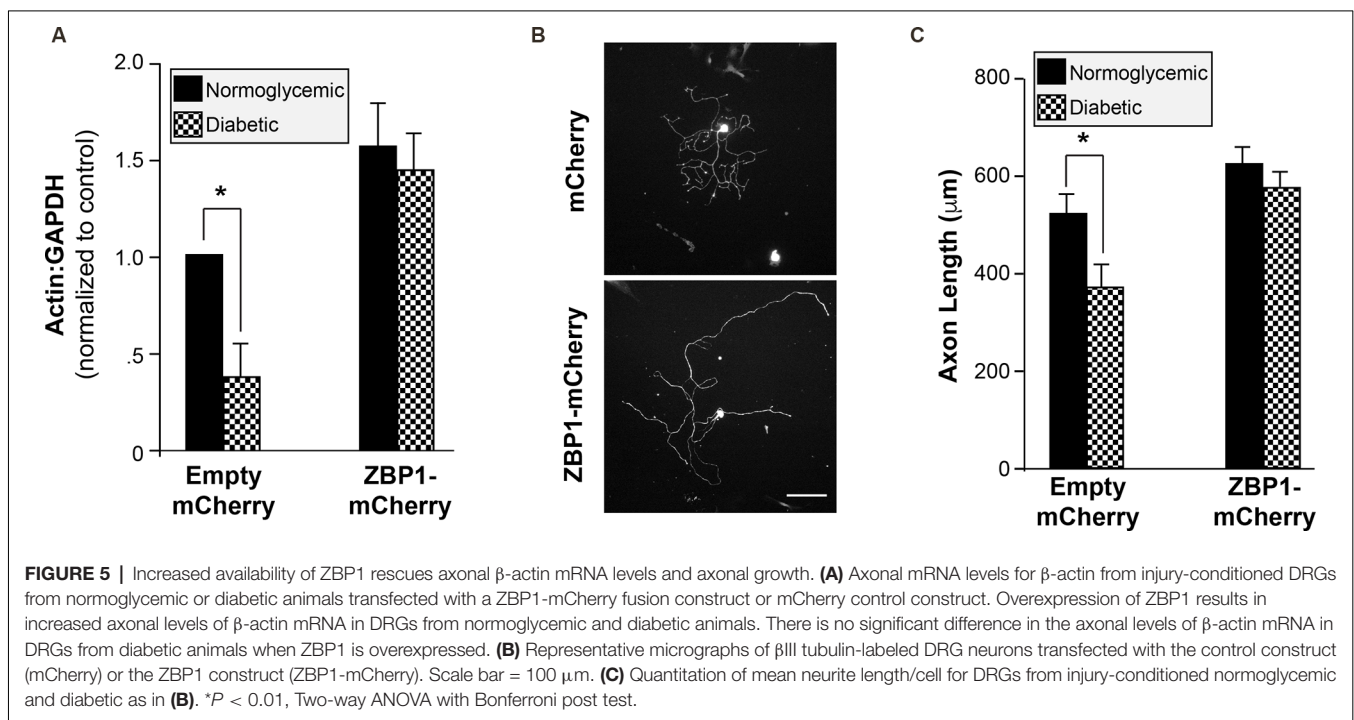
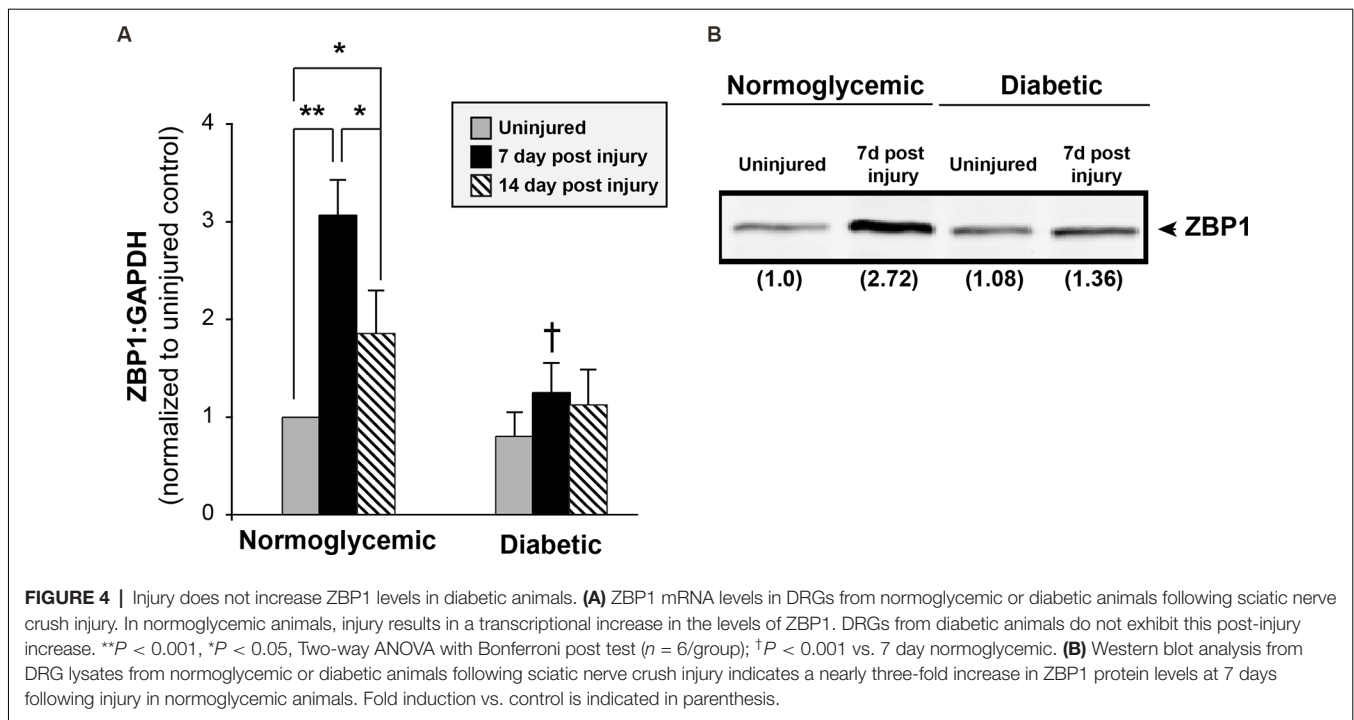


FIGURE 3 | Reduced axonal β -actin mRNA levels in diabetic animals. **(A)** Adult DRGs from normoglycemic or diabetic animals were cultured in microfluidic devices to isolate pure axonal RNA (scale bar = 50 μm). **(B)** Axonal mRNA levels for β -actin from injury-conditioned or naive DRGs from normoglycemic or diabetic animals. There is a significant decrease in the axonal levels of β -actin from diabetic animal only following injury-conditioning. $**P < 0.001$, Two-way ANOVA with Bonferroni post-test ($n = 6/\text{group}$). **(C)** Representative micrographs of FISH for β -actin mRNA (red) following injury-conditioning in normoglycemic and diabetic animals. Inset shows NF staining (green; scale bar = 10 μm). **(D)** Quantitative FISH signal intensity for axonal β -actin mRNA from DRG cultures is shown as average pixels/ $\mu\text{m}^2 \pm \text{SEM}$. Axonal β -actin mRNA was significantly decreased in the diabetic cultures compared to normoglycemic following injury-conditioning. $*P < 0.05$, Student's t -test, $n = 8/\text{group}$. **(E)** FISH on sciatic nerves indicates that compared to normoglycemic animals, diabetic animals have minimal β -actin mRNA (Red; arrows) in axons (NF staining; green). There is still abundant staining for β -actin mRNA in Schwann cells in the sciatic nerve (arrowheads; nuclear staining in blue). **(F)** The relative percentage of NF+ axons containing β -actin RNA signal. Neurofilament staining was used to identify axons within the sciatic nerves and create a mask for quantification. Images were thresholded into a binary signal and the percent area of fluorescent signal was quantified. Four sections per animal were imaged, quantified, and averaged. $*P < 0.05$, Student's t -test, $n = 6/\text{group}$. FISH, fluorescence *in situ* hybridization.



cAMP-Induced Expression of ZBP1 Is Lost in Diabetic Animals

Peripheral axon injury increases cAMP levels and activates the transcription of regeneration-associated genes; a response that is required for the regeneration of sensory neurons (Ma and Willis, 2015). cAMP levels in sciatic nerves of diabetic rats are significantly lower than normoglycemic animals (Shindo

et al., 1993a,b). To determine if diabetic animals failed to increase cAMP levels following injury, we measured cAMP in sciatic nerves of normoglycemic and diabetic rats before and after injury. Consistent with previous reports, diabetic animals showed a trend toward reduced basal levels of cAMP, though this did not reach significance (Figure 6A). Following injury, however, there was a significant reduction in the injury-induced

cAMP upregulation in sciatic nerves from diabetic animals compared with control normoglycemic animals (Figure 6A). We next tested whether ZBP1 levels could be altered in response to cAMP. DRGs treated with db-cAMP for 24 h showed increased levels of ZBP1 protein compared to untreated DRGs (Figure 6B). Consistent with this, we recorded an increase in ZBP1 mRNA levels after 8 h of db-cAMP treatment (Figure 6C). To test whether the failure to upregulate ZBP1 in DRGs from diabetic animals is due to the lack of elevated cAMP levels, we treated DRGs from diabetic animals with db-cAMP. After 24 h of db-cAMP treatment, there was a significant increase in ZBP1 mRNA levels compared to untreated (Figure 6D). Interestingly, ZBP1 levels did not reach those of DRGs from normoglycemic animals treated with db-cAMP for 24 h.

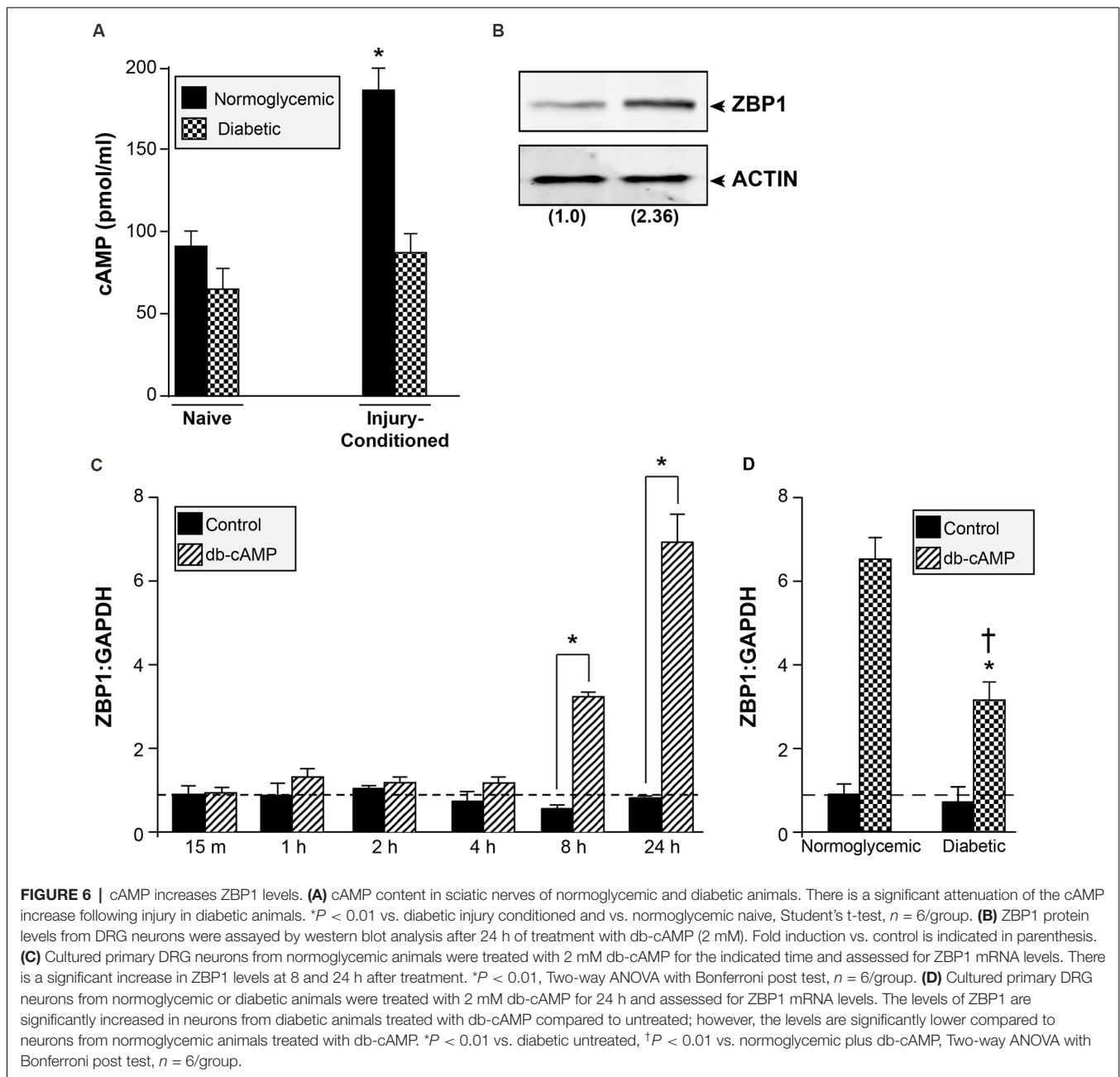
DISCUSSION

Despite the high incidence, morbidity and mortality, and economic burden of diabetic peripheral neuropathy (DPN), the pathophysiology of this disorder remains unclear. Several candidates have been postulated to cause DPN, including hyperglycemia and its metabolic consequences, oxidative stress, hypoxia due to accelerated vasculopathy, and alterations in neurotrophic factors (Vinik, 1999). Decreased axonal transport has also been reported in animal models of diabetes (Hellweg et al., 1994; Delcroix et al., 1997; Fernyhough et al., 1998), and could contribute to DPN pathophysiology. The most distal targets of the smallest PNS axons (e.g., nociceptive fibers) are generally first affected in DPN (Anand et al., 1994); the sheer distance separating the nerve ending from the cell body, coupled with the potential causes of DPN, may render PNS neurons less resistant to trauma in diabetes. Here, we demonstrate that axonal mRNA transport into these distal axons is compromised in diabetes, providing evidence in support of a previously unreported mechanism that could reduce the health of peripheral neuron axons.

In normoglycemic animals, an *in vivo* conditioning lesion to the sciatic nerve facilitates the subsequent regeneration of DRG axons. Here we show that diabetic animals appear unable to mount the full conditioning response that enables enhanced regeneration. Although injury-conditioned DRGs showed decreased axonal growth, uninjured DRG neurons showed no difference in growth, providing evidence that the ability to generate a conditioning response is reduced by diabetes. Since DRG cell-body sizes in both naive and injury-conditioned rats did not differ in the normoglycemic and diabetic groups, this suggests that axonal abnormalities are not due to changes in the overall composition of the DRG neuronal subtypes represented in our cultures; however, a more detailed analysis of the neuronal subtypes is required in order to completely discount this as a possibility. A regenerative deficit is also evident *in vivo* following injury, as both functional and morphological measurements of regeneration are attenuated following injury in diabetic animals. We have previously shown that regenerating axons of injury-conditioned DRG neurons are capable of local protein synthesis during rapid axonal regeneration and that this axonal protein synthesis is altered in response to injury signals (Willis et al.,

2005, 2007). Thus, the failure to properly mobilize mRNAs into the axons in response to injury has the potential to lead to deficits in axonal regeneration (Donnelly et al., 2011; Willis et al., 2011).

We have previously shown that ZBP1 levels are a limiting factor for regeneration. The present study, however, is the first report of a failure to upregulate ZBP1, leading to reduced axonal regeneration in a pathophysiological condition. The induction of gene expression by axon injury provides evidence for an active process by which injured neurons sense axonal damage to drive an adaptive response. This could be achieved by the disruption of the retrograde flow of target-derived trophic signals (i.e., loss of NGF; Raivich et al., 1991; Gold et al., 1993), activation of existing or newly synthesized local (axonal) factors that are retrogradely transported (i.e., DLK, JNK, STAT3, CREB; Hanz et al., 2003; Cavalli et al., 2005; Cox et al., 2008; Ben-Yaakov et al., 2012; Shin et al., 2012), and depolarization of the axon due to the disruption of the plasma membrane (i.e., Ca^{2+} influx leading to cAMP elevation; Ghosh-Roy et al., 2010; Cho et al., 2013). Ultimately, the arrival of these signals at the cell body would drive transcriptional changes that initiate a regenerative response. Whereas reduction in cAMP levels in the sciatic nerve of diabetic animals has been previously reported (Shindo et al., 1993a,b), here we show that this deficit is exacerbated following injury by a failure of cAMP to upregulate in response to injury. Reduced cAMP in peripheral nerves has been postulated to play a role in the pathogenesis of diabetic peripheral neuropathy, and here we present a possible mechanism for how the loss of cAMP can impact axonal function. It remains to be determined why cAMP levels in peripheral nerves are suppressed under diabetic conditions and the mechanism through which cAMP drives ZBP1 expression. In addition, when treated with db-cAMP in culture, DRGs from diabetic animals still do not upregulate the levels of ZBP1 to the same degree as those from normoglycemic animals. This suggests that the suppression of cAMP levels in the sciatic nerve of injured diabetic animals may account for some of the failure to upregulate ZBP1 levels. Additionally, it is likely that the neurons themselves are less responsive to the signal generated by cAMP. Understanding how the level of ZBP1 is regulated, and why its regulation fails following injury in the diabetic state, may provide new strategies to enhance axonal regeneration and overcome deficits that lead to peripheral neuropathy. Interestingly, there are considerable differences in many of the behavioral outcomes in diabetic rodent models, especially regarding thermal stimulation, with studies showing reduced, increased, or unchanged latencies (Miranda et al., 2021). The cause of these differences is unknown; however, variation in the experimental conditions, the strain of rodent used, or the age of the animals have all been postulated to explain these discordant results. Though the face validity of these rodent models is not necessarily recapitulated in this regard, the alteration in sensory processing is evident. It would be interesting to determine the extent to which these different perturbations in models, with their associated differences in thermal latency changes, correlate with altered dysregulation of ZBP1 levels and RNA axonal localization. In addition, RNA binding proteins other than ZBP1 could also be dysregulated, raising the possibility that multiple axonal RNAs are altered in



the diabetic state. Though we have focused on β -actin RNA as the canonical cargo for ZBP1 in this work, we have evidence that other ZBP1-cargos, such as GAP43 RNA, are also reduced (not shown), supporting our previous demonstration that ZBP1 levels are limiting for axonal transport of a “cassette” of RNAs (Donnelly et al., 2011). RNA profiling in axons from diabetic animals would help to determine the extent to which this is a global phenomenon resulting in widespread alteration in the axonal translome.

Absent from the results shown here is an understanding of the contribution that the Schwann cells play in both the failure to mount a full conditioning response and the subsequent reduced regeneration. These PNS glial cells are critical for the

proper function of the DRG neurons, and disease states such as diabetes have been shown to alter their function, resulting in neurodegeneration and pain. Indeed, evidence of mild axonal demyelination and remyelination is apparent even when the axon is normal, suggesting that Schwann cell abnormalities may be an early step in DPN pathology, and might be a primary cause of axonal damage (Malik et al., 2005; Gonçalves et al., 2018; Placheta-Györi et al., 2021). Experimental evidence supports a primary role for dysfunctional Schwann cells in the etiology of DPN. Exosomes isolated from Schwann cells grown in high glucose were sufficient to cause reduced axonal growth *in vitro* and the appearance of peripheral neuropathy characteristics *in vivo* (Jia et al., 2018). Given this, Schwann

cell-derived exosomes are an emerging interest as potential therapeutic approaches to treating DPN. A recent study by Poplawski and colleagues shows that Schwann cells can act to regulate gene expression in DRGs, especially those considered part of the RAG response and that this gene expression is altered when the Schwann cells are abnormal (Poplawski et al., 2018). These results point to a fundamental role for Schwann cell-sensory neuron communication in driving the regeneration response and may account for the failure to mount the conditioning response and upregulate ZBP1 shown here.

The prevailing theories for the underlying mechanism(s) driving diabetic peripheral neuropathy (DPN) are that either a dying back degeneration of axons or the accumulation of injuries along the length of the axon causes the distal-to-proximal progression that is common in DPN. In the first mechanism, the primary insult is thought to consist of impairment of synthesis and axonal transport of proteins, both in the anterograde and retrograde directions (Hellweg and Hartung, 1990; Delcroix et al., 1997; Fernyhough et al., 1998). This would naturally impact the longest axons of the body, and the most distal aspects of those axons, which are necessarily most dependent on proper axonal transport. The alternative possibility for the proximal-to-distal presentation is the accumulation of multiple injuries along the length of the axon (Dyck and Giannini, 1996; Thomas, 1999). Again, the longest axons would be more likely to accumulate these types of local injuries, resulting in their early dysfunction. The first mechanism assumes that it is loss of axonal *protein* transport that is the primary driver of axonal damage, rather than transport of alternative cargos such as mRNAs. The second mechanism does not account for the inability of the diabetic axons to repair injuries along the length of the axon, a process that under normal conditions is relatively robust. In addition, while evidence supporting either of these potential mechanisms exists, no emergent unifying theory encapsulating both of these possibilities while also accounting for the limitations described above has been described. Our data shown here account for both mechanisms as the underlying cause

of DPN and postulate a novel role for mRNA axonal transport in DPN.

DATA AVAILABILITY STATEMENT

The raw data supporting the conclusions of this article will be made available by the authors, without undue reservation.

ETHICS STATEMENT

The animal study was reviewed and approved by Weill Cornell Medical College Institutional Animal Care and Use Committee.

AUTHOR CONTRIBUTIONS

DW is the guarantor of this work and, as such, had full access to all data in the study and takes responsibility for the integrity of the data and the accuracy of the data analysis. JJ performed experiments, collected data, and wrote the manuscript (Figures 1–3). CJC performed experiments and collected data (Figure 3). CC performed experiments, collected data, and reviewed/edited the manuscript (Figures 1–4). DG, MP, and MC performed experiments and collected data (Figure 2). WM performed experiments, contributed to discussion and planning of experiments (Figure 5). TM performed experiments, collected and analyzed data, contributed to discussion and planning of experiments, and reviewed/edited the manuscript (Figures 1, 6). DW researched data and wrote the manuscript (Figure 6). All authors contributed to the article and approved the submitted version.

FUNDING

This work was supported by grants from the American Diabetes Association (1-12-BS-227; DW), NIH (National Institute of Nursing Research; NR010797; DW), and the Burke Foundation (DW).

REFERENCES

- Anand, P., Warner, G., and Parret, A. (1994). Nerve growth factor related small fiber dysfunction in human diabetic neuropathy. *Ann. Neurol.* 36:284A.
- Bassell, G. J., and Kelic, S. (2004). Binding proteins for mRNA localization and local translation and their dysfunction in genetic neurological disease. *Curr. Opin. Neurobiol.* 14, 574–581. doi: 10.1016/j.conb.2004.08.010
- Ben-Yakov, K., Dagan, S. Y., Segal-Ruder, Y., Shalem, O., Vuppalanchi, D., Willis, D. E., et al. (2012). Axonal transcription factors signal retrogradely in lesioned peripheral nerve. *EMBO J.* 31, 1350–1363. doi: 10.1038/emboj.2011.494
- Britt, P. A., Lu, Q., and Flanagan, J. G. (2002). Axonal protein synthesis provides a mechanism for localized regulation at an intermediate target. *Cell* 110, 223–235. doi: 10.1016/s0092-8674(02)00813-9
- Brunet, I., Weinl, C., Piper, M., Trembleau, A., Volovitch, M., Harris, W., et al. (2005). The transcription factor Engrailed-2 guides retinal axons. *Nature* 438, 94–98. doi: 10.1038/nature04110
- Campbell, D. S., and Holt, C. E. (2001). Chemotropic responses of retinal growth cones mediated by rapid local protein synthesis and degradation. *Neuron* 32, 1013–1026. doi: 10.1016/s0896-6273(01)00551-7
- Campbell, D. S., and Holt, C. E. (2003). Apoptotic pathway and MAPKs differentially regulate chemotropic responses of retinal growth cones. *Neuron* 37, 939–952. doi: 10.1016/s0896-6273(03)00158-2
- Cavalli, V., Kujala, P., Klumperman, J., and Goldstein, L. S. B. (2005). Sunday Driver links axonal transport to damage signaling. *J. Cell Biol.* 168, 775–787. doi: 10.1083/jcb.200410136
- Cho, Y., Sloutsky, R., Naegle, K. M., and Cavalli, V. (2013). Injury-induced HDAC5 nuclear export is essential for axon regeneration. *Cell* 155, 894–908. doi: 10.1016/j.cell.2013.10.004
- Cox, L. J., Hengst, U., Gurskaya, N. G., Lukyanov, K. A., and Jaffrey, S. R. (2008). Intra-axonal translation and retrograde trafficking of CREB promotes neuronal survival. *Nat. Cell Biol.* 10, 149–159. doi: 10.1038/ncb1677
- Craig, A. M., and Banker, G. (1994). Neuronal polarity. *Ann. Rev. Neurosci.* 17, 267–310. doi: 10.1146/annurev.ne.17.030194.001411
- De Gregorio, C., and Ezquer, F. (2021). Sensory neuron cultures derived from adult db/db mice as a simplified model to study type-2 diabetes-associated axonal regeneration defects. *Dis. Model Mech.* 14:dmm046334. doi: 10.1242/dmm.046334
- Delcroix, J. D., Tomlinson, D. R., and Fernyhough, P. (1997). Diabetes and axotomy-induced deficits in retrograde axonal transport of nerve growth

- factor correlate with decreased levels of p75LNTR protein in lumbar dorsal root ganglia. *Brain Res. Mol. Brain Res.* 51, 82–90. doi: 10.1016/s0169-328x(97)00215-5
- Donnelly, C. J., Willis, D. E., Xu, M., Tep, C., Jiang, C., Yoo, S., et al. (2011). Limited availability of ZBP1 restricts axonal mRNA localization and nerve regeneration capacity. *EMBO J.* 30, 4665–4677. doi: 10.1038/emboj.2011.347
- Dyck, P. J., and Giannini, C. (1996). Pathologic alterations in the diabetic neuropathies of humans: a review. *J. Neuropathol. Exp. Neurol.* 55, 1181–1193. doi: 10.1097/00005072-199612000-00001
- Farina, K. L., Huttelmaier, S., Musunuru, K., Darnell, R., and Singer, R. H. (2003). Two ZBP1 KH domains facilitate beta-actin mRNA localization, granule formation and cytoskeletal attachment. *J. Cell Biol.* 160, 77–87. doi: 10.1083/jcb.200206003
- Fernyhough, P., Diemel, L. T., and Tomlinson, D. R. (1998). Target tissue production and axonal transport of neurotrophin-3 are reduced in streptozotocin-diabetic rats. *Diabetologia* 41, 300–306. doi: 10.1007/s001250050907
- Forman, D. S., McQuarrie, I. G., Labore, F. W., Wood, D. K., Stone, L. S., Braddock, C. H., et al. (1980). Time course of the condition lesion effect on axonal regeneration. *Brain Res.* 182, 180–185. doi: 10.1016/0006-8993(80)90842-2
- Ghosh-Roy, A., Wu, Z., Goncharov, A., Jin, Y., and Chisholm, A. D. (2010). Calcium and cyclic AMP promote axonal regeneration in *Caenorhabditis elegans* and require DLK-1 kinase. *J. Neurosci.* 30, 3175–3183. doi: 10.1523/JNEUROSCI.5464-09.2010
- Gold, B. G., Storm-Dickerson, T., and Austin, D. R. (1993). Regulation of the transcription factor c-JUN by nerve growth factor in adult sensory neurons. *Neurosci. Lett.* 154, 129–133. doi: 10.1016/0304-3940(93)90188-q
- Gonçalves, N. P., Vægter, C. B., and Pallesen, L. T. (2018). Peripheral glial cells in the development of diabetic neuropathy. *Front. Neurol.* 9:268. doi: 10.3389/fneur.2018.00268
- Gu, W., Pan, F., Zhang, H., Bassell, G., and Singer, R. (2002). A predominantly nuclear protein affecting cytoplasmic localization of beta-actin mRNA in fibroblasts and neurons. *J. Cell Biol.* 156, 41–51. doi: 10.1083/jcb.200105133
- Gumy, L. F., Yeo, G. S. H., Tung, Y. C. L., Zivraj, K. H., Willis, D., Coppola, G., et al. (2011). Transcriptome analysis of embryonic and adult sensory axons reveals changes in mRNA repertoire localization. *RNA* 17, 85–98. doi: 10.1261/rna.2386111
- Hanz, S., Perlson, E., Willis, D., Zheng, J. Q., Massarwa, R., Huerta, J. J., et al. (2003). Axoplasmic importins enable retrograde injury signaling in lesioned nerve. *Neuron* 40, 1095–1104. doi: 10.1016/s0896-6273(03)00770-0
- Hellweg, R., and Hartung, H. D. (1990). Endogenous levels of nerve growth factor (NGF) are altered in experimental diabetes mellitus: a possible role for NGF in the pathogenesis of diabetic neuropathy. *J. Neurosci. Res.* 26, 258–267. doi: 10.1002/jnr.490260217
- Hellweg, R., Raivich, G., Hartung, H. D., Hock, C., and Kreutzberg, G. W. (1994). Axonal transport of endogenous nerve growth factor (NGF) and NGF receptor in experimental diabetic neuropathy. *Exp. Neurol.* 130, 24–30. doi: 10.1006/exnr.1994.1181
- Hill, C. E., Beattie, M. S., and Bresnahan, J. C. (2001). Degeneration and sprouting of identified descending supraspinal axons after contusive spinal cord injury in the rat. *Exp. Neurol.* 171, 153–169. doi: 10.1006/exnr.2001.7734
- Huttelmaier, S., Zenklusen, D., Lederer, M., Dichtenberg, J., Lorenz, M., Meng, X., et al. (2005). Spatial regulation of beta-actin translation by Src-dependent phosphorylation of ZBP1. *Nature* 438, 512–515. doi: 10.1038/nature04115
- Jia, L., Chopp, M., Wang, L., Lu, X., Szalad, A., and Zhang, Z. G. (2018). Exosomes derived from high-glucose-stimulated Schwann cells promote development of diabetic peripheral neuropathy. *FASEB J.* 32:fj201800597R. doi: 10.1096/fj.201800597R
- Khoshnoodi, M., Truelove, S., and Polydefkis, M. (2019). Effect of diabetes type on long-term outcome of epidermal axon regeneration. *Ann. Clin. Transl. Neurol.* 6, 2088–2096. doi: 10.1002/acn3.50904
- Koenig, E., Martin, R., Titmus, M., and Sotelo-Silveira, J. R. (2000). Cryptic peripheral ribosomal domains distributed intermittently along mammalian myelinated axons. *J. Neurosci.* 20, 8390–8400. doi: 10.1523/JNEUROSCI.20-22-08390.2000
- Lankford, K., Waxman, S., and Kocsis, J. (1998). Mechanisms of enhancement of neurite regeneration *in vitro* following a conditioning sciatic nerve lesion. *J. Comp. Neurol.* 391, 11–29. doi: 10.1002/(sici)1096-9861(19980202)391:1<11::aid-cne2>3.0.co;2-u
- Ma, T. C., and Willis, D. E. (2015). What makes a RAG regeneration associated?. *Front. Mol. Neurosci.* 8:43. doi: 10.3389/fnmol.2015.00043
- Malik, R. A., Tesfaye, S., Newrick, P. G., Walker, D., Rajbhandari, S. M., Siddique, I., et al. (2005). Sural nerve pathology in diabetic patients with minimal but progressive neuropathy. *Diabetologia* 48, 578–585. doi: 10.1007/s00125-004-1663-5
- McQuarrie, I. G. (1978). The effect of a conditioning lesion on the regeneration of motor axons. *Brain Res.* 152, 597–602. doi: 10.1016/0006-8993(78)91116-2
- McQuarrie, I. G., and Grafstein, B. (1981). Effect of condition lesion on optic nerve regeneration in goldfish. *Brain Res.* 216, 253–264. doi: 10.1016/0006-8993(81)90128-1
- Ming, G. L., Wong, S. T., Henley, J., Yuan, X. B., Song, H. J., Spitzer, N. C., et al. (2002). Adaptation in the chemotactic guidance of nerve growth cones. *Nature* 417, 411–418. doi: 10.1038/nature745
- Miranda, C. M., de Lima Campos, M., and Leite-Almeida, H. (2021). Diet, body weight and pain susceptibility—A systematic review of preclinical studies. *Neurobiol. Pain* 10:100066. doi: 10.1016/j.ynpai.2021.100066
- Niemi, J. P., Filous, A. R., DeFrancesco, A., Lindborg, J. A., Malhotra, N. A., Wilson, G. N., et al. (2017). Injury-induced gp130 cytokine signaling in peripheral ganglia is reduced in diabetes mellitus. *Exp. Neurol.* 296, 1–15. doi: 10.1016/j.expneurol.2017.06.020
- Perlson, E., Hanz, S., Ben-Yaakov, K., Segal-Ruder, Y., Segar, R., and Fainzilber, M. (2005). Vimentin-dependent spatial translocation of an activated MAP kinase in injured nerve. *Neuron* 45, 715–726. doi: 10.1016/j.neuron.2005.01.023
- Pham, V. M., Tu, N. H., Katano, T., Matsumura, S., Saito, A., and Yamada, A. (2018). Impaired peripheral nerve regeneration in type-2 diabetic mouse model. *Eur. J. Neurosci.* 47, 126–139. doi: 10.1111/ejn.13771
- Piper, M., Salih, S., Weinl, C., Holt, C. E., and Harris, W. A. (2005). Endocytosis dependent desensitization and protein synthesis-dependent resensitization in retinal growth cone adaptation. *Nat. Neurosci.* 8, 179–186. doi: 10.1038/nn1380
- Placheta-Györi, E., Brandstetter, L. M., Zemann-Schälls, J., Wolf, S., and Radtke, C. (2021). Myelination, axonal loss and schwann cell characteristics in axonal polyneuropathy compared to controls. *PLoS One.* 16:e0259654. doi: 10.1371/journal.pone.0259654
- Poplawski, G., Ishikawa, T., Brifault, C., Lee-Kubli, C., Regestam, R., Henry, K. W., et al. (2018). Schwann cells regulate sensory neuron gene expression before and after peripheral nerve injury. *Glia* 66, 1577–1590. doi: 10.1002/glia.23325
- Raivich, G., Hellweg, R., and Kreutzberg, G. W. (1991). NGF receptor-mediated reduction in axonal NGF uptake and retrograde transport following sciatic nerve injury and during regeneration. *Neuron* 7, 151–164. doi: 10.1016/0896-6273(91)90083-c
- Sango, K., Mizukami, H., Horie, H., and Yagihashi, S. (2017). Impaired axonal regeneration in diabetes. Perspective on the underlying mechanism from *in vivo* and *in vitro* experimental studies. *Front. Endocrinol. (Lausanne)* 8:12. doi: 10.3389/fendo.2017.00012
- Shin, J. E., Cho, Y., Beirowski, B., Milbrandt, J., Cavalli, V., and DiAntonio, A. (2012). Dual leucine zipper kinase is required for retrograde injury signaling and axonal regeneration. *Neuron* 74, 1015–1022. doi: 10.1016/j.neuron.2012.04.028
- Shindo, H., Tawata, M., and Onaya, T. (1993a). Cyclic adenosine 3',5'-monophosphate enhances sodium, potassium-adenosine triphosphatase activity in the sciatic nerve of streptozotocin-induced diabetic rats. *Endocrinology* 132, 510–516. doi: 10.1210/endo.132.2.7678791
- Shindo, H., Tawata, M., and Onaya, T. (1993b). Reduction of cyclic AMP in the sciatic nerve of rats made diabetic with streptozotocin and the mechanism involved. *J. Endocrinol.* 136, 431–438. doi: 10.1677/joe.0.1360431
- Smith, D. S., and Skene, P. (1997). A transcription-dependent switch controls competence of adult neurons for distinct modes of axon growth. *J. Neurosci.* 17, 646–658. doi: 10.1523/JNEUROSCI.17-02-00646.1997
- Thomas, P. K. (1999). Diabetic neuropathy: mechanisms and future treatment options. *J. Neurol. Neurosurg. Psychiatry* 67, 277–279. doi: 10.1136/jnnp.67.3.277
- Tiruchinapalli, D. M., Oleynikov, Y., Kelic, S., Shenoy, S. M., Hartley, A., Stanton, P. K., et al. (2003). Activity-dependent trafficking and dynamic

- localization of zipcode binding protein 1 and beta-actin mRNA in dendrites and spines of hippocampal neurons. *J. Neurosci.* 23, 3251–3261. doi: 10.1523/JNEUROSCI.23-08-03251.2003
- Twiss, J., Smith, D., Chang, B., and Shooter, E. (2000). Translational control of ribosomal protein L4 is required for rapid neurite extension. *Neurobiol. Dis.* 7, 416–428. doi: 10.1006/nbdi.2000.0293
- Verma, P., Chierzi, S., Codd, A. M., Campbell, D. S., Meyery, R. L., Holt, C. E., et al. (2005). Axonal protein synthesis and degradation are necessary for efficient growth cone regeneration. *J. Neurosci.* 25, 331–342. doi: 10.1523/JNEUROSCI.3073-04.2005
- Vinik, A. I. (1999). Diabetic neuropathy: pathogenesis and therapy. *Am. J. Med.* 107, 17S–26S. doi: 10.1016/s0002-9343(99)00009-1
- Willis, D. E., Li, K. W., Zheng, J.-Q., Smit, A. B., Kelly, T. K., Merianda, T. T., et al. (2005). Differential transport and local translation of cytoskeletal, injury-response and neurodegeneration protein mRNAs in axons. *J. Neurosci.* 25, 778–791. doi: 10.1523/JNEUROSCI.4235-04.2005
- Willis, D. E., and Twiss, J. L. (2011). Profiling axonal mRNA transport. *Methods Mol. Biol.* 714, 335–352. doi: 10.1007/978-1-61779-005-8_21
- Willis, D. E., van Niekerk, E. A., Sasaki, Y., Mesngon, M., Merianda, T. T., Williams, G. G., et al. (2007). Extracellular stimuli specifically regulate localized levels of individual neuronal mRNAs. *J. Cell Biol.* 178, 965–980. doi: 10.1083/jcb.200703209
- Willis, D. E., Xu, M., Donnelly, C. J., Tep, C., Kendall, M., Erenstheyn, M., et al. (2011). Axonal Localization of transgene mRNA in mature PNS and CNS neurons. *J. Neurosci.* 31, 14481–14487. doi: 10.1523/JNEUROSCI.2950-11.2011
- Wu, K. Y., Hengst, U., Cox, L. J., Macosko, E. Z., Jeromin, A., Urquhart, E. R., et al. (2005). Local translation of RhoA regulates growth cone collapse. *Nature* 436, 1020–1024. doi: 10.1038/nature03885
- Yasuda, H., Terada, M., Maeda, K., Kogawa, S., Sanada, M., Haneda, M., et al. (2003). Diabetic neuropathy and nerve regeneration. *Prog. Neurobiol.* 69, 229–285. doi: 10.1016/s0301-0082(03)00034-0
- Zhang, H. L., Eom, T., Oleynikov, Y., Shenoy, S. M., Liebelt, D. A., Dichtenberg, J. B., et al. (2001). Neurotrophin-induced transport of a beta-actin mRNP complex increases beta-actin levels and stimulates growth cone motility. *Neuron* 31, 261–275. doi: 10.1016/s0896-6273(01)00357-9
- Zheng, J.-Q., Kelly, T. K., Chang, B., Ryazantsev, S., Rajasekaran, A. K., Martin, K. C., et al. (2001). A functional role for intra-axonal protein synthesis during axonal regeneration from adult sensory neurons. *J. Neurosci.* 21, 9291–9303. doi: 10.1523/JNEUROSCI.21-23-09291.2001

Conflict of Interest: The authors declare that the research was conducted in the absence of any commercial or financial relationships that could be construed as a potential conflict of interest.

Publisher's Note: All claims expressed in this article are solely those of the authors and do not necessarily represent those of their affiliated organizations, or those of the publisher, the editors and the reviewers. Any product that may be evaluated in this article, or claim that may be made by its manufacturer, is not guaranteed or endorsed by the publisher.

Copyright © 2021 Jones, Costa, Cooney, Goldberg, Ponticello, Cohen, Mellado, Ma and Willis. This is an open-access article distributed under the terms of the Creative Commons Attribution License (CC BY). The use, distribution or reproduction in other forums is permitted, provided the original author(s) and the copyright owner(s) are credited and that the original publication in this journal is cited, in accordance with accepted academic practice. No use, distribution or reproduction is permitted which does not comply with these terms.



SARM1 Suppresses Axon Branching Through Attenuation of Axonal Cytoskeletal Dynamics

Andrea Ketschek¹, Sabrina M. Holland¹ and Gianluca Gallo^{1,2*}

¹ Shriners Hospitals Pediatric Research Center, Lewis Katz School of Medicine, Temple University, Philadelphia, PA, United States, ² Department of Neural Sciences, Lewis Katz School of Medicine, Temple University, Philadelphia, PA, United States

Axon branching is a fundamental aspect of neuronal morphogenesis, neuronal circuit formation, and response of the nervous system to injury. Sterile alpha and TIR motif containing 1 (SARM1) was initially identified as promoting Wallerian degeneration of axons. We now report a novel function of SARM1 in postnatal sensory neurons; the suppression of axon branching. Axon collateral branches develop from axonal filopodia precursors through the coordination of the actin and microtubule cytoskeleton. *In vitro* analysis revealed that cultured P0-2 dorsal root ganglion sensory neurons from a SARM1 knockout (KO) mouse exhibit increased numbers of collateral branches and axonal filopodia relative to wild-type neurons. In SARM1 KO mice, cutaneous sensory endings exhibit increased branching in the skin *in vivo* with normal density of innervation. Transient axonal actin patches serve as cytoskeletal platforms from which axonal filopodia emerge. Live imaging analysis of axonal actin dynamics showed that SARM1 KO neurons exhibit increased rates of axonal actin patch formation and increased probability that individual patches will give rise to a filopodium before dissipating. SARM1 KO axons contain elevated levels of drebrin and cortactin, two actin regulatory proteins that are positive regulators of actin patches, filopodia formation, and branching. Live imaging of microtubule plus tip dynamics revealed an increase in the rate of formation and velocity of polymerizing tips along the axons of SARM1 KO neurons. Stationary mitochondria define sites along the axon where branches may arise, and the axons of SARM1 KO sensory neurons exhibit an increase in stationary mitochondria. These data reveal SARM1 to be a negative regulator of axonal cytoskeletal dynamics and collateral branching.

Keywords: axon, SARM, actin, microtubule, cortactin, drebrin

INTRODUCTION

Morphogenesis of axons is a fundamental aspect of neurodevelopment. Although each neuron forms a single axon, the process of axon branching allows a single axon to form numerous connections with target neurons often in disparate regions of the nervous system (Lewis et al., 2013; Kalil and Dent, 2014; Menon and Gupton, 2018). A major form of axon branching is collateral axon branching wherein an axon gives rise to a new branch from along its shaft independent of the growth cone. Axon collateral branching is also of importance in the context of the response of the nervous system to injury, wherein branching induced in the injured scenario can be either

OPEN ACCESS

Edited by:

James N. Sleight,
University College London,
United Kingdom

Reviewed by:

Elisabetta Babetto,
University at Buffalo, United States
Lukas Neukomm,
University of Lausanne, Switzerland

*Correspondence:

Gianluca Gallo
Tue86088@temple.edu

Specialty section:

This article was submitted to
Neuroplasticity and Development,
a section of the journal
Frontiers in Molecular Neuroscience

Received: 17 June 2021

Accepted: 20 January 2022

Published: 21 February 2022

Citation:

Ketschek A, Holland SM and
Gallo G (2022) SARM1 Suppresses
Axon Branching Through Attenuation
of Axonal Cytoskeletal Dynamics.
Front. Mol. Neurosci. 15:726962.
doi: 10.3389/fnmol.2022.726962

adaptive or maladaptive (Onifer et al., 2011). Thus, understanding the cellular mechanisms of axon branching is of broad significance.

Collateral axon branching involves coordination of the axonal cytoskeleton (reviewed in Gallo, 2011; Kalil and Dent, 2014; Pacheco and Gallo, 2016; Armijo-Weingart and Gallo, 2017). The first step in collateral axon branching is formation of actin filament (F-actin)-dependent filopodia. Transient meshworks of dynamic F-actin along an axon, termed actin patches, serve as precursors to filopodia formation (reviewed in Gallo, 2011; Kalil and Dent, 2014). Promotion of axon branching by NGF involves upregulation of the rate of actin patch formation and, subsequently, formation of filopodia along axons (Ketschek and Gallo, 2010; Spillane et al., 2012). For a filopodium to mature into a branch, it must be invaded by an axonal microtubule. Stabilization of a microtubule within a filopodium allows the filopodium to mature into a branch, as it reorganizes its actin filament cytoskeleton, developing a small growth cone at its tip and increasing levels of microtubules. The cytoskeletal mechanism of axon branching has been shown to involve multiple actin and microtubule regulatory proteins, and it is strictly dependent on the coordination of actin and the cytoskeleton of microtubules (Pacheco and Gallo, 2016; Armijo-Weingart and Gallo, 2017). In the context of branching induced or suppressed by extracellular signals, the axis of PI3K signaling has been shown to have important roles in promoting the actin filament component of branching, including axonal translation of actin regulatory proteins important for branching, and PI3K signaling is impaired by branching inhibitory signals (reviewed in Gallo, 2011). Axonal organelles also have important roles in axon branching (reviewed in Winkle et al., 2016). Stationary mitochondria denote sites along an axon where axonal filopodia and, subsequently, branches develop (Courchet et al., 2013; Spillane et al., 2013; Tao et al., 2014; Sainath et al., 2017a). Increasing the motility of mitochondria and, thus, decreasing stationary mitochondria suppresses branching (Courchet et al., 2013); similarly, inhibiting the respiration of mitochondria suppresses branching (Spillane et al., 2013). Axonal mitochondria undergo transport into branches after their initial development and presumably power their continued extension (Spillane et al., 2013; Armijo-Weingart et al., 2019).

The TIR domain adaptor protein sterile alpha and TIR motif containing 1 (SARM1)/Myd-885 was initially considered to mediate aspect of immune function (Panneerselvam and Ding, 2015) and subsequently revealed to promote cell intrinsic axon Wallerian degeneration (Osterloh et al., 2012). Roles of SARM1 have also been described in neuronal cell death in toxic scenarios (Kim et al., 2007; Hou et al., 2013; Mukherjee et al., 2013; Summers et al., 2014). Knock down of SARM1 in hippocampal neurons results in decreased dendrite development and shorter axons (Chen et al., 2011). In neurons, SARM1 is mitochondrially targeted through an N-terminus-targeting sequence, although mitochondrial targeting is not required for its promotion of axon degeneration (Gerds et al., 2013). During the course of preliminary studies investigating the role of SARM1 in the regulation of microtubule loss during Wallerian degeneration, we noticed that cultured sensory neurons from SARM1 knockout

(KO) mice exhibited more complex axonal morphologies than wild-type counterparts. Here, we report that in sensory neurons, SARM1 KO results in increased axon branching due to the promotion of cytoskeletal dynamics underlying the formation of axonal filopodia and axonal microtubules plus tip dynamics, unveiling a negative regulatory role of SARM1 in the regulation of the axonal F-actin cytoskeleton.

MATERIALS AND METHODS

Culturing and Animals

The animal study was reviewed and approved by Temple University School of Medicine Institutional Animal Care and Use Committee. For culturing, pups were obtained from mating pairs of the same genotype: SARM1 KO (−/−) mice (Kim et al., 2007) and wild-type background C57BL/6. Mating pairs of SARM1 KO (−/−) and SARM1 wild type (WT, +/+) were initially derived from mating heterozygous (±) SARM1 KO pairs and genotyping the progeny, and then mating within genotype thereafter for subsequent mating.

Postnatal day (P) P0-2 mice were placed on ice for 10 min, and 1.5 DRGs were dissected per coverslip and placed in CMF-PBS + 5 mg/ml dispase (#11534200; Roche, Branchburg, NJ, United State) in 37° water bath for 15 min. A pellet was spun down for 30 s, and the supernatant was removed and replaced with trypsin (#MT25005CI; Thermo Fisher Scientific, Hampton, NH, United States) and placed back in the water bath. Following 10 min in trypsin, the pellet was spun down for 1 min, the supernatant was removed, and cells were re-suspended and triturated in 5 ml F12HS10. The cells were centrifuged for 5 min, the supernatant was removed, and the cells were re-suspended in a culturing medium containing F12H + 50 ng/ml NGF (#256-GF; R&D, Minneapolis, MN, United States). A 500-ml culturing medium containing dissociated cells was added to each coverslip or 300 μ l for each “videodish” (coverslip affixed to the bottom of a plastic Petri dish with a hole drilled in the center). The coverslips were coated using polylysine (100 μ g/ml (Cat # P9011; Sigma, St. Louis, MO, United States) and laminin (25 μ g/ml, Cat # 23017-015; Life Technologies, Carlsbad, CA, United States). Chondroitin sulfate proteoglycans (CSPG) substrata were prepared as previously described using embryonic day 14 chicken embryo CSPG mixtures (as in Silver et al., 2014; Sainath et al., 2017a,b).

The media used were as previously detailed (Lelkes et al., 2005). Briefly, the F12HS10 dissection medium consisted of Hams F12 1X with L-glutamine (#MT10080CV; Thermo Fisher Scientific, Hampton, NH, United States) containing 10% fetal bovine serum (#MT35011CV; Thermo Fisher Scientific, Hampton, NH, United States) and 1% HEPES 1M (#BP299-100; Thermo Fisher Scientific, Hampton, NH, United States). The F12H culturing medium consisted of F12 nutrient mix (#21700075; Thermo Fisher Scientific, Hampton, NH, United States) dissolved in 1 L of distilled water. The following ingredients were supplemented into the F12H culturing medium and were listed as final concentrations, 1% Hepes 1M (#BP299-100; Thermo Fisher Scientific, Hampton, NH, United States),

1% PSF (#BW17745E; Thermo Fisher Scientific, Hampton, NH, United States), 1% L-glutamine 200 mM (#MT25005CI; Thermo Fisher Scientific, Hampton, NH, United States), 4% sodium pyruvate 100 mM (#11360070; Thermo Fisher Scientific, Hampton, NH, United States). The F12H culturing medium was also supplemented with an additive cocktail containing the following ingredients: phosphocreatine (#P-7936; Sigma, St. Louis, MO, United States), apo-transferrin (#T-2252; Sigma, St. Louis, MO, United States), sodium selenate (#S-8295; Sigma, St. Louis, MO, United States), progesterone (#P-8783; Sigma, St. Louis, MO, United States), and insulin (#I-5500; Sigma, St. Louis, MO, United States).

Transfection and Plasmids

For transfection of plasmids into neurons, 30 mouse DRGs were dissociated as described above, and after F12HS10 was removed, neurons were suspended in a 100- μ l nucleofector solution (Cat# VPG-1002; Lonza) and gently resuspended through trituration. The DRG cell suspension was transferred to a nucleofector cuvette containing 15 μ g of plasmid DNA, and electroporated using Amaxa Nucleofector (program G-13). The electroporated solution was then immediately transferred to a tube containing the F12H medium as described above prior to plating. The mitochondrially targeted GFP expression plasmid used was previously described in Spillane et al. (2013), mCherry- β -actin as in Spillane et al. (2013), SARM1 (Chen et al., 2011; Addgene, #50707) was subcloned into pEGFP-N1 (Clontech), GFP-EB3 was as in Ketschek et al. (2007).

Immunocytochemistry

The following protocol was used for all staining purposes. Fixed cultures were blocked prior to each primary antibody application for 30 min using PBS supplemented with 10% goat serum (#G9023; Sigma, St. Louis, MO, United States) and 0.1% triton X-100 (#9002-93-1; Sigma, St. Louis, MO, United States) (GST). All antibodies were applied using GST. Primary and secondary antibody staining was performed at room temperature for 45 min. Washing in PBS was performed after primary and secondary staining. Prior to the coverslips being mounted with Vectashield (#H-1000; Vector), they were washed 3 \times with distilled water. Within a given experiment, replicates were initially fixed and stored in a blocking solution at 4°C until control and experimental samples could be stained in parallel on the same day prior to subsequent imaging.

To visualize cortactin (1:250, # AB11065, RRID:AB_297716; Abcam, Cambridge, United Kingdom) and Akt phosphorylated at T308 (pAkt; 1:100, #9275, RRID:AB329828; Cell Signaling Technology, Danvers, MA, United States), cultures were fixed with a final concentration of 4% PFA (#15710; EMS) and 5% sucrose (#S5-500; Thermo Fisher Scientific, Hampton, NH, United States). Secondary staining was performed using goat-anti-rabbit FITC (1:200, #F9887, RRID:AB_259816; Sigma, St. Louis, MO, United States). Actin filaments were stained using rhodamine phalloidin (1:20, #R415, RRID:AB_2572408; Invitrogen, Waltham, MA, United States). To visualize drebrin (1:100, M2F6, RRID:AB_299034; Abcam, Cambridge, United Kingdom), cultures were fixed with a final concentration

of 0.25% glutaraldehyde (#16300; EMS). Secondary staining was performed using goat-anti-mouse TRITC (1:400, #T5393, RRID:AB_261699; Sigma, St. Louis, MO, United States). Actin filaments were stained using DyLight 488 Phalloidin (1:20, Cat# 21833, RRID:AB_2532155; Thermo Fisher Scientific).

To determine the ratios of acetylated and tyrosinated tubulin compared to total tubulin, cultures were simultaneously fixed and extracted using 0.2% glutaraldehyde and 0.1% triton X-100 in a PHEM buffer (10 mM MES, 138 mM KCl, 3 mM MgCl, and 2 mM EGTA), followed by 15-min incubation with 2 mg/ml sodium borohydride (#Ac189301000; Thermo Fisher Scientific, Hampton, NH, United States) in CMF-PBS. Samples were stained with anti-acetylated tubulin (clone 6-11B-1) (1:100, #T6793, RRID:AB_477585; Sigma, St. Louis, MO, United States) or anti-tyrosinated tubulin (Tub1A2) (1:400, #T9028, RRID:AB_261811; Sigma, St. Louis, MO, United States). Secondary staining was performed with goat-anti-mouse TRITC (1:400, #T5393, RRID:AB_261699; Sigma, St. Louis, MO, United States). The samples were then blocked with 10% mouse serum for 20 min and counterstained with DM1A-FITC anti- α tubulin (1:100, #F2168, RRID:AB_476967; Sigma, St. Louis, MO, United States) to visualize total microtubule intensity.

Imaging

All imaging was performed using a Carl Zeiss 200M microscope equipped with an Orca ER camera (Hamamatsu, Shizuoka, Japan). Live cultures were placed in a heated microscope stage (Zeiss temperable insert P with objective heater) and kept at constant 39°C. Zeiss Live and fixed cultures were observed using a 100 \times , 1.3 numerical aperture objective for both phase and fluorescence microscopy. A time-lapse and quantitative analysis was performed using the interactive measurement module of the AxioVision Software. To visualize mitochondria, Mitotracker Red (0.05 nM, # M22425; Invitrogen, Waltham, MA, United States) was used according to the directions of the manufacturer. Cultures were incubated with a dye for 30 min, washed with a medium, and imaged 20 min following wash cycles. Acquisition rate was every 6 s for 10 min. For actin patch formation observation, cells were transfected with mCherry- β -actin. Images were taken every 6 s for 6 min. To visualize the tips of polymerizing microtubules, cells were transfected with GFP-EB3, and images were taken every 6 s for 5 min. Minimal light from a 100-W bulb was used, and 2 \times 2 camera binning was performed to increase sensitivity under low light exposure conditions.

Morphometrics

For analysis of the number of branches per unit length of axon in the stained samples to reveal microtubules and actin filaments, we followed the criteria previously defined in Spillane et al. (2013). Briefly, a collateral branch was defined as containing detectable stained microtubules and distally polarized actin filament cytoskeleton to differentiate from axonal filopodia that contained microtubules but retained the characteristic uniform distribution of actin filaments along their shaft. For analysis of the number of branches along the distal 50-micron termini of PGP9.5 labeled nerve fibers located in the stratum spinosum, we counted the number of tips visualized in maximal projections

of one-micron Z-stacks associated with individual fibers and subtracted one, as one would reflect the terminus of the fiber and not an additional branch. Growth cone area and the number of filopodia were measured and previously described (Jones et al., 2006) from images of the actin filament cytoskeleton of growth cones. Briefly, the area of the growth cones is measured from the “neck” of the growth cones to the distal most lamellipodial protrusion excluding filopodia. If a growth cone does not exhibit lamellipodia but only filopodia, or is collapsed, then area measurement is performed from the distal 5 microns of the axon shaft, representative of the mean length of growth cones that have lamellipodia. All length and area measurements were performed using the AxioVision software (Zeiss, Oberkochen, Germany).

Analysis of Length and Density of Mitochondria

Mitochondrial length and density were measured from mitochondria labeled with MitoTracker Red as described above. For detailed consideration of methodological issues related to these metrics along sensory axons (see Armijo-Weingart et al., 2019). Mitochondrial length was determined by line measurements spanning the two ends of the mitochondrion. Although most axonal mitochondria are linear, if bent, then segmented line analysis was performed to track the curvature of the mitochondria to obtain a full-length measurement. Mitochondria in clusters consisting of two or more are not amenable to the analysis described above and were excluded from measurements of length and density in all imaging sets. The lengths of the axon segments containing clusters of mitochondria were thus also excluded from the final determination of mitochondria density (mitochondria/unit length of axon).

Analysis of Actin Patches and EB3 Comets

Actin patches were analyzed following criteria and methods previously detailed (Loudon et al., 2006; Ketschek and Gallo, 2010; Spillane et al., 2012; Sainath et al., 2017a; Armijo-Weingart et al., 2019). Briefly, patch formation rate per unit length and time were determined by counting instances of patch formation as determined by the local intensity of mCherry-actin increasing above the cytoplasmic baseline, intensity, and size until dissipating back to baseline cytoplasmic intensity level. Duration of patch was the number of seconds from when a patch became detectable to when it dissipated. The proportion of patches giving rise to filopodia was determined by considering all patches that formed and whether they gave rise to a filopodial tip.

EB3 comet dynamics were imaged and analyzed as previously described (Ketschek et al., 2007; Spillane et al., 2012). Briefly, as with actin patches, the formation of a comet was defined as a localized increase in GFP-EB3 intensity increase above the cytoplasmic baseline and the comets formed by unit time and length of axon thus determined. Duration of a comet was defined as the time from when a comet became visible above the baseline level to when it dissipated and no longer visible above the baseline. The average velocity of comet advance during the lifespan of a comet was determined by dividing the

total distance advanced by the duration. For the measurements of comets, only comets that advanced anterogradely in axons were scored and those that entered growth cones were not counted, as for these parameters the analysis focused solely on axons. For determination of velocity and duration, the first 10 comets formed per axon were scored. The mean number of comets present per unit length of axon or within the growth cone was assessed by counting the number of visible comets at 30-s intervals within an axon or a growth cone. All distance measurements were performed using the AxioVision software (Zeiss, Oberkochen, Germany).

Quantification of Staining Intensity

All immunocytochemical samples within an experiment were processed in parallel prior to imaging and imaged during the same imaging session using identical imaging parameters and the microscopic setup described in the imaging section. Quantification of total microtubule intensity, ratios of tyrosinated and acetylated tubulin, and levels of cortactin, drebrin, and pAkt in the axons was performed by background subtraction as previously described (Jones et al., 2006; Spillane et al., 2012; Ketschek et al., 2016). Briefly, regions of interest (ROIs) encompassing the distal 50 μm of axon shafts but excluding axonal protrusions and growth cones were established along the length ranges of the axons described in the results. The same ROI was then used to perform background measurements by moving it off the axon and onto the substratum not containing cells. The background measurement was subtracted from the axonal measurement.

Immunohistochemistry and Intra-Epidermal Nerve Fiber Density and Branching Analysis

Skin biopsies were obtained from the footpad of age-matched adult mice. Biopsy samples were processed for immunohistochemistry, and Intra-Epidermal Nerve Fiber Density (IENFD) was determined by three independent observers as described in Himeno et al. (2011) from thirty-micrometer sections imaged using a 20 \times objective. Sections were stained with an anti-PGP9.5 antibody (# PA5-29012, 1:250; RRID:AB_2546488; Thermo Fisher Scientific, Hampton, NH, United States) and the secondary used was goat anti-rabbit FITC (1:200, #F9887; Sigma, St. Louis, MO, United States). Skin was fixed in 2% paraformaldehyde (vol/vol) for 3 h at 4°C. Following fixation, the tissue was washed with 0.1 M PBS 3 times (5 min/wash). The tissue was cryoprotected in 20% sucrose (wt/vol; 24–36 h) and sectioned with a cryostat. For immunostaining, 30- μm sections were cut to and placed in 0.1 M phosphate buffer. Sections were incubated in blocking solution for 1 h at room temperature (10% FBS, 0.1% Triton X-100 in PBS) and then with primary antibody overnight at 4°C on a shaker for 24–36 h. The primary antibody was washed 3 times (5 min/wash), followed by incubation with a secondary antibody for 2 h. The secondary antibody was washed as with the primary, and following 2 washes with dH₂O, sections were mounted onto coverslips. For analysis of branching along the

termini of individual sensory fibers in the sections, the sections were imaged at 20x and Z-stacks were obtained (using 1 micron z-intervals) and then maximal projections were generated from the Z-stacks using Image J. Branch number analysis was performed by counting the number of tips along the distal 50 microns of each nerve fiber and subtracting one (as reflective of the terminus of the axon itself). All analyses of the sections were performed blind to the genotype.

Statistical Analysis

All the statistical analyses were performed using Instat, and graphical data representation was performed using the Prism (both from GraphPad Software Inc., San Diego, CA, United States). The normality of data distributions was determined through Kolmogorov and Smirnov test. For presentation purposes, data sets wherein all the comparison groups were normally distributed are presented using mean and standard error of the mean (SEM). Data sets wherein one or more comparison groups exhibited a non-normal distribution are presented as individual data points and the median is presented. Comparisons of two groups were performed either by Welch *t*-test or Mann-Whitney test depending on the normalcy of the data sets. Multiple comparison *post hoc* tests were performed by Bonferroni and Dunn's test for parametric and non-parametric analyses, respectively. Categorical data sets are presented as percentages within category, but statistical analysis was performed on raw categorical data by Fisher exact test to compare 2×2 contingency tables, and chi squared test for independence on larger tables. For presentation, data sets that were determined to be normally distributed are presented using the relevant descriptive statistics of mean and SEM. Non-normal data sets are presented using dot plots to allow for assessment of the shape of the distribution, or histograms for distributions of the number of branches along distal axons. Sample sizes (*n*) denote the total number of independent observations in the data sets obtained from replicates, as detailed below.

Study Design

For *in vitro* immunostaining experiments, 3 mice/genotype were used to produce cultures on 3 separate days, with sampling distributed evenly across sessions. As noted above, for immunostaining and imaging, the cultures were processed in parallel prior to imaging and imaged during the same imaging session using identical imaging parameters and the microscopic setup described in the Imaging section. An ANOVA (parametric or non-parametric, determined by the assessment of distributions as described above) was performed for the relevant metric in the specific experiment within genotype across replicates to assess if differences could be discerned among replicates. In the absence of detected differences among the replicates, individual data points from the replicates were merged into a collective data set for each genotype within the experiment. The sizes of samples presented, thus, reflect the total number of data points obtained for a given metric from the data merged from the replicates. For live imaging, each axon was sampled from a separate culture spread across the replicates.

RESULTS

Axons of SARM1 Knockout Sensory Neurons Exhibit Increase in Number of Axon Collateral Branches

Postnatal day 0–2 dissociated sensory neurons from wild-type (WT) or SARM1 KO (–/– throughout) mice were cultured on polylysine- and laminin-coated substrates. Cultures were then fixed and stained to reveal F-actin using phalloidin and tubulin using anti- α -tubulin antibodies. SARM1 KO neurons exhibited an increase in the number of branches per unit length of axon relative to the WT neurons (**Figures 1A,B**). Axonal filopodia are the first structures formed in the process of collateral branch formation. SARM1 KO axons exhibited an elevated number of axonal filopodia (**Figure 1C**). Conversely, the overexpression of SARM1 in WT neurons decreased the number of filopodia along distal axons (**Figure 1C**; see **Figure 2A** for an example of exogenously expressed SARM1 along axons). These data indicate that SARM1 is a negative regulator of the number of axonal filopodia and, subsequently, branches *in vitro*.

CSPGs suppress axon collateral branching along sensory axons *in vivo* and *in vitro* through suppression of PI3K-Akt signaling and mitochondrial respiration (Fisher et al., 2011; Silver et al., 2014; Sainath et al., 2017a,b). To assess whether SARM1 KO may promote branching on a branch formation inhibitory substratum, we analyzed the number of branches along sensory axons cultured on CSPGs and laminin relative to laminin alone (as in Sainath et al., 2017a). SARM1 KO did not elevate the number of axon branches on a CSPG substratum (**Figures 1D,E**). Thus, although SARM1 KO promotes branching on a permissive substratum, it fails to do so under conditions wherein a major upstream regulatory pathway (PI3K) is impaired.

We also considered whether SARM1 KO might affect growth cone morphology. Analysis of growth cone area and the number of growth cone filopodia revealed decreases in both metrics in the SARM1 KO group relative to WT (**Figures 1F,G**). The medians of growth cone area and number of filopodia were decreased 30 and 33% in SARM1 KO relative to WT, respectively. The effects of SARM1 KO on increase in branching and axonal filopodial number, thus, do not translate into similar effects on growth cones, which exhibit a decrease in surface area and number of filopodia relative to WT.

SARM1 Knockout Cutaneous Sensory Endings in Skin Exhibit Increase in Terminal Branching

As the *in vitro* data show an increase in the number of axon branches along distal sensory axons, we addressed whether a similar phenotype would be evident *in vivo* within the peripheral target tissue of the sensory neurons, the skin. We addressed two aspects of skin innervation, the density of axons innervating the skin and the extent of formation of branches by distal axons in the skin. Analysis of the innervation density of cutaneous sensory fibers/axons stained

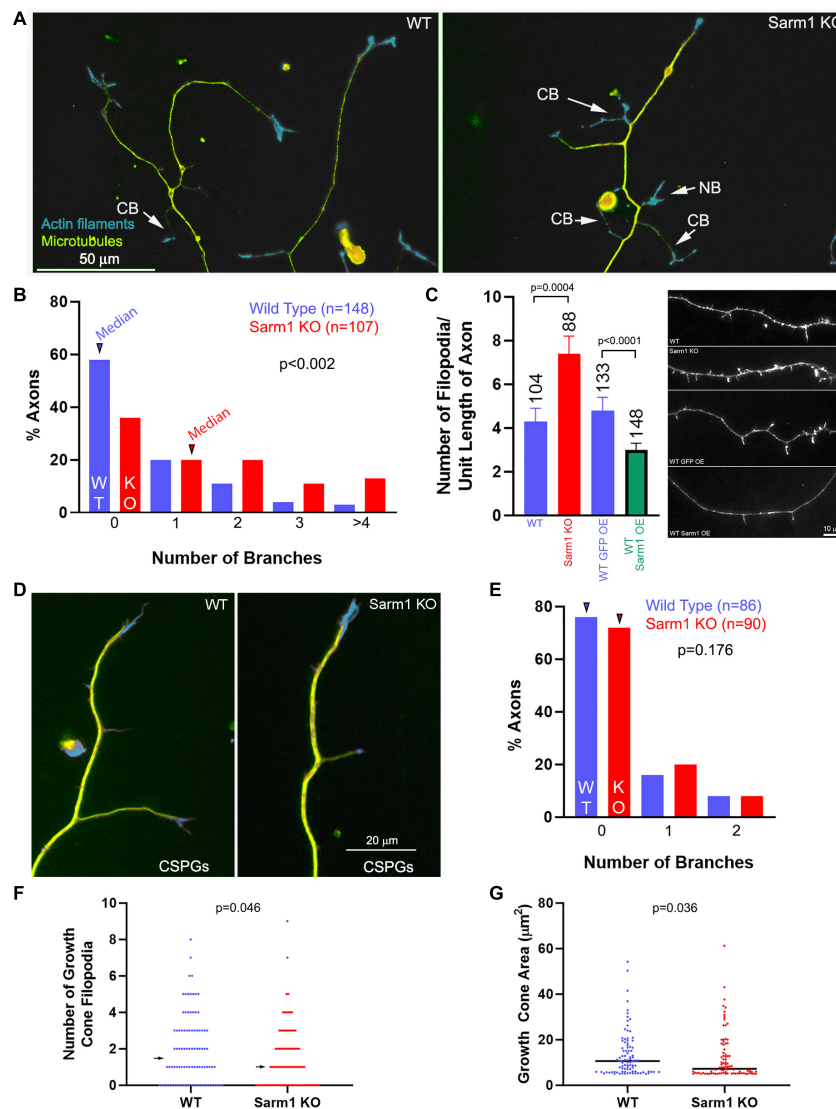


FIGURE 1 | Axons of cultured SARM1 KO neurons exhibit increased branching. **(A)** Examples of axons of cultured dissociated wild-type (WT) and SARM1 knockout (KO) sensory neurons stained to reveal the actin filament (rhodamine phalloidin) and microtubule (anti- α -tubulin antibody) cytoskeleton. CB = collateral branches defined by the presence of a microtubule array and polarized distal actin filaments. NB = a nascent branch that is developing a distal growth cone. **(B)** Histogram showing the distribution of branch number along the axons of WT and SARM1 KO axons. Arrowheads denote the medians. **(C)** Graph showing the number of filopodia along the axons of WT and SARM1 KO (two leftmost bars) and those of WT expressing mitochondrially targeted GFP and overexpressing GFP-SARM1 (two rightmost bars). Representative examples of axonal morphology are shown on the right of the graph (phalloidin staining revealing actin filaments). **(D)** Examples of WT and SARM1 KO neuron distal axons cultured on CSPG substrata. **(E)** Histogram showing the distribution of branch number along the axons of WT and SARM1 KO axons cultured on CSPGs. Arrowheads denote the medians. **(F)** Number of filopodia in the growth cones of WT and SARM1 KO neurons. Arrows denote medians. **(G)** Measurement of the area of WT and SARM1 KO neuron growth cones. Black bars denote medians. A measurement of 5–6 μm^2 reflects a growth cone with no lamellipodia, and the area is representative of the distal axon as specified in “Materials and Methods” section.

using antibodies against PGP9.5 in sections of footpad skin obtained from WT and KO adult mice did not show an increase in IENFD (Figures 3A,B), indicating that SARM1 does not have an impact on the targeting or retention of axons to the dermis. However, evaluation of the morphology of the distal 50 microns of nerve fiber endings, located within the stratum spinosum, showed increased complexity reflected by a greater number of distal branches (Figures 3C,D). Thus, both *in vitro* and *in vivo* distal sensory axons exhibit

increased morphological complexity characterized by higher levels of branching.

Axonal Mitochondria Exhibit Decreased Motility in SARM1 Knockout Postnatal Neurons

The positioning of stationary mitochondria along axons determines the sites of highest filopodium formation and

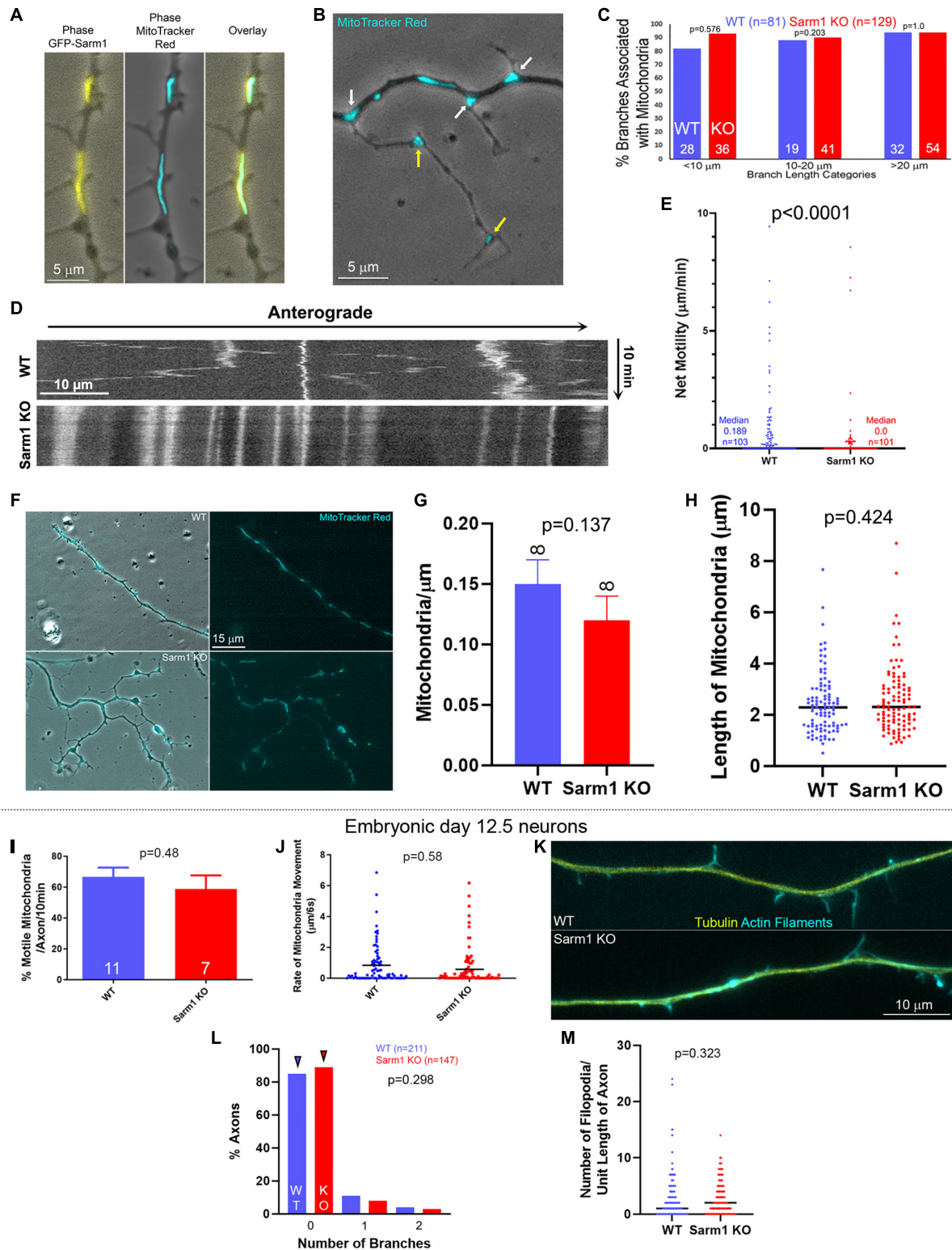


FIGURE 2 | Mitochondria along the axons of SARM1 KO neurons exhibit decreased motility. **(A)** Example of a WT axon expressing GFP-SARM1 and mitochondria labeled using Mitotracker Red. GFP-SARM1 is targeted to mitochondria. **(B)** Examples of MitoTracker Red-labeled mitochondria targeted to the base of branches and filopodia (white arrows) of a SARM1 KO axon. Yellow arrows denote mitochondria in established branches. Phase contrast imaging is performed to show axonal morphology. **(C)** Histogram of the percentage of axonal protrusions with axonal mitochondria present at the base. Axonal protrusions are divided into three length (Continued)

FIGURE 2 | classes. Those shorter than 10 μm reflect mostly filopodia and filopodia with some degree of distal polarization possibly reflective of the earliest stages of maturation into a branch. Those in the 10–20 μm bin reflect nascent branches, and those greater than 20 μm established branches with clear shafts and distal growth cones. **(D)** Kymograph of mitochondrial motility in WT and SARM1 KO axons. **(E)** Measurements of an index of net mitochondrial motility. The total summed displacement of a mitochondrion was determined during the entire imaging period regardless of directionality, and divided by the duration of the imaging period to obtain microns/min. Each datum reflects on a mitochondrion, sampled from 8 axons per group. Acquisition rate was every 6 s for 10 min. **(F)** Examples of WT and SARM1 KO axons with mitochondria labeled using MitoTracker red. **(G)** Density of mitochondria (mitochondria/ μm) along the WT and SARM1 KO axons imaged. **(H)** Lengths of mitochondria along the WT and SARM1 KO axons imaged. Each datum reflects a mitochondrion. The black line denotes the median. **(I–M)** The data are representative of embryonic day 12.5 sensory neurons. **(I)** Percent of motile mitochondria per video sequence of embryonic sensory axons labeled with MitoTracker Red. n = number of axons imaged. **(J)** Rate of mitochondrial movement in either direction, from all the mitochondria sampled along the axons in **(I)**. A rate of zero reflects an immotile mitochondrion. The p -value is for comparison between the WT and SARM1 KO groups considering only mitochondria with rates greater than zero (i.e., the moving population). Black lines denote the medians. **(K)** Examples of the morphology of the axons of embryonic sensory neurons. **(L)** Histogram showing the distribution of branch number along the axons of embryonic WT and SARM1 KO neurons. Arrowheads denote the medians. **(M)** Number of filopodia per unit length along the axons of WT and SARM1 KO neurons. Black bars denote the medians.

branching along sensory and central nervous system axons (reviewed in Smith and Gallo, 2018), and in sensory neurons SARM1 is targeted to the outer mitochondrial membrane through an N-terminus sequence (Gerdt et al., 2013). SARM1 is, thus, localized to an organelle with a fundamental role in the formation of filopodia and branches. Consistent with prior determination in sensory neurons (Gerdt et al., 2013), exogenously expressed full-length WT SARM1 containing the N-terminus mitochondrial targeting sequence localized to mitochondria (Figure 2A). Analysis of the bases of axonal protrusions associated with mitochondria within the axon shaft did not reveal a difference between WT and SARM1 KO neurons (Figures 2B,C), indicating that mitochondrion positioning at the bases of branches is not affected, although SARM1 KO axons exhibit a greater number of branches. During the formation of branches along the axons of sensory neurons, axonal mitochondria are transported into branches and populate the nascent branches (Spillane et al., 2013). To assess whether the targeting or retention of mitochondria into nascent branches from the main axon shaft might differ between WT and SARM1 KO neurons, we analyzed the same population of axons, as shown in Figure 2C, and determined the proportions of branches that contained one or more mitochondria. This analysis showed that 59 and 77% of branches in the 10–20- μm length range and 100 and 98% in the > 20- μm length range contained mitochondria in the WT and SARM1 KO neurons, respectively (Fisher exact test, $p = 0.203$ and 1, respectively). These data indicate that the targeting of mitochondria at the base and into the branches does not differ among the genotypes, and that the relationship between positioning of mitochondria and their targeting into nascent branches is maintained along the axons of SARM1 KO neurons.

A prior study using embryonic mouse sensory neurons determined that SARM1 KO does not affect mitochondrial membrane potential, density, or the percentage of actively transported mitochondria along the axons of cultured mouse embryonic day 12.5 sensory neurons (Summers et al., 2014). In contrast, through live imaging analysis of the motility of mitochondria labeled using Mitotracker Red dye, we found that mitochondria along P0-2 SARM1 KO neuron sensory axons exhibit less net motility than those along WT axons (Figures 2D,E). Analysis of the proportion of mitochondria that remained stationary showed that 67% ($n = 103$) and 37% ($n = 101$) remained stationary during the imaging period along

SARM1 KO and WT axons, respectively (Fisher's exact test, $p < 0.0001$). Consideration of the motility of mitochondria initially associated with branches or filopodia at the beginning of imaging did not reveal a difference in the proportion of mitochondria that remained stalled in the initial position between WT and SARM1 KO (Fisher's exact test, $p = 0.369$), indicating that the retention of mitochondria in branching/filopodial sites does not differ as a function of SARM1 KO and consistent with the prior analysis (Figures 2B,C). Analysis of the density of mitochondria per unit length of the axons or the length of mitochondria did not reveal any differences between WT and SARM1 KO (Figures 2F–H). Overall, the data indicate that although there are less motile mitochondria along the axons of SARM1 KO neurons, the association of mitochondria with sites of branching and filopodia and their retention in these sites does not vary between WT and SARM1 KO.

To address the differences in mitochondrial motility between the above data obtained from postnatal neurons and the study by Summers et al. (2014), we repeated the experiments using embryonic day 12.5 sensory neurons, the same developmental age as Summers et al. (2014) study. Consistent with Summers et al. (2014), we did not detect differences in mitochondrial motility within the axons of SARM1KO and WT embryonic sensory neurons (Figures 2I,J). Neither the proportion of mitochondria undergoing transport nor the distance they moved per unit time differed among the genotypes. Furthermore, the axons of SARM1 KO embryonic sensory neurons did not exhibit increased axon branching or number of filopodia along axons relative to WT (Figures 2K–M). Collectively, the data from embryonic and postnatal sensory neurons indicate that the branching phenotype of the SARM1 KO neurons is age-dependent and that the alterations in axonal mitochondrial motility observed in the postnatal neurons are correlated with increased axon branching.

Axons of SARM1 Knockout Neurons Exhibit Increase in Actin Filament Dynamics Underlying the Formation of Axonal Filopodia

Formation of axonal filopodia, the first step in axon branching, is dependent on axonal actin filament dynamics. Axonal actin patches serve as precursors to the emergence of axonal filopodia and present as transient local accumulations of actin filaments along axons (Figure 4A). While axons generate many patches,

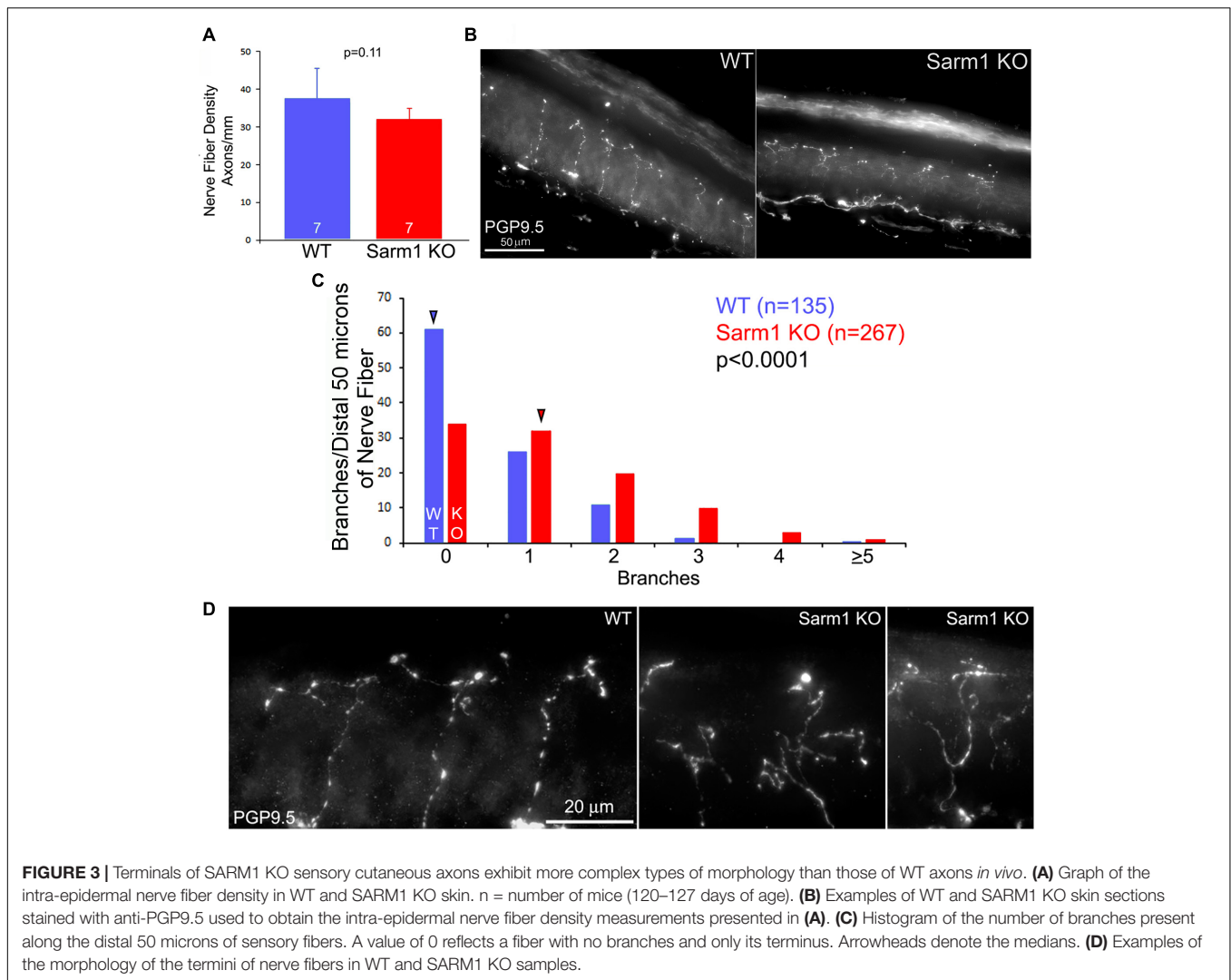


FIGURE 3 | Terminals of SARM1 KO sensory cutaneous axons exhibit more complex types of morphology than those of WT axons *in vivo*. **(A)** Graph of the intra-epidermal nerve fiber density in WT and SARM1 KO skin. n = number of mice (120–127 days of age). **(B)** Examples of WT and SARM1 KO skin sections stained with anti-PGP9.5 used to obtain the intra-epidermal nerve fiber density measurements presented in **(A)**. **(C)** Histogram of the number of branches present along the distal 50 microns of sensory fibers. A value of 0 reflects a fiber with no branches and only its terminus. Arrowheads denote the medians. **(D)** Examples of the morphology of the termini of nerve fibers in WT and SARM1 KO samples.

only a fraction gives rise to filopodia before dissipating. To address whether axonal actin dynamics might be impacted by SARM1 KO, WT and KO neurons were transfected with mCherry- β -actin expression plasmid prior to culturing. Live imaging and analysis of axonal actin dynamics were performed as previously described (Loudon et al., 2006; Ketschek and Gallo, 2010; Spillane et al., 2012; Sainath et al., 2017a; Armijo-Weingart et al., 2019). As in our prior study, we determined the rate of patch formation (patches/unit length of axon/unit time), duration (s) of patches, and percentage of patches that gave rise to filopodia along the distal 40 μ m of the axons, excluding the growth cones. SARM1 KO resulted in 75% increase in the rate of axonal actin patch formation along the distal 40 μ m of axons (Figures 4B,C). As the rate of actin patch formation decreases along the axons with increase in distance from the growth cones (Ketschek and Gallo, 2010; Spillane et al., 2011), we also analyzed the rates of formation in 10- μ m bins. The rates of formation were elevated in the 10–40 μ m distal segment of the axons, where axon branching is most prominent, but not in the distal most 0–10 μ m just proximal to the growth cones (Figure 4C). This

observation is consistent with the lack of promotion of growth cone morphology in the SARM1 KO neurons (Figures 1F,G). SARM1 KO also increased the proportion of actin patches that gave rise to filopodia by 48% (Figure 4D). SARM1 KO did not alter the duration of actin patches (Figure 4E). These data indicate that SARM1 negatively regulates the formation of axonal actin patches and the emergence of filopodia from actin patches.

Drebrin and cortactin are actin regulatory proteins that are targeted to axonal actin patches, and their experimental overexpression promotes the formation of axonal filopodia and branches (Spillane et al., 2011, 2012; Ketschek et al., 2016). Drebrin is also targeted to the base of axonal filopodia and promotes the entry of microtubule tips into filopodia (Ketschek et al., 2016). Therefore, we sought to determine the levels of drebrin and cortactin along the WT and SARM1 KO sensory axons. Quantitative immunocytochemical analysis of the levels of these proteins (as in Spillane et al., 2011, 2012; Ketschek et al., 2016) revealed both to be elevated along SARM1 KO distal axons relative to WT (Figures 4F–I). Analysis of the levels of axonal drebrin and cortactin within 20- μ m bins from 0 to 60 μ m

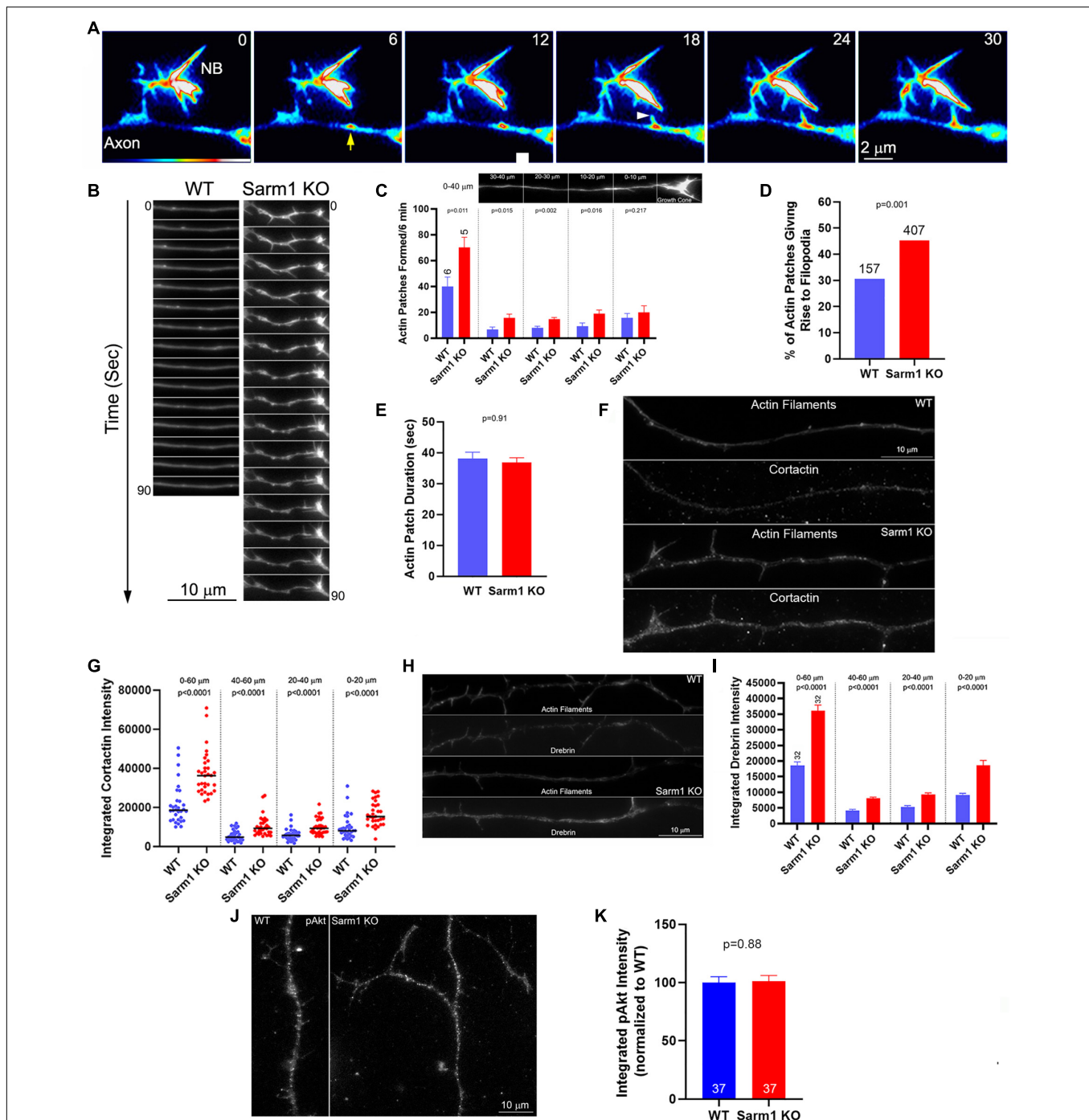


FIGURE 4 | Axons of SARM1 KO neurons exhibit increased rates of actin patch formation and emergence of filopodia. **(A)** Example of actin patch formation and emergence of a filopodium from an actin patch as imaged using mCherry-β-actin. The axon segment (SARM1 KO) contains a nascent branch (NB) (numbers in panels denote seconds). At 6 s, an actin patch forms (yellow arrow). At 18 s, a filopodium emerges from the actin patch (white arrowhead) and subsequently elongates. **(B)** Qualitative examples of axonal actin dynamics along WT and SARM1 KO. The axons of SARM1 KO neurons exhibited more frequent fluctuations at local levels of actin filaments and formation of filopodia. **(C)** Quantification of the rate of actin patch formation along axons. Leftmost bars show the rates along the distal 0–40 μm of the axon (0 defined as the point along the axon just proximal to the base of the growth cone (see image of the axon in the panel). Analysis of the rate of patch formation along the distal 0–40 μm divided into 10 μm bins is shown in the four rightmost sets of bar graphs. n = number of axons. **(D)** Proportion of axonal actin patches that give rise to filopodia is elevated in SARM1 KO neurons relative to WT. **(E)** Duration of actin patches does not differ between SARM1 KO and WT axons. **(F)** Examples of cortactin staining levels along distal WT and SARM1 axons. **(G)** Graph showing the quantification of cortactin along distal axons in the format initially shown in **(C)**. Black bars denoted medians. **(H)** Examples of drebrin staining levels along distal WT and SARM1 axons. **(I)** Graph showing the quantification of drebrin along distal axons. **(J)** Examples of axons stained with antibodies to Akt phosphorylated at T308 (pAkt). **(K)** Quantification of the integrated intensity of pAkt staining along axons.

revealed differences between WT and SARM1 KO axons within each length bin, indicating that the levels are uniformly increased along the axons. The levels of both cortactin and drebrin were elevated in the 0–20 μm bin relative to the 20–40 and 40–60 μm bins along the axons of both WT and SARM1 KO neurons (multiple comparison tests, $p < 0.001$ for all comparison with the exception of cortactin WT 0–20 vs. 20–40, $p < 0.01$). The 20–40 and 40–60 μm bins did not differ in any of the within genotype comparison groups. The distal (highest)-proximal gradient in the levels of cortactin and drebrin along the distal axons is consistent with the similar gradient in the rate of actin patch formation rates (Ketschek and Gallo, 2010; Spillane et al., 2011) and was not altered as a function of genotype. The data, thus, indicate that the increase in the number of axonal filopodia along the axons of SARM1 KO neurons is due to increase in the rate of formation of axonal actin patches along the axons and the probability that filopodia will emerge from the patches, consistent with a prior study indicating that regulation of the rate of axonal actin patch formation is a major regulatory node in the mechanism of axonal filopodium formation (Ketschek and Gallo, 2010; Spillane et al., 2011, 2012, 2013; Ketschek et al., 2016; Sainath et al., 2017b). The increases in the axonal levels of cortactin and drebrin are consistent with the concerted regulation of the actin regulatory mechanisms that underlie the promotion of actin patch formation and filopodium emergence from patches (Spillane et al., 2011, 2012, 2013).

The levels of axonal cortactin and branching of axons are positively regulated by the levels of PI3K-Akt signaling along the sensory axons (Ketschek and Gallo, 2010; Spillane et al., 2012). Thus, we assessed whether the levels of activated Akt, phosphorylated in the primary activating site of threonine 308, might be elevated along the axons of SARM1 KO neurons using previously published quantitative immunocytochemical methods (Sainath and Gallo, 2021). The axons of SARM1 KO neurons did not exhibit changes in levels of activated Akt (Figures 4J,K). These data are generally consistent with a prior study assessing that SARM1 does not regulate axon degeneration through regulation of Akt (Yang et al., 2015). Thus, the increase in levels of cortactin and axon branching along the axons of SARM1 KO neurons are not readily attributable to alterations in Akt signaling.

Axonal Filopodia of SARM1 Knockout Neurons Are More Dynamic

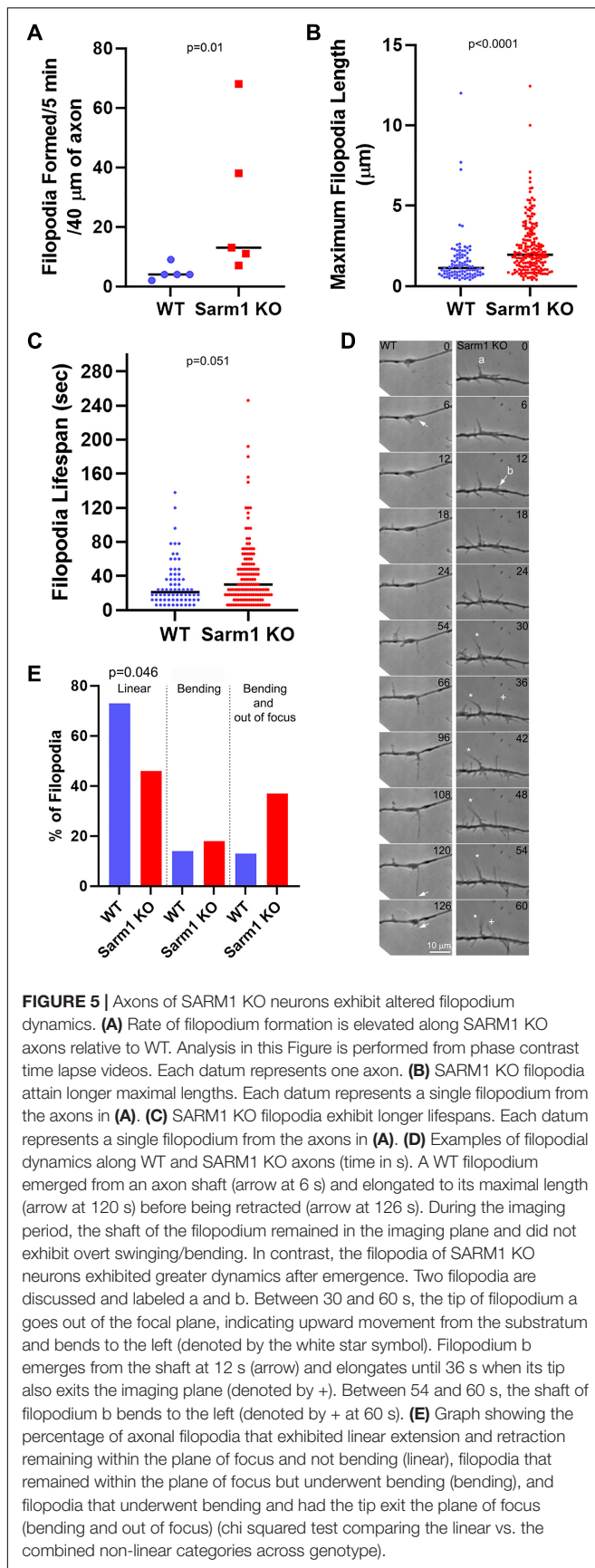
We next determined whether SARM1 KO might have an impact on aspects of filopodial dynamics after emergence by phase contrast optics. Consistent with the data from imaging actin dynamics (Figure 4), the axons of SARM1 KO neurons exhibited a higher rate of filopodium formation than those of WT neurons (Figure 5A). The median maximum length attained by filopodia increased by 73% along the KO axons (Figure 5B). Measurement of the lifespan of newly formed filopodia revealed that KO filopodia exhibited a 42% increase in median duration from the time of emergence to that of complete retraction into the axons (Figure 5C). Although the filopodia of KO axons exhibited longer life spans, the proportion of filopodia with lifespans greater than

60 s within genotype was not different between WT (25%) and SARM1 KO axons (28%) (Figure 5C), indicating that SARM1 KO does not increase the stabilization of filopodia for prolonged time periods (Fisher's exact test, $p = 0.684$).

Along the WT axons, filopodia initially emerge, and then their tips elongate in a linear manner remaining in close contact with the substratum until undergoing retraction back into the axon shaft (Figure 5D). In contrast, the filopodia of KO neurons exhibited a variety of behaviors including elevation from the substratum, buckling, and occasional collapsing upon themselves (Figure 5D) and 54% of the KO filopodia exhibited one or more of these behaviors in contrast to the 27% of WT (Figure 5E). The behavior of KO filopodia precluded an analysis of the rates of filopodial elongation and retraction, as the tip was not always available for tracking because of its movement out of the focal plane, thus, exclusion of filopodia that underwent these heightened dynamics from the sample would have skewed sampling. We note the caveat that maximal length was determined until the point filopodia exited the focal plane or if they returned to it and were longer, but this would result in underestimation of the length if a filopodium had extended further while out of the focal plane. However, even with this caveat, the filopodia extended to detectably longer lengths. The increase in the dynamics of axonal filopodia observed along the axons of SARM1 KO neurons might also contribute to the formation of axon branches by impacting the stage of branch maturation wherein actin dynamics are increased in filopodia that mature into branches and reorganize the filaments to attain a distally polarized distribution, but this issue will require additional consideration.

Axons of SARM1 Knockout Neurons Exhibit Increase in Microtubule Plus Tip Dynamics

The entry of microtubule plus tips into axonal filopodia is required for a filopodium to mature into a branch. Therefore, given the increase in branching observed along the SARM1 KO axons, we addressed whether axonal microtubule plus tip behavior may also be impacted. Microtubule plus tip polymerization can be tracked using fluorescently tagged end binding protein 3 (EB3; Stepanova et al., 2003). EB3 is recruited to a plus tip when the tip begins to polymerize and, when imaged, presents as a “comet” at the tip of a microtubule (Figure 6A). To obtain a general metric of the prevalence of comets in axons and growth cones, we counted the number of comets per axon and growth cones present in timelapse frames at 30-s intervals. There was a 68% increase in the mean number of GFP-EB3 comets along the distal axons (Figures 6A,B). The mean number of comets was also increased in the growth cones although by only 32% (Figure 6B), slightly less than half of the increase along the distal axons. In order to obtain additional insights, we analyzed multiple parameters of individual EB3 comet dynamics. The rate of new comet formation along the distal 50 microns of axons was approximately doubled in the SARM1 KO axons relative to those of the WT (Figure 6C). Although the duration (time from formation to dissipation) of



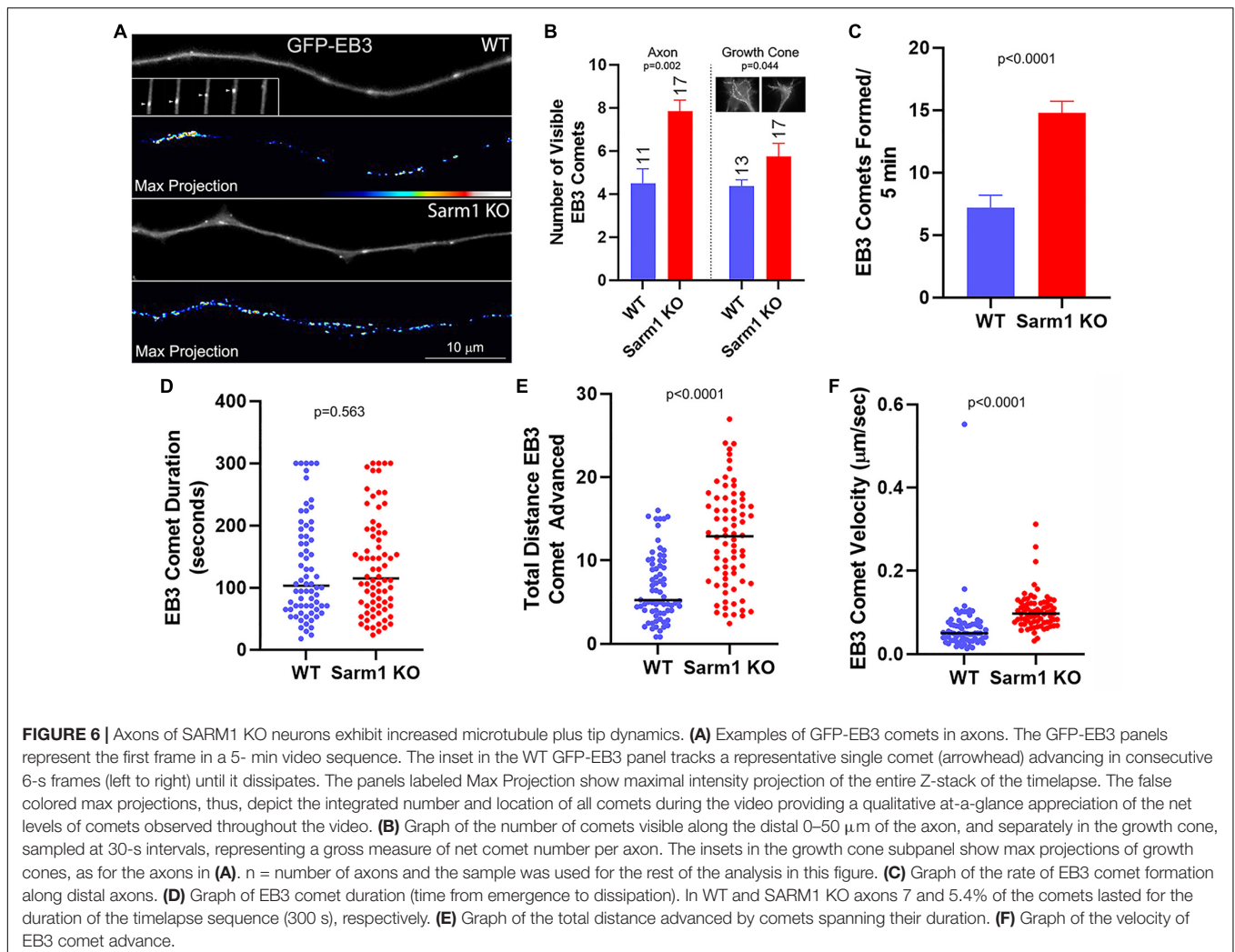
comets did not differ (**Figure 6D**), the total distance individual comets advanced within the axons during their duration was increased in the SARM1 KO axons (**Figure 6E**) because of increased comet advance velocity (**Figure 6F**). The axons of SARM1 KO neurons, thus, exhibit a greater probability of comet formation and a greater velocity of comet advance, reflective of the rate of microtubule plus tip polymerization.

As in the prior study, to measure the net levels of axonal microtubules, we used cultures that had been simultaneously fixed and permeabilized to remove soluble tubulin while retaining polymerized microtubules (e.g., Gallo and Letourneau, 1998). Measurement of the total staining intensity of α -tubulin, reflective of microtubules, in the distal 40 μ m of axons did not show a difference in net microtubule mass (**Figures 7A,B,D**). Tubulin is extensively post translationally modified. Following polymerization into the microtubule lattice, α -tubulin undergoes detyrosination and acetylation in a time-dependent manner (Janke and Magiera, 2020). Quantification of the ratio of acetylated and tyrosinated tubulin to total microtubule levels using fixed and permeabilized samples, as described above, did not show changes in the ratio of post translational modification between WT and SARM1 KO axons (**Figures 7B–E**). The differences in axonal plus tip dynamics between WT and SARM1 KO, thus, do not translate into altered net levels of microtubules or into the extent of acetylation or tyrosination of α -tubulin. The observed increases in axonal microtubule plus tip dynamics likely contribute to the promotion of axon branching along the axons of SARM1 KO neurons by promoting the targeting of microtubule plus tips into axonal filopodia, a required component of the formation of branches from filopodia.

DISCUSSION

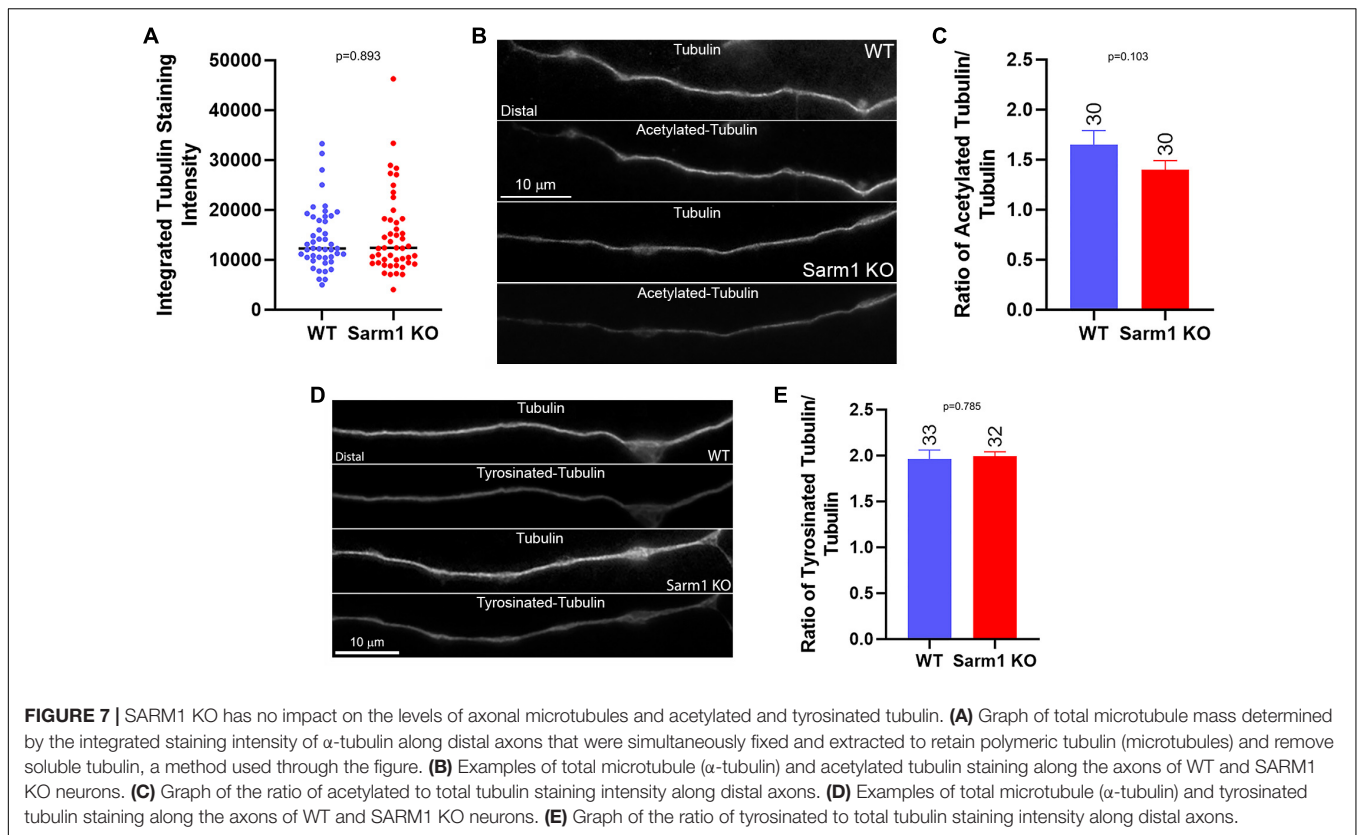
Axon collateral branching is regulated at multiple levels through the dynamics of the axonal cytoskeleton. Increases in the formation of filopodia promote the formation of branches at the first step in the mechanism. Similarly, increases in microtubule plus tip polymerization positively contribute to axon branching by increasing the availability of microtubule tips that can be targeted into axonal filopodia and initiate the process of maturation of a filopodium into a branch. This study demonstrates that genetic loss of SARM1 in sensory neurons results in increased branching, likely a consequence of the promotion of actin filaments and microtubule dynamics underlying the process of branching. The increase in filopodium formation is attributable to a concerted increase in the rate of formation of axonal actin patches, precursors to filopodial emergence, and an increase in the proportion of actin patches that give rise to filopodia. An increase in microtubule plus tip polymerization would result in increased tips available for entry into the base of axonal filopodia and, thus, increase the probability of a filopodium maturing into a branch.

In this study we observed that the axons of postnatal SARM1 KO sensory neurons exhibited less mitochondrial motility than the WT axons. The decrease in mitochondrial motility along the axons of postnatal SARM1 KO neurons is consistent with



the observed increases in branching, as stationary mitochondria determine sites where filopodia and branches preferentially form along axons (reviewed in Smith and Gallo, 2018). The increase in stationary mitochondria along the SARM1 KO axons suggests an explanation for at least one contribution of SARM1 KO to the increase in branching observed in the postnatal KO neurons; increasing the proportion of stationary mitochondria, therefore, results in increased sites of filopodia and branch formation along axons. Consistent with the report by Summers et al. (2014), which did not find an effect of SARM1 KO on mitochondrial motility along embryonic sensory axons, we similarly did not detect differences in mitochondrial motility along the axons of embryonic sensory neurons. Furthermore, the axons of embryonic sensory SARM1 KO neurons did not exhibit increased branching. Jointly, the data from postnatal and embryonic sensory neurons indicate a correlation between decreased axonal mitochondrial motility and increased axon branching. Additional studies will be required to determine experimentally through manipulation of mitochondrion-stalling mechanisms along axons whether the relationship is causal. Consistent with the neuron's age being a potential contributing

factor to the differences between embryonic and postnatal sensory neurons, as sensory neurons age they develop increased number of branches upon culturing, an effect reversed by a prior lesion to the axons that reverts to the neurons to a more immature mode of axon extension (Smith and Skene, 1997). Similarly, the number of stationary mitochondria along axons increases with the age of neurons (Lewis et al., 2016), in concert with increased expression levels of the mitochondrion-microtubule-anchoring protein syntaphilin (Zhou et al., 2016). The length of axonal mitochondria increases with the developmental age of sensory neurons (Armijo-Weingart et al., 2019), and the transport of axonal mitochondria is inversely proportional to the length of mitochondria (Misgeld et al., 2007; Narayanareddy et al., 2014). Thus, older neurons may be more prone to suppression of mitochondrial motility in the context of SARM1 KO and more predisposed toward the formation of axon branches. The mechanism through which SARM1 is impacting mitochondrial motility remains to be addressed. As SARM1 is targeted to the outer mitochondrial membrane (Gerdtts et al., 2013), it is poised to interfere or modulate aspects of the mechanism of active transport at the level of motor proteins or adaptors



(Schwarz, 2013; Smith and Gallo, 2018). Similarly, SARM1 may be modulating aspects of the microtubule-based mechanism of mitochondrial stalling (Zhou et al., 2016). Alternatively, SARM1 KO may also regulate the expression levels of proteins involved in mitochondrial transport or anchoring. Whether SARM1 KO has an impact on the transport of additional axonal cargoes remains to be addressed.

The axons of SARM1 KO neurons contained higher levels of the actin regulatory and collateral branch formation promoting-proteins drebrin and cortactin (Spillane et al., 2011, 2012; Ketschek et al., 2016). The current experiments were performed in the presence of neurotrophins. NGF induces intra-axonal translation of cortactin (Spillane et al., 2012; Ketschek et al., 2016), and axonal translation occurs preferentially at sites demarcated by stalled mitochondria (Spillane et al., 2013; Sainath et al., 2017a; Wong et al., 2017). The increase in the proportion of stalled mitochondria may, thus, also be contributing to the increases in levels of cortactin by increasing sites of localized translation along axons. In contrast, NGF increases the levels of axonal drebrin in a manner independent of translation (Ketschek et al., 2016). The increases in protein levels of cortactin and drebrin may also be due to decreased proteolysis, increased protein stability, increased transport into axons, or increased somatic transcription and/or translation. Future studies will be required to address these alternative but not mutually exclusive hypothetical mechanisms for the regulation of the axonal levels of cortactin and drebrin by SARM1 KO. Consistent with the possible role of SARM1 as

a negative regulator of axonal translation, Izadifar et al. (2021) recently reported that SARM1 may impede the synthesis of axon-protective proteins such as Nmnat.

The axons of SARM1 KO neurons exhibited elevated microtubule plus tip dynamics reflected in increased rates of comet formation and faster velocities of comet advance. This difference in dynamics may contribute to the increase in branching by providing a greater density of actively polymerizing tips within axons that may then undergo targeting into axonal filopodia. Drebrin binds actin filaments at the base of filopodia and promotes targeting of microtubule plus tips into axonal filopodia, thereby contributing to the microtubule-based component of the mechanism of branching (Ketschek et al., 2016). The increase in drebrin levels within SARM1 KO axons is, thus, expected to promote the entry of microtubule tips into axonal filopodia in concert with the increase in plus tip dynamics. As there is not a detectable increase in net microtubule mass along axons, the increase in plus tip dynamics may be counterbalanced by increase in catastrophes (when a tip undergoes a depolymerization event) or increase in mass below our detection range. Unfortunately, EB3 imaging does not allow for the analysis of microtubule depolymerization events, and because of the compact nature of the axonal microtubule array, individual microtubules in their entirety cannot be imaged live. The issue of whether there may be a concerted increase in tip depolymerization dynamics to counterbalance the increase in plus tip polymerization remains to be addressed. Vincristine is a microtubule-depolymerizing

agent that is used at low doses as a cancer therapeutic but results in peripheral neuropathy. SARM1 KO counters the effects of vincristine on peripheral nerves (Geisler et al., 2016). The effects of SARM1 KO on microtubule plus tip polymerization reported in this study may, at least in part, underlie the effects of SARM1 KO on vincristine neuropathy due to increase in actively polymerizing plus tips in axons in addition to the established role of SARM1 in the activation of the axonal degeneration mechanism. Although tubulin post-translational modifications of acetylation and tyrosination can serve as indirect reporters of net microtubule dynamics, they are regulated by upstream enzyme systems that are, in turn, regulated by additional mechanisms (Janke and Magiera, 2020). This study finds that increased plus tip dynamics do not correlate with levels of tubulin acetylation and tyrosination, which would be predicted to be decreased and increased, respectively, in the context of greater microtubule dynamics. It is, thus, possible that SARM1 KO may also be affecting the systems regulating these post-translational modifications, but this remains to be determined. Consistent with this notion, Chen et al. (2011) found that SARM1 levels negatively regulate the ratio of acetylated to total tubulin in COS-1 and neuro-2A cells. Alternatively, the effects of SARM1 KO on microtubules may be below the threshold to result in detectable changes in acetylation and tyrosination, or, as noted above, are countered by increases in catastrophes, thereby maintaining the microtubule array at WT levels of microtubule mass and levels of post-translational modifications.

The data indicate that, minimally, SARM1 KO promotes the formation of branches at the earliest steps in the mechanism, and the formation of axonal filopodia and axonal microtubule dynamics. However, future studies will be needed to determine if it might also have an impact on aspects of the maturation of filopodia into nascent branches and the subsequent stability of branches in varying stages of their development. Whether the effects of SARM1 KO on axonal shaft microtubule plus tips are also present within nascent branches was not determined in this study. As SARM1 is associated with mitochondria, and mitochondria are targeted normally to both the bases and within the shafts of branches, it is likely that microtubules within branches are also affected by SARM1 KO. MAP7 is a microtubule-associated protein that promotes branch stabilization by impacting microtubule depolymerization and modulating organelle transport (Tymanskyj et al., 2018; Tymanskyj and Ma, 2019). Whether MAP7 level or function may be altered in SARM1 KO neurons remains to be determined.

Inhibition of SARM1 is a potential therapeutic for axon degeneration and neuronal cytotoxicity (Gerdtts et al., 2016; Figley and DiAntonio, 2020). This study indicates that inhibition of SARM1 may also be able to manipulate the degree of axon collateral branching, often referred to as sprouting, in injury contexts. Injury-related axon sprouting can have beneficial or adverse effects on plasticity following a nervous system injury (Onifer et al., 2011). Inhibition of SARM1 may, thus, be worth considering in injury contexts wherein sprouting is beneficial, and similarly as potentially having an adverse “side-effect” if in a treatment context it may induce maladaptive sprouting.

SARM1 KO had more pronounced effects on axon shafts than on growth cones. Prior studies have also indicated that the growth cone and the axon shaft of sensory neurons are differentially regulated. For example, mitochondria exhibit more hyperpolarized potentials in growth cones of sensory neurons than along axon shafts (Verburg and Hollenbeck, 2008), and the elaboration of sensory neuron growth cones in response to NGF is not dependent on localized translation while the elaboration of axon branches and the underlying promotion of actin cytoskeletal dynamics are dependent on axonal translation (Roche et al., 2009; Spillane et al., 2012). We did not observe a promotion in growth cone morphology due to SARM1 KO, and the effects on actin patch formation along the axon shafts were not evident in the distal most 10 μm of the axons in proximity to the growth cones. Although EB3 comets were increased in the growth cones of SARM1 KO neurons, the relative increase was only about half of that observed along the axon shafts. As we did not perform an exhaustive analysis of the growth cones, there could be aspects of growth cone biology affected by SARM1 KO that may be unveiled by future investigations. It is possible that under the conditions of our study, performed on growth-promoting laminin and in the presence of neurotrophins, the growth cone is already at a maximal response level and, thus, cannot be further elaborated. If so, then SARM1 KO may have effects on growth cones in other environments such as growth inhibitory substrata or on mediating the response to growth cone collapsing signals.

In conclusion, this study determines that SARM1 KO results in increased axon collateral branching in postnatal sensory neurons, and that *in vivo* cutaneous SARM1 KO sensory endings have more complex types of morphology. Whether the *in vivo* phenotype may result in altered skin sensation or pain remains to be determined. Also, whether SARM1 KO will affect the branching morphogenesis of neuronal populations other than sensory neurons remains to be determined. However, a generalized role of SARM1 in negative regulation of axon morphology is suggested by the recent demonstration of a role of SARM1 in branching of mechanosensory neurons in *Drosophila* (Izadifar et al., 2021). The data presented herein provide a link between SARM1 and the suppression of the dynamics of both the axonal actin filament and microtubule cytoskeletons. The mechanisms linking SARM1 to cytoskeletal dynamics is a focus of ongoing studies. The observation that SARM1 fails to promote branching on branch-suppressing CSPGs, which attenuate an early signaling step in branch formation (PI3K-Akt activity), indicates that the effects of SARM1 are likely downstream of PI3K-Akt or other pathways impacted by CSPGs (Fisher et al., 2011). Consistently, Yang et al. (2015) did not find a role of SARM1 in the regulation of PI3K-Akt, but rather Akt suppresses MAPK activity that otherwise promotes SARM1-regulated axon degeneration (Walker et al., 2017), and in this study, we did not observe altered levels of Akt activation along the axons of SARM1 KO neurons. However, an axon injury activates MAPK, and SARM1 KO suppresses this activation (Yang et al., 2015), supporting the notion that SARM1 KO can have an impact on the function of signaling pathways, noting that the MAPK pathway is

also activated by growth factors. The microtubule cytoskeleton is under regulation by a multitude of kinases such as those involved in mediating SARM1-dependent axon degeneration (Mandelkowitz et al., 1995; Bogoyevitch and Kobe, 2006) and may, thus, be regulated through these signaling pathways. Although SARM1 KO was not found to affect the levels of activated Akt along axons, it may be fruitful to further determine if SARM1 may regulate other aspects of the intracellular signaling of extracellular signals that induce axon branching, such as NGF.

DATA AVAILABILITY STATEMENT

The raw data supporting the conclusions of this article will be made available by the authors, without undue reservation.

ETHICS STATEMENT

The animal study was reviewed and approved by the Institutional Animal Care and Use Committee, Lewis Katz School of Medicine.

REFERENCES

- Armijo-Weingart, L., and Gallo, G. (2017). It takes a village to raise a branch: cellular mechanisms of the initiation of axon collateral branches. *Mol. Cell Neurosci.* 84, 36–47. doi: 10.1016/j.mcn.2017.03.007
- Armijo-Weingart, L., Ketschek, A., Sainath, R., Pacheco, A., Smith, G. M., and Gallo, G. (2019). Neurotrophins induce fission of mitochondria along embryonic sensory axons. *Elife* 8:e49494. doi: 10.7554/eLife.49494
- Bogoyevitch, M. A., and Kobe, B. (2006). Uses for JNK: the many and varied substrates of the c-Jun N-terminal kinases. *Microbiol. Mol. Biol. Rev.* 70, 1061–1095. doi: 10.1128/MMBR.00025-06
- Chen, C. Y., Lin, C. W., Chang, C. Y., Jiang, S. T., and Hsueh, Y. P. (2011). Sarm1, a negative regulator of innate immunity, interacts with syndecan-2 and regulates neuronal morphology. *J. Cell Biol.* 193, 769–784. doi: 10.1083/jcb.201008050
- Courchet, J., Lewis, T. L. Jr., Lee, S., Courchet, V., Liou, D. Y., Aizawa, S., et al. (2013). Terminal axon branching is regulated by the LKB1-NUAK1 kinase pathway via presynaptic mitochondrial capture. *Cell* 153, 1510–1525. doi: 10.1016/j.cell.2013.05.021
- Figley, M. D., and DiAntonio, A. (2020). The SARM1 axon degeneration pathway: control of the NAD⁺ metabolome regulates axon survival in health and disease. *Curr. Opin. Neurobiol.* 63, 59–66. doi: 10.1016/j.conb.2020.02.012
- Fisher, D., Xing, B., Dill, J., Li, H., Hoang, H. H., Zhao, Z., et al. (2011). Leukocyte common antigen-related phosphatase is a functional receptor for chondroitin sulfate proteoglycan axon growth inhibitors. *J. Neurosci.* 31, 14051–14066. doi: 10.1523/JNEUROSCI.1737-11.2011
- Gallo, G. (2011). The cytoskeletal and signaling mechanisms of axon collateral branching. *Dev. Neurobiol.* 71, 201–220. doi: 10.1002/dneu.20852
- Gallo, G., and Letourneau, P. C. (1998). Localized sources of neurotrophins initiate axon collateral sprouting. *J. Neurosci.* 18, 5403–5414. doi: 10.1523/JNEUROSCI.18-14-05403.1998
- Geisler, S., Doan, R. A., Strickland, A., Huang, X., Milbrandt, J., and DiAntonio, A. (2016). Prevention of vincristine-induced peripheral neuropathy by genetic deletion of SARM1 in mice. *Brain* 139, 3092–3108. doi: 10.1093/brain/aww251
- Gerdts, J., Summers, D. W., Milbrandt, J., and DiAntonio, A. (2016). Axon self-destruction: new links among SARM1, MAPKs, and NAD⁺ Metabolism. *Neuron* 89, 449–460. doi: 10.1016/j.neuron.2015.12.023
- Gerdts, J., Summers, D. W., Sasaki, Y., DiAntonio, A., and Milbrandt, J. (2013). Sarm1-mediated axon degeneration requires both SAM and TIR interactions. *J. Neurosci.* 33, 13569–13580. doi: 10.1523/JNEUROSCI.1197-13.2013

AUTHOR CONTRIBUTIONS

GG designed the research, analyzed the data, and prepared the manuscript. AK and SH designed the research, conducted the research, analyzed the data, and revised the manuscript. All authors contributed to the article and approved the submitted version.

FUNDING

This project was supported by the NIH R21NS107586 (GG).

ACKNOWLEDGMENTS

We acknowledge that this investigation arose from a preliminary collaborative study with T. Ferguson (Biogen, neuromuscular development unit), a former member of the faculty at the Shriners Hospitals Pediatric Research Center. Ferguson also provided skin biopsies for the analysis of skin innervation and transferred the SARM1 KO and wild-type mouse colony to GG.

- Himeno, T., Kamiya, H., Naruse, K., Harada, N., Ozaki, N., Seino, Y., et al. (2011). Beneficial effects of exendin-4 on experimental polyneuropathy in diabetic mice. *Diabetes* 60, 2397–2406. doi: 10.2337/db10-1462
- Hou, Y. J., Banerjee, R., Thomas, B., Nathan, C., García-Sastre, A., Ding, A., et al. (2013). SARM is required for neuronal injury and cytokine production in response to central nervous system viral infection. *J. Immunol.* 191, 875–883. doi: 10.4049/jimmunol.1300374
- Izadifar, A., Courchet, J., Virga, D. M., Verreet, T., Hamilton, S., Ayaz, D., et al. (2021). Axon morphogenesis and maintenance require an evolutionary conserved safeguard function of Wnk kinases antagonizing Sarm and Axed. *Neuron* 109, 2864–2883.e8. doi: 10.1016/j.neuron.2021.07.006
- Janke, C., and Magiera, M. M. (2020). The tubulin code and its role in controlling microtubule properties and functions. *Nat. Rev. Mol. Cell Biol.* 21, 307–326. doi: 10.1038/s41580-020-0214-3
- Jones, S. L., Selzer, M. E., and Gallo, G. (2006). Developmental regulation of sensory axon regeneration in the absence of growth cones. *J. Neurobiol.* 66, 1630–1645. doi: 10.1002/neu.20309
- Kalil, K., and Dent, E. W. (2014). Branch management: mechanisms of axon branching in the developing vertebrate CNS. *Nat. Rev. Neurosci.* 15, 7–18. doi: 10.1038/nrn3650
- Ketschek, A., and Gallo, G. (2010). Nerve growth factor induces axonal filopodia through localized microdomains of phosphoinositide 3-kinase activity that drive the formation of cytoskeletal precursors to filopodia. *J. Neurosci.* 30, 12185–12197. doi: 10.1523/JNEUROSCI.1740-10.2010
- Ketschek, A., Spillane, M., Dun, X. P., Hardy, H., Chilton, J., and Gallo, G. (2016). Drebrin coordinates the actin and microtubule cytoskeleton during the initiation of axon collateral branches. *Dev. Neurobiol.* 76, 1092–1110. doi: 10.1002/dneu.22377
- Ketschek, A. R., Jones, S. L., and Gallo, G. (2007). Axon extension in the fast and slow lanes: substratum-dependent engagement of myosin II functions. *Dev. Neurobiol.* 67, 1305–1320. doi: 10.1002/dneu.20455
- Kim, Y., Zhou, P., Qian, L., Chuang, J. Z., Lee, J., Li, C., et al. (2007). MyD88-5 links mitochondria, microtubules, and JNK3 in neurons and regulates neuronal survival. *J. Exp. Med.* 204, 2063–2074. doi: 10.1084/jem.2007.0868
- Lelkes, P. I., Unsworth, B. R., Saporta, S., Cameron, D. F., and Gallo, G. (2005). “Culture of neuroendocrine and neuronal cells for tissue engineering,” in *Culture of Cells of Tissue Engineering*, ed. R. I. Freshney (Hoboken: John Wiley & Sons), 375–415. doi: 10.1002/0471741817.ch14

- Lewis, T. L. Jr., Courchet, J., and Polleux, F. (2013). Cell biology in neuroscience: cellular and molecular mechanisms underlying axon formation, growth, and branching. *J. Cell Biol.* 202, 837–848. doi: 10.1083/jcb.201305098
- Lewis, T. L. Jr., Turi, G. F., Kwon, S. K., Losonczy, A., and Polleux, F. (2016). Progressive decrease of mitochondrial motility during maturation of cortical axons In Vitro and In Vivo. *Curr. Biol.* 26, 2602–2608. doi: 10.1016/j.cub.2016.07.064
- Loudon, R. P., Silver, L. D., Yee, H. F. Jr., and Gallo, G. (2006). RhoA-kinase and myosin II are required for the maintenance of growth cone polarity and guidance by nerve growth factor. *J. Neurobiol.* 66, 847–867. doi: 10.1002/neu.20258
- Mandelkow, E. M., Biernat, J., Drewes, G., Gustke, N., Trinczek, B., and Mandelkow, E. (1995). Tau domains, phosphorylation, and interactions with microtubules. *Neurobiol. Aging* 16, 355–362. doi: 10.1016/0197-4580(95)00025-a
- Menon, S., and Gupton, S. (2018). Recent advances in branching mechanisms underlying neuronal morphogenesis. *F1000Res.* 7:F1000 Faculty Rev-1779. doi: 10.12688/f1000research.16038.1
- Misgeld, T., Kerschensteiner, M., Bareyre, F. M., Burgess, R. W., and Lichtman, J. W. (2007). Imaging axonal transport of mitochondria in vivo. *Nat. Methods* 4, 559–561. doi: 10.1038/nmeth1055
- Mukherjee, P., Woods, T. A., Moore, R. A., and Peterson, K. E. (2013). Activation of the innate signaling molecule MAVS by bunyavirus infection upregulates the adaptor protein SARM1, leading to neuronal death. *Immunity* 38, 705–716. doi: 10.1016/j.immuni.2013.02.013
- Narayanareddy, B. R., Vartiainen, S., Hariri, N., O'Dowd, D. K., and Gross, S. P. (2014). A biophysical analysis of mitochondrial movement: differences between transport in neuronal cell bodies versus processes. *Traffic* 15, 762–771. doi: 10.1111/tra.12171
- Onifer, S. M., Smith, G. M., and Fouad, K. (2011). Plasticity after spinal cord injury: relevance to recovery and approaches to facilitate it. *Neurotherapeutics* 8, 283–293. doi: 10.1007/s13311-011-0034-4
- Osterloh, J. M., Yang, J., Rooney, T. M., Fox, A. N., Adalbert, R., Powell, E. H., et al. (2012). dSarm/Sarm1 is required for activation of an injury-induced axon death pathway. *Science* 337, 481–484. doi: 10.1126/science.1223899
- Pacheco, A., and Gallo, G. (2016). Actin filament-microtubule interactions in axon initiation and branching. *Brain Res. Bull.* 126, 300–310. doi: 10.1016/j.brainresbull.2016.07.013
- Panneerselvam, P., and Ding, J. L. (2015). Beyond TLR signaling—The role of SARM in antiviral immune defense, apoptosis & development. *Int. Rev. Immunol.* 34, 432–444. doi: 10.3109/08830185.2015.1065826
- Roche, F. K., Marsick, B. M., and Letourneau, P. C. (2009). Protein synthesis in distal axons is not required for growth cone responses to guidance cues. *J. Neurosci.* 29, 638–652. doi: 10.1523/JNEUROSCI.3845-08.2009
- Sainath, R., and Gallo, G. (2021). Bioenergetic requirements and spatiotemporal profile of nerve growth factor induced PI3K-Akt signaling along sensory axons. *Front. Mol. Neurosci.* 14:726331. doi: 10.3389/fnmol.2021.726331
- Sainath, R., Ketschek, A., Grandi, L., and Gallo, G. (2017a). CSPGs inhibit axon branching by impairing mitochondria-dependent regulation of actin dynamics and axonal translation. *Dev. Neurobiol.* 77, 454–473. doi: 10.1002/dneu.22420
- Sainath, R., Armijo-Weingart, L., Ketschek, A., Xu, Z., Li, S., and Gallo, G. (2017b). Chondroitin sulfate proteoglycans negatively regulate the positioning of mitochondria and endoplasmic reticulum to distal axons. *Dev. Neurobiol.* 77, 1351–1370. doi: 10.1002/dneu.22535
- Schwarz, T. L. (2013). Mitochondrial trafficking in neurons. *Cold Spring Harb. Perspect. Biol.* 5:a011304. doi: 10.1101/cshperspect.a011304
- Silver, L., Michael, J. V., Goldfinger, L. E., and Gallo, G. (2014). Activation of PI3K and R-Ras signaling promotes the extension of sensory axons on inhibitory chondroitin sulfate proteoglycans. *Dev. Neurobiol.* 74, 918–933. doi: 10.1002/dneu.22174
- Smith, D. S., and Skene, J. H. (1997). A transcription-dependent switch controls competence of adult neurons for distinct modes of axon growth. *J. Neurosci.* 17, 646–658. doi: 10.1523/JNEUROSCI.17-02-00646.1997
- Smith, G. M., and Gallo, G. (2018). The role of mitochondria in axon development and regeneration. *Dev. Neurobiol.* 78, 221–237. doi: 10.1002/dneu.22546
- Spillane, M., Ketschek, A., Donnelly, C. J., Pacheco, A., Twiss, J. L., and Gallo, G. (2012). Nerve growth factor-induced formation of axonal filopodia and collateral branches involves the intra-axonal synthesis of regulators of the actin-nucleating Arp2/3 complex. *J. Neurosci.* 32, 17671–17689. doi: 10.1523/JNEUROSCI.1079-12.2012
- Spillane, M., Ketschek, A., Jones, S. L., Korobova, F., Marsick, B., Lanier, L., et al. (2011). The actin nucleating Arp2/3 complex contributes to the formation of axonal filopodia and branches through the regulation of actin patch precursors to filopodia. *Dev. Neurobiol.* 71, 747–758. doi: 10.1002/dneu.20907
- Spillane, M., Ketschek, A., Merianda, T. T., Twiss, J. L., and Gallo, G. (2013). Mitochondria coordinate sites of axon branching through localized intra-axonal protein synthesis. *Cell Rep.* 5, 1564–1575. doi: 10.1016/j.celrep.2013.11.022
- Stepanova, T., Slemmer, J., Hoogenraad, C. C., Lansbergen, G., Dortland, B., De Zeeuw, C. I., et al. (2003). Visualization of microtubule growth in cultured neurons via the use of EB3-GFP (end-binding protein 3-green fluorescent protein). *J. Neurosci.* 23, 2655–2664. doi: 10.1523/JNEUROSCI.23-07-02655.2003
- Summers, D. W., DiAntonio, A., and Milbrandt, J. (2014). Mitochondrial dysfunction induces Sarm1-dependent cell death in sensory neurons. *J. Neurosci.* 34, 9338–9350. doi: 10.1523/JNEUROSCI.0877-14.2014
- Tao, K., Matsuki, N., and Koyama, R. (2014). AMP-activated protein kinase mediates activity-dependent axon branching by recruiting mitochondria to axon. *Dev. Neurobiol.* 74, 557–573. doi: 10.1002/dneu.22149
- Tymanskyj, S. R., and Ma, L. (2019). MAP7 prevents axonal branch retraction by creating a stable microtubule boundary to rescue polymerization. *J. Neurosci.* 39, 7118–7131. doi: 10.1523/JNEUROSCI.0775-19.2019
- Tymanskyj, S. R., Yang, B. H., Verhey, K. J., and Ma, L. (2018). MAP7 regulates axon morphogenesis by recruiting kinesin-1 to microtubules and modulating organelle transport. *Elife* 7:e36374. doi: 10.7554/eLife.36374
- Verburg, J., and Hollenbeck, P. J. (2008). Mitochondrial membrane potential in axons increases with local nerve growth factor or semaphorin signaling. *J. Neurosci.* 28, 8306–8315. doi: 10.1523/JNEUROSCI.2614-08.2008
- Walker, L. J., Summers, D. W., Sasaki, Y., Brace, E. J., Milbrandt, J., and DiAntonio, A. (2017). MAPK signaling promotes axonal degeneration by speeding the turnover of the axonal maintenance factor NMNAT2. *Elife* 6:e22540. doi: 10.7554/eLife.22540
- Winkle, C. C., Taylor, K. L., Dent, E. W., Gallo, G., Greif, K. F., and Gupton, S. L. (2016). Beyond the cytoskeleton: the emerging role of organelles and membrane remodeling in the regulation of axon collateral branches. *Dev. Neurobiol.* 12, 1293–1307. doi: 10.1002/dneu.22398
- Wong, H. H., Lin, J. Q., Ströhl, F., Roque, C. G., Cioni, J. M., Cagnetta, R., et al. (2017). RNA docking and local translation regulate site-specific axon remodeling in vivo. *Neuron* 95, 852–868.e8. doi: 10.1016/j.neuron.2017.07.016
- Yang, J., Wu, Z., Renier, N., Simon, D. J., Uryu, K., Park, D. S., et al. (2015). Pathological axonal death through a MAPK cascade that triggers a local energy deficit. *Cell* 160, 161–176. doi: 10.1016/j.cell.2014.11.053
- Zhou, B., Yu, P., Lin, M. Y., Sun, T., Chen, Y., and Sheng, Z. H. (2016). Facilitation of axon regeneration by enhancing mitochondrial transport and rescuing energy deficits. *J. Cell Biol.* 214, 103–119. doi: 10.1083/jcb.201605101

Conflict of Interest: The authors declare that the research was conducted in the absence of any commercial or financial relationships that could be construed as a potential conflict of interest.

Publisher's Note: All claims expressed in this article are solely those of the authors and do not necessarily represent those of their affiliated organizations, or those of the publisher, the editors and the reviewers. Any product that may be evaluated in this article, or claim that may be made by its manufacturer, is not guaranteed or endorsed by the publisher.

Copyright © 2022 Ketschek, Holland and Gallo. This is an open-access article distributed under the terms of the Creative Commons Attribution License (CC BY). The use, distribution or reproduction in other forums is permitted, provided the original author(s) and the copyright owner(s) are credited and that the original publication in this journal is cited, in accordance with accepted academic practice. No use, distribution or reproduction is permitted which does not comply with these terms.



LIS1 and NDEL1 Regulate Axonal Trafficking of Mitochondria in Mature Neurons

Jai P. Pandey, Liang Shi, Remi A. Brebion and Deanna S. Smith*

Department of Biological Sciences, University of South Carolina, Columbia, SC, United States

OPEN ACCESS

Edited by:

James N. Sleight,
University College London,
United Kingdom

Reviewed by:

Alessio Vagnoni,
King's College London,
United Kingdom
Gerardo Morfini,
University of Illinois at Chicago,
United States

*Correspondence:

Deanna S. Smith
deannasm@biol.sc.edu

Specialty section:

This article was submitted to
Molecular Signalling and Pathways,
a section of the journal
Frontiers in Molecular Neuroscience

Received: 21 December 2021

Accepted: 10 February 2022

Published: 07 April 2022

Citation:

Pandey JP, Shi L, Brebion RA and
Smith DS (2022) LIS1 and
NDEL1 Regulate Axonal Trafficking of
Mitochondria in Mature Neurons.
Front. Mol. Neurosci. 15:841047.
doi: 10.3389/fnmol.2022.841047

Defective mitochondrial dynamics in axons have been linked to both developmental and late-onset neurological disorders. Axonal trafficking is in large part governed by the microtubule motors kinesin-1 and cytoplasmic dynein 1 (dynein). Dynein is the primary retrograde transport motor in axons, and mutations in dynein and many of its regulators also cause neurological diseases. Depletion of LIS1, famous for linking dynein deregulation to lissencephaly (smooth brain), in adult mice leads to severe neurological phenotypes, demonstrating post-developmental roles. LIS1 stimulates retrograde transport of acidic organelles in cultured adult rat dorsal root ganglion (DRG) axons but findings on its role in mitochondrial trafficking have been inconsistent and have not been reported for adult axons. Here we report that there is an increased number of mitochondria in cross-sections of sciatic nerve axons from adult LIS1^{+/-} mice. This is probably related to reduced dynein activity as axons from adult rat nerves exposed to the dynein inhibitor, ciliobrevin D also had increased numbers of mitochondria. Moreover, LIS1 overexpression (OE) in cultured adult rat DRG axons stimulated retrograde mitochondrial transport while LIS1 knockdown (KD) or expression of a LIS1 dynein-binding mutant (LIS1-K147A) inhibited retrograde transport, as did KD of dynein heavy chain (DHC). These findings are consistent with our report on acidic organelles. However, KD of NDEL1, a LIS1 and dynein binding protein, or expression of a LIS1 NDEL1-binding mutant (LIS1-R212A) also dramatically impacted retrograde mitochondrial transport, which was not the case for acidic organelles. Manipulations that disrupted retrograde mitochondrial transport also increased the average length of axonal mitochondria, suggesting a role for dynein in fusion or fission events. Our data point to cargo specificity in NDEL1 function and raise the possibility that defects in the LIS1/NDEL1 dynein regulatory pathway could contribute to mitochondrial diseases with axonal pathologies.

Keywords: axon, mitochondria, dynein, DRG, sciatic nerve, LIS1, NDEL1

INTRODUCTION

Because of its role in human brain development LIS1 has been studied by developmental neuroscientists for over two decades (Reiner et al., 1993; Hirotsune et al., 1998; Smith et al., 2000; Saillour et al., 2009; Reiner and Sapir, 2013; Markus et al., 2020). Dominant mutations in the gene encoding LIS1, *PAFAH1B1*, cause lissencephaly (smooth brain; Wynshaw-Boris, 2007; Saillour et al., 2009). Although rare, lissencephaly is a devastating disorder characterized by severe cognitive and motor impairment, worsening seizures, and childhood lethality. Preclinical studies have demonstrated that decreasing LIS1 protein expression disrupts the timing of mitosis and neural differentiation as well as the migration of neural precursors in the developing brain, and LIS1^{+/-} mice have been used as a model to study cellular functions of LIS during brain development (Hirotsune et al., 1998; Wynshaw-Boris, 2007; Hebbar et al., 2008a; Yingling et al., 2008; Hippenmeyer et al., 2010; Moon et al., 2014; Xiang and Qiu, 2020). Several studies indicate that the expression of LIS1 in these mice is reduced by around 50% (Yan et al., 2003; Hebbar et al., 2008a; Sebe et al., 2013; Toba et al., 2013). Excessive LIS1 expression is also deleterious in both humans and mice, so LIS1 expression levels must be precisely regulated (Bi et al., 2009).

LIS1 is highly conserved across animal and fungal species, and all tested orthologs, from yeast to human, bind directly to dynein's two heavy chains (DHCs); DHCs hydrolyze ATP and contact microtubules for processive cargo transport (Xiang and Qiu, 2020). Our cell-based studies led us to hypothesize that mammalian LIS1 stimulates dynein activity, and in our hands, purified LIS1 modestly but consistently increased the ATPase activity of purified bovine brain dynein (Smith et al., 2000; Mesngon et al., 2006; Hebbar et al., 2008b; Pandey and Smith, 2011; Hines et al., 2018). However, other studies contradicted this, and substantial data, especially using *in vitro* assays, indicated that LIS1 inhibits dynein; see Markus et al. (2020). The story remained confusing until recently when new studies refined the consensus view of how LIS1 regulates the motor. Large, multi-subunit dynein complexes can adopt a closed, autoinhibited conformation (the phi particle) or an open conformation (Zhang et al., 2017). Other dynein subunits interact with dynactin and one of several cargo adaptors, both of which are required for robust processive movement of mammalian dynein along microtubules—dynactin and activating cargo adaptors only interact with the open form, and the tripartite Dynein/Dynactin/Adaptor complex is referred to as the DDA complex (Reck-Peterson et al., 2018; Urnavicius et al., 2018; Olenick and Holzbaur, 2019; Canty and Yildiz, 2020; Lee et al., 2020; Xiang and Qiu, 2020). The newest model is that LIS1 binding to DHC stabilizes the open conformation, resulting in a higher proportion of motors able to form active DDA complexes (Qiu et al., 2019; Elshenawy et al., 2020; Htet et al., 2020; Marzo et al., 2020; McKenney, 2020). Moreover, LIS1 promotes the formation of adaptor complexes containing two motors (D₂DA complexes) which generate more force and likely have

longer processive runs (Elshenawy et al., 2020; Htet et al., 2020).

Dynein is the primary motor driving retrograde transport in axons (Guedes-Dias and Holzbaur, 2019). Our studies using LysoTracker to label acidic organelles in cultured adult rat and mouse sensory neurons showed that increasing the ratio of LIS1 to dynein stimulated retrograde axonal transport, while a missense LIS1 mutation that prevents LIS1 from binding to dynein (LIS1-K147A) severely disrupted retrograde transport, as did an shRNA targeting LIS1 (Pandey and Smith, 2011). LIS1 and dynein interact with NDEL1, and a homolog, NDE1 (Niethammer et al., 2000; Sasaki et al., 2000; Bradshaw and Hayashi, 2017). In some cases, phosphorylated NDEL1 appears to work with LIS1 to stimulate dynein (Niethammer et al., 2000; Sasaki et al., 2000; Hebbar et al., 2008b; Pandey and Smith, 2011; Klinman et al., 2017). However, in cultured DRG axons, NDEL1 KD or expression of a LIS1 missense mutation that blocks NDEL1 binding but not dynein binding (LIS1-R212A) had only a minimal impact on retrograde transport of acidic organelles (Pandey and Smith, 2011). Moreover, no increase in ATPase activity was observed when NDEL1 was included in our ATPase assay (unpublished results). Others reported that LIS1 reduced ATPase activity (Yamada et al., 2008). To our knowledge, the role of NDEL1/NDE1 in the DDA/D₂DA complex is not yet known.

Inducing LIS1 depletion in 2-month-old mice resulted in the rapid onset of neurological phenotypes and death, demonstrating a critical postdevelopmental role (Hines et al., 2018). The most likely cause was disrupted sensorimotor and cardiorespiratory circuits, possibly due to altered axonal transport. The adult nervous system is uniquely dependent on a continuous energy supply for synaptic function, and mitochondrial trafficking abnormalities are clearly associated with later onset neurological disease (Misgeld and Schwarz, 2017; Castora, 2019; Mandal and Drerup, 2019; Rangaraju et al., 2019; Han et al., 2020; Yang et al., 2021). Because of this, we reasoned that a disruption in mitochondrial dynamics could be involved in the phenotype. We have now carried out MitoTracker transport studies in adult DRG cultures and found clear roles for both LIS1 and NDEL1. We uncovered a surprising difference between acidic organelles and mitochondria with respect to NDEL1. We also found LIS1 and NDEL1 perturbations that reduce trafficking increase mitochondrial size, suggesting that these regulators play a role in fission or fusion events.

METHODS

Electron Microscopy of Sciatic Nerve Sections

LIS1^{+/-} Nerves

Sciatic nerve segments were dissected from adult LIS1^{+/-} mice and fixed overnight in 2.5% glutaraldehyde at 4°C. Fixed nerves were sent to the electron microscopy core facility at the UofSC school of medicine for processing and electron microscopy using a JEOL 1400 plus system (Peabody, MA, USA).

Ciliobrevin-D Releasing Nerve Cuffs

PEVA (polyethylene vinyl acetate, Sigma Aldrich, St. Louis, MO, USA, #340502) nerve cuffs were used to release a small molecule inhibitor of dynein, ciliobrevin-D (EMD Millipore, Burlington, MA, USA # 25041) directly onto the sciatic nerve of adult rats (Smith and Skene, 1997; Schneider et al., 2017). Ciliobrevin-D was dissolved in DMSO and added to a 10% solution of PEVA dissolved in methylene chloride to a final concentration of 1 mM. This requires heating to 60°C. DMSO only was used to make control cuffs. The liquid PEVA/drug mixture was poured into a flat mold, flash-frozen on dry ice, and the solvent evaporated with anhydrous calcium sulfate at -20°C for 1 week. The solid yet pliable sheets were cut into strips, 1 mm wide, and wrapped around the exposed sciatic nerve at mid-thigh. Ends were superglued together, then the muscle and skin are sutured, and the cuffs left in place for 48 h, after which nerve segments under the cuffs were dissected and fixed overnight in 2.4% glutaraldehyde at 4°C. Sections were analyzed blinded, in that the person counting mitochondria in axonal cross-sections did not know whether sections were from LIS1[±] mice or wild-type (WT) littermates or from the animals exposed to ciliobrevin-D or DMSO only.

Immunoprecipitation and Western Blotting of Nerve Extracts

Sciatic nerve segments were removed 48 h after cuff application. Nerves were Dounce-homogenized in ice cold 50 mM Tris, pH 8.0, 250 mM NaCl, 0.5% NP40, and halt protease and phosphatase inhibitor cocktail (ThermoFisher, Waltham, MA, USA, 78440). Homogenates were centrifuged at 30,000 × g for 30 min. Supernatants were split into two new tubes and immunoprecipitated with anti-dynein intermediate chain antibody coupled to agarose (Santa Cruz Biotechnology Inc., USA, sc-13524 AC) or normal mouse IgG coupled to agarose (Santa Cruz Biotechnology Inc., USA, sc-2343) for 2 h at 4°C with rocking. Beads were washed three times in lysis buffer and precipitated proteins separated by 10% acrylamide SDS-PAGE and transferred to PVDF membrane for probing with the dynein intermediate chain antibody (Santa Cruz Biotechnology Inc., USA, sc-13524).

RNAi and Mammalian Expression Constructs and Antibodies

Complementary hairpin sequences to *LIS1*, *DYNC1H1* (*DHC*) and *NDEL1* in the pSil-EGFP vector (RRID:Addgene_52675) were provided by LH Tsai (MIT) and have been well characterized (Shu et al., 2004; Hebbar et al., 2008b; Pandey and Smith, 2011; Klinman and Holzbaur, 2015). *LIS1*: GAGTTGTGCTGATGACAAG (1,062–1,080 bp), *DYNC1H1*: GAAGGTCATGAGCCAAGAA (9,753–9,771 bp), *NDEL1*: GCAGGTCTCAGTGTTAGAA (276–294 bp). Scrambled sequences were generated from these sequences and have been shown to have no effect on the expression of the relevant proteins. These scrambled sequences were used as controls for each specific shRNA. To generate HA-LIS1, HA-LIS1-K147A, and HA-LIS1-R212A, full-length murine LIS1 and point mutants of LIS1 (provided by A. Musacchio) were subcloned

into a pCruzHA vector (Santa Cruz Biotechnology, Inc., Dallas, TX, USA). Axons were labeled for dynein using the dynein intermediate chain 74.1 mouse monoclonal antibody (Santa Cruz Biotechnology Inc., Dallas, TX, USA, sc-13524).

DRG Culture and Transfection

Primary cultures of sensory neurons from 4 to 6 lumbar DRG of adult rats were prepared as described in (Smith and Skene, 1997), with a few minor changes. Briefly, neurons in 3-month-old male Sprague Dawley rats were conditioned for rapid axon elongation by sciatic nerve crush 48 h prior to harvesting. This allows long axons to be imaged before non-neuronal cells proliferate because mitochondria from these cells can obscure imaging of axonal mitochondria. This also allows us to avoid mitotic toxins such as cytosine arabinoside which reportedly can impact mitochondrial DNA synthesis and compromise mitochondrial function (Zhuo et al., 2018). Following enzymatic and mechanical dissociation, suspended cells were subjected to centrifugation through a 15% sucrose solution to reduce the number of smaller glial cells. Neurons were transfected immediately after dissection using the small cell number SCN Basic Nucleofector kit for primary neurons (Amaxa Biosystems, Walkersville, MD, USA, VSPI #1003). All LIS1, DHC, or NDEL1 expressing constructs were co-transfected with an EGFP vector (pEGFP-C1, Clontech, Mountain View, CA, USA, # V012024) to identify transfected neurons. Following transfection, neurons were resuspended in Hamm's F14 medium (Biowest, Nuaille, France) supplemented with 10% horse serum (Biowest, Nuaille, France) and buffered with 25 mM HEPES, then plated onto German glass coverslips (Fisher, Waltham, MA, USA) coated with 10 µg/ml poly-D-lysine (Sigma, St. Louis, MO, USA) and 10 µg/ml laminin (EMD, Millipore, Burlington, MA, USA). Neurons were used within 3–4 days of culture for transport studies.

Fluorescence Time-Lapse Microscopy

After exposure to 100 nM Mitotracker Red CMXRos (Invitrogen, Waltham, MA, USA, M7512) for 20 min, coverslips were transferred into a fresh medium containing 25 mM Hepes, pH 7.4, and 10 mM OxyFluor (Oxyrase, Inc OF-0005), in a water-heated custom-built microscope stage warmed to 37°C. EGFP-positive, 100 µm long axon segments that were clearly linked to a specific neuronal cell body and did not cross over other axons were selected for analysis. Axon segments were chosen that were at least 20 µm from cell bodies or growth cones because the direction of movement seemed to be different close to these regions (more anterograde near growth cones, more retrograde near cell bodies). Time-lapse microscopy was performed using an Axiovert 200 inverted microscope (Carl Zeiss Inc., Jena, Germany) equipped with C-Apo 63X/1.2 W/0.2 water-immersion objective. Digital images were acquired every 2.6 s for 4 min (92 frames) using a charge-coupled camera (AxioCam HRm, Carl Zeiss Inc., Jena, Germany) linked to AxioVision software (version 4.7, Carl Zeiss Inc., Jena, Germany).

Analysis of Percentage of Mitochondria Moving in Axons

To determine the percentage of mitochondria moving and their direction, kymographs were generated from time-lapse movies using Image J open-source image processing software and the KymoToolBox Plugin. Cultures from three different rats were used to control for individual differences. For each condition, 12 100 μm axon segments were imaged (four per coverslip). Imaged axon segments were at least 20 μm from cell bodies, growth cones or branch points. Analyses were carried out blinded, so that the person analyzing the kymographs did not know which treatment was being analyzed. A segmented line tool was used to isolate individual organelle tracks in the kymographs. Lines that showed less than 5 μm displacement in either direction during the recording interval were categorized as static mitochondria. Lines that sloped toward the right only, with no switching at any point, with a net displacement of >5 μm were categorized as retrogradely moving mitochondria. Lines that sloped to the left only with no switching at any point, with a net displacement of >5 μm were categorized as anterograde. Mitochondria that showed net displacement of >5 μm in both directions at any point during the interval were categorized as both, and organelles that had no displacements >5 μm were categorized as static. Mitochondria typically exhibited runs of variable lengths in either direction with intermittent pauses. We deemed these runs “motile events” and focused on the analysis of retrograde motile events (RMEs). A single organelle could produce several RMEs between pauses or anterograde runs. Many of these are shorter than 5 μm , but overall retrograde displacement for an individual organelle would be the sum of the retrograde motile events, and this needed to be greater than 5 μm or it was categorized as static. These static organelles sometimes “wobble” a few microns but do not undergo sustained processive movement in either direction.

Analysis of Average Speeds and Run Lengths of Retrograde Motile Events

ImageJ software with a manual tracking plug-in that allows retrieval of object coordinates for image frames of time-lapse series of images was used to determine run lengths and speeds. If an organelle did not reach an average speed of 0.1 $\mu\text{m}/\text{s}$ during three consecutive time-lapse intervals it was taken as a pause. If the organelle moved again later, it was considered a new motile event. Average run length and velocities were determined by finding the average value for new track positions for each RME. Mean velocities of all frames in an RME were determined for each RME. The percentage of motile events with average velocities >0.5 $\mu\text{m}/\text{s}$ was also determined. Retrograde flux in $\mu\text{m}/\text{min}$ was calculated as the sum of net displacements of all RMEs for each of the three experiments (animals, 12 axons from each animal) divided by the recording interval time (4 min).

Analysis of Mitochondrial Length

Mitochondria labeled with MitoTracker Red could be visualized in neurons fixed in 4% paraformaldehyde for 10 min at 37°C. Axons in three separate cultures from three different animals were analyzed. To avoid errors that might arise by measuring different axonal regions, we limited the analysis of mitochondria

to long unbranched axons or to long axonal segments between branch points at least 30 μm from the branch points. We did not include mitochondria in growth cones or in axonal segments within 20 μm from the beginning of the growth cone or 30 μm from the axon hillock. Five axons segments were analyzed in each culture, and the total of 15 segments analyzed contained between 116 and 134 mitochondria.

Statistics

GraphPad Prism 9, USA was used to determine statistical significance for percent retrograde, run lengths, and speeds, using nonparametric one-way ANOVA with a Kruskal Wallis test. For all quantified results, except retrograde flux, Dunn’s multiple comparisons test was used and the false discovery rate was controlled for using the two-stage step-up method of Benjamini, Krieger, and Yekutieli. Statistical significance for retrograde flux was determined by one-way ANOVA with Tukey’s multiple comparisons test. The bootstrap sampling distributions shown below the scatter plots were generated using estimationstatistics.com (Ho et al., 2019) for a shared control (either scrRNA, EGFP, or both). Each mean difference is depicted as a dot. Each 95% confidence interval is indicated by the ends of the vertical error bars.

RESULTS

Altered Mitochondrial Distribution in the Sciatic Nerve Caused by Reduced LIS1 Expression or Pharmacological Inhibition of Dynein

LIS1^{+/-} mice have often been used to study the cellular consequences of LIS1 haploinsufficiency. Although the mice experience some developmental delay and have hyperexcitability in some brain regions, adult mice appear healthy, reproduce normally, and do not show signs of neurodegeneration such as leg clasping upon tail suspension. We did not detect fewer axons in adult LIS1^{+/-} mouse sciatic nerves, and adult DRG neurons from LIS1^{+/-} animals appeared to extend normal axons in culture compared to those from LIS1^{+/+} littermates (Pandey and Smith, 2011). Total iKO in adult DRG neurons resulted in shorter axons but these were sufficiently long to carry our axonal transport studies (Hines et al., 2018).

To determine if mitochondria distribution is altered in adult LIS1^{+/-} axons *in situ*, electron micrographs (EMs) of sciatic nerve cross-sections from three mice (and three WT littermate controls) were examined. **Figure 1A** shows two myelinated axons, but we examined both myelinated and unmyelinated axons to ensure we counted both motor and sensory neurons. Around half of the axonal cross-sections in both LIS1^{+/-} and WT nerves had no visible mitochondria (**Figure 1B**). The percentage of axons with greater than two mitochondria per axon was increased from 16.4% in the WT nerves to 30.1% in the LIS1^{+/-} nerves. At the same time, the percentage with only one mitochondrion was reduced from 34.2% to 17.9%, and the percentage with four or more mitochondria increased from 3.4% to 8.9%. Significantly fewer LIS1^{+/-} axons had only

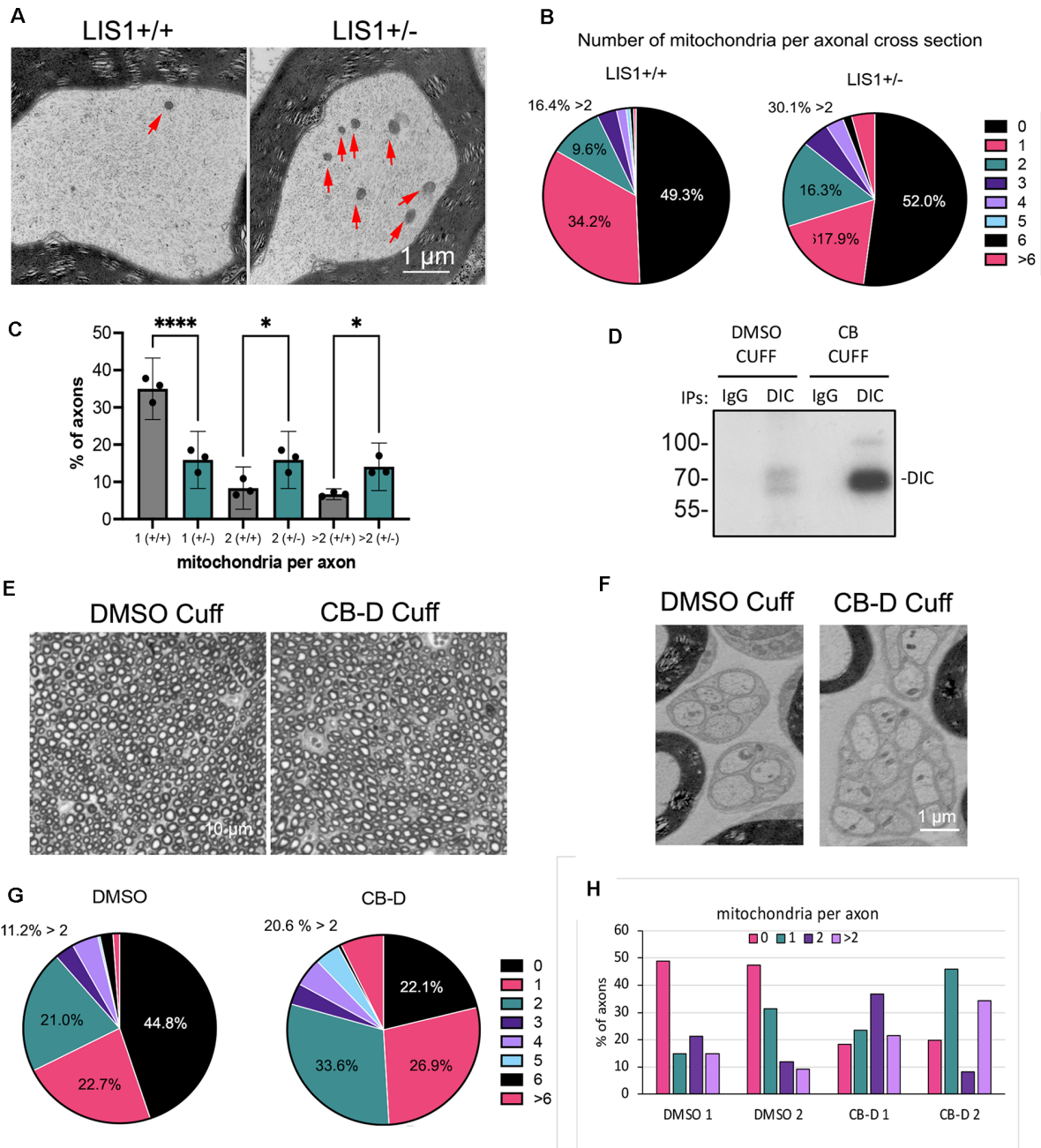


FIGURE 1 | More mitochondria are observed in sciatic nerve axonal cross-section from LIS1^{+/-} mice or rat nerves exposed to Ciliobrevin-D. **(A)** Representative electron micrographs of cross-sections of myelinated axons in sciatic nerves from adult WT LIS1 and LIS1^{+/-} mice at mid-thigh. Red arrows point to mitochondria within the axoplasm. EM images from three different mice of each genotype were analyzed for numbers of mitochondria per axon. **(B)** The pie graphs show the percentage of all axonal cross-sections that contained the indicated number of mitochondria (1 - >6). A total of 676 LIS1^{+/+} axons and 405^{+/-} axons from three mice of each genotype were included, approximately equal numbers per animal. The variation is not because of degeneration but simply a matter of number of axons in each EM micrograph, which was variable. **(C)** The bar graph shows the mean of data (+/- 95% CI) from the three mice in each category. Axons with 0 mitochondria were excluded because the numbers were large and the differences in one mitochondrion, two mitochondria, or >2 mitochondria were less clear. Significance determined by ANOVA using Holm-Šidák's multiple comparisons test. *****p* < 0.0001; **p* > 0.05. **(D)** Ciliobrevin-D (CB-D) was used to inhibit dynein by placing PEVA nerve cuffs impregnated with the compound around adult rat sciatic nerve in mid-thigh. After 48 h dynein had accumulated under a CB-D cuff but not a DMSO control cuff as seen in the IP-Western for dynein intermediate chain (DIC). **(E)** Brightfield image of nerve sections stained for EM shows that the nerves look normal and have similar numbers of axons. **(F)** Unmyelinated axons in Remak bundles also appeared healthy in both DMSO and CB-D treated nerves. **(G)** The pie graphs show the percentage of all axonal cross-sections that contained the indicated number of mitochondria (1 - >6). 150 DMSO axons and 105 CB-D axons from two rats were included. **(H)** The bar graph shows the percentage with 0, 1, 2 or >2 mitochondria for each DMSO treated nerve and each CB-D treated nerve.

one mitochondrion per axon ($p < 0.0001$). Significantly more had ≥ 2 mitochondria ($p = 0.035$; **Figure 1C**).

A similar trend was observed when dynein was inhibited pharmacologically, although we only tested this in two adult rats. We used pliable PEVA nerve cuffs for the release of the dynein inhibitor, ciliobrevin-D (CB-D, onto the mid-region of adult rat sciatic nerves for 48 h. Control cuffs contained only DMSO. A Western blot of dynein intermediate chain immunoprecipitated from nerve segments immediately under the cuffs demonstrated that dynein had accumulated under the CB-D cuff, but not the DMSO cuff, suggesting an interference with dynein-dependent transport in the nerve exposed to CB-D (**Figure 1D**). We counted the number of mitochondria per axon in EMs sections of nerve segments taken from under the cuffs. Neither the drug nor the cuffs themselves appeared to physically damage the nerve as can be seen in the low magnification images in **Figure 1E**. There did not appear to be significant degeneration or loss of axons. Even small unmyelinated fibers in Remak bundles appeared intact (**Figure 1F**). CB-D reduced the percentage of axons with no mitochondria from 42.9% to 22.1% (**Figure 1G**). The percentage with two or more mitochondria per axon increased from 36.2% to 58.4%. **Figure 1H** shows the percentages of axons with 0, 1, 2, or >2 mitochondria from all four nerves. Both CB-D-cuffed nerves showed a trend towards more mitochondria per axon (**Figure 1H**).

Together these data suggest that reducing LIS1 expression or inhibiting dynein pharmacologically alters mitochondrial dynamics in axons *in vivo*, but the precise mechanisms by which these manipulations cause the accumulation of mitochondria in sciatic nerve axons is not known. Inhibition of dynein by Ciliobrevin-D also impacts anterograde transport in cultured neurons, so altered anterograde or retrograde transport could contribute to the phenotype, as could changes in docking and or fission or fusion (Roossien et al., 2015; Sainath and Gallo, 2015). Dynein is important for microtubule sliding and the establishment and maintenance of uniform microtubule polarity in axons (Rao et al., 2017). Dynein inhibition could thus disrupt anterograde transport by disrupting the uniform microtubule polarity in axons. Also, if microtubules being moved anterogradely by dynein normally have attached organelles, then disrupting this process could prevent those anterograde movements.

Both LIS1 and NDEL1 KD Reduce Motile Mitochondria Cultured Adult Rat DRG Axons

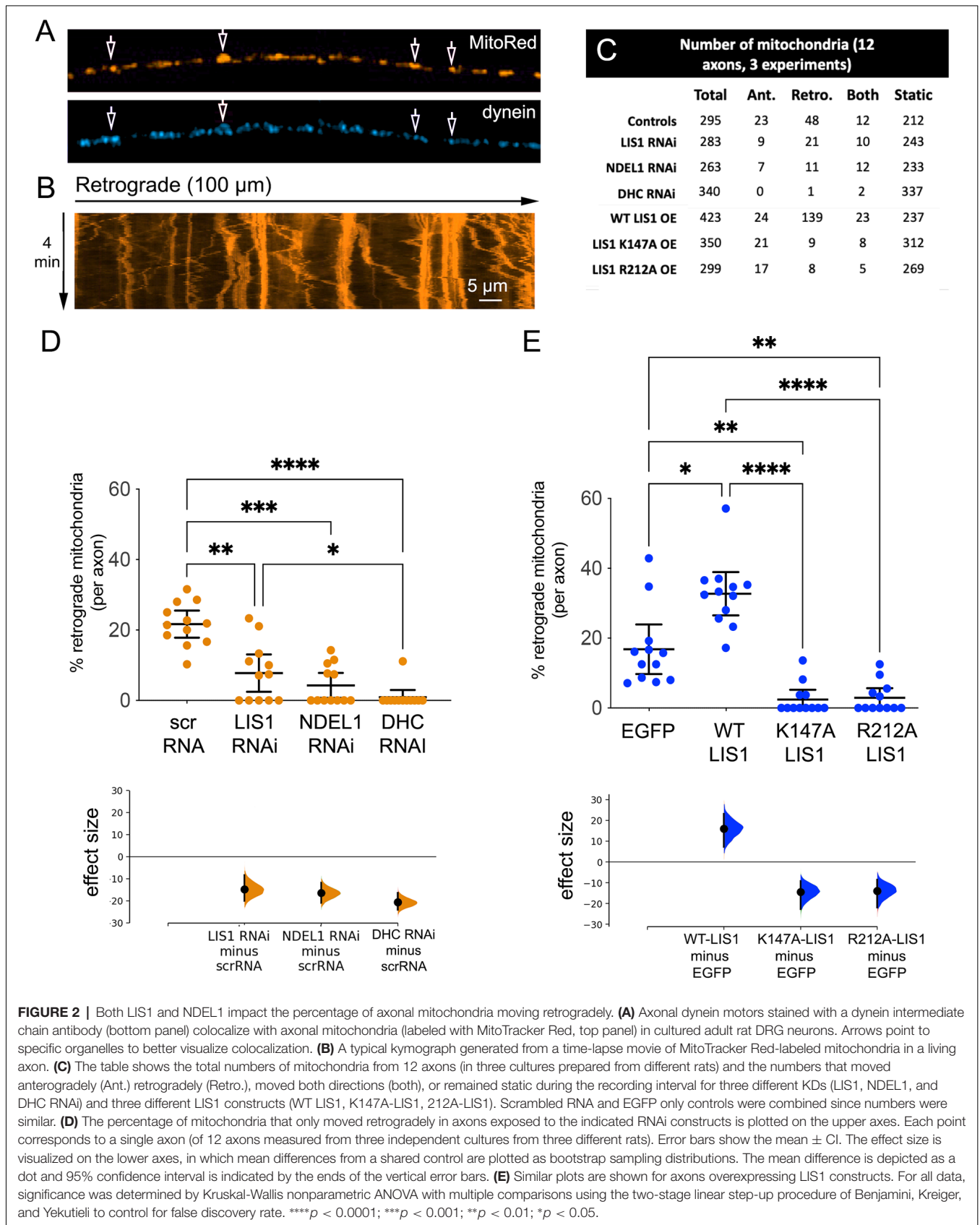
DRG axons extend only axon-like projections, with 95% of microtubule minus-ends oriented towards the cell body (Heidemann et al., 1981; Baas et al., 1988; Kleele et al., 2014; Foster et al., 2022). Mitochondria that move retrogradely towards the cell body are very likely being conveyed by minus-end directed dynein motors. However, dynein has been observed to colocalize with mitochondria moving in both directions, and dynein and kinesin motors can bind to the same organelle (Hirokawa et al., 1990; Schwarz, 2013; Lin and Sheng, 2015). In fixed, cultured adult rat DRG axons immunofluorescently-

labeled dynein can be observed near a subset of MitoTracker Red-labeled mitochondria, and so likely contributes to trafficking events in these axons (**Figure 2A**). After 3–4 days, kymographs generated from time-lapse movies of MitoTracker Red-labeled mitochondria in living axons (**Figure 2B**) were used to determine the number of mitochondria that moved retrogradely or remained static during the 4-min recording interval.

In control axons, ~ 10 –30% underwent retrograde-only motility. To knockdown LIS1, NDEL1, or DHC, short hairpin RNAs (shRNAs) were introduced into newly dissociated neurons as described in (Pandey and Smith, 2011). Precise comparison of reduced protein levels after RNAi transfection using western blotting is difficult in adult DRG neurons because of sparse cultures and relatively low transfection efficiency. However, these same DHC, NDEL1, and LIS1 RNAi constructs reduce endogenous proteins in 3T3 cells by $>60\%$ (Shu et al., 2004), and we reported that the axonal immunofluorescence of each protein was dramatically reduced when neurons were transfected with the same shRNA constructs (Pandey and Smith, 2011). Twelve axon segments from three different DRG cultures from three different rats were analyzed for each condition. **Figure 2C** shows the total numbers of mitochondria in each set, and the numbers that moved anterogradely, retrogradely, switched directions one or more times, or remained static during the recording interval. KD of LIS1 and DHC reduced the numbers moving in both retrograde and anterograde directions as was the case for acidic organelles. Unexpectedly, NDEL1 KD also impacted these numbers to a much greater extent than we reported for acidic organelles. We focused on retrograde movements for the remainder of the study as these are the most likely to be driven by dynein. The percentage of retrograde mitochondria per axon after RNAi treatment is plotted in **Figure 2D**. LIS1 and DHC KD significantly reduced the percentage of mitochondria that underwent retrograde-only motility ($p < 0.0001$ and $p = 0.0017$, respectively). NDEL1 KD had a significant inhibitory effect ($p = 0.0001$), which was not observed for acidic organelles (Pandey and Smith, 2011). While this might be explained by differences in knockdown efficiency of the specific shRNAs in the two different studies, we used the same DRG culture protocols, the same constructs, and the same transfection method in both studies, so it is impossible that NDEL1 has a different, and possibly more critical, role in mitochondrial transport than in transport of acidic organelles.

OE of WT-LIS1, but Not Dynein- or NDEL1-Binding Mutants, Increases the Percentage of Mitochondria Moving Retrogradely in Adult Rat DRG Axons

OE of WT LIS1 increased the number of mitochondria moving retrogradely or in both directions but did not increase the number moving anterogradely (table, **Figure 2C**, and $p = 0.03$, **Figure 2E**). Expression of the dynein-binding mutant, LIS1-K147A, was not able to stimulate retrograde transport, and as with acidic organelles, significantly reduced the percentage of



retrograde mitochondria during the recording interval ($p = 0.001$, **Figure 2E**). Again surprisingly, the NDEL1-binding mutant LIS1-R212A was very effective at reducing the percentage of retrograde mitochondria ($p < 0.0001$), in stark contrast to that observed for acidic organelles labeled with LysoTracker. Interestingly neither mutant has a strong impact on the numbers of anterograde organelles (**Figure 2C**). Together the over expression data supports the idea that NDEL1 is uniquely involved in the dynein-dependent transport of mitochondria in axons.

LIS1 and NDEL1 shRNAs Shorten Run Lengths and Reduce Velocities of Retrograde Motile Events (RMEs)

We used manual tracking software to measure distinct “motile events” that occurred between pauses or directional changes. A single organelle can undergo multiple motile events during the recording interval. These can be in either direction and/or be separated by pauses. Run lengths and average speeds are easily calculated from the manual tracking data. Both LIS1 KD and NDEL1 KD significantly reduced average run lengths ($p = 0.0002$, and $p < 0.0001$, respectively) and the average speeds ($p = 0.0001$, and $p < 0.0001$, respectively) for individual RMEs (**Figures 3A,B**). The manual tracking data allowed us to calculate overall retrograde flux (RF) which is the sum of retrograde displacements of all organelles (263–340) in all axons (12) divided by the 4-min recording interval time). LIS1 and NDEL1 KD significantly reduced RF. The control RF was 4.6 $\mu\text{m}/\text{min}$. RF after LIS1 KD was 1.8 $\mu\text{m}/\text{min}$ ($p = 0.0013$) and after NDEL1 KD 1.7 $\mu\text{m}/\text{min}$ ($p = 0.0011$).

OE of WT-LIS1, but Not Dynein- or NDEL1-Binding Mutants, Increases Run Lengths and Velocities of Retrograde Motile Events

OE of WT LIS1 significantly increased total RME run lengths ($p < 0.0001$), while neither of the two mutant proteins were able to do so (**Figure 3C**). LIS1-K147A and LIS1-R212A NDEL1 both significantly reduced run lengths compared to the controls ($p < 0.0001$ and $p = 0.036$, respectively). A similar pattern was observed with average speeds ($p < 0.0001$ and $p = 0.034$, respectively, **Figure 3D**). 70.97% of RMEs measured in LIS1 OE axons reached speeds of 0.5 $\mu\text{m}/\text{s}$ or greater, compared to just 26.85% in control axons. Again LIS1-K147A and LIS1-R212A reduced this (K147A, 1.47% R212A, 7.5%) WT LIS1 OE also significantly increased RF ($9.4 \pm 2.1 \mu\text{m}/\text{min}$ compared to $5.4 \pm 0.7 \mu\text{m}/\text{min}$ for the control; $p = 0.010$). LIS1-K147A and LIS1-R212A both significantly reduced RF (K147A, $1.68 \pm 0.4 \mu\text{m}/\text{min}$, $p = 0.0152$; R212A, $1.46 \pm 0.4 \mu\text{m}/\text{min}$, $p = 0.0110$).

LIS1 and NDEL1 Impact the Length of Individual Mitochondria in DRG Axons

Most mitochondria labeled with Mitotracker Red in axons appear as discreet organelles whose length parallel to the axon is greater than their width (**Figure 4A**). This is particularly true

in the mid axon region that is not adjacent to cell bodies, growth cones, or branch points. We measured the lengths of over 100 individual mitochondria per condition in axonal mid-regions. Surprisingly, mitochondria were significantly longer under conditions that reduced retrograde transport parameters ($p < 0.0001$ in each case, **Figure 4B**). These conditions included LIS- K147A and LIS1-R212A OE as well as LIS1 and NDEL1 KD. DHC KD also increased mitochondria lengths, supporting the idea that reduced dynein-dependent transport is involved in this size change. Interestingly, WT LIS1 did not significantly impact mitochondrial length, which suggests that normal axonal dynein activity is sufficient for maintaining normal lengths, while reducing axonal dynein activity is disruptive to normal regulation.

DISCUSSION

This work supports a model in which both LIS1 and NDEL1 positively impact dynein-dependent retrograde mitochondrial transport and potentially play a role in fission and fusion events. The finding that reduced LIS1 expression in mice or inhibition of dynein in rats resulted in more mitochondria in the sciatic nerve cross-section might reflect reduced overall retrograde and anterograde transport. Dynein colocalizes with mitochondria moving in either direction so it is likely that kinesin and dynein coordinate the transport of individual mitochondria (Hirokawa et al., 1990; Lin and Sheng, 2015). In COS-7 cells TRAK2 can stimulate kinesin-driven anterograde transport of mitochondria and dynein-dependent retrograde transport (Fenton et al., 2021). There are also several studies in which inhibiting one motor leads to reduced transport in both directions (Hancock, 2014), as we observed for dynein or LIS1 KD in cultured sensory neurons. However, this might not be the case *in vivo*. Unopposed anterograde transport of mitochondria in sciatic nerve axons could theoretically account for the increased numbers. Alternatively, more mitochondria might be apparent per cross sections if LIS1 loss or dynein inhibition causes individual mitochondria to be longer *in vivo*. Finally, reducing LIS1 expression or dynein function might result in upregulation of local anchoring of mitochondria by syntaphilin, which was recently shown to be modulated by the LIS1 and NDEL1 interacting protein disrupted in schizophrenia (DISC1; Park et al., 2016). While the trend towards increased mitochondria is similar between the LIS1^{+/-} nerves and the CB-D cuffed nerves, it is interesting that the mitochondria number in LIS1^{+/+} and DMSO control nerves are different. This could reflect differences in animal size, with rats potentially requiring more dynamic mitochondria, but we cannot rule out that the cuffs are having an effect. Future studies will be needed to determine the mechanism behind our *in vivo* observations.

Cellular toxicity or altered microtubule dynamics caused by reduced dynein activity could indirectly result in altered mitochondrial dynamics in our studies. However, axons did not appear to be degenerating and cell numbers were not reduced, so we have therefore interpreted our results in the context of recent models for LIS1 regulation of dynein. For example, LIS1 KD

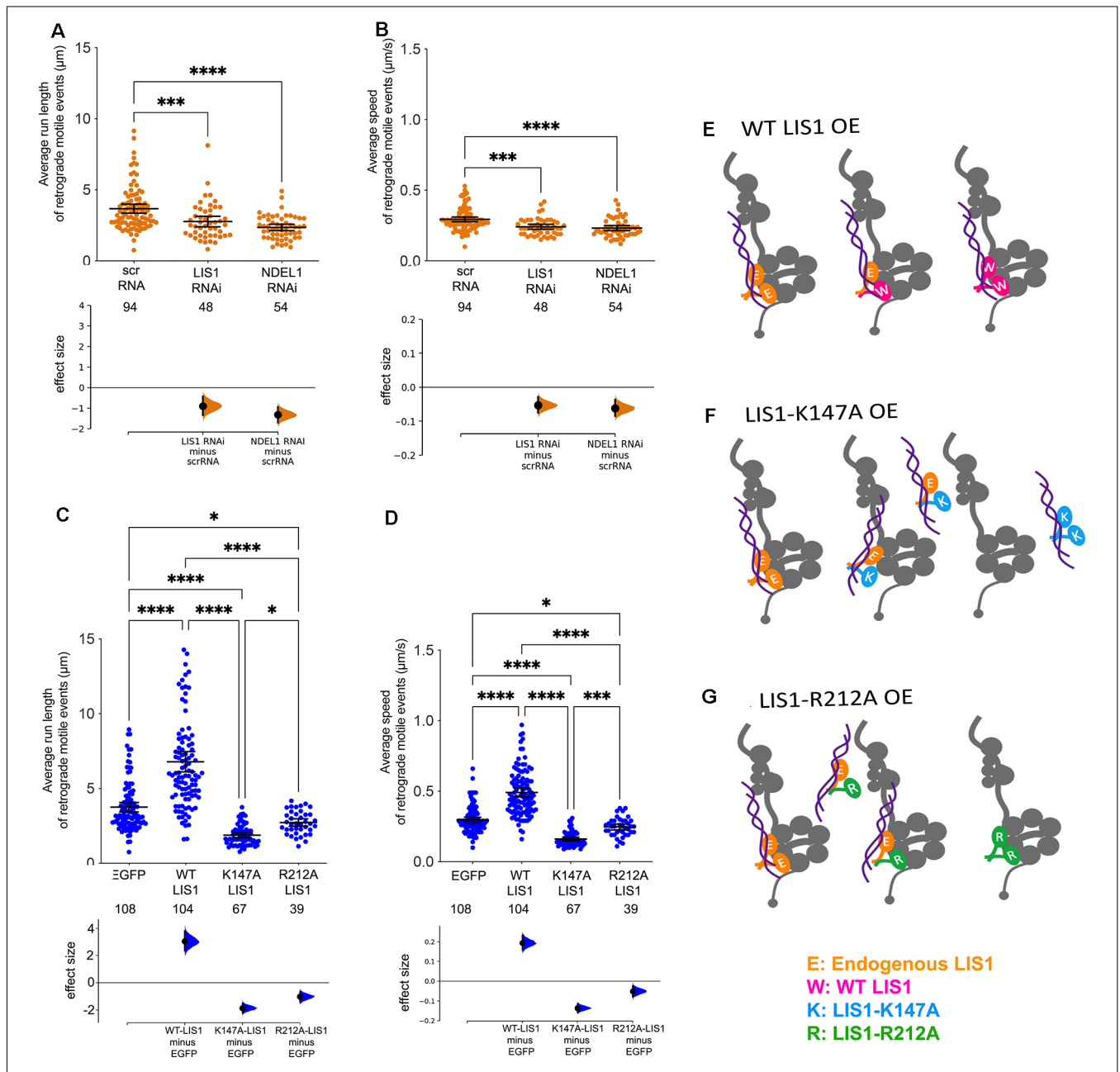
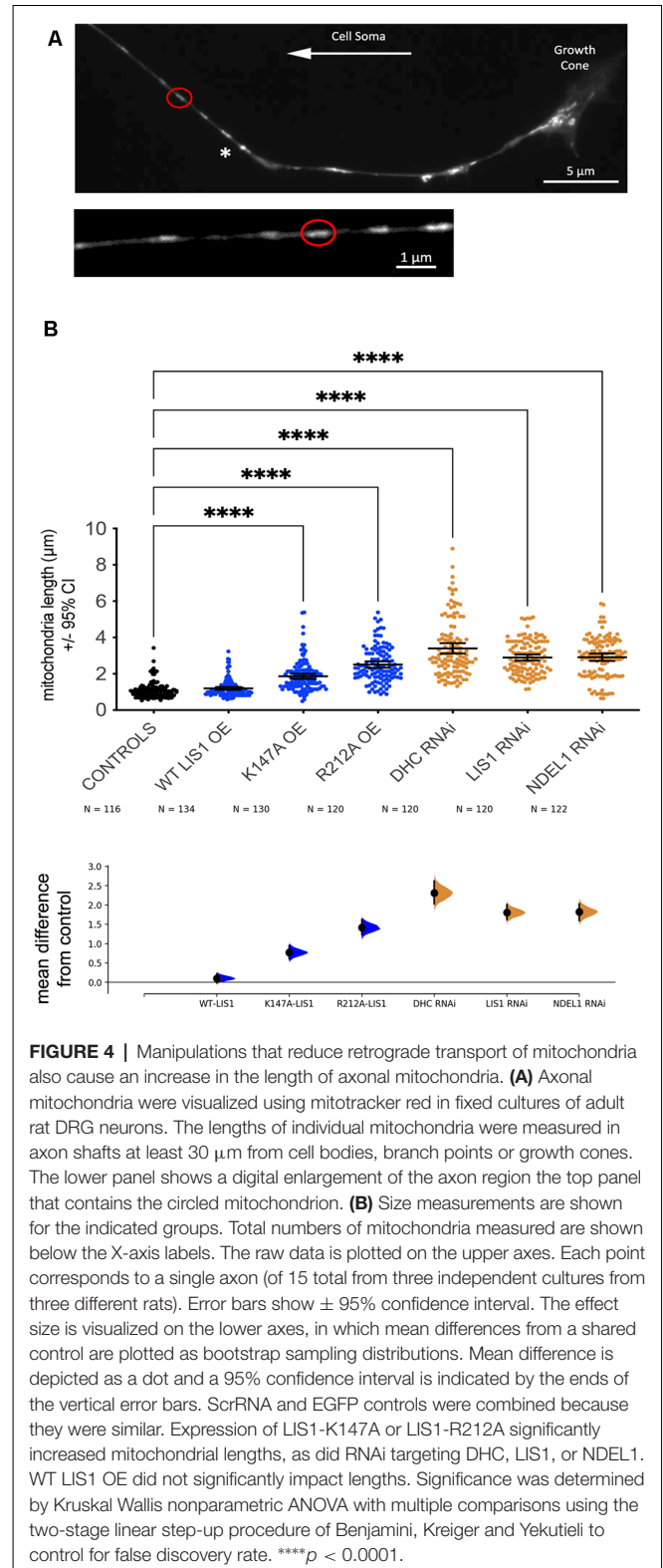


FIGURE 3 | Both LIS1 and NDEL1 impact the run lengths and average speeds of retrograde motile events (RMEs). **(A–D)** Average run lengths and average velocities of RMEs of axonal mitochondria were determined using manual tracking software. The data is from 12 axon segments imaged in DRG cultures from three different adult rats (four axons from each rat). Each axon segment typically had 10–30 mitochondria, some of which moved during the recording interval. A single mitochondrion can undergo more than one RME. The numbers of individual RMEs measured in all 12 axon segments per condition are shown below the X-axis labels. Run lengths **(A)** and average speeds **(B)** are significantly reduced by RNAi-mediated KD of LIS1, NDEL1, or DHC. The raw data is plotted on the upper axes. Each point corresponds to a single axon (of 12 axons measured from three independent cultures from three different rats). Error bars show the mean ± 95% confidence interval. The effect size is visualized on the lower axes, in which mean differences from a shared control are plotted as bootstrap sampling distributions. Mean difference is depicted as a dot and 95% confidence interval is indicated by the ends of the vertical error bars. OE of WT LIS1 significantly increases both the run lengths **(C)** and average speeds **(D)** of RMEs, while both LIS1-K147A or LIS1-R212A significantly reduce run lengths and average speeds. For all data, significance was determined by Kruskal-Wallis nonparametric ANOVA with multiple comparisons using the two-stage linear step-up procedure of Benjamini, Krueger and Yekutieli to control for false discovery rate. *****p* < 0.0001; ****p* < 0.001; **p* < 0.05. **(E–G)** Schematics depicting potential impacts of OE of different LIS1 constructs. **(E)** WT-LIS1 (W, pink) could form homodimers and heterodimers with endogenous LIS1 (E, orange) all of which are likely able to stimulate dynein. **(F)** LIS1-K147A (K, blue) homodimers should not be able to bind to and stimulate dynein but may sequester NDEL1 away from endogenous LIS1/dynein complexes. Heterodimers with endogenous LIS1 may partially bind to dynein and NDEL1, but given our results, this likely to exert dominant negative effects on dynein activation. **(G)** LIS1-R212A (R, green) homodimers may bind to dynein but should not be complexed with NDEL1. Heterodimers with endogenous LIS1 may only partially bind to dynein and NDEL1, again likely exerting dominant negative effects.

likely reduces the proportion of “open” dynein available to form active DDA and D₂DA complexes with mitochondrial cargo adaptors like TRAK and MIRO (Birsa et al., 2013; Fenton et al., 2021). In this scenario, a greater number of dynein motors would be non-processive, and fewer processive motors would contain multiple dynein motors. The former could explain the reduced numbers of retrogradely moving mitochondria, and the latter could explain the shorter/slower RMEs. In contrast, OE of WT-LIS1 would increase the proportion of active DDA and D₂DA complexes, explaining the increase in numbers of retrogradely moving mitochondria as well as longer/faster RMEs. A recent study showed that dynein-mediated transport of TRAK2, a cargo adaptor for mitochondria, is minimal unless LIS1 is present at a sufficient level, further supporting a role for LIS1 in mitochondria transport (Fenton et al., 2021). We recognize that WT-LIS1 OE might stimulate retrograde mitochondrial flux by another mechanism, such as sequestering dynein inhibitors, but to date, this has not been demonstrated. It is telling that a LIS1 isoform with a missense mutation that blocks its interaction with dynein not only was unable to stimulate retrograde mitochondrial flux but significantly reduced flux. LIS1-K147A retains its ability to homodimerize and interact with NDEL1, indicating that it is properly folded, and suggesting a possible mechanism for its dominant negative impact. Indeed, the expression of the mutant blocked the ability of dynein to coprecipitate endogenous LIS1 and reduced its ability to coimmunoprecipitate NDEL1 (Pandey and Smith, 2011).

One fascinating aspect of our study is the finding that both NDEL1 KD and the expression of LIS1-R212A, a mutant that retains its ability to bind to dynein but not to NDEL1, dramatically inhibited retrograde mitochondria transport dynamics. It is not clear how the presence of NDEL1 (or NDE1) impacts the formation of DDA and D₂DA complexes, but our data suggest it might be relevant, at least in the case of mitochondria, as the NDEL1 manipulations used in this study had minimal impact on acidic organelles labeled with LysoTracker. Our study places LIS1 as a positive dynein regulator with respect to mitochondria in adult rat sensory neurons, which is consistent with an earlier report of LIS1 KD in embryonic hippocampal neurons (Shao et al., 2013). In that study LIS1 KD was much more impactful on mitochondrial transport than NDEL1 KD, so developmental age or regenerative state could impact mechanisms controlling dynein. In drosophila wing axons LIS1 KD increased retrograde mitochondrial flux suggesting species differences that might also be found for NDEL1 (Vagnoni et al., 2016).

One caveat of our study is that we do not know the precise stoichiometry of LIS1, NDEL1, and dynein in DRG axons, and we do not know how overexpression of exogenous proteins impacts this stoichiometry. In a previous study, we estimated the molar ratio of LIS1 to dynein to be 1:28 in extracts from adult rat brain (Mesngon et al., 2006). This ratio is likely higher in axons given the importance of axonal transport and the potentially lower ratio of LIS1 to dynein in glial cells. In COS-7 cells all three overexpressed, tagged LIS1 constructs expressed at approximately the same level



as endogenous LIS1 protein when using a LIS1 antibody to probe western blots (Pandey and Smith, 2011). Overexpressed WT-LIS1 appears to bind more efficiently to dynein than endogenous LIS1 so this construct may be outcompeting

endogenous LIS1 for dynein binding (Pandey and Smith, 2011). The overexpressed LIS1 appears to be functional given the observed stimulated transport. R212A-LIS1 also appeared to interact more robustly with dynein. This mutant may bind to dynein without binding to NDEL1, and/or may dimerize with endogenous LIS1, which might reduce the ability of LIS1 dimers to interact with NDEL1. Either event appears to be detrimental to normal mitochondrial transport. K147A-LIS1 did not Co-IP with dynein but appeared to be binding to and sequestering endogenous LIS1 away from dynein (Pandey and Smith, 2011). Interestingly K147A-LIS1 was able to co-precipitate more myc-tagged NDEL1 than HA-tagged WT-LIS1, so this mutant may also sequester NDEL1 away from dynein. Both events could contribute to the reduced transport seen in axons when that construct is expressed. The schematics in **Figures 3E–G** illustrate some of the complexes that may be present in cells expressing the exogenous LIS1 constructs. Further studies will be needed to understand all of the potential dominant negative impacts the exogenous proteins have on protein interactions including those other proteins not considered here (cargo adaptors, etc.).

Another issue that will need to be addressed is the role of phosphorylation of NDEL1 by cyclin-dependent kinases on mitochondrial transport (Niethammer et al., 2000; Sasaki et al., 2000; Hebbbar et al., 2008b; Pandey and Smith, 2011; Klinman et al., 2017). The role of these kinases in controlling the formation of active dynein complexes has not been explored and needs to be further investigated. There is some controversy around how CDK5 activation/inhibition impacts axonal transport. In our hands, CDK5 inhibition disrupted transport, but others have observed that CDK5 inhibition increased transport; future studies will need to address this discrepancy and clarify the role of phosphorylated and unphosphorylated NDEL1 on dynein complex formation and specific cargo transport (Pandey and Smith, 2011; Klinman and Holzbaur, 2015; Klinman et al., 2017; Chapman et al., 2019). There are also likely to be regulatory posttranslational modifications to individual polypeptides in the DDA complex itself.

The adult brain, and in particular synapses, require a large amount of energy provided mainly by mitochondria (Misgeld and Schwarz, 2017; Mandal and Drerup, 2019; Han et al., 2020). Mitochondrial recycling at synapses is thought to involve retrograde transport of spent organelles by dynein. Our inducible knockout of LIS1 in adult mice demonstrated clear postdevelopmental roles for the protein, notably regulation of axonal transport in mature sensorimotor and cardiorespiratory neurons in the hindbrain, spinal cord, and peripheral nervous system (Hines et al., 2018). Precise regulation of dynein activity by LIS1 is likely to be critical as there is evidence that increased levels of LIS1 in both humans and mice can disrupt normal brain development (Bi et al., 2009). In humans, increased LIS1 expression causes structural abnormalities in the brain, severe developmental delay, and failure to thrive (Bi et al., 2009). In mice, overexpression by about 20% caused abnormalities in the cells of the developing brain, including alterations in cellular polarity and in migration.

It would be interesting to determine if induced, conditional overexpression of LIS1 in adult mice would produce neurological phenotypes like our induced KO. NDEL1 also has roles beyond embryonic development as reducing expression postnatally in forebrain excitatory neurons in mice caused spatial learning and memory deficits and seizures and short lifespan (10 weeks) in adult mice (Gavrilovici et al., 2021). Our data suggest that one possible mechanism contributing to pathologies in adult LIS1 and NDEL1 KO mice is that reduced mitochondrial recycling at synapses leads to synaptic energy deficits and compromised circuitry. Dynein has been shown to deliver the fission protein DRP 1 to mitochondria, which could be the underlying mechanism for our observation that reduced dynein function results in longer mitochondria (Varadi et al., 2004). It will be important to determine if and how LIS1 and NDEL1 impact mitochondrial fission and fusion events and the delivery of DRP1.

DATA AVAILABILITY STATEMENT

The raw data supporting the conclusions are included in the article, further inquiries can be directed to the corresponding author/s.

ETHICS STATEMENT

The animal study was reviewed and approved by The Institutional Animal Care and Use Committee, University of South Carolina.

AUTHOR CONTRIBUTIONS

JP performed all experiments. LS and RB analyzed the data and edited the manuscript. DS planned the study and wrote the manuscript. All authors contributed to the article and approved the submitted version.

FUNDING

This work was supported by NIH R01 NS056314 (National Institute of Neurological Disorders and Stroke; Principal Investigator DS). This study was made possible in part by Grant # 2019-P-01 from the South Carolina Spinal Cord Injury Research Fund. However, contents do not necessarily represent the policy of the SCIRF and do not imply endorsement by the funding agency.

ACKNOWLEDGMENTS

We are very grateful to Edsel Pena, Kristy Welshhans, Fabienne Poulaine, and Aaron Jasnow for help with statistical analyses. We are also very grateful to Jeffrey Davis and Robert Price for help with electron microscopy.

REFERENCES

- Baas, P. W., Deitch, J. S., Black, M. M., and Banker, G. A. (1988). Polarity orientation of microtubules in hippocampal neurons: uniformity in the axon and nonuniformity in the dendrite. *Proc. Natl. Acad. Sci. U S A* 85, 8335–8339. doi: 10.1073/pnas.85.21.8335
- Bi, W., Sapir, T., Shchelochkov, O. A., Zhang, F., Withers, M. A., Hunter, J. V., et al. (2009). Increased LIS1 expression affects human and mouse brain development. *Nat. Genet.* 41, 168–177. doi: 10.1038/ng.302
- Birsa, N., Norkett, R., Higgs, N., Lopez-Domenech, G., and Kittler, J. T. (2013). Mitochondrial trafficking in neurons and the role of the Miro family of GTPase proteins. *Biochem. Soc. Trans.* 41, 1525–1531. doi: 10.1042/BST20130234
- Bradshaw, N. J., and Hayashi, M. A. (2017). NDE1 and NDEL1 from genes to (mal)functions: parallel but distinct roles impacting on neurodevelopmental disorders and psychiatric illness. *Cell. Mol. Life Sci.* 74, 1191–1210. doi: 10.1007/s00018-016-2395-7
- Canty, J. T., and Yildiz, A. (2020). Activation and regulation of cytoplasmic dynein. *Trends Biochem. Sci.* 45, 440–453. doi: 10.1016/j.tibs.2020.02.002
- Castora, F. J. (2019). Mitochondrial function and abnormalities implicated in the pathogenesis of ASD. *Prog. Neuropsychopharmacol. Biol. Psychiatry* 92, 83–108. doi: 10.1016/j.pnpbp.2018.12.015
- Chapman, D. E., Reddy, B. J. N., Huy, B., Bovyn, M. J., Cruz, S. J. S., Al-Shammari, Z. M., et al. (2019). Regulation of *in vivo* dynein force production by CDK5 and 14-3-3 ϵ and KIAA0528. *Nat. Commun.* 10:228. doi: 10.1038/s41467-018-08110-z
- Elshenawy, M. M., Kusacki, E., Volz, S., Baumbach, J., Bullock, S. L., and Yildiz, A. (2020). Lis1 activates dynein motility by modulating its pairing with dynactin. *Nat. Cell Biol.* 22, 570–578. doi: 10.1038/s41556-020-0501-4
- Fenton, A. R., Jongens, T. A., and Holzbaur, E. L. F. (2021). Mitochondrial adaptor TRAK2 activates and functionally links opposing kinesin and dynein motors. *Nat. Commun.* 12:4578. doi: 10.1038/s41467-021-24862-7
- Foster, H. E., Ventura Santos, C., and Carter, A. P. (2022). A cryo-ET survey of microtubules and intracellular compartments in mammalian axons. *J. Cell Biol.* 221:e202103154. doi: 10.1083/jcb.202103154
- Gavrilovici, C., Jiang, Y., Kirovski, I., Sterley, T. L., Vandal, M., Bains, J., et al. (2021). Behavioral deficits in mice with postnatal disruption of ndel1 in forebrain excitatory neurons: implications for epilepsy and neuropsychiatric disorders. *Cereb. Cortex Commun.* 2:tgaa096. doi: 10.1093/texcom/tgaa096
- Guedes-Dias, P., and Holzbaur, E. L. F. (2019). Axonal transport: driving synaptic function. *Science* 366:eaaw9997. doi: 10.1126/science.aaw9997
- Han, S., Jeong, Y. Y., Sheshadri, P., Su, X., and Cai, Q. (2020). Mitophagy regulates integrity of mitochondria at synapses and is critical for synaptic maintenance. *EMBO Rep.* 21:e49801. doi: 10.15252/embr.201949801
- Hancock, W. O. (2014). Bidirectional cargo transport: moving beyond tug of war. *Nat. Rev. Mol. Cell Biol.* 15, 615–628. doi: 10.1038/nrm3853
- Hebbar, S., Guillotte, A. M., Mesngon, M. T., Zhou, Q., Wynshaw-Boris, A., and Smith, D. S. (2008a). Genetic enhancement of the Lis1 $^{+/-}$ phenotype by a heterozygous mutation in the adenomatous polyposis coli gene. *Dev. Neurosci.* 30, 157–170. doi: 10.1159/000109860
- Hebbar, S., Mesngon, M. T., Guillotte, A. M., Desai, B., Ayala, R., and Smith, D. S. (2008b). Lis1 and Ndel1 influence the timing of nuclear envelope breakdown in neural stem cells. *J. Cell Biol.* 182, 1063–1071. doi: 10.1083/jcb.200803071
- Heidemann, S. R., Landers, J. M., and Hamborg, M. A. (1981). Polarity orientation of axonal microtubules. *J. Cell Biol.* 91, 661–665. doi: 10.1083/jcb.91.3.661
- Hines, T. J., Gao, X., Sahu, S., Lange, M. M., Turner, J. R., Twiss, J. L., et al. (2018). An essential postdevelopmental role for lis1 in mice. *eNeuro* 5:ENEURO.0350-17.2018. doi: 10.1523/ENEURO.0350-17.2018
- Hippenmeyer, S., Youn, Y. H., Moon, H. M., Miyamichi, K., Zong, H., Wynshaw-Boris, A., et al. (2010). Genetic mosaic dissection of Lis1 and Ndel1 in neuronal migration. *Neuron* 68, 695–709. doi: 10.1016/j.neuron.2010.09.027
- Hirokawa, N., Sato-Yoshitake, R., Yoshida, T., and Kawashima, T. (1990). Brain dynein (MAP1C) localizes on both anterogradely and retrogradely transported membranous organelles *in vivo*. *J. Cell Biol.* 111, 1027–1037. doi: 10.1083/jcb.111.3.1027
- Hirotsune, S., Fleck, M. W., Gambello, M. J., Bix, G. J., Chen, A., Clark, G. D., et al. (1998). Graded reduction of Pafah1b1 (Lis1) activity results in neuronal migration defects and early embryonic lethality. *Nat. Genet.* 19, 333–339. doi: 10.1038/1221
- Ho, J., Tumkaya, T., Aryal, S., Choi, H., and Claridge-Chang, A. (2019). Moving beyond P values: data analysis with estimation graphics. *Nat. Methods* 16, 565–566. doi: 10.1038/s41592-019-0470-3
- Htet, Z. M., Gillies, J. P., Baker, R. W., Leschziner, A. E., DeSantis, M. E., and Reck-Peterson, S. L. (2020). LIS1 promotes the formation of activated cytoplasmic dynein-1 complexes. *Nat. Cell Biol.* 22, 518–525. doi: 10.1038/s41556-020-0506-z
- Kleele, T., Marinkovic, P., Williams, P. R., Stern, S., Weigand, E. E., Engerer, P., et al. (2014). An assay to image neuronal microtubule dynamics in mice. *Nat. Commun.* 5:4827. doi: 10.1038/ncomms5827
- Klinman, E., and Holzbaur, E. L. (2015). Stress-induced CDK5 activation disrupts axonal transport via Lis1/Ndel1/Dynein. *Cell Rep.* 12, 462–473. doi: 10.1016/j.celrep.2015.06.032
- Klinman, E., Tokito, M., and Holzbaur, E. L. F. (2017). CDK5-dependent activation of dynein in the axon initial segment regulates polarized cargo transport in neurons. *Traffic* 18, 808–824. doi: 10.1111/tra.12529
- Lee, I. G., Cason, S. E., Alqassim, S. S., E.Holzbaur, L. F., and Dominguez, R. (2020). A tunable LIC1-adaptor interaction modulates dynein activity in a cargo-specific manner. *Nat. Commun.* 11:5695. doi: 10.1038/s41467-020-19538-7
- Lin, M. Y., and Sheng, Z. H. (2015). Regulation of mitochondrial transport in neurons. *Exp. Cell Res.* 334, 35–44. doi: 10.1016/j.yexcr.2015.01.004
- Mandal, A., and Drerup, C. M. (2019). Axonal transport and mitochondrial function in neurons. *Front. Cell. Neurosci.* 13:373. doi: 10.3389/fncel.2019.00373
- Markus, S. M., Marzo, M. G., and McKenney, R. J. (2020). New insights into the mechanism of dynein motor regulation by lissencephaly-1. *eLife* 9:e59737. doi: 10.7554/eLife.59737
- Marzo, M. G., Griswold, J. M., and Markus, S. M. (2020). Pac1/LIS1 stabilizes an uninhibited conformation of dynein to coordinate its localization and activity. *Nat. Cell Biol.* 22, 559–569. doi: 10.1038/s41556-020-0492-1
- McKenney, R. J. (2020). LIS1 cracks open dynein. *Nat. Cell Biol.* 22, 515–517. doi: 10.1038/s41556-020-0500-5
- Mesngon, M. T., Tarricone, C., Hebbar, S., Guillotte, A. M., Schmitt, E. W., Lanier, L., et al. (2006). Regulation of cytoplasmic dynein ATPase by Lis1. *J. Neurosci.* 26, 2132–2139. doi: 10.1523/JNEUROSCI.5095-05.2006
- Misgeld, T., and Schwarz, T. L. (2017). Mitostasis in neurons: maintaining mitochondria in an extended cellular architecture. *Neuron* 96, 651–666. doi: 10.1016/j.neuron.2017.09.055
- Moon, H. M., Youn, Y. H., Pemble, H., Yingling, J., Wittmann, T., and Wynshaw-Boris, A. (2014). LIS1 controls mitosis and mitotic spindle organization via the LIS1-NDEL1-dynein complex. *Hum. Mol. Genet.* 23, 449–466. doi: 10.1093/hmg/ddt436
- Niethammer, M., Smith, D. S., Ayala, R., Peng, J., Ko, J., Lee, M. S., et al. (2000). NUDEL is a novel Cdk5 substrate that associates with LIS1 and cytoplasmic dynein. *Neuron* 28, 697–711. doi: 10.1016/s0896-6273(00)00147-1
- Olenick, M. A., and Holzbaur, E. L. F. (2019). Dynein activators and adaptors at a glance. *J. Cell Sci.* 132:jcs227132. doi: 10.1242/jcs.227132
- Pandey, J. P., and Smith, D. S. (2011). A Cdk5-dependent switch regulates Lis1/Ndel1/dynein-driven organelle transport in adult axons. *J. Neurosci.* 31, 17207–17219. doi: 10.1523/JNEUROSCI.4108-11.2011
- Park, C., Lee, S. A., Hong, J. H., Suh, Y., Park, S. J., Suh, B. K., et al. (2016). Disrupted-in-schizophrenia 1 (DISC1) and Syntrophin collaborate to modulate axonal mitochondrial anchoring. *Mol. Brain* 9:69. doi: 10.1186/s13041-016-0250-2
- Qiu, R., Zhang, J., and Xiang, X. (2019). LIS1 regulates cargo-adaptor-mediated activation of dynein by overcoming its autoinhibition *in vivo*. *J. Cell Biol.* 218, 3630–3646. doi: 10.1083/jcb.201905178
- Rangaraju, V., Lewis, T. L., Jr., Hirabayashi, Y., Bergami, M., Motori, E., Cartoni, R., et al. (2019). Pleiotropic mitochondria: the influence of mitochondria on neuronal development and disease. *J. Neurosci.* 39, 8200–8208. doi: 10.1523/JNEUROSCI.1157-19.2019
- Rao, A. N., Patil, A., Black, M. M., Craig, E. M., Myers, K. A., Yeung, H. T., et al. (2017). Cytoplasmic dynein transports axonal microtubules in a polarity-sorting manner. *Cell Rep.* 19, 2210–2219. doi: 10.1016/j.celrep.2017.05.064
- Reck-Peterson, S. L., Redwine, W. B., Vale, R. D., and Carter, A. P. (2018). The cytoplasmic dynein transport machinery and its many cargoes. *Nat. Rev. Mol. Cell Biol.* 19, 382–398. doi: 10.1016/j.celrep.2017.05.064

- Reiner, O., Carrozzo, R., Shen, Y., Wehnert, M., Faustinella, F., Dobyns, W. B., et al. (1993). Isolation of a Miller-Dieker lissencephaly gene containing G protein beta-subunit-like repeats. *Nature* 364, 717–721. doi: 10.1038/364717a0
- Reiner, O., and Sapir, T. (2013). LIS1 functions in normal development and disease. *Curr. Opin. Neurobiol.* 23, 951–956. doi: 10.1016/j.conb.2013.08.001
- Roossien, D. H., Miller, K. E., and Gallo, G. (2015). Ciliobrevins as tools for studying dynein motor function. *Front. Cell. Neurosci.* 9:252. doi: 10.3389/fncel.2015.00252
- Saillour, Y., Carion, N., Quelin, C., Leger, P. L., Boddaert, N., Elie, C., et al. (2009). LIS1-related isolated lissencephaly: spectrum of mutations and relationships with malformation severity. *Arch. Neurol.* 66, 1007–1015. doi: 10.1001/archneurol.2009.149
- Sainath, R., and Gallo, G. (2015). The dynein inhibitor Ciliobrevin D inhibits the bidirectional transport of organelles along sensory axons and impairs NGF-mediated regulation of growth cones and axon branches. *Dev. Neurobiol.* 75, 757–777. doi: 10.1002/dneu.22246
- Sasaki, S., Shionoya, A., Ishida, M., Gambello, M. J., Yingling, J., Wynshaw-Boris, A., et al. (2000). A LIS1/NUDEL/cytoplasmic dynein heavy chain complex in the developing and adult nervous system. *Neuron* 28, 681–696. doi: 10.1016/s0896-6273(00)00146-x
- Schneider, C., Langer, R., Loveday, D., and Hair, D. (2017). Applications of ethylene vinyl acetate copolymers (EVA) in drug delivery systems. *J. Control Release* 262, 284–295. doi: 10.1016/j.jconrel.2017.08.004
- Schwarz, T. L. (2013). Mitochondrial trafficking in neurons. *Cold Spring Harb. Perspect. Biol.* 5:a011304. doi: 10.1101/cshperspect.a011304
- Sebe, J. Y., Bershteyn, M., Hirotsune, S., Wynshaw-Boris, A., and Baraban, S. C. (2013). ALLN rescues an *in vitro* excitatory synaptic transmission deficit in Lis1 mutant mice. *J. Neurophysiol.* 109, 429–436. doi: 10.1152/jn.00431.2012
- Shao, C. Y., Zhu, J., Xie, Y. J., Wang, Z., Wang, Y. N., Wang, Y., et al. (2013). Distinct functions of nuclear distribution proteins LIS1, Ndel1 and NudCL in regulating axonal mitochondrial transport. *Traffic* 14, 785–797. doi: 10.1111/tra.12070
- Shu, T., Ayala, R., Nguyen, M. D., Xie, Z., Gleeson, J. G., and Tsai, L. H. (2004). Ndel1 operates in a common pathway with LIS1 and cytoplasmic dynein to regulate cortical neuronal positioning. *Neuron* 44, 263–277. doi: 10.1016/j.neuron.2004.09.030
- Smith, D. S., Niethammer, M., Ayala, R., Zhou, Y., Gambello, M. J., Wynshaw-Boris, A., et al. (2000). Regulation of cytoplasmic dynein behaviour and microtubule organization by mammalian Lis1. *Nat. Cell Biol.* 2, 767–775. doi: 10.1038/35041000
- Smith, D. S., and Skene, J. H. (1997). A transcription-dependent switch controls competence of adult neurons for distinct modes of axon growth. *J. Neurosci.* 17, 646–658. doi: 10.1523/JNEUROSCI.17-02-00646.1997
- Toba, S., Tamura, Y., Kumamoto, K., Yamada, M., Takao, K., Hattori, S., et al. (2013). Post-natal treatment by a blood-brain-barrier permeable calpain inhibitor, SNJ1945 rescued defective function in lissencephaly. *Sci. Rep.* 3:1224. doi: 10.1038/srep01224
- Urnavicius, L., Lau, C. K., Elshenawy, M. M., Morales-Rios, E., Motz, C., Yildiz, A., et al. (2018). Cryo-EM shows how dynactin recruits two dyneins for faster movement. *Nature* 554, 202–206. doi: 10.1038/nature25462
- Vagnoni, A., Hoffmann, P. C., and Bullock, S. L. (2016). Reducing Lissencephaly-1 levels augments mitochondrial transport and has a protective effect in adult *Drosophila* neurons. *J. Cell Sci.* 129, 178–190. doi: 10.1242/jcs.179184
- Varadi, A., Johnson-Cadwell, L. I., Cirulli, V., Yoon, Y., Allan, V. J., and Rutter, G. A. (2004). Cytoplasmic dynein regulates the subcellular distribution of mitochondria by controlling the recruitment of the fission factor dynamin-related protein-1. *J. Cell Sci.* 117, 4389–4400. doi: 10.1242/jcs.01299
- Wynshaw-Boris, A. (2007). Lissencephaly and LIS1: insights into the molecular mechanisms of neuronal migration and development. *Clin. Genet.* 72, 296–304. doi: 10.1111/j.1399-0004.2007.00888.x
- Xiang, X., and Qiu, R. (2020). Cargo-mediated activation of cytoplasmic dynein *in vivo*. *Front. Cell Dev. Biol.* 8:598952. doi: 10.3389/fcell.2020.598952
- Yamada, M., Toba, S., Yoshida, Y., Haratani, K., Mori, D., Yano, Y., et al. (2008). LIS1 and NDEL1 coordinate the plus-end-directed transport of cytoplasmic dynein. *EMBO J.* 27, 2471–2483. doi: 10.1038/emboj.2008.182
- Yan, W., Assadi, A. H., Wynshaw-Boris, A., Eichele, G., Matzuk, M. M., and Clark, G. D. (2003). Previously uncharacterized roles of platelet-activating factor acetylhydrolase 1b complex in mouse spermatogenesis. *Proc. Natl. Acad. Sci. U S A* 100, 7189–7194. doi: 10.1073/pnas.1236145100
- Yang, D., Ying, J., Wang, X., Zhao, T., Yoon, S., Fang, Y., et al. (2021). Mitochondrial dynamics: a key role in neurodegeneration and a potential target for neurodegenerative disease. *Front. Neurosci.* 15:654785. doi: 10.3389/fnins.2021.654785
- Yingling, J., Youn, Y. H., Darling, D., Toyo-Oka, K., Pramparo, T., Hirotsune, S., et al. (2008). Neuroepithelial stem cell proliferation requires LIS1 for precise spindle orientation and symmetric division. *Cell* 132, 474–486. doi: 10.1016/j.cell.2008.01.026
- Zhang, K., Foster, H. E., Rondelet, A., Lacey, S. E., Bahi-Buisson, N., Bird, A. W., et al. (2017). Cryo-EM reveals how human cytoplasmic dynein is auto-inhibited and activated. *Cell* 169, 1303–1314.e18. doi: 10.1016/j.cell.2017.05.025
- Zhuo, M., Gorgun, M. F., and Englander, E. W. (2018). Neurotoxicity of cytarabine (Ara-C) in dorsal root ganglion neurons originates from impediment of mtDNA synthesis and compromise of mitochondrial function. *Free Radic. Biol. Med.* 121, 9–19. doi: 10.1016/j.freeradbiomed.2018.04.570

Conflict of Interest: The authors declare that the research was conducted in the absence of any commercial or financial relationships that could be construed as a potential conflict of interest.

Publisher's Note: All claims expressed in this article are solely those of the authors and do not necessarily represent those of their affiliated organizations, or those of the publisher, the editors and the reviewers. Any product that may be evaluated in this article, or claim that may be made by its manufacturer, is not guaranteed or endorsed by the publisher.

Copyright © 2022 Pandey, Shi, Brebion and Smith. This is an open-access article distributed under the terms of the Creative Commons Attribution License (CC BY). The use, distribution or reproduction in other forums is permitted, provided the original author(s) and the copyright owner(s) are credited and that the original publication in this journal is cited, in accordance with accepted academic practice. No use, distribution or reproduction is permitted which does not comply with these terms.



SARM1 Depletion Slows Axon Degeneration in a CNS Model of Neurotropic Viral Infection

Colin L. Crawford¹, Christina Antoniou², Lina Komarek^{1,3}, Verena Schultz¹, Claire L. Donald⁴, Paul Montague¹, Susan C. Barnett¹, Christopher Linington¹, Hugh J. Willison¹, Alain Kohl⁴, Michael P. Coleman^{2*} and Julia M. Edgar^{1,3*}

¹ Institute of Infection, Immunity and Inflammation, College of Medical, Veterinary and Life Sciences, University of Glasgow, Glasgow, United Kingdom, ² John van Geest Centre for Brain Repair, Cambridge, United Kingdom, ³ Department of Neurogenetics, Max Planck Institute of Experimental Medicine, Göttingen, Germany, ⁴ MRC-University of Glasgow Centre for Virus Research, Glasgow, United Kingdom

OPEN ACCESS

Edited by:

Pabitra Sahoo,
University of South Carolina,
United States

Reviewed by:

Yongcheol Cho,
Daegu Gyeongbuk Institute of Science
and Technology (DGIST), South Korea
Yasushi Kitaoka,
St. Marianna University School of
Medicine, Japan

*Correspondence:

Julia M. Edgar
julia.edgar@glasgow.ac.uk
Michael P. Coleman
mc469@cam.ac.uk

Specialty section:

This article was submitted to
Molecular Signalling and Pathways,
a section of the journal
Frontiers in Molecular Neuroscience

Received: 22 January 2022

Accepted: 18 February 2022

Published: 13 April 2022

Citation:

Crawford CL, Antoniou C, Komarek L,
Schultz V, Donald CL, Montague P,
Barnett SC, Linington C, Willison HJ,
Kohl A, Coleman MP and Edgar JM
(2022) SARM1 Depletion Slows Axon
Degeneration in a CNS Model of
Neurotropic Viral Infection.
Front. Mol. Neurosci. 15:860410.
doi: 10.3389/fnmol.2022.860410

Zika virus (ZIKV) is a neurotropic flavivirus recently linked to congenital ZIKV syndrome in children and encephalitis and Guillain-Barré syndrome in adults. Neurotropic viruses often use axons to traffic to neuronal or glial cell somas where they either remain latent or replicate and proceed to infect new cells. Consequently, it has been suggested that axon degeneration could represent an evolutionarily conserved mechanism to limit viral spread. Whilst it is not known if ZIKV transits in axons, we previously reported that ZIKV infection of glial cells in a murine spinal cord-derived cell culture model of the CNS is associated with a profound loss of neuronal cell processes. This, despite that postmitotic neurons are relatively refractory to infection and death. Here, we tested the hypothesis that ZIKV-associated degeneration of neuronal processes is dependent on activation of Sterile alpha and armadillo motif-containing protein 1 (SARM1), an NADase that acts as a central executioner in a conserved axon degeneration pathway. To test this, we infected wild type and *Sarm1* homozygous or heterozygous null cell cultures with ZIKV and examined NAD⁺ levels as well as the survival of neurons and their processes. Unexpectedly, ZIKV infection led to a rapid SARM1-independent reduction in NAD⁺. Nonetheless, the subsequent profound loss of neuronal cell processes was SARM1-dependent and was preceded by early changes in the appearance of β -tubulin III staining. Together, these data identify a role for SARM1 in the pathogenesis of ZIKV infection, which may reflect SARM1's conserved prodegenerative function, independent of its NADase activity.

Keywords: Zika virus, neurofilament, tubulin (microtubules), glia, nicotinamide adenine dinucleotide

INTRODUCTION

The emergence of mosquito-borne Zika virus (ZIKV; a positive-strand RNA virus of the *Flaviviridae* family) in Pacific Ocean islands and the Americas added this previously little-known pathogen to the list of neurotropic flaviviruses (Baud et al., 2017; Gubler et al., 2017; Pierson and Diamond, 2018; Pardy and Richer, 2019). The association of ZIKV with multiple neurological complications including congenital ZIKV syndrome, encephalitis and Guillain-Barré syndrome (Gulland, 2016) makes it particularly important to understand the underlying mechanism. We previously demonstrated that post-mitotic murine CNS neurons are relatively refractory to

infection by ZIKV, which productively infects oligodendroglia and astroglia in murine models of the perinatal CNS (Cumberworth et al., 2017; Schultz et al., 2021). Surprisingly, despite the paucity of infected neuronal somas and insignificant death of neurons, ZIKV infection led to a profound loss of axons and dendrites (Cumberworth et al., 2017). Thus, we hypothesized this involves a mechanism related to Wallerian degeneration, where axons also die independently from the soma (Coleman and Höke, 2020), following insults that include physical injury, toxins, and genetic mutation (Osterloh et al., 2012; Conforti et al., 2014; Coleman and Höke, 2020).

SARM1 (Sterile alpha and armadillo motif-containing protein 1) has a well-established role in Wallerian degeneration and is regarded as a central executioner in this conserved axon degeneration pathway involving NAD-related metabolism. The SARM1 TIR domain has NAD⁺ consuming glycohydrolase (NADase) activity, considered critical for its prodegenerative capacity (Essuman et al., 2017; Horsefield et al., 2019), although it has additional NADP hydrolase and base exchange activities that could also play important roles (Angeletti et al., 2021). As axons are often used by neurotropic viruses to enter neuronal and glial somas where the cellular machinery they use to replicate is located (Richards et al., 2021) it has been suggested that the known response of SARM1 to bunyavirus or rabies virus infection (both negative strand RNA viruses) could represent a mechanism to limit the spread of neurotropic virus (Mukherjee et al., 2013; Sundaramoorthy et al., 2020).

Notably, SARM1 also has a role in innate immunity since it contains a highly conserved Toll/IL-1 receptor (TIR) domain-containing protein, classified as a member of the toll-like receptor (TLR) adaptor family (Carty and Bowie, 2019). However, unlike other TLR adapters, SARM1 is predominantly expressed in neurons (Lin et al., 2014) and was initially described as an inhibitor of TLR signaling (Carty et al., 2006). Subsequent studies have suggested positive contributions of SARM1 to innate immunity through activation of transcriptional programmes that regulate the production of cytokines and chemokines, including in the nervous system (Carty and Bowie, 2019; Hopkins et al., 2021).

The SARM1-dependent loss of axons and dendrites with absent or delayed neuronal cell death following infection by bunyavirus (Mukherjee et al., 2013) or rabies virus (Sundaramoorthy et al., 2020) could thus provide an intriguing link between innate immunity and axon degeneration mechanisms. To investigate any role SARM1 may play in ZIKV-induced death of neuronal processes, we infected CNS myelinating spinal cord cultures from wild type mice, or *Sarm1* heterozygous or homozygous null mice (Kim et al., 2007) on a type I interferon receptor (*Ifnar1*) null background; the last to facilitate infection (Miner and Diamond, 2017). As previously (Cumberworth et al., 2017), *Sarm1* wild type neuronal soma were relatively refractory to infection, but glial cell infection was accompanied by progressive degeneration of neuronal processes. In contrast, there was prolonged survival of neuronal processes in *Sarm1* null cultures, accompanied by increased infection and death of neuronal somas. Surprisingly, this pro-degenerative role of SARM1 appeared to be independent of its NADase activity,

although ZIKV infection itself caused NAD⁺ depletion in all three *Sarm1* genotypes.

METHODS AND MATERIALS

Mice

Type I interferon receptor deficient (*Ifnar1*^{-/-}) mice, which recapitulate aspects of human ZIKV infection and disease (Miner and Diamond, 2017) (129S7/SvEvBrdBkl-Hprt^b-m2 background; B&K Universal) and *Sarm1*^{-/-} mice (maintained on a C57BL6/J background) (Kim et al., 2007) were bred to produce *Ifnar1*^{+/-}::*Sarm1*^{+/-} mice. These were further crossed to produce *Ifnar1*^{-/-}::*Sarm1*^{+/-} mice from which *Ifnar1*^{-/-}::*Sarm1*^{+/+}, *+/+* or *-/-* embryos were generated. Mice were maintained in Tecniplast 1284L Blue line IVC cages, in a 12-h light/dark cycle and provided *ad libitum* with sterile food and water. Mice were time-mated and pregnant females were killed by rising CO₂ overdose and cervical dislocation on embryonic day (E) 13. All animal studies were approved by the Ethical Committee of the University of Glasgow and licensed by the UK Home Office (Project License number PPL P78DD6240).

Myelinating Cell Cultures

Myelinating cell cultures were established using E13 mouse spinal cord as described in detail previously (Thomson et al., 2006; Bijland et al., 2019), with the exception that cultures were generated from single embryos rather than pooled embryos. A small piece of tail (~1mm) was taken for retrospective genotyping.

Genotyping

Genomic DNA was extracted from ear (adult) or tail (embryo) biopsies using a protocol modified from Truett et al. (2000). Briefly, tissue was lysed at 95°C for 90 min in 50 mM NaOH. Following neutralization with 10% v/v 1 M Tris pH 5, the resultant solution was vortexed and diluted 1:10 in nuclease-free water. *Ifnar1* genotyping was conducted as described previously (Cumberworth et al., 2017). For *Sarm1* genotyping, 1 μl of the diluted genomic DNA lysate was amplified in a 12.5 μl PCR reaction in a 1x RedTaq Reaction mix (Sigma-Aldrich) comprising 0.4 mM dNTP, 0.06 U/μl RedTaq Polymerase, 3 mM MgCl₂ and 0.2 μM *Sarm1* primers. Cycling parameters were an initial denaturation at 95°C for 5 min, then 35 cycles (95°C 1 min; 60°C 1 min; 72°C 1 min) followed by a final elongation at 72°C for 10 min. The PCR products were resolved on standard 2% TAE agarose gels.

Sarm1 primers were described previously (Gilley et al., 2015). Primer pairs 5'-ACGCCTGGTTTCTTACTCTACG-3' and 5'-CCTTACCTCTTGC GGGTGATGC-3' amplify wild type *Sarm1*, producing a 508-bp product. Primers 5'-GGTAGCCGGATCAAGCGTATGC-3' and 5'-CTCATCTCCGGGCCTTTTCGACC-3' amplifies the neomycin resistance cassette retained in the knockout allele (Kim et al., 2007), producing a 450-bp product.

Infection of Cultures With ZIKV

The Brazilian strain of ZIKV, ZIKV/H. sapiens/Brazil/PE243/2015 (GenBank accession number KX197192; abbreviated ZIKV PE243; referred to subsequently as ZIKV) has been described previously (Donald et al., 2016). CNS cultures were infected with ZIKV at a multiplicity of infection (MOI) of 0.3 or 0.6 for 1 h at 37°C in 2% fetal bovine serum (FBS) in cell culture grade PBS (10010023, Gibco™) as described previously (Cumberworth et al., 2017). Controls (mock-infected) were treated in parallel with vehicle only (2% FBS in PBS). Following incubation, the inoculum was aspirated, and the cultures returned to serum-free differentiation medium (Bijland et al., 2019). Media was partially replenished every 2 days.

For immunocytochemistry, cultures were fixed at 24 h post infection (hpi) or 6 days post infection (dpi) in 8% paraformaldehyde for 1 h at room temperature and subsequently stored in PBS at 4°C before staining. For NAD⁺ assay, cells were collected at 24 hpi.

Measurements of NAD⁺ Levels

Samples were prepared for NAD⁺ quantification using the NAD/NADH-Glo™ assay (G9071, Promega) according to the manufacturer's instructions. Briefly, at 24 hpi, a cell scraper was used to remove cell monolayers from glass coverslips (2 × 35 mm dish per sample, 3 coverslips per dish) and these were transferred to a microcentrifuge tube. The cells were pelleted by centrifugation on a benchtop centrifuge at 13,000 RPM for 30 s. Supernatant was discarded and cells rinsed once in 1 ml PBS containing cOmplete™ EDTA-free protease inhibitor (11873580001, Sigma-Aldrich) before repeat centrifugation. The cells were lysed in 100 μl of bicarbonate-based lysis buffer (100 mM Na₂CO₃, 20 mM NaHCO₃, 10 mM nicotinamide, 0.05% Triton-X 100, 1% dodecyltrimethylammonium bromide) by vortexing for ~1 min. Cell debris and insoluble material was then pelleted by centrifugation at 13,000 RPM for 10 min before the supernatant was transferred to a fresh 1.5 ml reaction tube. Pierce™ BCA Protein Assay Kit (23225, Thermo Fisher) was used according to the manufacturer's instructions to determine protein concentrations. Cell lysates were prepared to 0.5 mg/ml in lysis solution. 12.5 μg lysate was then incubated in 12.5 μl 0.4 M HCl at 60°C for 15 min, allowed to cool to room temperature, and neutralized with 12.5 μl 0.5 M Tris base. The samples were then snap-frozen and transported between institutions on dry ice. For determination of NAD⁺ levels, 10 μl of each neutralized reaction was mixed with 10 μl of the NAD-Glo detection reagent (prepared following manufacturer's instructions) on ice, in wells of a 384-well white polystyrene microplate (Corning). The plate and contents were incubated at room temperature for 50 min before luminescence was read using a GloMax® Explorer plate reader (Promega). Concentrations of NAD⁺ are expressed as nmol/mg of protein.

Immunocytochemistry

Post-fixation, cells were permeabilized in ethanol (−20°C; 10 min) and incubated in primary antibodies in blocking buffer (10% goat serum in PBS containing 2x NaCl [274 mM final] and 1% BSA) overnight at 4°C. Mouse anti-ZIKV (Aalto Bio, clone

0302156; 1 in 500) was used in combination with rabbit anti-NeuN (Sigma-Aldrich, ABN78; 1 in 500). Mouse IgG1 SMI31 anti-phosphorylated heavy and medium chain neurofilament (BioLegend, 801601; 1 in 1,500) and mouse IgG2a anti-β-Tubulin III (Sigma-Aldrich, T8578; 1 in 200) were applied simultaneously. After washing, secondary antibodies (goat anti-mouse IgG1 Alexa 488/568/647 and goat anti-rabbit IgG or goat anti-mouse IgG2a Alexa 568/647; 1 in 1,000; Invitrogen) were applied for 1 h at room temperature. Coverslips were mounted on glass slides in Mowiol® 4-88 (Sigma-Aldrich) mounting medium with DAPI (1 μg/ml; D1306, Invitrogen).

Image Capture

For quantification of cell density and neurofilament staining, fluorescence microscopy and image capture were performed using a Zeiss Axio Imager M2 fluorescent microscope with standard epifluorescence optics and Zen Blue software (Carl Zeiss AG, Germany). To avoid bias, fields of view (FoV) were selected in the blue (DAPI) channel and images were captured (10 images from across each coverslip) at x20 magnification in the red, far red, green and blue channels. Representative images for illustration were obtained using the same microscope and software or with a Zeiss LSM 880 Confocal Microscope using a Zeiss Plan-Apochromat 63×/1.4 oil immersion objective and Zen Black software.

Quantification of Cells

A rectangular area of interest (AoI) of 111,488 μm² was placed on each image and immunostained cells or DAPI +ve nuclei, respectively, within and touching west and north borders were quantified. Only immunopositive cells with a DAPI +ve nucleus qualified. The average cell density per AOI was converted to cells/mm² using the formula, cell density per AOI/area of AOI μm² × 1,000,000. Pyknotic nuclei were distinguished from healthy nuclei on the basis of size and homogeneity and intensity of DAPI staining; pyknotic nuclei being condensed and intensely labeled (Cummings and Schnellmann, 2004). Experimenters were blinded to genotypes and three (of nine) sets of images were each quantified by two experimenters (average values were used) for quality control purposes.

Quantification of Neurofilament Staining

Digital images of representative fields of view obtained from cell cultures immunostained with antibody SMI31 that recognizes phosphorylated heavy (H) and medium (M) chain neurofilament, were used to quantify the densities of neuronal processes. A Fiji (Schindelin et al., 2012) macro was recorded to analyse all images identically. To specifically select linear structures, a

TABLE 1 | MOI ZIKV used in experiments quantifying neurofilament and β-tubulin III staining.

	WT	Het	KO
MOI 0.3	1	3	3
MOI 0.6	2	2	2
Total	3	5	5

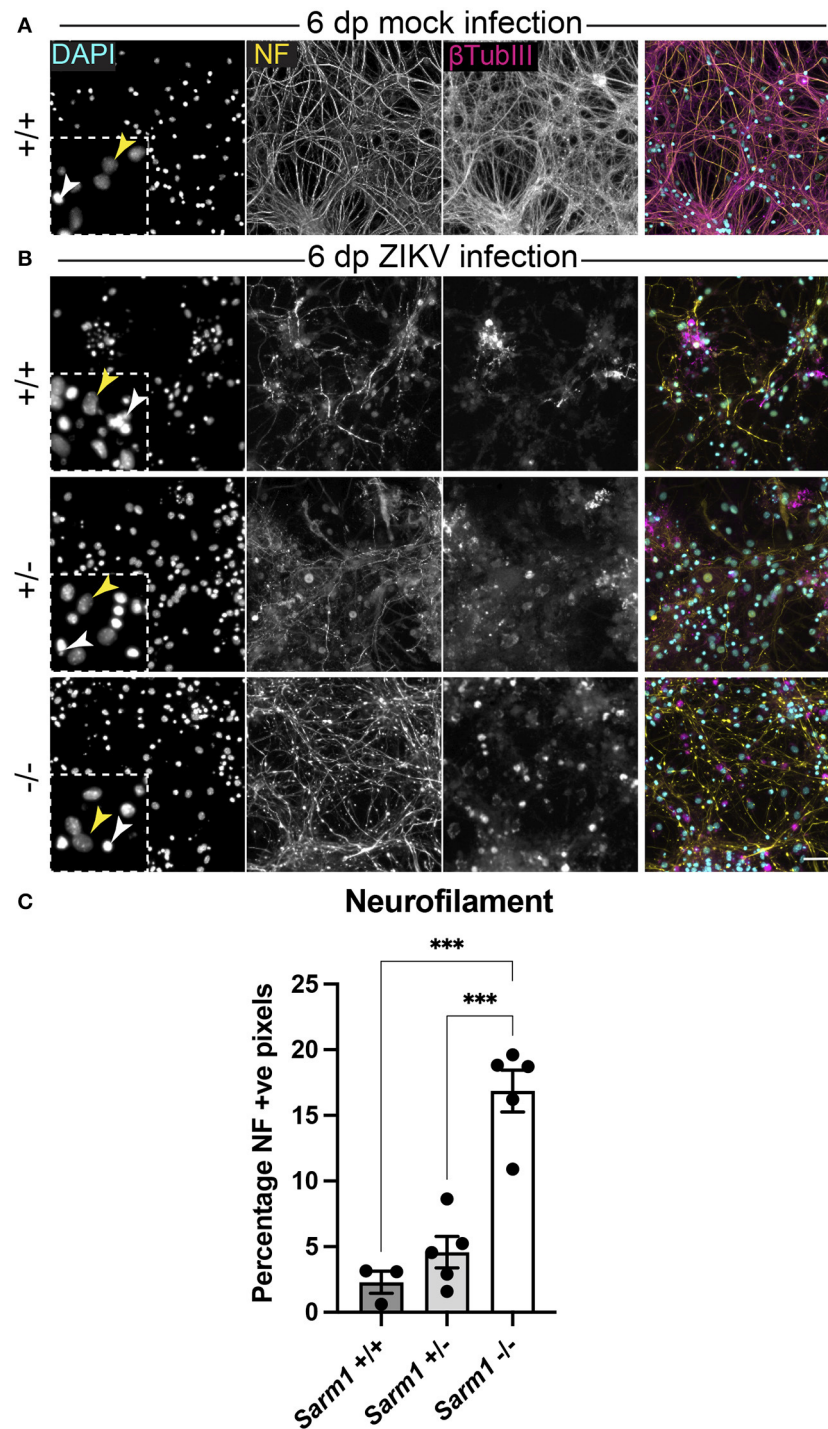


FIGURE 1 | SARM1 depletion delays degeneration of neuronal processes. **(A)** Mock infected *Sarm1*^{+/+} cultures appeared healthy at 6 dpi, with numerous pale DAPI +ve nuclei (yellow arrowhead in inset), relatively few pyknotic nuclei (white arrowhead) and dense neurofilament (NF) and β -tubulin III (β -TubIII) positive cell processes. **(B)** ZIKV infected cultures appeared altered at the same time point, with several pyknotic nuclei (white arrowheads in insets) and fragmented neurofilament and β -tubulin III-stained neuronal processes. This was most obvious in *Sarm1*^{+/+} and *Sarm1*^{+/-} cultures whereas neurofilament appeared relatively preserved in *Sarm1*^{-/-} cultures. Bar: 50 μ m. **(C)** Quantification of neurofilament positive pixels as a proportion of all pixels demonstrated a significant preservation of neuronal processes in *Sarm1*^{-/-} cultures compared to *Sarm1*^{+/+} or +/-. Bars represent mean \pm S.E.M. ****p* < 0.001.

threshold between 12 and 30 (depending on staining) was used and debris was filtered out using the “analyze particles” function with the following parameters: size = 250.00-infinity, circularity = 0.00–0.30. The “histogram” function was then used to obtain the number of positive pixels. Macro to quantify axon densities in Fiji:

```
setOption("ScaleConversions", true);
run("8-bit");
setAutoThreshold("Default dark");
//run("Threshold...");
setThreshold(12, 255);
run("Analyze Particles...", "size=250.00-Infinity
circularity=0.00-0.30 show=Masks display_in_situ");
getHistogram(values, counts, 2);
Array.print(counts);
```

Statistical Analysis

Analyses were performed using GraphPad Prism 9 software (GraphPad Software Inc., San Diego, CA). Significance is indicated as <math><0.05</math> (*), <math><0.001</math> (***) and <math><0.0001</math> (****). A one-way ANOVA was used to compare cell densities or neurofilament stained area across three *Sarm1* genotypes, using independent cultures each generated from a single embryo from a minimum of 3–4 independent litters per analysis. A two-way ANOVA was used to compare NAD⁺ concentrations between mock-infected and infected cultures, across all three genotypes, using independent cultures each generated from a single embryo from 3 independent dams.

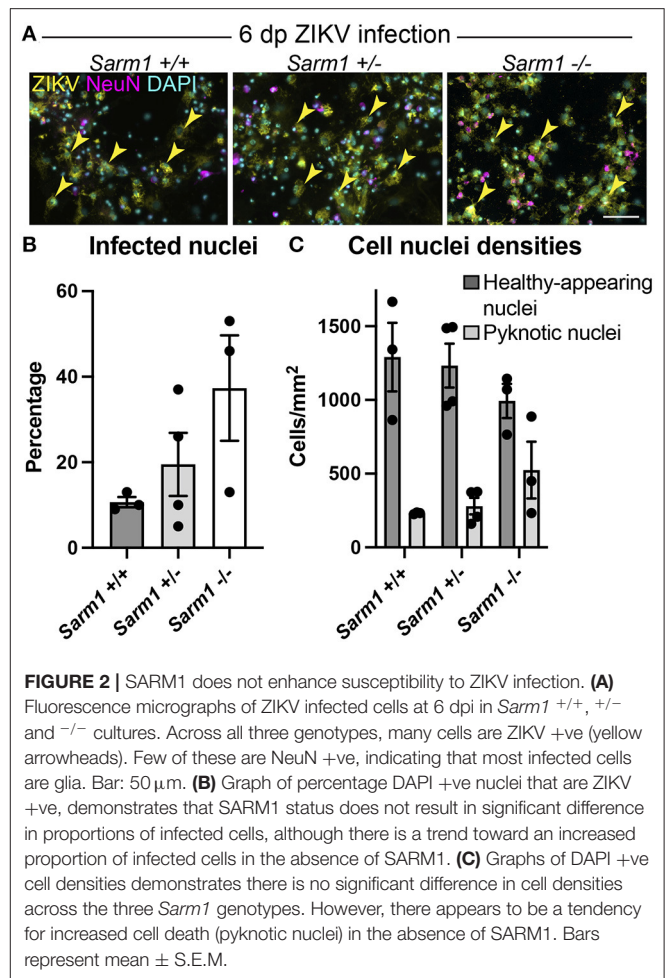
RESULTS

SARM1 Depletion Preserves Axons Following ZIKV Infection

Embryonic murine spinal cord-derived myelinating cell cultures contain all major neural cell types including choline acetyltransferase positive motor neurons that project to the body's periphery *in vivo*, oligodendrocyte progenitors (OPCs), myelinating oligodendrocytes, astrocytes and microglia. To determine if SARM1 depletion (*Sarm1*^{-/-}) or haploinsufficiency (*Sarm1*^{+/-}) conserves axons, we infected cultures generated from *Sarm1*^{+/+} (control), *Sarm1*^{+/-} or *Sarm1*^{-/-} mice with MOI 0.3 or 0.6 ZIKV (Table 1) and stained them with antibody to phosphorylated H- and M-neurofilament or β -tubulin III, at 6 dpi (Figure 1). Quantification of neurofilament staining demonstrated statistically significant preservation of neuronal cell processes in infected *Sarm1*^{-/-} cultures compared to *Sarm1*^{+/+} controls. SARM1 haploinsufficiency conferred no benefit at this time point (Figure 1).

Removing SARM1 Does Not Reduce Susceptibility of Cells to Infection

To confirm that the observed decrease in degeneration of neuronal processes in the absence of SARM1 does not simply reflect reduced infection in *Sarm1*^{-/-} cultures, we quantified the proportion of DAPI +ve cell nuclei (both healthy-appearing and pyknotic) that were ZIKV +ve, in each of the three genotypes. We ruled out a decrease in the proportion of productively infected



cells at 6 dpi, instead, observing a trend toward an increase in the proportion of infected cells in the *Sarm1*^{-/-} cultures (Figures 2A,B). We ruled out the possibility this was due to differences in cell densities between genotypes (Figures 2A,C). Thus, protection of neuronal processes does not result from there being reduced numbers of productively infected cells in the absence of SARM1.

ZIKV Infection Leads to a Rapid Depletion of NAD⁺ Independent of *Sarm1* Genotype

SARM1 is an NADase that depletes axons of NAD⁺ following a variety of insults. Furthermore, the NS3 domain of ZIKV itself has been shown to deplete NAD⁺ by a PARP1-dependent mechanism in HeLa cells (Xu et al., 2019). To determine if there is depletion of NAD⁺ upon ZIKV infection of CNS cells, we first determined a time point to assay NAD⁺ concentrations, prior to overt cellular injury. At 24 hpi, staining of DAPI +ve cell nuclei revealed little difference between infected cultures of either of the three *Sarm1* genotypes and their mock-infected controls (Figures 3A,B and Supplementary Figure 1), suggesting the absence of overt ZIKV infection-related cell death at this time point, as quantified previously (Cumberworth et al.,

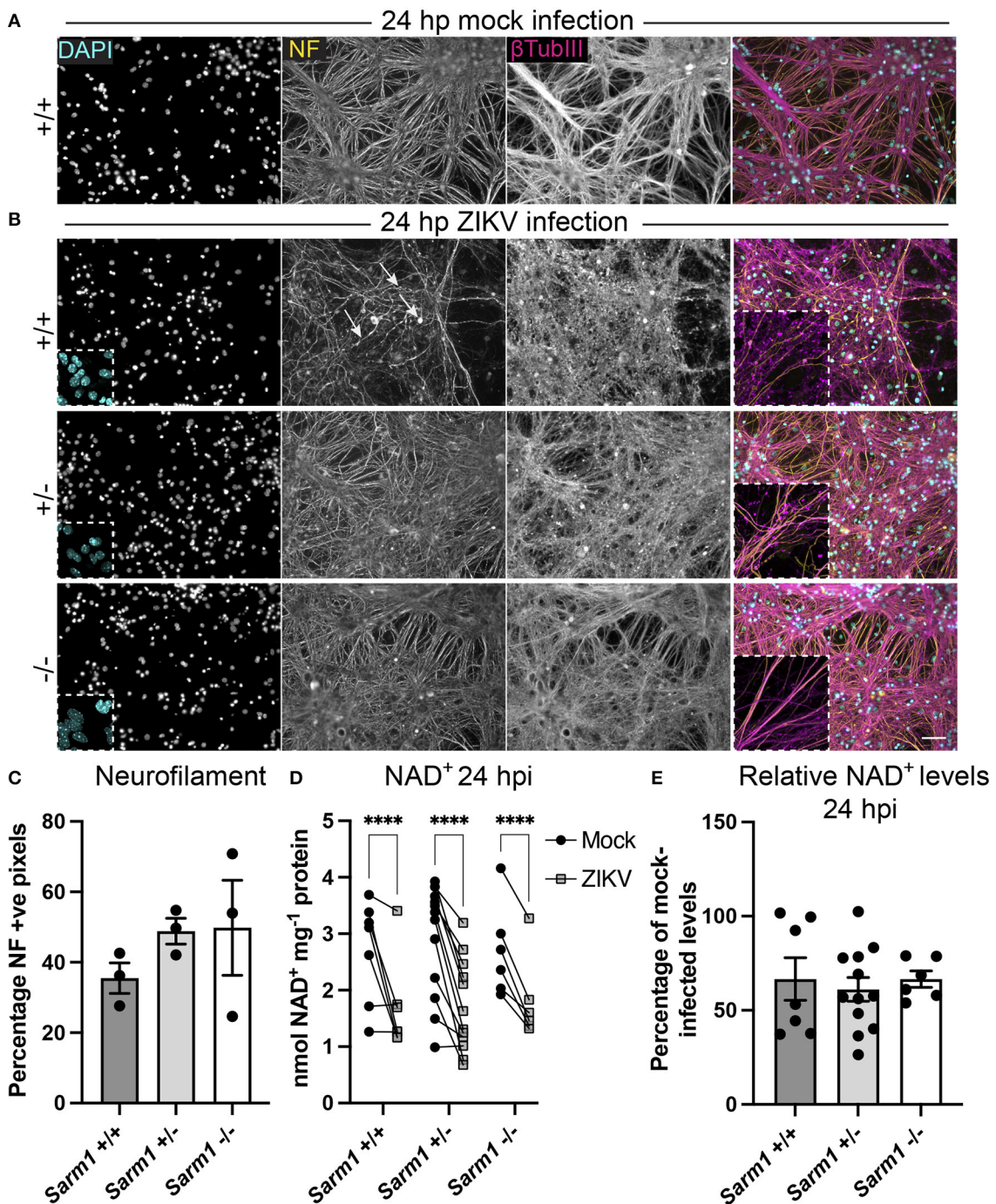


FIGURE 3 | ZIKV infection depletes NAD⁺ levels independent of SARM1 at 24 hpi. **(A)** Mock infected *Sarm1*^{+/+} cultures appear healthy at 24 hpi. DAPI +ve cell nuclei are abundant and neurofilament (NF) and β -tubulin III-stained neuronal processes appear dense and smooth. Bar: 50 μ m. **(B)** At 24 hpi with ZIKV, DAPI +ve cell nuclei appear similar in terms of density and appearance across all three *Sarm1* genotypes, although there is already evidence of subtle injury to neuronal cell processes in *Sarm1*^{+/+} (arrows indicate irregularly stained neurofilament +ve structures) and *Sarm1*^{+/-} cultures, most obvious with β -tubulin III staining. In contrast, neuronal processes in *Sarm1*^{-/-} cultures appear dense and smooth, as in the mock-infected controls (see also **Supplementary Figure 1**). **(C)** Neurofilament positive pixels as a percentage of all pixels per AOI is similar across all three genotypes suggesting that neuronal processes remain viable at this timepoint. **(D)** Compared to levels in matched mock-infected controls (black circles), NAD⁺ levels are significantly reduced in ZIKV-infected cultures (gray squares) at 24 hpi. **(E)** The relative reduction in NAD⁺ in ZIKV infected cultures in comparison to their mock-infected controls is similar across all three genotypes. Bars represent mean \pm S.E.M. **** $p < 0.0001$.

2017). Nonetheless, despite that staining for phosphorylated H- and M-neurofilament (antibody clone SMI31) demonstrated similar positive pixel densities across all the three genotypes (Figure 3C), subtle changes in morphology of some neuronal processes in ZIKV-infected *Sarm1*^{+/+} cultures could be seen at this time point (arrows; Figure 3B). This was confirmed by β -tubulin III staining which provided evidence for fragmentation of the microtubule network in ZIKV-infected *Sarm1*^{+/+} and *Sarm1*^{+/-}, but not *Sarm1*^{-/-} cultures or mock-infected controls (Figures 3A,B and Supplementary Figure 1). Quantification of NAD⁺ levels at 24 hpi demonstrated a similar significant decrease in NAD⁺ levels in ZIKV-infected cultures of each of the three *Sarm1* genotypes, in comparison to their matched mock-infected controls (Figure 3D). The degree of NAD⁺ reduction was most consistent in *Sarm1*^{-/-} cultures and more variable in wild type and heterozygous controls, most particularly when NAD⁺ levels were below 2 nmol/mg⁻¹ protein in mock-infected control cultures. On average, NAD⁺ levels were reduced to ~60% of mock-infected control levels, across all three genotypes (Figure 3E). Together, these data demonstrate that whilst degeneration of neuronal processes is expedited by SARM1, NAD⁺ depletion at 24 hpi is independent of SARM1. NAD⁺ levels were not assessed at later time points due to confounding consequences of leakage of NAD⁺ from dying cells and injured axons.

SARM1-Dependent Degeneration of Neuronal Cell Processes Preserves Neuronal Somas

As some neurotropic viruses use microtubule-dependent axon transport to reach the neuronal soma, the changes observed in microtubule staining at 24 hpi led us to ask whether SARM1-dependent mechanisms might limit infection of neuronal somas. To address this, we examined infected NeuN +ve somas across the three *Sarm1* genotypes (Figure 4A). Compared to *Sarm1*^{+/+}, we observed a significant increase in the proportion of infected neuronal somas in *Sarm1*^{-/-} cultures and a similar trend in *Sarm1*^{+/-} cultures (Figure 4B), that did not reflect differences in the total number of NeuN positive cells of any genotype (Figure 4C). Correspondingly, we observed a significant increase in the proportion of pyknotic neurons in *Sarm1*^{-/-} cultures compared to *Sarm1*^{+/+} cultures. *Sarm1*^{+/-} cultures had, on average, an intermediate proportion of pyknotic neurons, likely reflecting SARM1 haploinsufficiency (Figure 4D). Together, these data suggest that SARM1-dependent degeneration of neuronal processes limits infection and death of neuronal somas.

DISCUSSION

Our data provide novel evidence of a SARM1-dependent mechanism of degeneration of neuronal processes following ZIKV infection. Further, this involves neither an increase in ZIKV infected cells nor increased susceptibility of neuronal somas to cell death. On the contrary, at least at the time point tested, the proportions of infected and/or dying neurons were significantly enhanced in the absence of SARM1. Furthermore,

we provide evidence in primary CNS cell cultures for the physiological relevance of a previous report of ZIKV-induced NAD⁺ depletion in HeLa cells (Xu et al., 2019). Surprisingly, although NAD⁺ depletion has been suggested to make SARM1 activation more likely (Figley et al., 2021) we found no clear evidence of any additional depletion of NAD⁺ under conditions (ZIKV-infection) where SARM1 contributes to axon loss. Indeed, since most infected cells in our mixed neural cell cultures are glia (Cumberworth et al., 2017), it may be that depletion of glial NAD⁺ makes the largest contribution to the fall we observed. Irrespective of the cellular localization of NAD⁺ depletion, it appears that the mechanism by which SARM1 contributes to degeneration of neuronal processes following ZIKV infection is independent of its NADase activity.

One possible explanation for these findings is that degeneration of neuronal processes in this context could result from one of the additional enzyme activities of SARM1, which include NADP hydrolysis and cyclisation, and base exchange of nicotinamide of NAD(P) with other endogenous pyridine bases such as nicotinic acid (Zhao et al., 2019; Angeletti et al., 2021; Figley et al., 2021). These may lead to reduced ROS buffering capability due to lowering of NADPH, or to calcium mobilization due to generation of NaADP, the most potent known calcium mobilizing signal (Galione et al., 2000; Angeletti et al., 2021). Indeed, a *circa* 50% decline in NAD⁺, as observed here at 24 hpi, is not sufficient to kill axons or cells since doses of NAMPT inhibitor FK866 that depletes NAD⁺ to or beyond this level, are not lethal (Di Stefano et al., 2015). Transected *Sarm1*^{-/-} sciatic nerve axons also survive more than a week after the fall in NAD⁺ passes 50% of basal levels (Gilley et al., 2015). Thus, it will be important to investigate these other potential mediators of SARM1 activity, or indeed any novel activities that are found for this multifunctional enzyme, in future work.

One limitation of our study is that the NAD⁺ assay is based on cell culture lysates and therefore it cannot discriminate cell or cell compartment-specific effects. Regarding this, it is worth noting that ZIKV protein NS3 itself potently activates a nuclear poly (ADP-ribose) polymerase, PARP1, in HeLa and glioma cells that results in NAD⁺ depletion and cell death at 48 h post-treatment in the former (Xu et al., 2019). As PARP1 is also one of the main NAD⁺ consuming enzymes in neural cells (Klimova and Kristian, 2019), it seems reasonable to speculate that it is responsible for the *circa* 50% NAD⁺ depletion at 24 hpi in our ZIKV infected neural cell cultures. Consequently, we cannot exclude the possibility that a SARM1-dependent depletion of NAD⁺ specifically in neuronal processes is masked in these mixed neural cell type cultures. We also cannot rule out a SARM1-dependent fall in NAD⁺ at later timepoints, rapidly followed by degeneration of neuronal processes, since if this were to happen it would be confounded by cell death and extremely difficult to capture the optimal time point to detect it.

Degeneration of neuronal processes following ZIKV infection occurs independently of overt infection or death of neuronal somas in *Sarm1* wild type cultures [the current study and Cumberworth et al. (2017)]. This raises the intriguing possibility that it represents a neuroprotective mechanism designed to limit

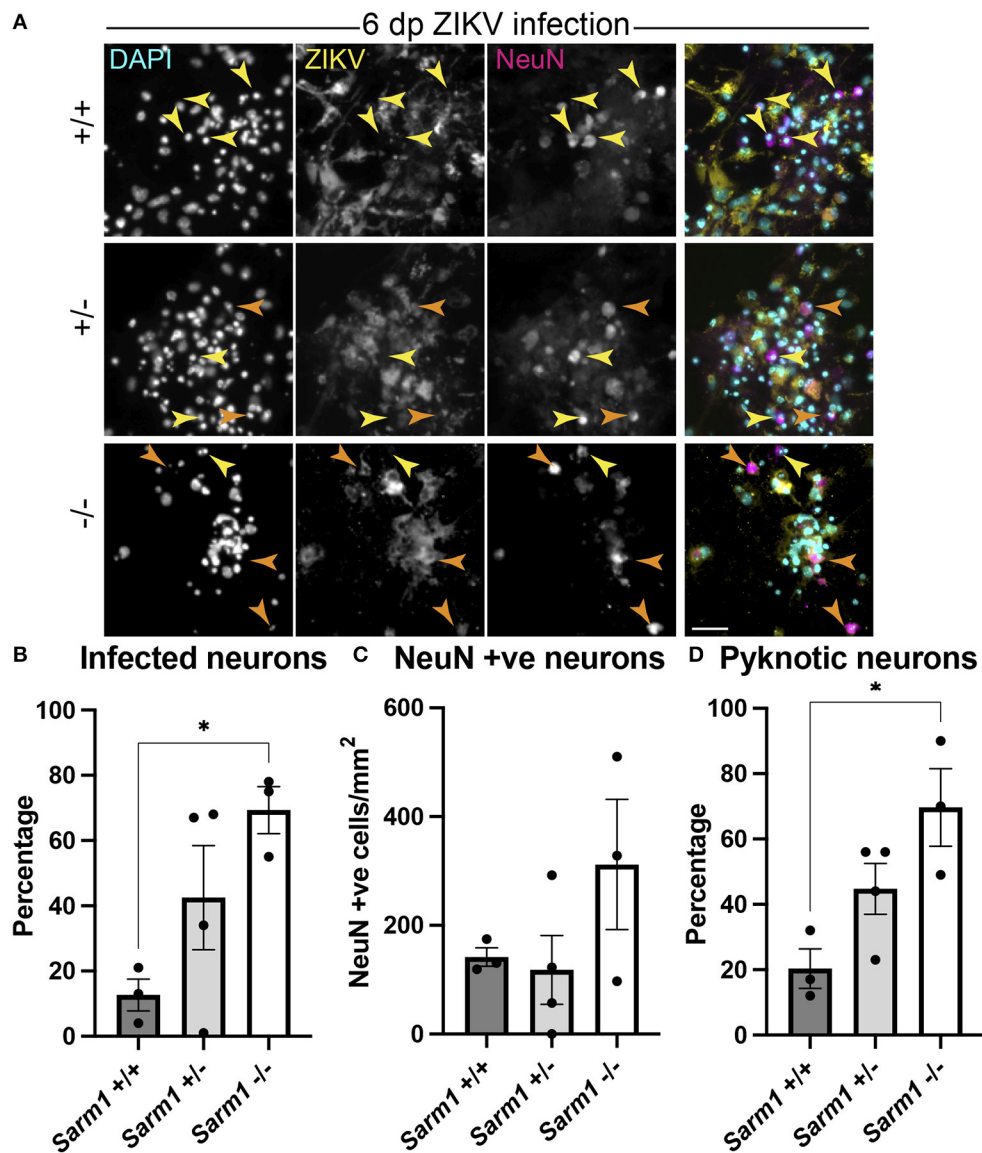


FIGURE 4 | SARM1-dependent degeneration of neuronal processes limits infection and death of neurons. **(A)** Fluorescence micrographs of ZIKV infected *Sarm1*^{+/+}, *Sarm1*^{+/-} and *Sarm1*^{-/-} cultures at 6 dpi. In wild type cultures (*Sarm1*^{+/+}), most NeuN +ve neurons are not ZIKV +ve (yellow arrowheads) whereas in *Sarm1*^{-/-} cultures, many NeuN +ve neurons are ZIKV +ve (orange arrowheads). In *Sarm1*^{+/-} cultures, both ZIKV +ve (orange arrowheads) and -ve (yellow arrowheads) NeuN +ve cells are evident. Bar: 50 μ m. **(B)** Graph of proportions of NeuN +ve infected cells, demonstrates a significantly greater proportion of NeuN +ve neurons are ZIKV +ve in *Sarm1*^{-/-} cultures compared to *Sarm1*^{+/+} control. **(C)** This does not reflect a significant difference in NeuN +ve cell densities in *Sarm1*^{-/-} cultures compared to *Sarm1*^{+/+} controls. **(D)** There is a significant increase in the proportion of pyknotic NeuN +ve nuclei in *Sarm1*^{-/-} cultures compared to *Sarm1*^{+/+} controls. Bars represent mean \pm S.E.M. * $p < 0.05$ (defined in M&M).

viral spread, as proposed previously (Mukherjee et al., 2013; Sundaramoorthy et al., 2020). Neuronal processes, especially axons, are highly reliant on microtubule-dependent transport for function and survival (De Vos et al., 2008; Magiera et al., 2018; Guedes-Dias and Holzbaur, 2019; Kelliher et al., 2019; Koppers and Fariás, 2021), and several neurotropic viruses including Theiler's virus, herpes simplex virus, poliovirus, rabies virus, and West Nile virus (WNV), transit in axons, likely relying on microtubule-dependent transport to reach their targets (Salinas

et al., 2009 and reviewed in Richards et al., 2021). Thus, the significant increase in infection and death of neuronal somas in SARM1-depleted cultures (with delayed degeneration of neuronal processes) suggests that ZIKV can be transported in this way too and that SARM1-dependent degeneration of neuronal processes limits its spread to neuronal somas. Nonetheless, the possibility that the SARM1-dependent intrinsic immune capacity of neurons (Wang et al., 2018) protects these cells in *Sarm1*^{+/+} cultures, should not be discounted.

It is noteworthy that widespread changes in neuronal-specific β -tubulin III immunostaining were observed as early as 24 h post-ZIKV infection. This raises the intriguing possibility that, more generally, activation of evolutionarily conserved SARM1 hampers the retrograde transportation of some viruses from the site of entry at the body's periphery, even prior to axon destruction. In support of this suggestion is the fact that SARM1 participates in microtubule posttranslational modification (Chen et al., 2011), suggesting that activation of SARM1 could have a rapid impact on motor protein binding and cargo (including virus) transport.

The initial trigger for SARM1-dependent degeneration of neuronal processes following ZIKV infection could act through gain or loss of function, for example, through cytotoxicity, failure of trophic support from neighboring glia, or a combination of both. If a soluble cytotoxic factor is involved, neuronal processes seem particularly susceptible since all cell types are, in principle, equally exposed in cell culture where they are bathed in media. Nitric oxide is one potential cytotoxic molecule that causes Wallerian degeneration changes in electrically active axons at low micromolar concentrations (Smith et al., 2001). Failure of support from oligodendrocytes and astrocytes (Stassart et al., 2018; Duncan et al., 2021; Veloz Castillo et al., 2021) infected with ZIKV is another possibility. These cells provide energy metabolites to neurons (Pellerin et al., 1998; Fünfschilling et al., 2012; Lee et al., 2012), although energy insufficiency due to failed energy substrate provision is unlikely in this context because neuronal processes are suffused in a glucose-rich media *in vitro*. Nonetheless, oligodendrocytes and astrocytes confer axon support through multiple mechanisms that could be relevant in the context of ZIKV infection, such as regulating ion and glutamate homeostasis (Verkhatsky and Nedergaard, 2018; Hart and Karimi-Abdolrezaee, 2021), performing anti-oxidant functions (Baxter and Hardingham, 2016; Mukherjee et al., 2020), and enhancing axonal energy metabolism by deacetylating mitochondrial proteins (Chamberlain et al., 2021).

CNS complications of ZIKV infection in adults are rare, but include encephalitis, meningitis, myelitis, meningoencephalitis, transverse myelitis and neuropsychiatric symptoms (Carteaux et al., 2016; Galliez et al., 2016; Mécharles et al., 2016; da Silva et al., 2017; Zucker et al., 2017; Brito Ferreira et al., 2020). However, ZIKV infection has been linked to the peripheral neuropathy, Guillain-Barré syndrome (Oehler et al., 2014; Pinto-Díaz et al., 2017). Roles for SARM1 in other viral neuropathies have been reported. Mice lacking SARM1 are more susceptible to WNV infection, with reduced survival and enhanced neuronal death in the brainstem (Szretter et al., 2009), and this has been confirmed in a new CRISPR/Cas9-generated SARM1 null mouse that excludes any contribution from passenger mutations co-inherited with SARM1 from the original 129 strain ES cells (Uccellini et al., 2020). Similarly, a recent study demonstrated that different field strains of lyssavirus ("rabies") cause SARM1-dependent axon degeneration in CNS and PNS mouse neurons, further supporting a role of SARM1

in neurotropic viral infection (Sundaramoorthy et al., 2020). The authors showed that the SARM1-mediated axon loss prevents the spread of virus along interconnected neurons, suggesting a possible host-defense mechanism restricting virus infection. The subsequent loss of neuronal processes in this and our study, possibly as a result of such a neuronal defense response, would be consistent with our observation that ZIKV-induced neuronal soma death increases in the absence of SARM1, and could thus represent a mechanism underlying neurological complications in rabies and ZIKV infection. It may even help to explain the evolutionary advantage of a mechanism for rapid axon degeneration, which otherwise appears paradoxical. It will be of great interest to further understand the effects of these and other viruses on SARM1-dependent axon loss, on NAD^+ levels, and the roles of these mechanisms in viral neuropathies.

DATA AVAILABILITY STATEMENT

The original contributions presented in the study are included in the article/**Supplementary Materials**, further inquiries can be directed to the corresponding author.

ETHICS STATEMENT

The animal study was reviewed and approved by Ethics Review Committee of the University of Glasgow.

AUTHOR CONTRIBUTIONS

JE and MC: study design and supervision. CC, CA, LK, and VS: experimentation. CD: viral propagation. PM: genotyping. CC, LK, and JE: data analysis. JE, MC, CA, and CC: manuscript draft. JE, CC, and LK: figure composition. All authors: manuscript editing and approval. HW, JE, AK, MC, SB, and CL: funding. All authors contributed to the article and approved the submitted version.

FUNDING

This project was partially funded through the European Union's Horizon 2020 research and innovation programme under ZikaPLAN Grant Agreement No. 734584 (HW, JE, SB, and CL); the UK Medical Research Council (MC_UU_12014/8 and MR/N017552/1) (AK); CSO and University of Glasgow SPRINT PhD programme studentship to CLC (JE); an MRC DTP Award and Gates Scholarship (CA); the John and Lucille van Geest Foundation (MC).

SUPPLEMENTARY MATERIAL

The Supplementary Material for this article can be found online at: <https://www.frontiersin.org/articles/10.3389/fnmol.2022.860410/full#supplementary-material>

REFERENCES

- Angeletti, C., Amici, A., Gilley, J., Loreto, A., Trapanotto, A. G., Antoniou, C., et al. (2021). SARM1 is a multi-functional NAD(P)ase with prominent base exchange activity, all regulated by multiple physiologically-relevant NAD metabolites. *iScience*. 25:103812. doi: 10.1016/j.isci.2022.103812
- Baud, D., Musso, D., Vouga, M., Alves, M. P., and Vulliamoz, N. (2017). Zika virus: a new threat to human reproduction. *Am. J. Reprod. Immunol.* 77. doi: 10.1111/aji.12614
- Baxter, P. S., and Hardingham, G. E. (2016). Adaptive regulation of the brain's antioxidant defences by neurons and astrocytes. *Free Radic. Biol. Med.* 100, 147–152. doi: 10.1016/j.freeradbiomed.2016.06.027
- Bijland, S., Thomson, G., Euston, M., Michail, K., Thümmel, K., Mücklich, S., et al. (2019). An in vitro model for studying CNS white matter: functional properties and experimental approaches. [version 1; peer review: 2 approved]. *F1000Research* 8, 117. doi: 10.12688/f1000research.16802.1
- Brito Ferreira, M. L., Militão de Albuquerque, M. de F. P., de Brito, C. A. A., de Oliveira França, R. F., Porto Moreira, Á. J., de Moraes Machado, et al. (2020). Neurological disease in adults with Zika and chikungunya virus infection in Northeast Brazil: a prospective observational study. *Lancet Neurol.* 19, 826–839. doi: 10.1016/S1474-4422(20)30232-5
- Carteaux, G., Maquart, M., Bedet, A., Contou, D., Brugières, P., Fourati, S., et al. (2016). Zika Virus associated with meningoencephalitis. *N. Engl. J. Med.* 374, 1595–1596. doi: 10.1056/NEJMc1602964
- Carty, M., and Bowie, A. G. (2019). SARM: from immune regulator to cell executioner. *Biochem. Pharmacol.* 161, 52–62. doi: 10.1016/j.bcp.2019.01.005
- Carty, M., Goodbody, R., Schröder, M., Stack, J., Moynagh, P. N., and Bowie, A. G. (2006). The human adaptor SARM negatively regulates adaptor protein TRIF-dependent Toll-like receptor signaling. *Nat. Immunol.* 7, 1074–1081. doi: 10.1038/ni1382
- Chamberlain, K. A., Huang, N., Xie, Y., LiCausi, F., Li, S., Li, Y., et al. (2021). Oligodendrocytes enhance axonal energy metabolism by deacetylation of mitochondrial proteins through transcellular delivery of SIRT2. *Neuron* 109, 3456–3472.e8. doi: 10.1016/j.neuron.2021.08.011
- Chen, C.-Y., Lin, C.-W., Chang, C.-Y., Jiang, S.-T., and Hsueh, Y.-P. (2011). *Sarm1*, a negative regulator of innate immunity, interacts with syndecan-2 and regulates neuronal morphology. *J. Cell Biol.* 193, 769–784. doi: 10.1083/jcb.201008050
- Coleman, M. P., and Höke, A. (2020). Programmed axon degeneration: from mouse to mechanism to medicine. *Nat. Rev. Neurosci.* 21, 183–196. doi: 10.1038/s41583-020-0269-3
- Conforti, L., Gilley, J., and Coleman, M. P. (2014). Wallerian degeneration: an emerging axon death pathway linking injury and disease. *Nat. Rev. Neurosci.* 15, 394–409. doi: 10.1038/nrn3680
- Cumberworth, S. L., Barrie, J. A., Cunningham, M. E., de Figueiredo, D. P. G., Schultz, V., Wilder-Smith, A. J., et al. (2017). Zika virus tropism and interactions in myelinating neural cell cultures: CNS cells and myelin are preferentially affected. *Acta Neuropathol. Commun.* 5, 50. doi: 10.1186/s40478-017-0450-8
- Cummings, B. S., and Schnellmann, R. G. (2004). Measurement of cell death in mammalian cells. *Curr. Protoc. Pharmacol.* Chapter 12, Unit 12.18. doi: 10.1002/0471141755.ph1208s25
- da Silva, I. R. F., Frontera, J. A., Bispo de Filippis, A. M., Nascimento, O. J. M. do, and RIO-GBS-ZIKV Research Group (2017). Neurologic complications associated with the Zika virus in Brazilian adults. *JAMA Neurol.* 74, 1190–1198. doi: 10.1001/jamaneurol.2017.1703
- De Vos, K. J., Grierson, A. J., Ackerley, S., and Miller, C. C. J. (2008). Role of axonal transport in neurodegenerative diseases. *Annu. Rev. Neurosci.* 31, 151–173. doi: 10.1146/annurev.neuro.31.061307.090711
- Di Stefano, M., Nascimento-Ferreira, I., Orsomando, G., Mori, V., Gilley, J., Brown, R., et al. (2015). A rise in NAD precursor nicotinamide mononucleotide (NMN) after injury promotes axon degeneration. *Cell Death Differ.* 22, 731–742. doi: 10.1038/cdd.2014.164
- Donald, C. L., Brennan, B., Cumberworth, S. L., Rezelj, V. V., Clark, J. J., Cordeiro, M. T., et al. (2016). Full genome sequence and sRNA interferon antagonist activity of Zika virus from Recife, Brazil. *PLoS Negl. Trop. Dis.* 10, e0005048. doi: 10.1371/journal.pntd.0005048
- Duncan, G. J., Simkins, T. J., and Emery, B. (2021). Neuron-oligodendrocyte interactions in the structure and integrity of axons. *Front. Cell Dev. Biol.* 9, 653101. doi: 10.3389/fcell.2021.653101
- Essuman, K., Summers, D. W., Sasaki, Y., Mao, X., DiAntonio, A., and Milbrandt, J. (2017). The SARM1 toll/interleukin-1 receptor domain possesses intrinsic nad⁺ cleavage activity that promotes pathological axonal degeneration. *Neuron* 93, 1334–1343.e5. doi: 10.1016/j.neuron.2017.02.022
- Figley, M. D., Gu, W., Nanson, J. D., Shi, Y., Sasaki, Y., Cunnea, K., et al. (2021). SARM1 is a metabolic sensor activated by an increased NMN/NAD⁺ ratio to trigger axon degeneration. *Neuron* 109, 1118–1136.e11. doi: 10.1016/j.neuron.2021.02.009
- Fünfschilling, U., Supplie, L. M., Mahad, D., Boretius, S., Saab, A. S., Edgar, J., et al. (2012). Glycolytic oligodendrocytes maintain myelin and long-term axonal integrity. *Nature* 485, 517–521. doi: 10.1038/nature11007
- Galione, A., Patel, S., and Churchill, G. C. (2000). NAADP-induced calcium release in sea urchin eggs. *Biol. Cell* 92, 197–204. doi: 10.1016/S0248-4900(00)01070-4
- Galliez, R. M., Spitz, M., Rafful, P. P., Cagy, M., Escosteguy, C., Germano, C. S. B., et al. (2016). Zika virus causing encephalomyelitis associated with immunoactivation. *Open Forum Infect. Dis.* 3, ofw203. doi: 10.1093/ofid/ofw203
- Gilley, J., Orsomando, G., Nascimento-Ferreira, I., and Coleman, M. P. (2015). Absence of SARM1 rescues development and survival of NMNAT2-deficient axons. *Cell Rep.* 10, 1974–1981. doi: 10.1016/j.celrep.2015.02.060
- Gubler, D. J., Vasilakis, N., and Musso, D. (2017). History and emergence of Zika virus. *J. Infect. Dis.* 216, S860–S867. doi: 10.1093/infdis/jix451
- Guedes-Dias, P., and Holzbaur, E. L. F. (2019). Axonal transport: driving synaptic function. *Science* 366, eaaw9997. doi: 10.1126/science.aaw9997
- Gulland, A. (2016). Zika virus is a global public health emergency, declares WHO. *BMJ* 352, i657. doi: 10.1136/bmj.i657
- Hart, C. G., and Karimi-Abdolrezaee, S. (2021). Recent insights on astrocyte mechanisms in CNS homeostasis, pathology, and repair. *J. Neurosci. Res.* 99, 2427–2462. doi: 10.1002/jnr.24922
- Hopkins, E. L., Gu, W., Kobe, B., and Coleman, M. P. (2021). A novel NAD signaling mechanism in axon degeneration and its relationship to innate immunity. *Front. Mol. Biosci.* 8, 703532. doi: 10.3389/fmolb.2021.703532
- Horsefield, S., Burdett, H., Zhang, X., Manik, M. K., Shi, Y., Chen, J., et al. (2019). NAD⁺ cleavage activity by animal and plant TIR domains in cell death pathways. *Science* 365, 793–799. doi: 10.1126/science.aax1911
- Kelliher, M. T., Saunders, H. A., and Wildonger, J. (2019). Microtubule control of functional architecture in neurons. *Curr. Opin. Neurobiol.* 57, 39–45. doi: 10.1016/j.conb.2019.01.003
- Kim, Y., Zhou, P., Qian, L., Chuang, J.-Z., Lee, J., Li, C., et al. (2007). MyD88-5 links mitochondria, microtubules, and JNK3 in neurons and regulates neuronal survival. *J. Exp. Med.* 204, 2063–2074. doi: 10.1084/jem.20070868
- Klimova, N., and Kristian, T. (2019). Multi-targeted effect of nicotinamide mononucleotide on brain bioenergetic metabolism. *Neurochem. Res.* 44, 2280–2287. doi: 10.1007/s11064-019-02729-0
- Koppers, M., and Farias, G. G. (2021). Organelle distribution in neurons: logistics behind polarized transport. *Curr. Opin. Cell Biol.* 71, 46–54. doi: 10.1016/j.celb.2021.02.004
- Lee, Y., Morrison, B. M., Li, Y., Lengacher, S., Farah, M. H., Hoffman, P. N., et al. (2012). Oligodendroglia metabolically support axons and contribute to neurodegeneration. *Nature* 487, 443–448. doi: 10.1038/nature11314
- Lin, C.-W., Liu, H.-Y., Chen, C.-Y., and Hsueh, Y.-P. (2014). Neuronally-expressed *Sarm1* regulates expression of inflammatory and antiviral cytokines in brains. *Innate Immun.* 20, 161–172. doi: 10.1177/1753425913485877
- Magiera, M. M., Bodakuntla, S., Žiak, J., Lacomme, S., Marques Sousa, P., Leboucher, S., et al. (2018). Excessive tubulin polyglutamylolation causes neurodegeneration and perturbs neuronal transport. *EMBO J.* 37, e100440. doi: 10.15252/embj.2018100440
- Mécharles, S., Herrmann, C., Poullain, P., Tran, T.-H., Deschamps, N., Mathon, G., et al. (2016). Acute myelitis due to Zika virus infection. *Lancet* 387, 1481. doi: 10.1016/S0140-6736(16)00644-9
- Miner, J. J., and Diamond, M. S. (2017). Zika virus pathogenesis and tissue tropism. *Cell Host Microbe* 21, 134–142. doi: 10.1016/j.chom.2017.01.004
- Mukherjee, C., Kling, T., Russo, B., Miebach, K., Kess, E., Schifferer, M., et al. (2020). Oligodendrocytes provide antioxidant defense function for

- neurons by secreting ferritin heavy chain. *Cell Metab.* 32, 259–272. doi: 10.1016/j.cmet.2020.05.019
- Mukherjee, P., Woods, T. A., Moore, R. A., and Peterson, K. E. (2013). Activation of the innate signaling molecule MAVS by bunyavirus infection upregulates the adaptor protein SARM1, leading to neuronal death. *Immunity* 38, 705–716. doi: 10.1016/j.immuni.2013.02.013
- Oehler, E., Watrin, L., Larre, P., Lepercq-Goffart, I., Lastère, S., Valour, F., et al. (2014). Zika virus infection complicated by Guillain-Barré syndrome – case report, French Polynesia, December 2013. *Eurosurveillance* 19, 20720. doi: 10.2807/1560-7917.ES2014.19.9.20720
- Osterloh, J. M., Yang, J., Rooney, T. M., Fox, A. N., Adalbert, R., Powell, E. H., et al. (2012). dSarm/Sarm1 is required for activation of an injury-induced axon death pathway. *Science* 337, 481–484. doi: 10.1126/science.1223899
- Pardy, R. D., and Richer, M. J. (2019). Zika virus pathogenesis: from early case reports to epidemics. *Viruses* 11, 886. doi: 10.3390/v11100886
- Pellerin, L., Pellegrini, G., Bittar, P. G., Charnay, Y., Bouras, C., Martin, J. L., et al. (1998). Evidence supporting the existence of an activity-dependent astrocyte-neuron lactate shuttle. *Dev. Neurosci.* 20, 291–299. doi: 10.1159/000017324
- Pierson, T. C., and Diamond, M. S. (2018). The emergence of Zika virus and its new clinical syndromes. *Nature* 560, 573–581. doi: 10.1038/s41586-018-0446-y
- Pinto-Díaz, C. A., Rodríguez, Y., Monsalve, D. M., Acosta-Ampudia, Y., Molano-González, N., Anaya, J.-M., et al. (2017). Autoimmunity in Guillain-Barré syndrome associated with Zika virus infection and beyond. *Autoimmun. Rev.* 16, 327–334. doi: 10.1016/j.autrev.2017.02.002
- Richards, A., Berth, S. H., Brady, S., and Morfini, G. (2021). Engagement of neurotropic viruses in fast axonal transport: mechanisms, potential role of host kinases and implications for neuronal dysfunction. *Front. Cell. Neurosci.* 15, 684762. doi: 10.3389/fncel.2021.684762
- Salinas, S., Bilsland, L. G., Henaff, D., Weston, A. E., Keriell, A., Schiavo, G., et al. (2009). CAR-associated vesicular transport of an adenovirus in motor neuron axons. *PLoS Pathog.* 5, e1000442. doi: 10.1371/journal.ppat.1000442
- Schindelin, J., Arganda-Carreras, I., Frise, E., Kaynig, V., Longair, M., Pietzsch, T., et al. (2012). Fiji: an open-source platform for biological-image analysis. *Nat. Methods* 9, 676–682. doi: 10.1038/nmeth.2019
- Schultz, V., Cumberworth, S. L., Gu, Q., Johnson, N., Donald, C. L., McCanney, G. A., et al. (2021). Zika virus infection leads to demyelination and axonal injury in mature CNS cultures. *Viruses* 13. doi: 10.3390/v13010091
- Smith, K. J., Kapoor, R., Hall, S. M., and Davies, M. (2001). Electrically active axons degenerate when exposed to nitric oxide. *Ann. Neurol.* 49, 470–476. doi: 10.1002/ana.96
- Stassart, R. M., Möbius, W., Nave, K.-A., and Edgar, J. M. (2018). The axonmyelin unit in development and degenerative disease. *Front. Neurosci.* 12, 467. doi: 10.3389/fnins.2018.00467
- Sundaramoorthy, V., Green, D., Locke, K., O'Brien, C. M., Dearnley, M., and Bingham, J. (2020). Novel role of SARM1 mediated axonal degeneration in the pathogenesis of rabies. *PLoS Pathog.* 16, e1008343. doi: 10.1371/journal.ppat.1008343
- Szretter, K. J., Samuel, M. A., Gilfillan, S., Fuchs, A., Colonna, M., and Diamond, M. S. (2009). The immune adaptor molecule SARM modulates tumor necrosis factor alpha production and microglia activation in the brainstem and restricts West Nile Virus pathogenesis. *J. Virol.* 83, 9329–9338. doi: 10.1128/JVI.00836-09
- Thomson, C. E., Hunter, A. M., Griffiths, I. R., Edgar, J. M., and McCulloch, M. C. (2006). Murine spinal cord explants: a model for evaluating axonal growth and myelination in vitro. *J. Neurosci. Res.* 84, 1703–1715. doi: 10.1002/jnr.21084
- Truett, G. E., Heeger, P., Mynatt, R. L., Truett, A. A., Walker, J. A., and Warman, M. L. (2000). Preparation of PCR-quality mouse genomic DNA with hot sodium hydroxide and tris (HotSHOT). *BioTechniques* 29, 52–54. doi: 10.2144/00291bm09
- Uccellini, M. B., Bardina, S. V., Sánchez-Aparicio, M. T., White, K. M., Hou, Y.-J., Lim, J. K., et al. (2020). Passenger mutations confound phenotypes of SARM1-deficient mice. *Cell Rep.* 31, 107498. doi: 10.1016/j.celrep.2020.03.062
- Veloz Castillo, M. F., Magistretti, P. J., and Calì, C. (2021). l-lactate: food for thoughts, memory and behavior. *Metabolites* 11, 548. doi: 10.3390/metabo11080548
- Verkhratsky, A., and Nedergaard, M. (2018). Physiology of astroglia. *Physiol. Rev.* 98, 239–389. doi: 10.1152/physrev.00042.2016
- Wang, Q., Zhang, S., Liu, T., Wang, H., Liu, K., Wang, Q., et al. (2018). Sarm1/Myd88-5 regulates neuronal intrinsic immune response to traumatic axonal injuries. *Cell Rep.* 23, 716–724. doi: 10.1016/j.celrep.2018.03.071
- Xu, G., Li, S., Liu, X., Gao, P., Chen, X., Wang, H., et al. (2019). PARP-1 mediated cell death is directly activated by ZIKV infection. *Virology* 537, 254–262. doi: 10.1016/j.virol.2019.08.024
- Zhao, Z. Y., Xie, X. J., Li, W. H., Liu, J., Chen, Z., Zhang, B., et al. (2019). A cell-permeant mimetic of NMN activates SARM1 to produce cyclic ADP-ribose and induce non-apoptotic cell death. *iScience* 15, 452–466. doi: 10.1016/j.isci.2019.05.001
- Zucker, J., Neu, N., Chiriboga, C. A., Hinton, V. J., Leonardo, M., Sheikh, A., et al. (2017). Zika virus-associated cognitive impairment in adolescent, 2016. *Emerg. Infect. Dis.* 23, 1047–1048. doi: 10.3201/eid2306.162029

Conflict of Interest: The authors declare that the research was conducted in the absence of any commercial or financial relationships that could be construed as a potential conflict of interest.

Publisher's Note: All claims expressed in this article are solely those of the authors and do not necessarily represent those of their affiliated organizations, or those of the publisher, the editors and the reviewers. Any product that may be evaluated in this article, or claim that may be made by its manufacturer, is not guaranteed or endorsed by the publisher.

Copyright © 2022 Crawford, Antoniou, Komarek, Schultz, Donald, Montague, Barnett, Linington, Willison, Kohl, Coleman and Edgar. This is an open-access article distributed under the terms of the Creative Commons Attribution License (CC BY). The use, distribution or reproduction in other forums is permitted, provided the original author(s) and the copyright owner(s) are credited and that the original publication in this journal is cited, in accordance with accepted academic practice. No use, distribution or reproduction is permitted which does not comply with these terms.

Advantages of publishing in Frontiers



OPEN ACCESS

Articles are free to read for greatest visibility and readership



FAST PUBLICATION

Around 90 days from submission to decision



HIGH QUALITY PEER-REVIEW

Rigorous, collaborative, and constructive peer-review



TRANSPARENT PEER-REVIEW

Editors and reviewers acknowledged by name on published articles

Frontiers

Avenue du Tribunal-Fédéral 34
1005 Lausanne | Switzerland

Visit us: www.frontiersin.org

Contact us: frontiersin.org/about/contact



REPRODUCIBILITY OF RESEARCH

Support open data and methods to enhance research reproducibility



DIGITAL PUBLISHING

Articles designed for optimal readership across devices



FOLLOW US

@frontiersin



IMPACT METRICS

Advanced article metrics track visibility across digital media



EXTENSIVE PROMOTION

Marketing and promotion of impactful research



LOOP RESEARCH NETWORK

Our network increases your article's readership